Synthesis and Coordination Chemistry of Multidentate Ligands Based on Nitrogen-Containing Heterocyclic Phenanthridine Moieties

by

Rajarshi Mondal

A Thesis submitted to the Faculty of Graduate Studies of

The University of Manitoba

in partial fulfilment of the requirements of the degree of

Doctor of Philosophy

Department of Chemistry

University of Manitoba

Winnipeg

To my parents and Tunu & Zunu

Abstract:

This project explored the synthesis of bi-functional neutral donor ligands using π-extended phenanthridine system which can stabilize the late transition metals. My interest would be the phenanthridine ring of 14 π-electron polycyclic heteroaromatic system, which is the building block of my ligands and the properties of this extended aromatic system while binding with late transition metals and comparing with smaller congener quinoline precursor for understanding the effect of site dependent π extension. The application and properties of designed metal complexes have been extensively studied. The study of using π-extended phenanthridine as a ligand and its metal complexes would open a new window of opportunities.

A synthetic route to bromo functionalization of benzo-fused N-heterocyclic phenanthridine, enabling the constructions of both phosphinophenanthridine and NHC carbene-phenanthridine have been devised, which are heterobifunctional Lewis base containing both phosphine/carbene and phenanthridine donors. The coordination chemistry for both phosphine/carbene ligands with ions of late first-row transition metals has been explored.

4-Bromophenanthridine was synthesized by Suzuki cross-coupling/condensation, 6-substitution was conducted by reaction between phenanthridinone and phosphine(V) oxyhalide. The installation of phosphine was directed by lithium-halogen exchange of 4-bromophenanthridine. The carbenes were placed by the reaction between 6-halophenanthridine and corresponding imidazole in high temperature.

A series of halide bridge Cu complexes were synthesized using phosphino-phenanthridine ligand to check the effect of site selective π-extension on emission property by comparing with smaller congener quinoline based Cu complexes. Further study leads to design of sterically encumbered

phenanthridine for diminishing the excited state geometric orientation. A relative effect of counterion in solid-state emission lifetime has also been studied.

A group of octahedral d^8 metal complexes were synthesized by using both phosphine/carbene ligands to study the metal to ligand charge transfer and its lifetime. The potential of these complexes for use in the field of photosensitizer was also discussed.

Phosphino ligand based Fe complexes have been synthesized and their use in the filed of hydrogenation catalysis has also been discussed.

Acknowledgements:

At first, I would like to express my gratitude to my advisor, Dr. David E. Herbert, for the great opportunity to do a PhD under his supervision. I admire his extensive knowledge and vast experience in the field of Chemistry. I also appreciate his patience and kindness not just as a teacher but also as a friend, philosopher and guide during the past five years. I would like to thank my committee members Dr. Phil Hultin, Dr. Rebecca L. Davis, Dr. Jamie Ritch and Dr. Kevin Fraser for their valuable input and feedback. I appreciate Dr. Hultin for helping me to improve my presentation and communication skills. However, I deeply grieve that I cannot express my endless gratitude to Dr. Hultin in person.

I also appreciate help of all my collaborators. I acknowledge Dr. Marat, Dr. Davidson and Mark Cooper (Geology Department) who helped me with my NMR experiments and X-ray analysis respectively. I want to show my appreciation to other faculty members, staff and technicians of the Chemistry Department. I thank all my lab members of past six years, especially Pavan Mandapati, Issiah Lozada, Patrick Giesbrecht, Jason Braun, Dion Nemez for being great friends and helping each other teach/learn to grow as scientists as well as my undergrads Robert Ortiz and Olha Stotska. I would also like to thank Dr. Davis's, Dr. Budzelaar's, Dr. Kroeker's and Dr. Nemykin's lab members for their help and assisting me with chemicals.

I am grateful to my Mom-Dad, my wife Zinnia and my family who have always supported me in every aspect of my life with their love, blessings, help and encouragement throughout this journey.

With Love and respect,

Rajarshi (Raj)

Table of Contents:

List of Figures:

List of Schemes:

List of Tables:

List of Abbreviations:

DFT: Density Functional Theory

TDDFT: Time Dependent Density Functional Theory

TADF: Thermally Activated Delayed Fluorescence

MLCT: Metal to Ligand Charge Transfer

DCM: Dichloromethane

DME: Dimethoxyethane

DMF: *N,N*'-Dimethylformamide

DMSO: Dimethyl sulfoxide

Et_2O: Diethyl ether

THF: Tetrahydrofuran

EtOH: Ethanol

MeOH: Methanol

EtOAc: ethyl acetate

Cp*: Pentamethylcyclopentadienide

MO: Molecular orbital

HOMO: Highest occupied molecular orbital

LUMO: Lowest unoccupied molecular orbital

SOMO: Singly occupied molecular orbital

^{i}Pr: isopropyl

Me: Methyl

^{n}Bu: *n*-butyl

^{t}Bu: tert-butyl

NMR: Nuclear Magnetic Resonance

VT-NMR: Variable temperature- Nuclear Magnetic Resonance

XRD: X-ray Diffraction

RT: Room temperature

Hr: Hour

Min: Minute

ps: picosecond

OLED: Organic Light Emitting Diode

sec: secondary

tert: tertiary

Chapter 1: Introduction:

1.1 Ligand design and Coordination chemistry:

Organometallic coordination chemistry is a major part of chemistry where organic molecules combined with metallic elements give rise to new compounds with versatile properties. The focus of this thesis is mostly on developing new ligand environments for late transition metals (such as Fe, Ru, Ni, Cu and Zn), to enable applications of the resulting coordination complexes in different fields of chemistry. Organometallic compounds are widely applicable in fields such as small molecule activation, catalysis (for both academic and industrial scale), optoelectronics, photosensitizers, solar cell, drug synthesis medicinal and many more.[1] For instance the use of 2-phenylpyridine as a *C^N* binding ligand in coordination complexes of heavy metal cations such as Ir led to the invention of tris[2-phenylpyridinato-C^2,N]iridium(III) and its application in green light sources in organic light emitting diodes (OLEDs).[1a] This highlights how, when trying to achieve versatile applications and properties, ligand design plays an important role. These complexes now appear in screens commercialized by the Samsung company.[1a] Metal binding also depends on specific ligand design, binding site and certain geometry.

1.1.1 Classification of Ligands:

Ligands, atoms or groups of atoms that coordinate to central atoms, range from simple mono-functional or bifunctional spectator ligands, to intricate ligand system such as non-innocent/redox active ligands. Ligands can be classified based on the number of binding sites (denticity) or charge of the ligand while binding with metal ions. Ligands with only one donor/binding site are called unidentate or monodentate, with more than one donor site are called

multidentate or polydentate (**Figure 1.1**). Bi- or tridentate to hexa or octadentate ligands are familiar as multidentate ligands. Certain type of tridentate ligands called "pincer" ligands are well known for catalyst design, mostly with transition metals.[2,3] Multidentate ligands with more than one donor site bind strongly with metal ions using all possible binding site, and their complexes show stability over monodentate ligands. This is referred to as the "chelate effect".[4] The 'chelate effect' represents that multidentte ligands bind strongly with metal ion than monodentate igands.

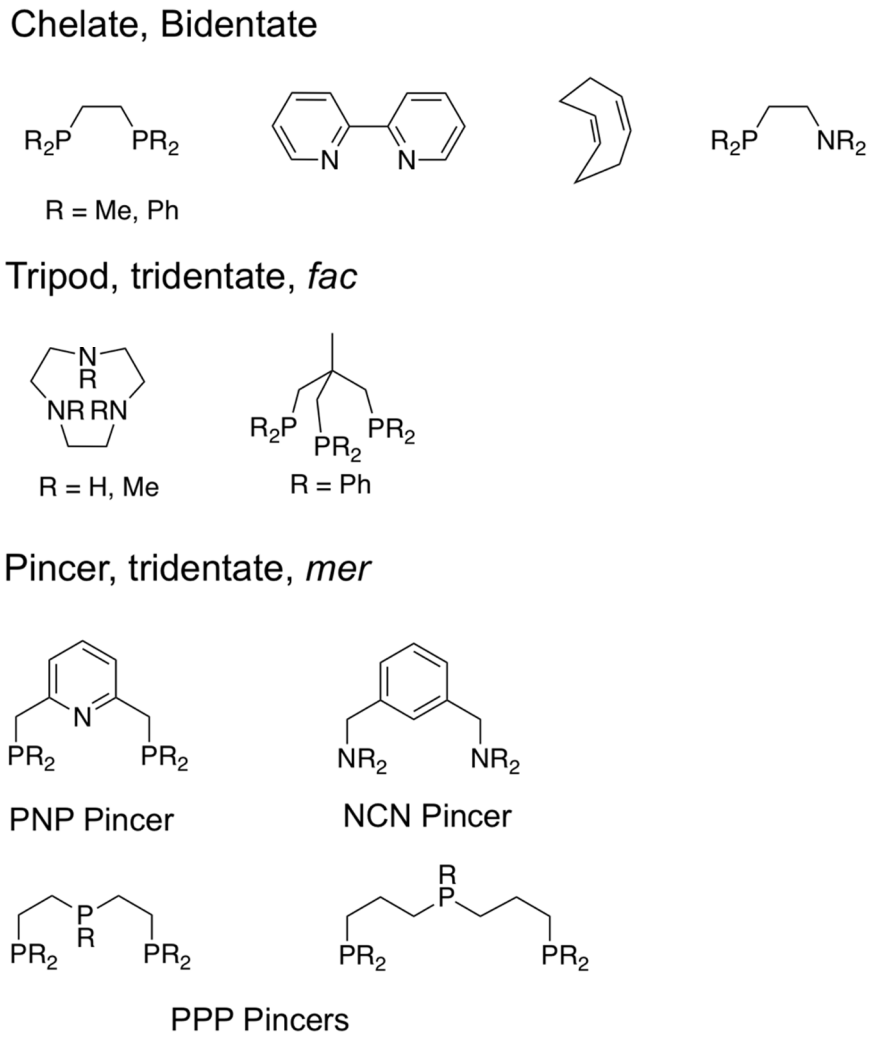

Figure 1. 1. Selected familiar ligands type representing different binding preferences.[4]

Ligands can also be classified on the basis of bond formation. In organometallic chemistry, we can consider two types of ligands: (1) covalent ligand or 'X-type', and (2) dative or 'L'-type ligands.[5] The covalent ligands form bonds with metal ion by donating one electron to the bond, while the other electron is donated from the metal. The covalent ligands could be explained as charged ligands, often called 'anionic or negative' donor ligands, as they can dissociate from the metal to form stable anionic units. Dative ligands form bonds with the metal ion by providing both electrons to the bond; no electrons come from the metal ion. Upon dissociation from a metal centre, dative ligands form stable, 'neutral' species (**Figure 1.2**). Based on number of electron donation, ligands have also been termed, such as one-electron donating ligand called 'X-type', two electron 'L-type', three-electron 'LX' type, four-electron 'L_2', five-electron 'L_2X' etc.

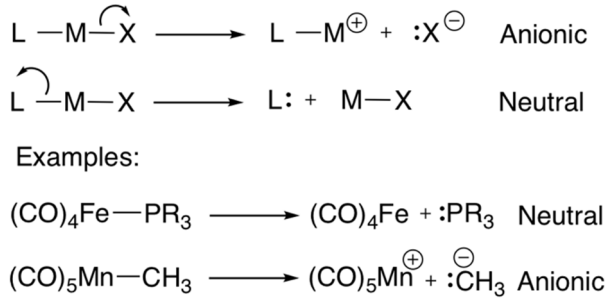

Figure 1. 2: Examples of anionic and neutral type ligand.[5]

We could also consider the degree of covalency vs. ionic interaction in a coordinate bond. The larger the difference of electronegativity between two elements, the higher the ionic character. This helps us to differentiate between 'hard' and 'soft' type ligand. The hard ligands are mostly small in size, not easy to polarize and preferably form strong bonding with hard metals whearas soft ligands are easily polarizable. Metals/cations could also be differentiated as hard or soft. Hard-soft combination of metal-ligand interaction is weak. Thus, hard-hard or soft-

soft metal-ligand interaction is very strong and can be classified as ionic bond. For example, HgI_2 is an example of soft-soft metal-ligand interaction. Similarly, F^- is a hard ligand and I^- is weak ligand. Since H^+ is a hard cation and could bind with both F^- and I^- and forms acid. Accordingly, HF is a weak acid (pKa +3) and HI is a strong acid (pKa -9.5).[4]

When forming a bond, the bonding interaction between metal and ligand can be characterized based on the types of electron sharing. As discussed earlier, dative ligands such as CO, PPh_3 donate two electrons to the metal for bond formation. Similarly, some molecules with π-bonds such as C_2H_4, RCH=O, O_2, can share their π-bond electron pair to form a new σ-bond to a metal. Some molecules can also bind to metals by sharing a σ-bonding pair of electrons for bond formation; the resultant "sigma complexes" of H-H, R_3Si-H are common. Some ligands only accept electron from metal does not contribute electron to the bond such as Lewis acid BF_3. These are considered 'Z-type' ligands.

Back donation from metal to ligand is also very important for coordination complex formation. This back-donation (or back-bonding) happens in case of some strong field ligands with vacant π* orbital such as CO. Back-bonding happens from filled dπ orbital to ligand π* orbital after a symmetrical overlap between metal and ligand orbital. This can help to stabilize molecules with metal atoms in low oxidation states by delocalizing metal electron density to the ligands. Apart from carbon monoxide, C_2H_4 and CN etc. can engage in these interactions. The extent of back donation can be physically determined by the IR spectroscopy even for C_2H_4. The change in bond order due high electron density affects the stretching frequency of the ligand.

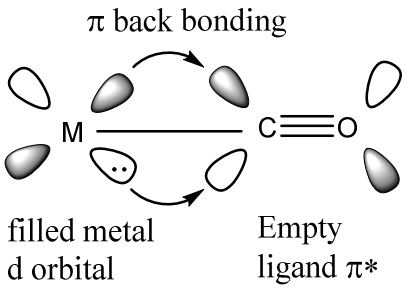

Figure 1. 3 : Metal to ligand π-back bonding in π-acidic ligand.[4]

1.1.2. Privileged Ligand Design:

For centuries, scientists have been trying to develop novel molecules that work efficiently in different fields of chemistry. For instance, catalysts that help to overcome difficult reactions with high productivity and selectivity, complexes which can be applied in material science or medicinal chemistry with high efficiency and so on. For example, in the field of catalysis, some ligands show highest performance with different metals such as chiral phosphine-oxazoline[6], (*N*^*N*) bisoxazolines[7], salens[7]. By research and development, scientists developed privileged class of organometallic complexes that perform with extraordinary efficiency at low cost. These designed ligands are considered as privileged with a certain core structure to have broad application with different metal ions. It is always intriguing to develop widely applicable ligand motifs.

1.1.3. Difference of Organometallic and Coordination Compounds:

Metal-ligand complexes are all coordination complexes. However, for being organometallic there should be a metal-carbon bond (M-C) in the complex. However, (M-N, M-P, M-O) bonded

complexes are considered as coordination complexes. In an organometallic bond, metal possess cationic character due to high electronegativity of carbon. As discussed earlier, a metal-carbon bond is usually covalent due to low electronegativity difference between metal and carbon atom.[4] Hence, in coordination compounds with other elements, metals form ionic type bonds due to high electronegativity difference.

Some ligands such as H and SiR_3 have low electronegativity differences with metals while forming complexes.[4] Due to observed covalent character, they are also considered as organometallic compounds. In modern day catalysis, many coordination compounds act as organometallic in the intermediate state by forming bond with carbon atom such as in hydrogenation reactions with Wilkinson's catalyst.

1.1.4. Complex Geometry:

Coordination complexes adopt different geometries depending on the number of coordinating ligands and, for transition metals, electronic considerations as well. Typically, three to six coordinated transition metal complexes are most common. However, examples of more than six coordinate complexes are known; for example, $[CpMo(CO)_3(H_2O)]^+$ is a seven coordinate complex, with the Cp ring considered to occupy three coordination sites.[5] In general, three coordinated transition complexes adopt trigonal planar or pyramidal geometries, four coordinated are tetrahedral or square planar, five coordinated are trigonal bipyramidal or square pyramidal and six coordinated are octahedral or trigonal prismatic.

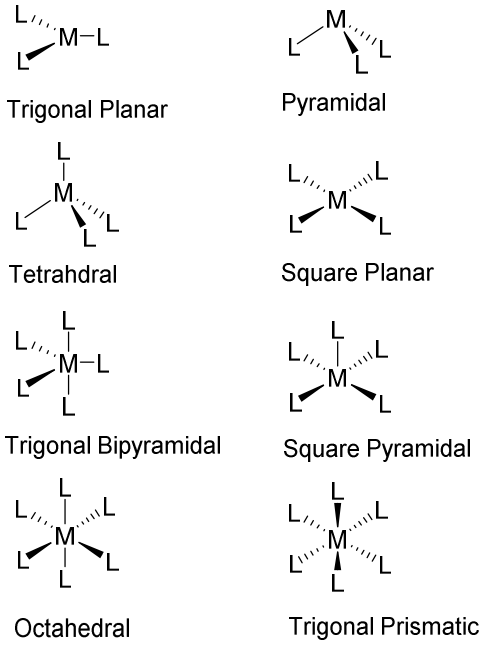

Figure 1. 4: Familiar geometries of transition metal complexes in its different coordination mode.[5]

In general, there are two basic reasons for a molecule to adopt a geometrical orientation, one is electronics and the other is sterics. In case of transition metals, electronic effect can predominate over steric effects for large enough metal centres. In these cases, the d electronic configuration strongly influences the geometry of the complex. For instance d^8 complexes of second and third-row metals prefer square planar geometry over tetrahedral. Due to small size of the 3d metals, analogous complexes can be stable in tetrahedral geometries. For example, $Ni(II)Cl_2$ complexes of bulky bidentate phosphine ligands prefer tetrahedral geometry. In comparison, introducing cyclometalated aryl group as a strong field ligand around Ni forms square planar Ni(II) complexes. Contrasting results has also been reported for Fe(II) alkyl complexes while binding bidentate chelate ligands. It can be concluded that for obtaining suitable geometry, both the steric and electronic effects play a great role in transition metal coordination chemistry.

1.2. Bidentate Neutral P^N and C^N type ligands and their metal Complexes:

1.2.1 *P^N* Ligand:

As part of my PhD research, I have investigated new *P^N* bidentate ligands. The *P^N* type ligands have been widely applied in the field of organometallic chemistry. Multidentate *P^N* types are well known to bind with late transition metals. Very common *P^N* ligands combine phosphine-amine type ligand system, producing a combination of both soft and hard donors.[8] Phosphine is a soft centre whereas the nitrogen provides the hard centre which allow these type of ligands to make coordination complexes with middle to late transition metals, concerning the metal ion's hard-softness. The phosphorus centre shows both σ-donor as well as weak π-acceptor as empty σ* orbital presence and the N centre provides σ-donor and rigidity as well. These ligands could stabilize the metal ions of its different oxidation states, as *P^N* type ligand could be neutral donor or anionic donor where N centre operates as amide group.

P donor centre:
-Soft
-σ-donor and π-aceptor
-Electronically control by changing the R1 and R2 group

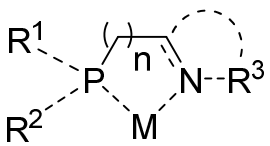

N donor centre:
-hard
-σ-donar
-Sp^2 hybridization on N, decreases basicity
-Nitrogen group incorporation provides chelate rigidity

Figure 1. 5: *P^N* ligand general properties.[9]

Multidentate *P^N* ligands have extensive variations such as bidentate, tridentate pincer type and tetradentate as well. The application of these types of complexes are in the field of asymmetric catalysis, polymer synthesis, hydroboration[10], hydrosilylation[11], dehydrogenation and hydrogenation reactions[12] and photoemissive material synthesis.[13] One of the eminent forms

of *P^N* ligand are called PHOX (Phosphinooxazolines).[6] These bidentate *P^N* type ligands are very useful in asymmetric catalysis such as regio and enantio selective conjugate addition to enones, C-N and C-C coupling reaction, enantioselective hydrogenation of alkene, imine and ketone. A well-known application of these types of ligands is Pd catalyzed allylic alkylation. Ward[14] and Moberg[15] disclosed the electronic differences of these types of *P^N* ligands by using a *P^N* ligand with C_2 or pseudo-C_2 symmetry.

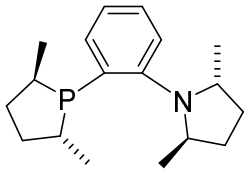

Figure 1. 6: Moberg's ligand[15]

The chirality insertion into the product could be controlled by changing the functional groups of ligand phenyl backbone, similarly by changing the -R group of oxazoline ring (**Scheme 1.1**). The unsymmetrical ligand environment helps to acquire better asymmetry during catalytic synthesis of enantioselective products.

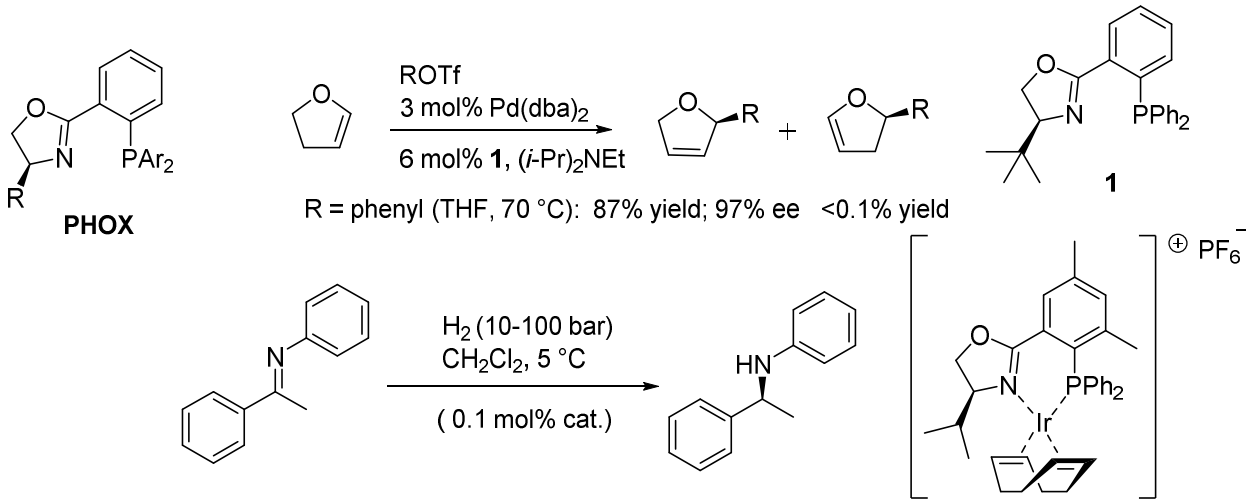

Scheme 1. 1: Catalytic hydrogenation of imine by Ir catalyst based on PN oxazoline ligand.[6]

Phosphine oxazoline based Ni complexes also showed activity towards ethylene oligomerization reaction in both mono and halide bridging dinuclear geometry.[16]

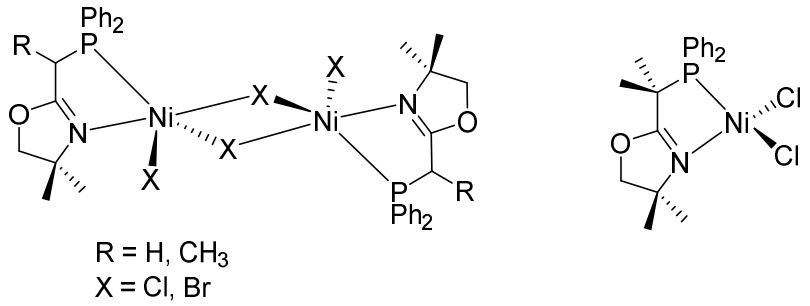

Figure 1. 7: Phosphine oxazoline based Ni complexes useful for ethylene oligomerization.[16]

Bidentate *P^N* ligand based mid or late transition metal complexes are useful for the catalytic ethylene polymerization and oligomerization.[17] Quinoline derived *P^N* ligand (**Figure 1.8**) based square planar Ni(II) complexes **1** and **2** have been used for ethylene oligomerization and Pd(II) complexes are used for copolymerization of styrene with CO.[18]

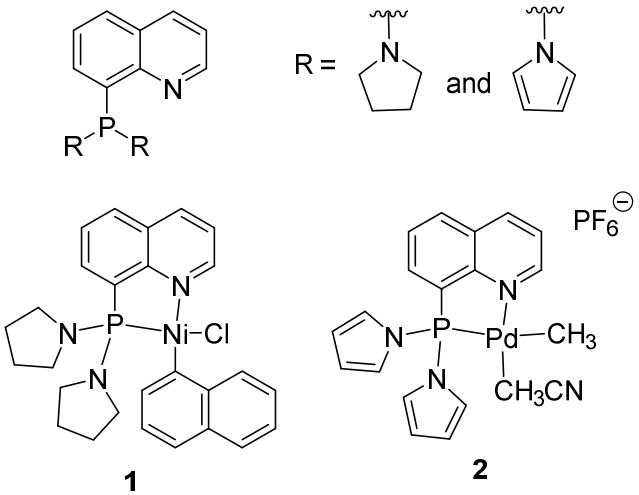

Figure 1. 8: Quinoline P^N ligand based Ni and Pd complexes useful for ethylene oligomerization and copolymerization.[18]

In a recently reported publication, *P^N* ligand based Cr complexes (**1Cr**) showed better performance over *N^N* or *P^P* type bidentate donor for ethylene polymerization reaction.[19] For Fe(III) metal ion with bidentate (**PN-1**) ligand, showed efficient activity for polymerisation following Atom Transfer Radical Polymerization (ATRP) technique (**Figure 1.9**).[20]

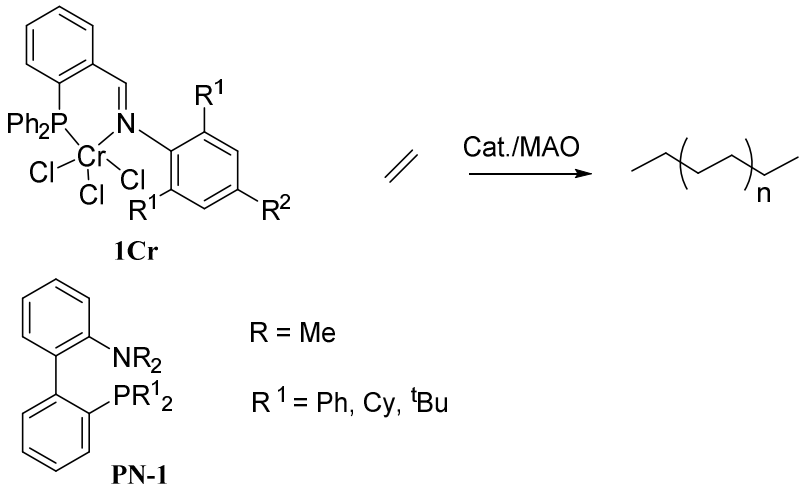

Figure 1. 9: *P^N* ligand based Cr (**1Cr**) for ethylene polymerisation and Fe with **PN-1** ligand shows efficient ATRP.

Both Kamer[21] and Sun[22] reported also simple *P^N* ligand with late transition metal based ethylene oligomerization catalyst showed efficient results (**Scheme 1.2**).

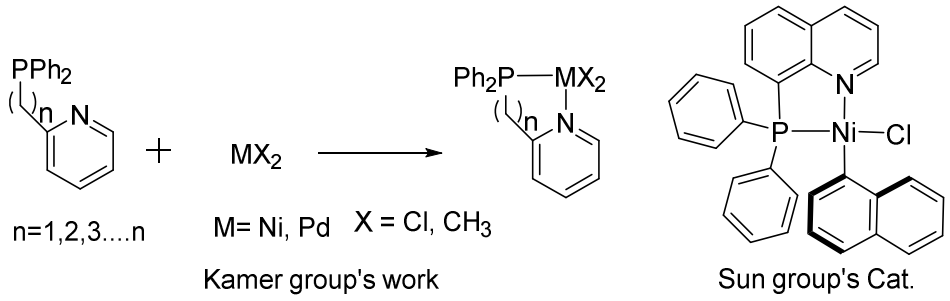

Scheme 1. 2: Ni and Pd catalyst of Kamer group and Sun group's Ni catalyst for ethylene polymerisation.

Bidentate dimethylamino *P^N* ligand with d^{10} metal Cu(I) complexes have been used for catalytic C-C coupling (Suzuki−Miyaura) reaction (**Scheme 1.3**).[23]

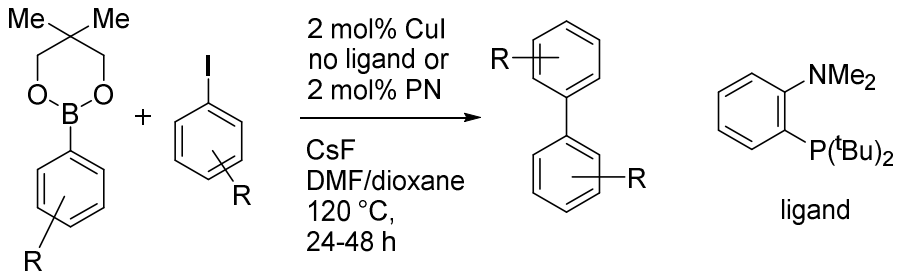

Scheme 1. 3: Cu (I) catalyzed C-C coupling using strong base medium.[23]

P^N ligand based Pd catalyzed Buchwald-Hartwig Amination of substituted aromatic halides was reported with very efficient isolated yield.[24,25,26]

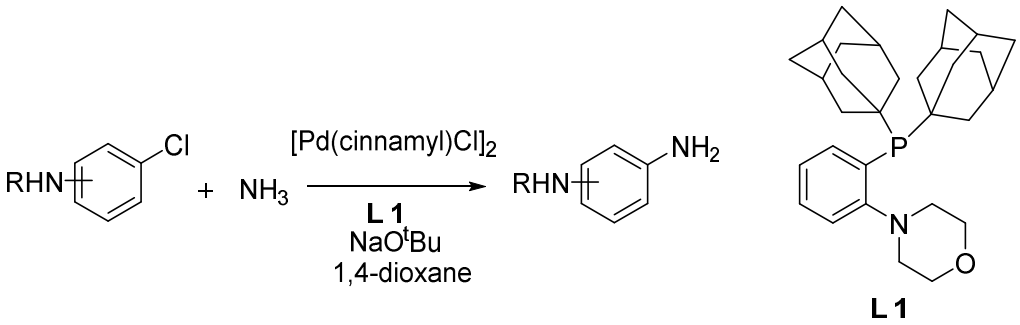

Scheme 1. 4: Pd (I) catalyzed C-N coupling of aromatic halogens.[24,25]

In addition to catalysis, complexes of *P^N* bidentate ligands have also been extensively used in the preparation photoemissive materials for the application in the field of organic light emitting diodes (OLEDs). Yersin's group designed halide bridge Cu complexes based on simple bidentate *P^N* ligand (**Figure 1.10**).

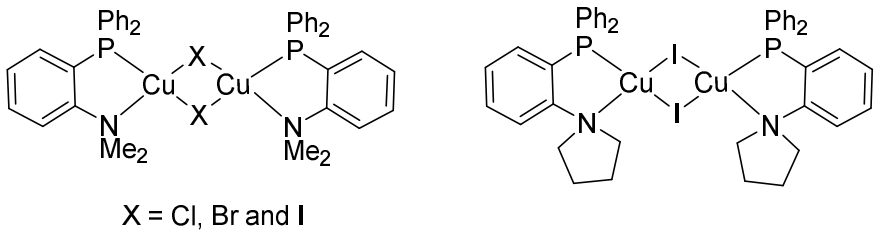

Figure 1. 10: Halide bridge Cu (I) complexes for solid state emission.

Cu(I) complexes are coordinated to bidentate *P^N* ligand in tetrahedral fashion by bridging halide. The complexes are solid-state photoemissive under UV light. All the complexes strongly emit in the blue region.[27]

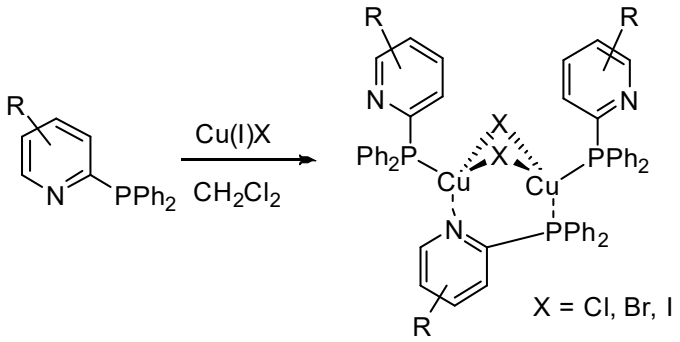

Scheme 1. 5: Halide bridge Cu (I) complexes for solid-state emission.

The series of halide bridge dinuclear Cu complexes of *P^N* pyridylphosphine ligands showed very intense photoluminescence properties. The quantum yield of emission reached up to 95%. Metal and halide bridge combined charge transfer to ligand was observed.[13] Similarly, monometallic Cu complex with quinoline based PN ligand,[28] as Cu(I) with PF_6 counter ion formed tetrahedral environment (**Figure 1.11**). The Cu complex emitted at around ~640 nm at room temperature.[28] 8-(diphenylphonphino)quinoline based Zn complex also showed photoemissive property, however the emission is mostly ligand based.[29]

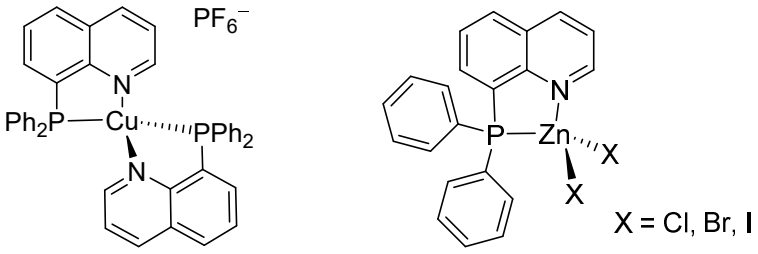

Figure 1. 11: Quinoline phosphine ligand based Cu(I) and Zn(II) complexes.

1.2.2 *C^N* Ligand; NHCs:

We have also investigated the combination of *N*-heterocyclic carbenes (NHC) with aromatic *N*-heterocycles to produce carbene-based, bidentate, asymmetric *C^N* donor ligands. Previous publications reported high reactivity of complexes of similar carbene based *C^N* donor over *P^N* donor in some reactions such as hydrogenation of olefins.[30] Carbenes were first isolated by Bertrand and co-workers as phosphorus and silicon substituents.[31] Around early 90's Arduengo and coworkers reported the first isolable, stable *N*-heterocyclic carbene. Application of NHCs is widely in four major fields such as homogeneous catalysis, metallopharmaceuticals, surface chemistry and materials chemistry.[32] NHCs could be coordinated to transition metals and main group elements and also other organic unit for different applications.

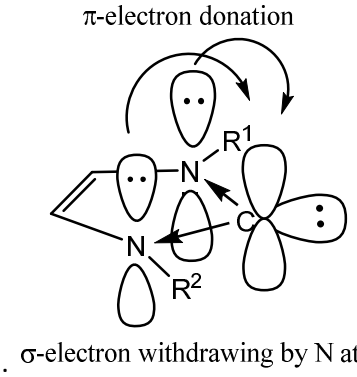

Figure 1. 12: Orbital contribution and overlap of *N*-heterocyclic carbene.

NHCs are electron rich σ-donors and weak π-acceptors (**Figure 1.12**).[32] These type of carbenes are singlet donors, called Fisher type carbenes. The N atoms play a crucial role for stabilization of the carbene carbon (C) by providing the π-electron density to the empty p-orbital of carbon centre and lowering the energy of the occupied σ-orbital by inductively electron withdrawing. The functional groups ($R^1$and R^2) also provide great stability by providing electron density to the nitrogen atoms. The electronics can be controlled by changing the R^1 and R^2. NHCs bind with transition metal very promptly by mostly σ-donation and partially π-back donation. **Figure 1.13** shows some notable examples.

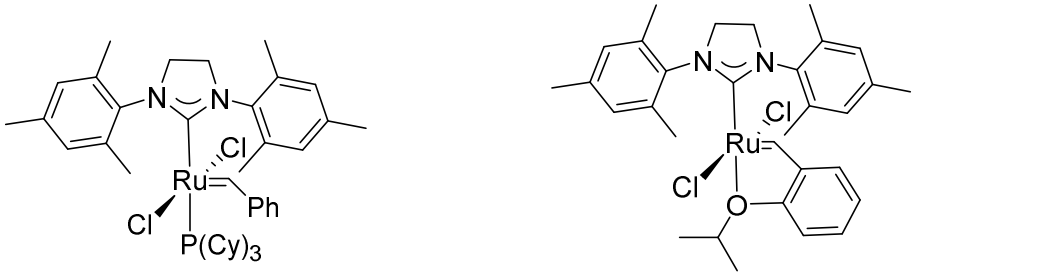

Grubbs second-generation catalyst Hoveyda-Grubbs second generation Catalyst

Figure 1. 13: *N*-heterocyclic carbene based Grubbs second-generation and Hoveyda-Grubbs second generation catalyst.

Both these 2nd generation NHC based catalysts; Grubbs catalyst[33] and Hoveyda-Grubbs catalyst[34] are extremely active for olefin metathesis reactions such as cross metathesis, ring closing metathesis and ring-opening metathesis polymerization.[35] The first generation catalyst was based on phosphine ligand and 2nd generation catalyst was made by replacing phosphine by carbenes which provides better activity as well as the stability towards air and moisture. The modification of bulky carbene functional groups helps to enrich electron density at the metal centre, resulting in the extra stability of the catalysts and supply enantioselectivity to the product.

In materials chemistry, NHCs are also widely applied. Very recently Wärmark and coworkers published a NHC based Fe(III) complex which is photoemissive at room temperature with lifetime of 2.0 nanosecond and 2% quantum yield (**Figure 1.14**). This is the first strongly photoluminescence Fe(III) complex ever reported. The potential application of this complex is in the field of OLEDs, designing photosensitizer and photochemical synthesis.[36] Another example is the bis-NHC based pyridine ligand-supported Fe complex (**Figure 1.15**) which shows an 18 ps excited state lifetime, and has potential application in the field of photosensitizers.[37]

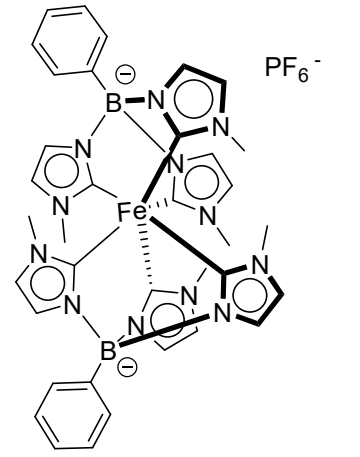

Figure 1. 14: *N*-heterocyclic carbene based Fe(III) complex, photo-emissive Fe(III) complex.

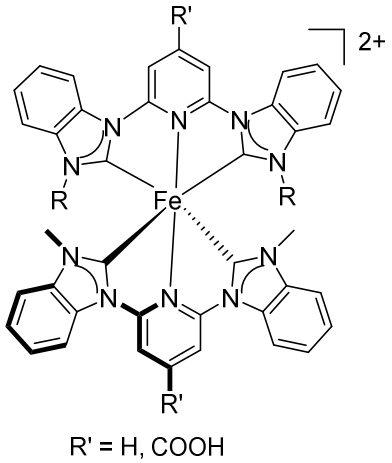

Figure 1. 15: Pyridine based N-heterocyclic CNC pincer ligand complexes of Fe(II).

We would like to synthesis asymmetric NHCs by having aromatic *N*-heterocycles as a functional group. There are reported examples potentially very interesting. Gornitzka group has published these bipyridine and quinoline based NHCs with different late transition metals such as Au, Ag showing potential of antimalarial[38] antiplasmodial[39] and antileishmanial[40] activity (**Figure 1.16**).

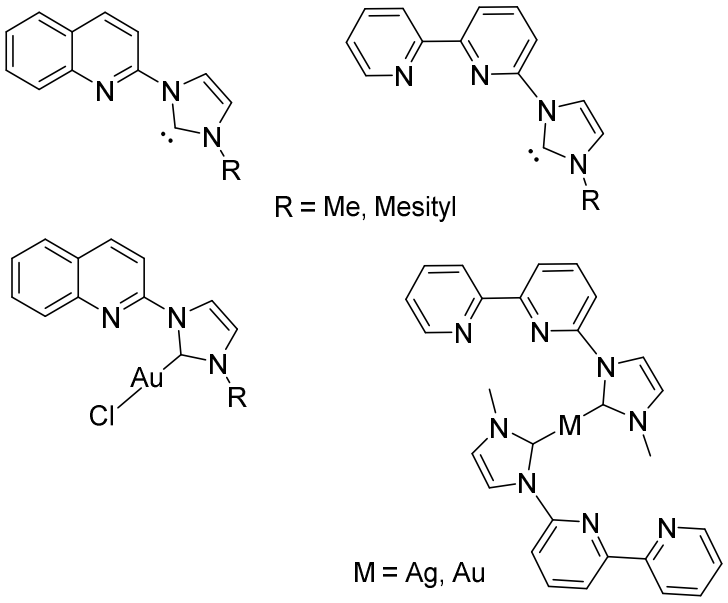

Figure 1. 16: Bipyridine and quinoline based *N*-heterocyclic carbene complexes of Ag and Au metals.

1.3. Phenanthridine:

Phenanthridine is a conjugated π-aromatic system, well known for its use in different fields of chemistry,[41,42]. Polycyclic heteroaromatics (PHAs) have pulled scientists' attention from the last few decades for its usefulness in various industrial applications.[43] The structure and numbering of phenanthridine has been represented in **Figure 1.17**.

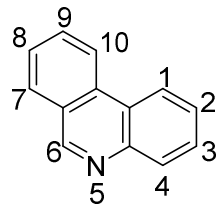

Figure 1. 17: Numbering of phenanthridine.

Phenanthridine is a 14π electronic system with melting point of 106 °C and the boiling point of 349 °C/ 769 Torr and the p*K*a 4.47 at 22 °C.[44] Phenanthridine is sparingly soluble in water and can be crystallized from ethanol, forming needle shaped crystals.[42] It is analogous to phenanthrene, replacing one of the C=C bond by a C=N bond ("imine" bond) at the middle benzene ring. The X-ray structure of phenanthridine, studied by P. Rademacher, shows the molecule is planar and the mean deviation at C=N bond about 0.002 Å from mean plane.[45] Their study also suggested the similarity of the two outer benzo rings with free benzene, while structural differences where observed between the central pyridinyl ring with free pyridine. Phenanthridine is the structural isomer of acridine. Being a benzo-fused ring system, phenanthridine is a thermally stable molecule.

Although phenanthridine is under the group of benzo-fused pyridines, it has exceptionally distinguished properties than pyridine, quinoline and acridine, such as an "imine" type C=N bond. This results from only having 14 total π-electrons, meaning the middle C_5N ring cannot have aromatic character if the outer two rings do. This allows for example, easy reduction of C=N bond to synthesis of dihydrophenanthridine and completely destroys the aromaticity of the middle pyridine ring.[46] Zouchoune and coworkers have performed theoretical DFT study on free phenanthridine system. They observed that free phenanthridine contains C_s symmetry and the energy gap between HOMO and LUMO 2.98 eV. The HOMO of phenanthridine is distributed

almost all over the ring, but the LUMO is only localized in C_6=N_5 bond. The presence of electronegative N atom makes C=N bond as π-acceptor and other part of the ring as π-donor.[47]

1.3.1. History of Phenanthridine:

Phenanthridine was first reported by Pictet and his co-workers around 1891 by doing pyrolysis of benzylideneaniline.[48] Later a different method was published by Gräbe and Wander in 1893, which was Hoffmann reaction of 2,2'-amidobiphenyl carboxylic acid to synthesize phenanthridinone followed by distillation with Zn dust to get the phenanthridine.[48] Derivatization of phenanthridines were started early 19th century by different research groups, but not that thoroughly until Walls group in 1931 discovered the therapeutic use of phenanthridine.[48] In 1938 Walls group reported outstanding trypanocidal activity of phenanthridine derivatives.[48] Although no effective progress was observed in phenanthridine and its corresponding chemistry before the invention of characterization techniques such as NMR or X-ray, around late 19th century it acquired scientist's interest. However, despite of having characterization technique, there were very few publications reported in the metal complex coordination chemistry, organometallic chemistry and using phenanthridine as a ligand. Our focus is to prepare functionalized phenanthridines that can bind with metal ions to check complex coordination chemistry and study the properties for applications in the field of organometallics, materials, catalysis and others.

1.3.2. Why Phenanthridine is Unique from Pyridine, Quinoline and Acridine:

I have already discussed how phenanthridine shows similarities to pyridine, quinoline and acridine. However, phenanthridine has distinguished properties than these serious of molecules

because of its structural orientation. Although phenanthridine is structural isomer of acridine, the middle pyridine ring of phenanthridine can be thought of as containing less aromatic character than the outside rings. In support of this, the bond lengths of the middle pyridine in phenanthridine are exceptionally different than pyridine and the other pyridine containing compounds.[45] The C=N bond of phenanthridine is immensely shorter than the (around ~1.29 Å) pyridine, quinoline and acridine (Figure 19).[47] This C=N bond length of pyridine is very similar to an imine like bond. Such diagnostic properties could also be observed in phenanthrene C=C bond of middle benzene ring.[45]

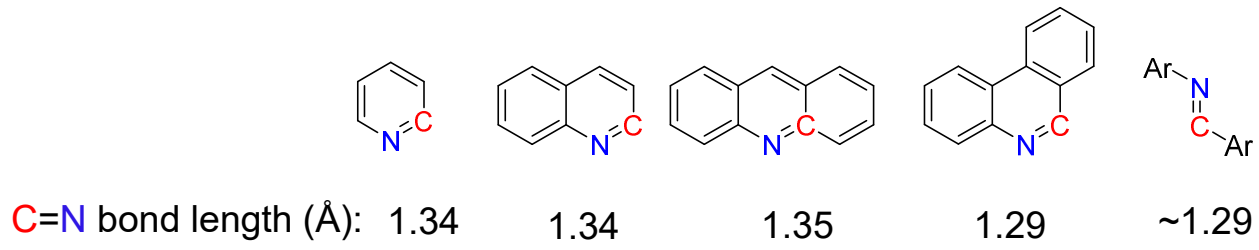

Figure 1. 18: Imine (C=N) bond length in different pyridine substituent.[47,48]

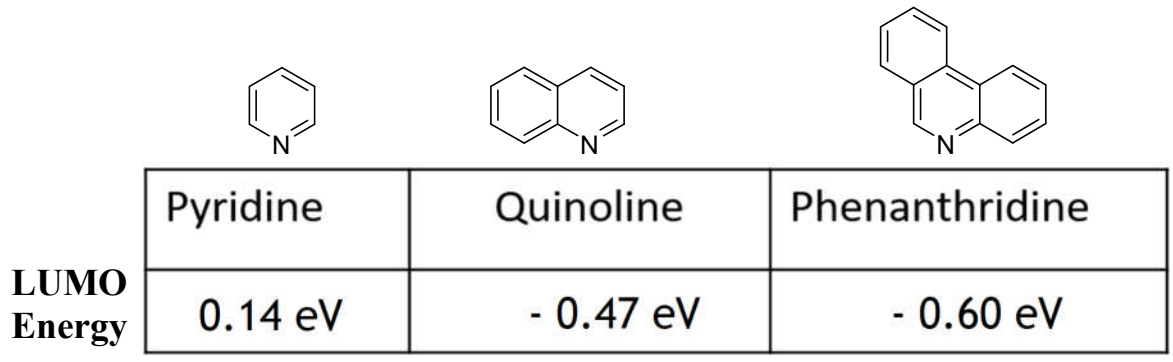

Figure 1. 19: Effect of π-extension on LUMO energy.[49]

1.3.3. Applications of Phenanthridine:

Benzo-fused π-extended phenanthridine derivatives are well known for their application in assorted fields. For instance, phenanthridine based dyes such as ethidium bromide (**Scheme 1.6**) have been used in medicinal chemistry,[50] red fluorescence is observed while binding with RNA. Phenanthridine has also been used in the filed of bioimaging[51], sensors[52] and photoemissive material synthesis, and phenanthridine itself has been used in H_2 activation and transfer hydrogenation[53] chemistry. Several potential applications and developments are yet to be disclosed, which made us interested to study phenanthridine system very closely. Some previously reported most interesting work is discussed as follows.

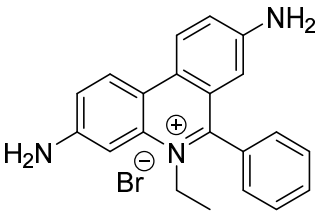

Ethidium bromide

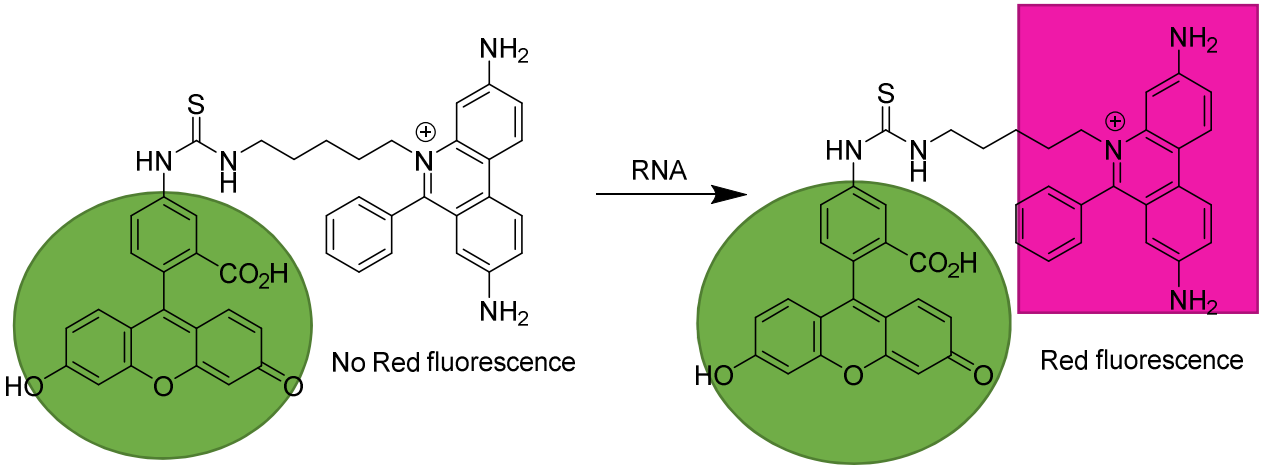

Scheme 1. 6: Cell imaging application of ethidium bromide.[50]

Ethidium bromide, a versatile compound based on phenanthridine moiety is well known as anti-trypanosomal drug for African cattle.[54] It is also useful for agarose gel electrophoresis

technique as it binds with DNA and could be visible under UV-lamp during the separation of DNA fragment.[55] Having luminescent property, phenanthridine could be used to make molecular probe to physiologically differentiate among the ATP, ADP and AMP which is very important for studying the enzymatic reactions. Pierre group has designed a Tb based ATP sensor which in absence of ATP, charge transfer from phenanthridine to lanthanide producing luminescence, but in presence of ATP the emission is totally quenched (**Scheme 1.7**).[56]

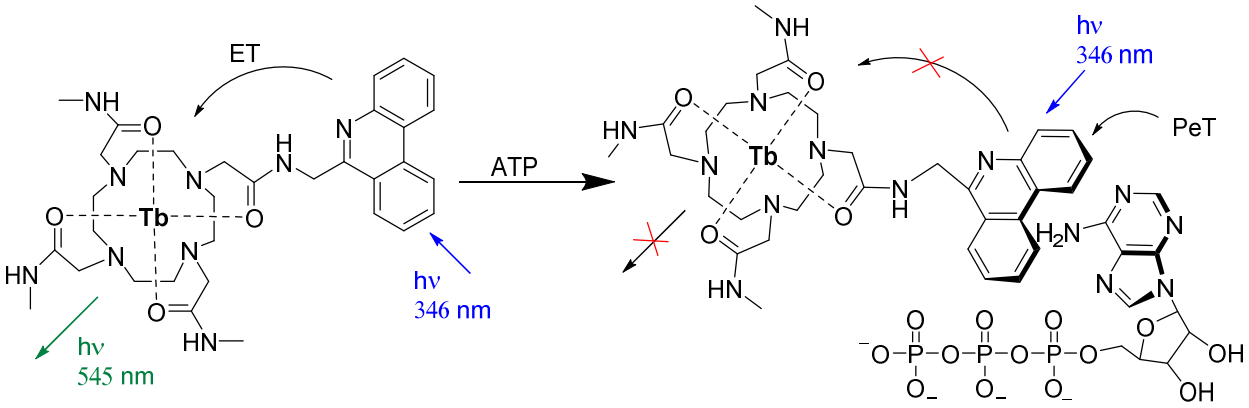

Scheme 1. 7: Use of phenanthridine in luminescent probes for biological systems.[56]

Cisplatin is Pt metal based square planar complex coordinated with NH_3 and Cl ligand in cis fashion, used in diverse cancer research fields,[57] although various amine and *N*-heterocycles such as pyridine (e.g., pyriplatin; **Figure 1.20**) has been used in Pt core to improve efficacy and discard the side effects of cisplatin. The concept of using phenanthriplatin over previously used Pt complexes, is for better activity towards cultured cancer cell.[58] Phenanthriplatin has only one binding site towards DNA, but much better cytotoxicity in cancer cells using the chiral feature and ligand steric with a high potential of use in the future as an anti-cancer drug.[59,60]

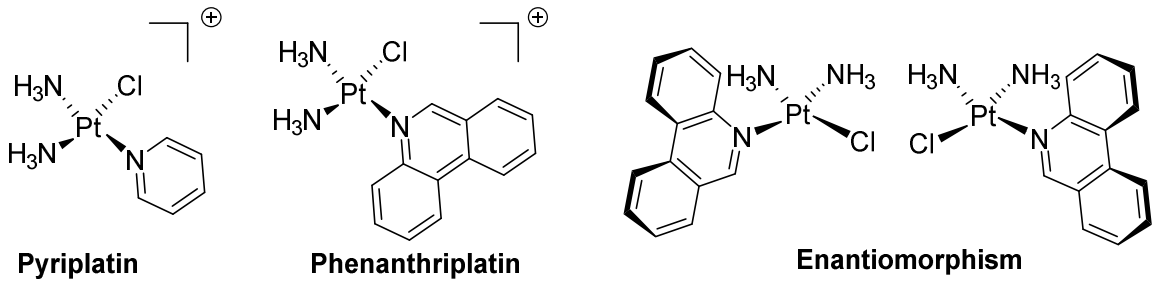

Figure 1. 20: Use of phenanthridine for synthesizing anti-cancer agent.

P^N ligand-based Cu(I) halide emissive complexes were discussed previously. Therefore, the example of bidentate *P^N* ligand of phenanthridine has been reported by Yersin group. Phenanthridine phosphine ligand (6-diphenylphosphino phenanthridine) based Cu(I) complexes are emissive in solid state. The complex **A** (**Scheme 1.8**) has been synthesized by reaction of PN-phenanthridine ligand and CuI in DCM at room temperature. The iodo-Cu(I) complex dimer emits at 627 nm at room temperature. The application of these complexes are in the organic light emitting diodes (OLEDs).

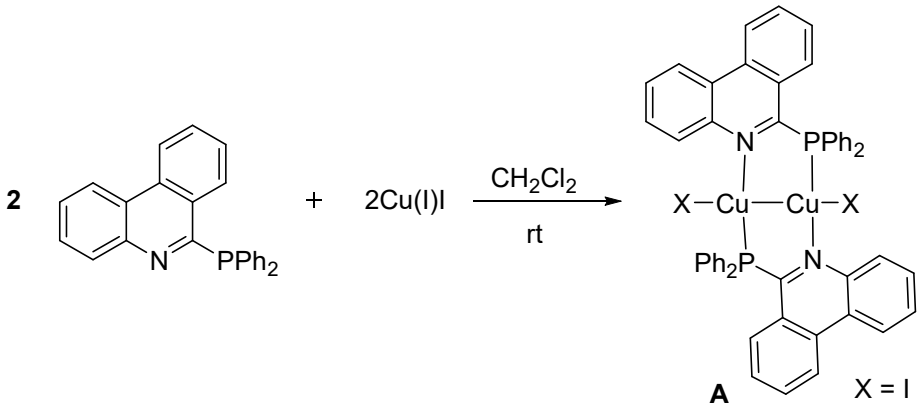

Scheme 1. 8: Use of phenanthridine based *P^N* ligand for designing photoemissive materials by Yersin group.

Similarly, the Ir complexes are photoemissive with phenanthridine based cyclometalated bidentate *C^N* ligand. As seen in **Figure 1.21**, the complex **A** emits at around 656 nm and complex **B** at 665 nm in DCM solution state at around ambient temperature. These red emitting complexes have potential to be used in OLEDs as well.[61]

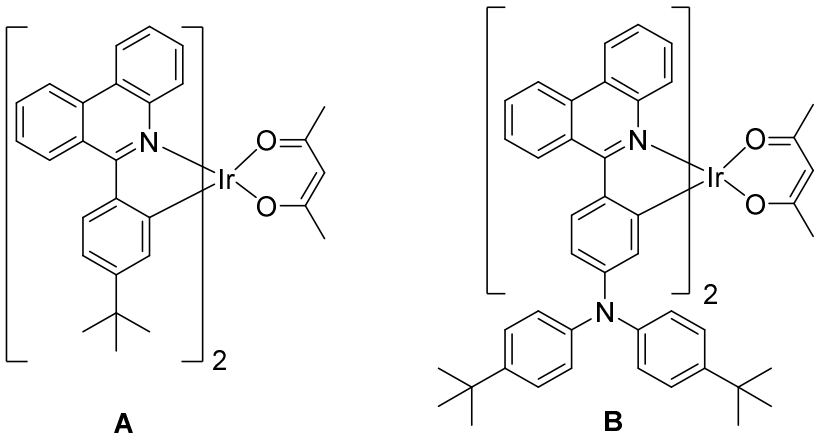

Figure 1. 21: Use of phenanthridine based cyclometalated C^N ligand for designing photoemissive materials.

The gold complexes of phenanthridine are photoemissive at room temp in DMSO solution. The complexes are synthesized by reaction with gold salt with phenanthridine itself as ligand.[62]

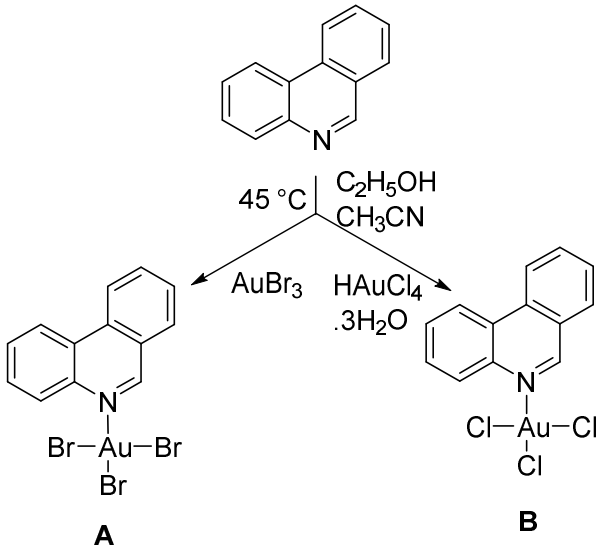

Scheme 1. 9: Use of phenanthridine for designing Au based photoemissive materials.

Complexes of Re metal based on tridentate *N^N^N* ligands exhibit antiproliferative activity towards very low concentration (micromolar scale) of cancer cells. This ligand is *N^N^N* type pincer ligand with bis-phenanthridine moiety, formed in octahedral geometry around Re(I) centre with bromide as a counterion. [63] Phenanthridine based complex showed higher selectivity and activity over its quinoline derived version. Potential applications of this complex include use as an anti-cancer drug.

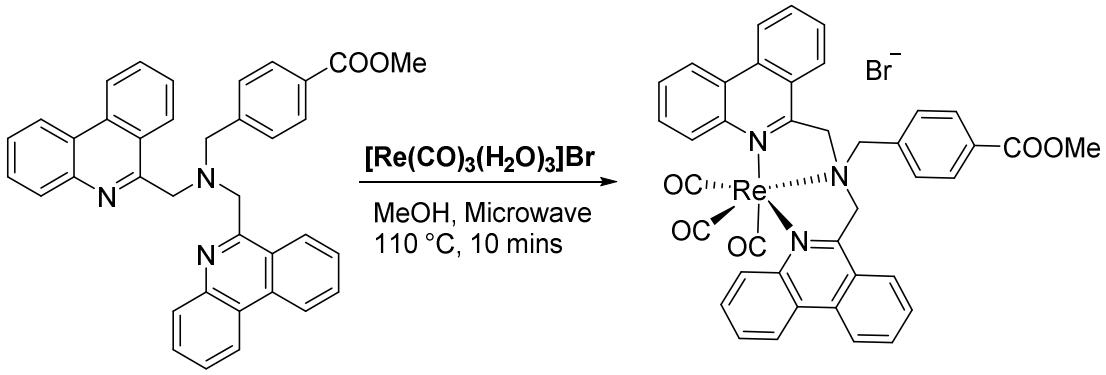

Scheme 1. 10: Use of phenanthridine for designing Re based anti cancer agent.

Phenanthridine has also been used in the catalytic biomimetic hydrogenation reaction. In the catalytic reaction, phenanthridine performed as biologically active molecule NAD(P)H to activate H_2 gas in presence of metal ion, itself converting to dihydrophenanthridne. The hydrogen equivalent then could be transfered to the organic substrate from dihydrophenanthridine and regenerate phenanthridine in the catalytic cycle. Zhou group used phenanthridine to activate H_2 gas in presence of Ru(II) complex and transfer the H_2 equivalent to an organic substrate such as benzoxazinones, benzoxazines, quinoxalines and quinolines.[53]

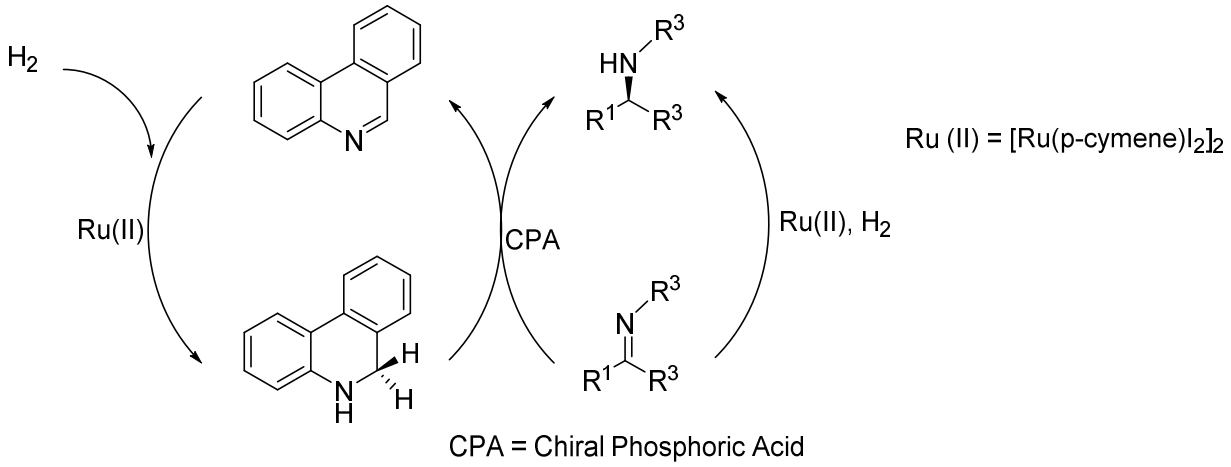

Scheme 1. 11: Use of phenanthridine as a bio-mimic NADP(H) model for hydrogenation of imine.

Similar example was published by the Beller group for biomimetic reduction of α-keto/α-Imino ester by Fe catalyst. The phenanthridine has been used as exogenous ligand for hydrogen transfer from metal centre to the product. A chiral ligand has been used to bind with Fe centre to stabilize the metal centre and also provide the enantioselectivity to the product.[64,65]

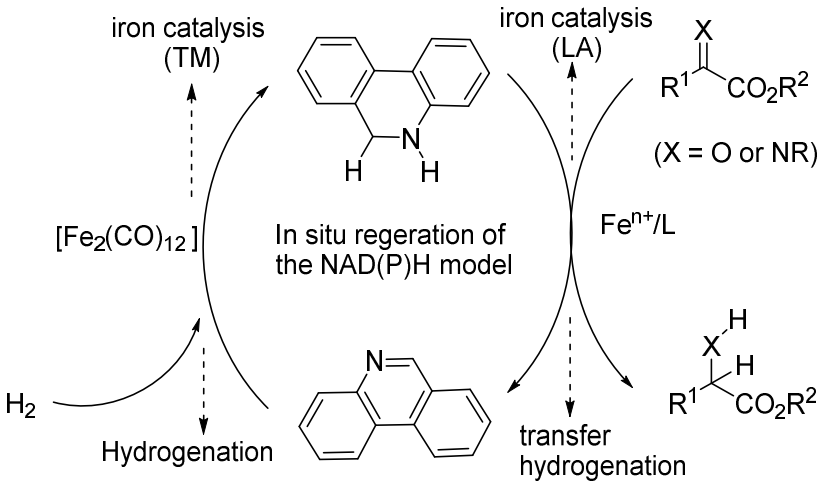

Scheme 1. 12: Use of phenanthridine as a bio-mimic NADP(H) model with Fe catalyst.

1.3.4. Phenanthridine: Our lab's progress

Since 2014, the Herbert Group at the University of Manitoba has been working on phenanthridine system. As a group, we have successfully developed derivatives of phenanthridine such as 4-bromophenanthridine followed by synthesizing the different variations such as phosphine or amido based ligands. We are studying the phenanthridine substituted ligand design and their coordination properties with the transition metal. We are also interested in disclosing the unexplored side of the phenanthridine as a molecule itself and activation of phenanthridine for using it in various reactions. I hereby discus some of our published work based on phenanthridine system from our lab. Our group has designed the tridentate *N^N^N* type pincer ligand based on benzo-fused π-extended phenanthridine system and formation of metal complexes with d^{10} metal ions and comparison with the quinoline based substitutent to investigate the effect of π-extention (**Figure 1.22**).[66]

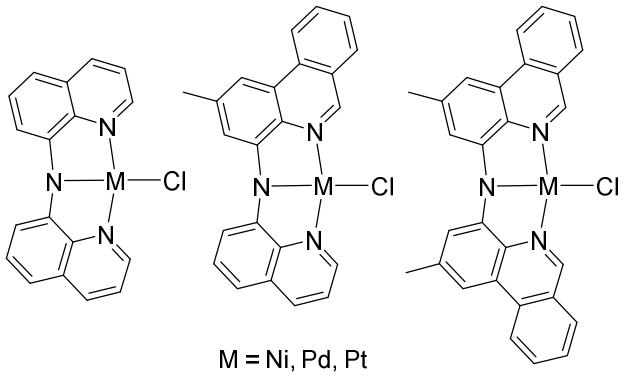

Figure 1. 22: Use of phenanthridine for designing *N^N^N* donor pincer type ligand based d^{10} metal complexes.

The effect of π-extension has been observed on UV-Vis absorption spectroscopy as slightly red shift from quinoline to phenanthridine as lowest energy band is considered. Theoretical DFT calculation showed that the effect of π-conjugation really impact the atomic contribution to the LUMO and LUMO+1, but only very slight change was observed of the absorption spectra. The transition for quinolino-amido metal complexes were obtained as HOMO to LUMO where as phenanthridine amido complexes have HOMO to LUMO+1 transition and for the phenanthridine quinoline amido complex both the HOMO to LUMO and HOMO to LUMO+1 transition was observed.[66] Our group has also developed metal-free electrochemical synthesis of dihydrophenanthridine from phenanthridine in presence of an acid (**Scheme 1.13**). The electrochemically generated hydrogen equivalents could be transferred to the "imine" like C=N bond of phenanthridine to synthesize stable dihydrophenanthridine.[46]

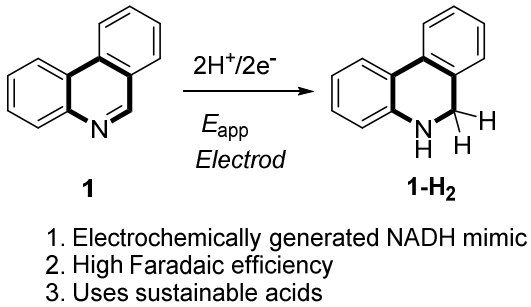

Scheme 1. 13: Electrochemically synthesis of dihydrophenanthridine.

1,2-dihydrophenanthrdine is well known for performing as the biomimetic hydride shuttles with late transition metals for the transfer hydrogenation reaction. The interesting chemistry here is potentially metal free hydrogen transfer to the organic substrate to obtain value added hydrogenated products such as amine or alcohols and regeneration of phenanthridine **(Scheme 14)**.[46]

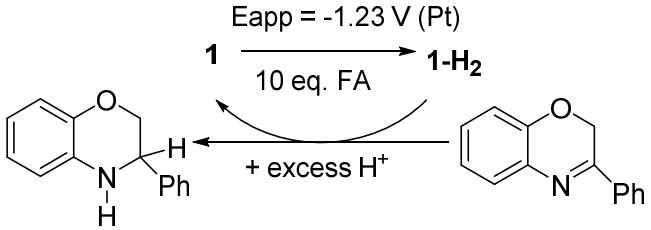

Scheme 1. 14: Hydrogen transfer to an organic substrate using phenanthridine.

1.4. Description of Thesis and Acknowledgments:

As a PhD candidate I have been working on a project that is based on designing neutral bidentate (*P^N*) and (*C^N*) type ligand on phenanthridine system (**Figures 1.23** and **1.24**). I have installed a phosphine group in the 4-position of the phenanthridine system to make bidentate *P^N* ligand. I am interested in studying the coordination chemistry of this novel *P^N* ligand with late transition metals and compare the properties such as photophysical, electrochemical with quinoline version. I would also like to disclose the catalytic activity of the phenanthridine system as *P^N* ligand while binding with late transition metal and study catalytic synthesis of value added organic substrate.

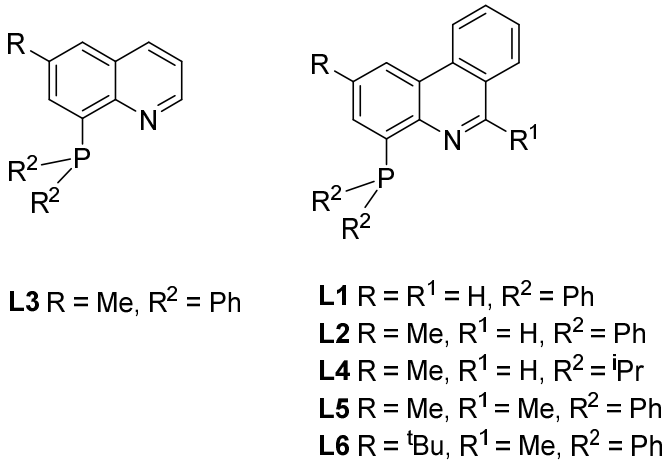

Figure 1. 23: Target *P^N* ligand.

Moreover, I have introduced an imidazolium group to the 6-position of phenanthridine to synthesize *C^N* ligand precursors. The *C^N* ligand was synthesized by deprotonation of imidazolium proton in basic medium. I am interested to find out π-extended *C^N* ligand effect on electronics while binding with late transition metal ions in octahedral geometry. Potential applications of these complexes are in the field of photosensitizers, photochemical synthesis.

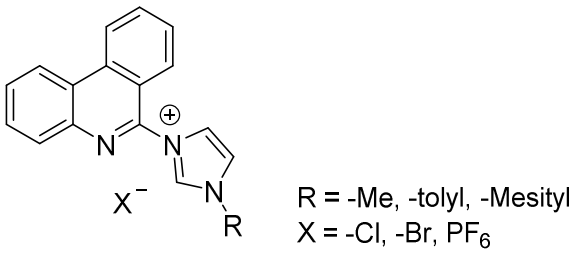

Figure 1. 24: Target *C^N* precursors.

1.4.1. Acknowledgments:

Chapter 1:

This chapter was inspired from the book of R. H. Crabtree '*The Organometallic Chemistry of the Transition Metals*, Seventh edition.; John Wiley & Sons, Inc.: Hoboken, NJ, 2019' and J. F. Hartwig '*Organotransition Metal Chemistry : From Bonding to Catalysis*; University Science Books: Sausalito, Calif, 2010'. Part of this chapter was also motivated from my co-worker Pavan Mandapati and Patrick K. Giesbrecht's research work.

Chapter 2:

Parts of this chapter were published as "Nickel(II), Copper(I) and Zinc(II) Complexes Supported by a (4-Diphenylphosphino)Phenanthridine Ligand". Mondal, R.; Giesbrecht, P. K.; Herbert, D. E. *Polyhedron* **2016**, *108*, 156–162. I, Rajarshi Mondal, was responsible for complete synthesis of the *P^N* ligand, metal complexes, characterization of the complexes and performing photo-spectroscopic technique with the help Dr. Mazdak Khajehpour. Patrick K. Giesbrecht was performed all cyclic voltammetry experiments. Dr. David E. Herbert and Jason D. Braun completed all the crystal structures in this chapter. Dr. Mazdak Khajehpour is appreciatively acknowledged for assistance with collecting excitation and emission spectra and for use of a spectrofluorometer. The preliminary draft of the paper was prepared by myself, and modified into its publication format in collaboration with my advisor, Dr. David E. Herbert.

Chapter 3:

Part of this chapter's work was published as "Site-Selective Benzannulation of N-Heterocycles in Bidentate Ligands Leads to Blue-Shifted Emission from $[(P\text{^}N)Cu]_2(\mu\text{-}X)_2$ Dimers." Mondal,

R.; Lozada, I. B.; Davis, R. L.; Williams, J. A. G.; Herbert, D. E. *Inorg. Chem.* **2018**, *57* (9), 4966–4978. I, Rajarshi Mondal was responsible for complete synthesis of metal complexes, characterization of the complexes, cyclic voltammetry experiments and performing solution state UV-Vis experiments. Dr. David E. Herbert has completed all the crystal structures into a publication standard. Dr. J. A. Gareth Williams has completed and processed as presented all the experimental spectroscopic data. Issiah B. Lozada was performed all the theoretical experiments, analysis and draft preparation for theatrical calculation section of the mentioned paper with the help of Dr. Rebecca L. Davis. I am grateful to Prof. Mazdak Khajehpour for access to UV−Vis spectrometer and to Prof. Viktor N. Nemykin for helpful discussions. The preliminary draft of the paper was prepared by myself, which was modified into its publication format by Dr. David E. Herbert.

Chapter 4:

Part of this chapter's work was published as "Exploiting synergy between ligand design and counterion interactions to boost room temperature phosphorescence from Cu(I) compounds". Mondal, R.; Lozada, I. B.; Davis, R. L.; Williams, J. A. G.; Herbert, D. E. *J. Mater. Chem. C.* **2019**, *7*, 3772–3778. I, Rajarshi Mondal was responsible for complete synthesis of metal complexes, characterization of the complexes, cyclic voltammetry experiments and performing solution state UV-Vis experiments. Dr. David E. Herbert has completed all the crystal structures into a publication standard. Dr. J. A. Gareth Williams has completed and processed as presented all the experimental spectroscopic data. Issiah B. Lozada performed all the theoretical experiments, analysis and draft preparation for theoretical section of the mentioned paper with the help of Dr. Rebecca L. Davis. I am grateful to Prof. Mazdak Khajehpour for access to a

UV−Vis spectrometer. The preliminary draft of the chapter was prepared by myself which was modified into its publication format by Dr. David E. Herbert.

Chapter 5:

I, Rajarshi Mondal was responsible for complete synthesis of metal complexes, characterization of the complexes, cyclic voltammetry experiments and performing solution state UV-Vis experiments. Dr. David E. Herbert and Jason D. Braun has completed all the crystal structures into a publication standard. I, Rajarshi Mondal was performed spectro-electrochemistry with the help of Dr. Yuriy V. Zatsikha. I am grateful to Prof. Viktor N. Nemykin for access to the spectrometer for spectroelectrochemistry. I am grateful to Prof. Mazdak Khajehpour for access to UV−Vis spectrometer and Dr. Johan van Lierop of physics department for Mössbauer spectroscopy. The preliminary draft of the chapter was prepared by myself, which was modified into its publication format by Dr. David E. Herbert.

Chapter 6:

I, Rajarshi Mondal was responsible for complete synthesis of metal complexes, characterization of complexes and catalysis. Dr. David E. Herbert has completed all the crystal structures into a publication standard. The preliminary draft of the chapter was written by myself, which was modified into its publication format by Dr. David E. Herbert.

1.5. References:

(1) Elsevier, C. J.; Reedijk, J.; Walton, P. H.; Ward, M. D. Ligand Design in Coordination Chemistry: Approaches to New Catalysts, New Materials, and a More Sustainable

Environment. *Dalton Trans.* **2003**, 1869–1880. (1a) University of Southern California. Scientists Find a Cheaper Way to Light up OLED Screens. *ScienceDaily*, February 7, 2019.

(2) Peris, E.; Crabtree, R. H. Key Factors in Pincer Ligand Design. *Chem. Soc. Rev.* **2018**, *47*, 1959–1968.

(3) Lawrence, M. A. W.; Green, K.-A.; Nelson, P. N.; Lorraine, S. C. Review: Pincer Ligands—Tunable, Versatile and Applicable. *Polyhedron* **2018**, *143*, 11–27.

(4) Crabtree, R. H. *The Organometallic Chemistry of the Transition Metals*, Seventh edition.; John Wiley & Sons, Inc.: Hoboken, NJ, 2019.

(5) Hartwig, J. F. *Organotransition Metal Chemistry : From Bonding to Catalysis*; University Science Books: Sausalito, Calif, 2010.

(6) Helmchen, G.; Pfaltz, A. Phosphinooxazolines-A New Class of Versatile, Modular P,N-Ligands for Asymmetric Catalysis. *Acc. Chem. Res.* **2000**, *33*, 336–345.

(7) Fan, Q.-H.; Li, Y.-M.; Chan, A. S. C. Recoverable Catalysts for Asymmetric Organic Synthesis. *Chem. Rev.* **2002**, *102*, 3385–3466.

(8) Espinet, P.; Soulantica, K. Phosphine-Pyridyl and Related Ligands in Synthesis and Catalysis. *Coord. Chem. Rev.* **1999**, *193–195*, 499–556.

(9) Carroll, M. P.; Guiry, P. J. P,N Ligands in Asymmetric Catalysis. *Chem. Soc. Rev.* **2014**, *43*, 819–833.

(10) Kwong, F. Y.; Yang, Q.; Mak, T. C. W.; Chan, A. S. C.; Chan, K. S. A New Atropisomeric P,N Ligand for Rhodium-Catalyzed Asymmetric Hydroboration. *J. Org. Chem.* **2002**, *67*, 2769–2777.

(11) Tao, B.; Fu, G. C. Application of a New Family of P,N Ligands to the Highly

Enantioselective Hydrosilylation of Aryl Alkyl and Dialkyl Ketones. *Angew. Chem. Int. Ed.* **2002**, *41*, 3892–3894.

(12) Zell, T.; Milstein, D. Hydrogenation and Dehydrogenation Iron Pincer Catalysts Capable of Metal–Ligand Cooperation by Aromatization/Dearomatization. *Acc. Chem. Res.* **2015**, *48*, 1979–1994.

(13) Zink, D. M.; Baechle, M.; Baumann, T.; Nieger, M.; Kuehn, M.; Wang, C.; Klopper, W.; Monkowius, U.; Hofbeck, T.; Yersin, H.; et al. Synthesis, Structure, and Characterization of Dinuclear Copper(I) Halide Complexes with P^N Ligands Featuring Exciting Photoluminescence Properties. *Inorg. Chem.* **2013**, *52*, 2292–2305.

(14) Ward, T. R. Regioselectivity of Nucleophilic Attack on [Pd(Allyl)(Phosphine)(Imine)] Complexes: A Theoretical Study. *Organometallics* **1996**, *15*, 2836–2838.

(15) Vasse, J.-L.; Stranne, R.; Zalubovskis, R.; Gayet, C.; Moberg, C. Influence of Steric Symmetry and Electronic Dissymmetry on the Enantioselectivity in Palladium-Catalyzed Allylic Substitutions. *J. Org. Chem.* **2003**, *68*, 3258–3270.

(16) Speiser, F.; Braunstein, P.; Saussine, L.; Welter, R. Nickel Complexes with Oxazoline-Based P,N-Chelate Ligands: Synthesis, Structures, and Catalytic Ethylene Oligomerization Behavior. *Organometallics* **2004**, *23*, 2613–2624.

(17) Daugulis, O.; Brookhart, M. Polymerization of Ethylene with Cationic Palladium and Nickel Catalysts Containing Bulky Nonenolizable Imine−Phosphine Ligands. *Organometallics* **2002**, *21*, 5926–5934.

(18) Sirbu, D.; Consiglio, G.; Gischig, Sebastian. Palladium and Nickel Complexes of (P,N)-Ligands Based on Quinolines: Catalytic Activity for Polymerization and Oligomerization. *J. Organomet. Chem.* **2006**, *691*, 1143–1150.

(19) Zheng, Q.; Zheng, D.; Han, B.; Liu, S.; Li, Z. Chromium Complexes Supported by the Bidentate PN Ligands: Synthesis, Characterization and Application for Ethylene Polymerization. *Dalton Trans.* **2018**, *47*, 13459–13465.

(20) Khan, M. Y.; Zhou, J.; Chen, X.; Khan, A.; Mudassir, H.; Xue, Z.; Lee, S. W.; Noh, S. K. Exploration of Highly Active Bidentate Ligands for Iron (III)-Catalyzed ATRP. *Polymer* **2016**, *90*, 309–316.

(21) Flapper, J.; Kooijman, H.; Lutz, M.; Spek, A. L.; van Leeuwen, P. W. N. M.; Elsevier, C. J.; Kamer, P. C. J. Nickel and Palladium Complexes of Pyridine-Phosphine Ligands as Ethene Oligomerization Catalysts. *Organometallics* **2009**, *28*, 1180–1192.

(22) Sun, W.-H.; Li, Z.; Hu, H.; Wu, B.; Yang, H.; Zhu, N.; Leng, X.; Wang, Honggen. Synthesis and Characterization of Novel Nickel(Ii) Complexes Bearing N,P Ligands and Their Catalytic Activity in Ethylene Oligomerization. *New J. Chem.* **2002**, *26*, 1474–1478.

(23) Gurung, S. K.; Thapa, S.; Kafle, A.; Dickie, D. A.; Giri, R. Copper-Catalyzed Suzuki–Miyaura Coupling of Arylboronate Esters: Transmetalation with (PN)CuF and Identification of Intermediates. *Org. Lett.* **2014**, *16*, 1264–1267.

(24) Tardiff, B. J.; McDonald, R.; Ferguson, M. J.; Stradiotto, Mark. Rational and Predictable Chemoselective Synthesis of Oligoamines via Buchwald-Hartwig Amination of (Hetero)Aryl Chlorides Employing Mor-DalPhos. *J. Org. Chem.* **2012**, *77*, 1056–1071.

(25) Crawford, S. M.; Lavery, C. B.; Stradiotto, M. BippyPhos: A Single Ligand With Unprecedented Scope in the Buchwald–Hartwig Amination of (Hetero)Aryl Chlorides. *Chem. – A Eur. J.* **2013**, *19*, 16760–16771.

(26) Lundgren, R. J.; Peters, B. D.; Alsabeh, P. G.; Stradiotto, M. A P,N-Ligand for Palladium-Catalyzed Ammonia Arylation: Coupling of Deactivated Aryl Chlorides, Chemoselective

Arylations, and Room Temperature Reactions. *Angew. Chem. Int. Ed.* **2010**, *49*, 4071–4074.

(27) Leitl, M. J.; Kuechle, F.-R.; Mayer, H. A.; Wesemann, L.; Yersin, Hartmut. Brightly Blue and Green Emitting Cu(I) Dimers for Singlet Harvesting in OLEDs. *J. Phys. Chem. A* **2013**, *117*, 11823–11836.

(28) Suzuki, T.; Yamaguchi, H.; Hashimoto, A.; Nozaki, K.; Doi, M.; Inazumi, N.; Ikeda, N.; Kawata, S.; Kojima, M.; Takagi, H. D. Orange and Yellow Crystals of Copper(I) Complexes Bearing 8-(Diphenylphosphino)Quinoline: A Pair of Distortion Isomers of an Intrinsic Tetrahedral Complex. *Inorg. Chem.* **2011**, *50*, 3981–3987.

(29) Tsukuda, T.; Nishigata, C.; Arai, K.; Tsubomura, Taro. Photophysical Properties of Copper(I) and Zinc(II) Complexes Containing Phosphinoquinoline Ligands. *Polyhedron* **2009**, *28*, 7–12.

(30) Schumacher, A.; Bernasconi, M.; Pfaltz, A. Chiral N-Heterocyclic Carbene/Pyridine Ligands for the Iridium-Catalyzed Asymmetric Hydrogenation of Olefins. *Angew. Chem. Int. Ed.* **2013**, *52*, 7422–7425.

(31) Igau, Alain.; Grutzmacher, Hansjorg.; Baceiredo, Antoine.; Bertrand, Guy. Analogous .Alpha.,.Alpha.'-Bis-Carbenoid, Triply Bonded Species: Synthesis of a Stable .Lambda.3-Phosphino Carbene-.Lambda.5-Phosphaacetylene. *J. Am. Chem. Soc.* **1988**, *110*, 6463–6466.

(32) Hopkinson, M. N.; Richter, C.; Schedler, M.; Glorius, F. An Overview of N-Heterocyclic Carbenes. *Nature* **2014**, *510*, 485.

(33) Chatterjee, A. K.; Choi, T.-L.; Sanders, D. P.; Grubbs, R. H. A General Model for Selectivity in Olefin Cross Metathesis. *J. Am. Chem. Soc.* **2003**, *125*, 11360–11370.

(34) Garber, S. B.; Kingsbury, J. S.; Gray, B. L.; Hoveyda, A. H. Efficient and Recyclable Monomeric and Dendritic Ru-Based Metathesis Catalysts. *J. Am. Chem. Soc.* **2000**, *122*, 8168–

8179.

(35) Gessler, S.; Randl, S.; Blechert, S. Synthesis and Metathesis Reactions of a Phosphine-Free Dihydroimidazole Carbene Ruthenium Complex. *Tetrahedron Lett.* **2000**, *41*, 9973–9976.

(36) Kjær, K. S.; Kaul, N.; Prakash, O.; Chábera, P.; Rosemann, N. W.; Honarfar, A.; Gordivska, O.; Fredin, L. A.; Bergquist, K.-E.; Häggström, L.; et al. Luminescence and Reactivity of a Charge-Transfer Excited Iron Complex with Nanosecond Lifetime. *Science* **2019**, *363*, 249.

(37) Harlang, T. C. B.; Liu, Y.; Gordivska, O.; Fredin, L. A.; Ponseca Jr, C. S.; Huang, P.; Chábera, P.; Kjaer, K. S.; Mateos, H.; Uhlig, J.; et al. Iron Sensitizer Converts Light to Electrons with 92% Yield. *Nat. Chem.* **2015**, *7*, 883.

(38) Hemmert, C.; Fabié, A.; Fabre, A.; Benoit-Vical, F.; Gornitzka, H. Synthesis, Structures, and Antimalarial Activities of Some Silver(I), Gold(I) and Gold(III) Complexes Involving N-Heterocyclic Carbene Ligands. *Eur. J. Med. Chem.* **2013**, *60*, 64–75.

(39) Hemmert, C.; Ramadani, A. P.; Boselli, L.; Fernández Álvarez, Á.; Paloque, L.; Augereau, J.-M.; Gornitzka, H.; Benoit-Vical, F. Antiplasmodial Activities of Gold(I) Complexes Involving Functionalized N-Heterocyclic Carbenes. *Bioorg. Med. Chem.* **2016**, *24*, 3075–3082.

(40) Zhang, C.; Bourgeade Delmas, S.; Fernández Álvarez, Á.; Valentin, A.; Hemmert, C.; Gornitzka, H. Synthesis, Characterization, and Antileishmanial Activity of Neutral N-Heterocyclic Carbenes Gold(I) Complexes. *Eur. J. Med. Chem.* **2018**, *143*, 1635–1643.

(41) Tumir, L.-M. *Beilstein J. Org. Chem.* **2014**, *10*, 2930.

(42) Keller, P. A. Phenanthridines. *ChemInform* **2005**, *36*.

(43) Stępień, M.; Gońka, E.; Żyła, M.; Sprutta, N. Heterocyclic Nanographenes and Other Polycyclic Heteroaromatic Compounds: Synthetic Routes, Properties, and Applications. *Chem. Rev.* **2017**, *117*, 3479–3716.

(44) Keller, P. A. *Sci. Synth.:Oxidation of Phenanthridines* **2005**, *15*, 1094.

(45) Brett, W. A.; Rademacher, P.; Boese, R. Redetermination of the Structure of Phenanthridine. *Acta Crystallogr., Sect. C: Cryst. Struct. Commun.* **1993**, *C49*, 1564–1566.

(46) Giesbrecht, P. K.; Nemez, D. B.; Herbert, D. E. Electrochemical Hydrogenation of a Benzannulated Pyridine to a Dihydropyridine in Acidic Solution. *Chem. Commun.* **2018**, 338–341.

(47) Benmachiche, A.; Zendaoui, S.-M.; Bouaoud, S.-E.; Zouchoune, B. Electronic Structure and Coordination Chemistry of Phenanthridine Ligand in First-Row Transition Metal Complexes: A DFT Study. *Int. J. Quantum. Chem.* **2013**, *113*, 985–996.

(48) Theobald, R. S.; Schofield, K. The Chemistry of Phenanthridine and Its Derivatives. *Chem. Rev.* **1950**, *46*, 170–189.

(49) *Handbook of Heterocyclic Chemistry*, 3rd ed.; Katritzky, A. R., Series Ed.; Elsevier: Amsterdam, 2010.

(50) Stevens, N.; O'Connor, N.; Vishwasrao, H.; Samaroo, D.; Kandel, E. R.; Akins, D. L.; Drain, C. M.; Turro, N. J. Two Color RNA Intercalating Probe for Cell Imaging Applications. *J. Am. Chem. Soc.* **2008**, *130*, 7182–7183.

(51) Raszeja, L.; Maghnouj, A.; Hahn, S.; Metzler-Nolte, Nils. A Novel Organometallic ReI Complex with Favourable Properties for Bioimaging and Applicability in Solid-Phase Peptide Synthesis. *ChemBioChem* **2011**, *12*, 371–376.

(52) Bakić, M. T.; Jadreško, D.; Hrenar, T.; Horvat, G.; Požar, J.; Galić, N.; Sokol, V.; Tomaš, R.; Alihodžić, S.; Žinić, M.; et al. Fluorescent Phenanthridine-Based Calix[4]Arene Derivatives: Synthesis and Thermodynamic and Computational Studies of Their Complexation with Alkali-Metal Cations. *RSC Adv.* **2015**, *5*, 23900–23914.

(53) Chen, Q.-A.; Gao, K.; Duan, Y.; Ye, Z.-S.; Shi, L.; Yang, Y.; Zhou, Y.-Gui. Dihydrophenanthridine: A New and Easily Regenerable NAD(P)H Model for Biomimetic Asymmetric Hydrogenation. *J. Am. Chem. Soc.* **2012**, *134*, 2442–2448.

(54) Roy Chowdhury, A.; Bakshi, R.; Wang, J.; Yildirir, G.; Liu, B.; Pappas-Brown, V.; Tolun, G.; Griffith, J. D.; Shapiro, T. A.; Jensen, R. E.; et al. The Killing of African Trypanosomes by Ethidium Bromide (Killing Trypanosomes by Ethidium Bromide). *PLoS Pathogens* **2010**, *6*, e1001226.

(55) Sigmon, J.; Larcom, L. L. The Effect of Ethidium Bromide on Mobility of DNA Fragments in Agarose Gel Electrophoresis. *Electrophoresis* **1996**, *17*, 1524–1527.

(56) Weitz, E. A.; Chang, J. Y.; Rosenfield, A. H.; Pierre, V. C. A Selective Luminescent Probe for the Direct Time-Gated Detection of Adenosine Triphosphate. *J. Am. Chem. Soc.* **2012**, *134*, 16099–16102.

(57) *Analogue-Based Drug Discovery*; Fischer, János., Ganellin, C. R. (C. R., Series Eds.; Wiley-VCH: Weinheim ;, 2006.

(58) Johnstone, T. C.; Suntharalingam, K.; Lippard, S. J. The Next Generation of Platinum Drugs: Targeted Pt(II) Agents, Nanoparticle Delivery, and Pt(IV) Prodrugs. *Chem. Rev.* **2016**, *116*, 3436–3486.

(59) Park, G. Y.; Wilson, J. J.; Song, Y.; Lippard, S. J. Phenanthriplatin, a Monofunctional DNA-Binding Platinum Anticancer Drug Candidate with Unusual Potency and Cellular Activity Profile. *Proc. Natl. Acad. Sci. U.S.A* **2012**, *109*, 11987.

(60) Johnstone, T. C.; Lippard, S. J. The Chiral Potential of Phenanthriplatin and Its Influence on Guanine Binding. *J. Am. Chem. Soc.* **2014**, *136*, 2126–2134.

(61) Jiang, B.; Gu, Y.; Qin, J.; Ning, X.; Gong, S.; Xie, G.; Yang, Chuluo. Deep-Red Iridium(III)

Complexes Cyclometalated by Phenanthridine Derivatives for Highly Efficient Solution-Processed Organic Light-Emitting Diodes. *J. Mater. Chem. C* **2016**, *4*, 3492–3498.

(62) Alizadeh, R.; Hafezeffati, S.; Amani, V.; Khavasi, H. R.; Harms, K. Synthesis, Characterization, Crystal Structure Determination, and Luminescence Properties of Two New Gold(III) Complexes with Phenanthridine Ligand. **2015**, *146*, 581.

(63) König, M.; Siegmund, D.; Raszeja, L. J.; Prokop, A.; Metzler-Nolte, N. Resistance-Breaking Profiling and Gene Expression Analysis on an Organometallic ReI–Phenanthridine Complex Reveal Parallel Activation of Two Apoptotic Pathways. *Med. Chem. Commun.* **2018**, 173–180.

(64) Lu, L.-Q.; Li, Y.; Junge, K.; Beller, Matthias. Relay Iron/Chiral Bronsted Acid Catalysis: Enantioselective Hydrogenation of Benzoxazinones. *J. Am. Chem. Soc.* **2015**, *137*, 2763–2768.

(65) Lu, L.-Q.; Li, Y.; Junge, K.; Beller, Matthias. Iron-Catalyzed Hydrogenation for the In Situ Regeneration of an NAD(P)H Model: Biomimetic Reduction of α-Keto-/α-Iminoesters. *Angew. Chem. Int. Ed.* **2013**, *52*, 8382–8386.

(66) Mandapati, P.; Giesbrecht, P. K.; Davis, R. L.; Herbert, D. E. Phenanthridine-Containing Pincer-like Amido Complexes of Nickel, Palladium, and Platinum. *Inorg. Chem.* **2017**, *56*, 3674–3685.

Chapter 2:

2.1. Abstract:

A synthetic route to 4/6-bromophenanthridine has been devised, enabling the construction of phosphinophenanthridine and N-heterocyclic carbene ligands, which are heterobifunctional Lewis bases containing both phosphine/carbene and a common phenanthridine donor. The coordination chemistry of ligands with late transition metals such as nickel, zinc, silver, ruthenium and iridium have been explored. The solid-state structure of nickel complexes showed ability of PN ligands to support both square planar and tetrahedral geometries. N-hetrocyclic carbene ligand showed octahedral geometry with Ru and Ir metals. Electrochemical and luminescence studies revealed both metal and ligand-based redox activity and emissive properties.

2.2. Introduction:

The potential for stable, directional bonding to metal ions, in conjunction with an electronically accessible extended π-system, has prompted the use of benzo-fused *N*-heterocycles-based ligand frameworks in coordination chemistry and enabled a number of useful applications. Extended *N*-heterocycles exhibit rich and varied coordination chemistry, both as monodentate ligands and as various sections of multidentate frameworks. For example, metal complexes of molecules such as 8-hydroxyquinoline have had impact in the application and development of organic light emitting diodes,[1] while complexes of 1,10-phenanthrolines[2] have found application in fields ranging from optoelectronics,[3] to the construction of molecular machines,[4] small-molecule activation and catalysis.[5]

In contrast to better known relatives, such as quinoline[6,7,8,9] and acridine,[5] phenanthridine is less common in ligand frameworks. As a monodentate ligand, phenanthridine can be noticed in the platin drug candidate, *cis*-[$Pt(NH_3)_2$(phenanthridine)Cl]NO_3 (phenanthriplatin), which exhibits novel antineoplastic behaviour compared with its pyridine analog.[10] Tris(4-phenanthridinolato) complexes of lithium[11] and aluminum[12] have been used as light-emitting components of electroluminescent devices. Re(I) complexes of *fac*-binding, tridentate bis(phenanthridinylmethyl)amines show relevant luminescence properties (red-shifted absorption maxima, lower excitation energies, large Stokes shifts, reduced sensitivity towards dioxygen quenching and emission in the orange region of the visible spectrum) for live-cell fluorescence imaging applications.[13]

In comparison, there has been a recent rejuvenation of interest in the organic chemistry,[14,15,16] biological properties, and photophysical applications of phenanthridine itself and its derivatives.[17] This chapter describes the construction of various (4-aryl/alkylphosphino)phenanthridines and 6-arylimidazolium phenanthridine salts as heterobifunctional ligands of both phosphine and carbene phenanthridine donor units, and their coordination chemistry with late transition metal ions. Metal complexes of (4-diphenylphosphino)phenanthridine show redox activity and luminescence attributable to the presence of a phenanthridinyl unit in the ligand backbone. For designing the metallo-carbene complexes, the precursor salts could be deprotonated by using base to generate free carbene followed by binding with the metal ions.

2.3. Results and Discussion:

To access all the proligands (**L1-L5**), I first explored routes to (4-bromo)phenanthridines (**Figure 2.1** and **Scheme 2.1**; **1-Br** to **5-Br**) via a tandem Pd-catalyzed cross-coupling and condensation.[18] Ray and coworkers reported the use of a similar strategy in the production of 2-substituted phenanthridines from *N*-(2-iodo-aryl)-formamides.[19,20] I explored (4-bromo)phenanthridine synthesis by optimizing the reaction condition of **1-Br**. While a range of conditions was screened (**Table 2.1**), the simplest route using 2,6-dibromoaniline was found to give acceptable, if low, yields (35-40%) of pure 4-bromophenanthridine (**1-Br**) following column chromatography. No significant increase in yield was observed using either- 2,6-dibromo-*N*-acetanilide or the trifluoroborate salt of 2-formylboronic acid; the gain in yield was not found to outweigh the additional synthetic steps required (entries 7-12 and 15). Anhydrous reaction conditions caused a shutdown of the overall reactivity (entries 14 and 15). The target compound 4-bromophenanthridine was isolated as a light yellow solid.

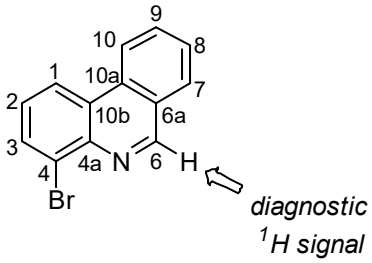

Figure 2. 1: Numbering of **1-Br.**

1-Br was characterized by 1-and 2D ^{1}H and ^{13}C NMR spectroscopy. ^{1}H NMR spectroscopy confirmed the construction of the asymmetric three fused phenanthridine ring system, with a diagnostic singlet for the H in the 6-position observed at 9.39 ppm in $CDCl_3$ with strong one-

bond coupling to a corresponding ^{13}C signal at 154.5 ppm (^{13}C–^{1}H HSQC). This downfield-shifted, deshielded signal is considered 'diagnostic' for phenanthridines, as the HC=N unit of the central pyridine ring has imine-type character (rather than 'pyridine'-type character) and the electronegative 'N' atom induces a deshielding situation for imine carbon and corresponding proton (-H) as well that is less attenuated by aromaticity than for typical pyridine rings. No imine bond (C=N) formation was observed between aldehyde and amine in the absence of Pd catalyst, implying that C-C coupling reaction precedes the construction of C=N bond which formed via intra-molecular condensation reaction.

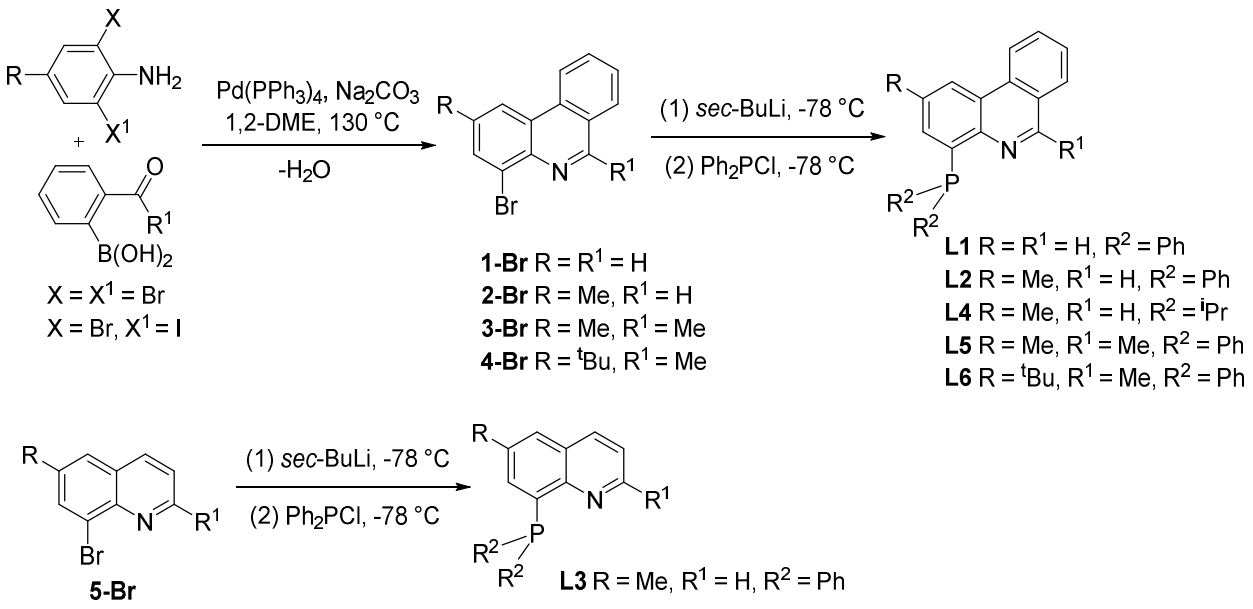

Scheme 2. 1: Bidentate PN ligand synthesis.

Table 2. 1: Conditions attempted for the synthesis of **1-Br**.

Entry	Catalyst (mol %)	Base	Solvent	T (°C)	t (h)	Yield[a] (%)
1	$Pd(PPh_3)_4$ (10)	$K_3PO_{4(aq)}$	DMF	100	5	13
2	$Pd(PPh_3)_4$ (10)	$K_3PO_{4(aq)}$	DMF	100	24	13
3	$Pd(PPh_3)_4$ (10)	$K_3PO_{4(aq)}$	Toluene	100	5	9
4	$Pd(PPh_3)_4$ (10)	Na_2CO_3	Toluene/EtOH	100	5	--
5	$Pd(PPh_3)_4$ (10)	$Na_2CO_{3(aq)}$	DME	100	5	31
6	$Pd(PPh_3)_4$ (2)	$Na_2CO_{3(aq)}$	DME	100	5	32
7[b]	$Pd(PPh_3)_4$ (5)	$Na_2CO_{3(aq)}$	DME	100	5	35
8[b]	$Pd(PPh_3)_4$ (2)	$Na_2CO_{3(aq)}$	DME	100	5	22
10[c]	$Pd(PPh_3)_4$ (10)	$K_3PO_{4(aq)}$	DME	100	5	13
11[c]	$Pd(PPh_3)_4$ (10)	$Na_2CO_{3(aq)}$	DME	100	5	25
12[c]	$Pd(PPh_3)_4$ (5)	$NaHCO_{3(aq)}$	DME	100	5	31
13	$Pd(OAc)_2$ /PPh_3 (0.08:1)	$Na_2CO_{3(aq)}$	DME	100	5	24
14	$Pd(PPh_3)_4$ (2)	Na_2CO_3 (anhyd.)	DME	100	5	trace
15[c]	$Pd(PPh_3)_4$ (2)	Na_2CO_3 (anhyd.)	DME	100	5	7

[a] Isolated yield following column chromatography.
[b] Potassium trifluoroborate salt of 2-formylphenylboronic acid
[c] 2,6-dibromo-*N*-acetanilide was used in place of 2,6-dibromoaniline

Other functionalized (4-bromo)phenanthridines (**2-Br** to **5-Br**) were then synthesized by following these optimized conditions.[21] Using *para*-substituted 2-bromo-6-iodo-4-methylaniline and 2-formylphenylboronic acid, **2-Br** could be isolated in high yield (~90%). 4-substituted anilines are easily iodinated, and the resulting iodoarenes are more active towards Pd-catalyzed C-C coupling than bromoarenes, resulting higher yield than seen for **1-Br**. A modified isolation technique of product was also developed for synthesis of **2-Br** to **4-Br** compared with our published procedure.[21] On completion of the reaction, the reaction mixture solution was evaporated using a rotary evaporator to give a deep brown solid. The product could then be extracted with DCM and passed through a short plug of silica. A bright deep orange solution was pumped dry and crystallized from ethanol. A bright yellowish white solid was isolated (~85-90%). In this way I could circumvent the acid workup and column technique of the published procedure, while maintaining similar isolated yield.

Comparing the various (4-bromo)phenanthridines, the diagnostic proton resonance for the hydrogen nucleus in the 2-position observed by ^{1}H NMR spectroscopy for **2-Br** (4-bromo-2-methylphenanthridine) is shifted upfield (9.29 ppm in $CDCl_3$**)** compared to that of **1-Br**, which could be due to the inductive donation effect of the 2-methyl substituent increasing the electron density of the phenanthridine ring system. To target molecular rigidity (see below) and increase solubility, I designed **3-Br** and **4-Br** which bear a methyl group at the 6-position and a *tert*-butyl or methyl at the 2-position. To do so, I used 2-acetylphenyl boronic acid with the appropriate aniline to build the tricyclic framework with decent yields of ~85% (**Scheme 2.1**).

2.3.1. Ligand Design: Bidentate *P^N* Donor Ligands:

With 4-halo-phenanthridines in hand, the proligands **L1**, **L2**, **L3**, **L4** and **L5** were all accessed via similar fashion of lithium halogen exchange of the appropriate 4-bromophenanthridine, followed by quenching with a phosphine electrophile (R_2PCl where R = is either phenyl or isopropyl). The diphenylphosphinyl group was installed for **L1**, **L2**, **L4** and **L5** via lithium halogen exchange using *sec*-BuLi at -78 °C in diethyl ether, followed by quenching with Ph_2PCl (one equivalent) at the same temperature. The reactions were generally efficient and the phosphinophenanthridines could be isolated by redissolving the dried residue in DCM and filtering through Celite. Volatiles were then remove to isolate a crude material, which was then washed with degassed ethanol to obtain faint yellow solids. **L1** was isolated as 72% yield whereas the yields of **L2**, **L4** and **L5** were 63%, 61% and 67%, respectively.

The *P^N* proligands were characterized by ^{1}H, $^{13}C\{^{1}H\}$ and $^{31}P\{^{1}H\}$ NMR spectroscopy. The diagnostic singlet resonance for the hydrogen nucleus in the 6-position of **L1** was observed at 9.23 ppm in $CDCl_3$, whereas for **L2**, this same resonance is observed slightly upfield at 9.19

ppm, consistent with the result what was observed for the parent bromophenanthridines. X-ray quality single crystals of **L1** were grown from a mixture of CH_2Cl_2 and Et_2O via vapour diffusion. The X-ray diffraction study confirmed the structure of assigned ligand in solution (**Figure 2.2**). The solid state structure disclosed a shorter bond length for the C(1)=N(1) [1.3005(15) Å; **Table 2.2**] unit of the central pyridine ring of **L1** compared with 8-(diphenylphosphino)quinoline [1.3196(17)][22] but very close to the bond length for the same C=N bond in phenanthridine itself.[23] Otherwise, no remarkable changes were observed in the bond lengths or angles for **L1** compared with phenanthridine. The detailed synthesis and characterization of **L3** is given in Chapter **5**, **L4** in Chapter **4** and **L5** in Chapter **3**.

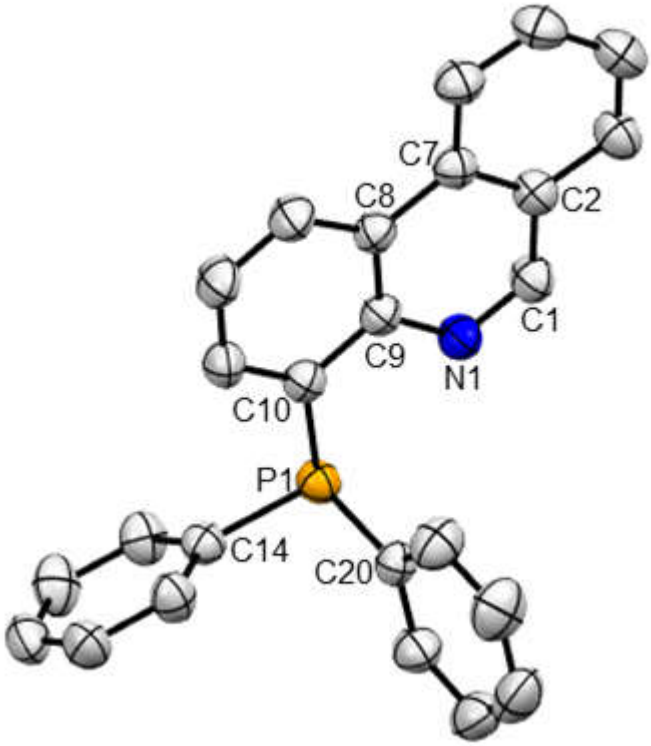

Figure 2.2. ORTEP[24] of L**1** with thermal ellipsoids shown at 50 % probability levels.

Table 2. 2: Selected bond distances (Å) and angles (°) for **L1**:

Selected Bonds	(Å)	Selected Angles	(°)
C(1)-N(1)	1.3005(15)	C(20)-P(1)-C(10)	102.85(5)
C(1)-C(2)	1.4329(16)	C(20)-P(1)-C(14)	100.71(5)
C(2)-C(7)	1.4085(16)	C(10)-P(1)-C(14)	102.73(5)
C(7)-C(8)	1.4464(16)		
C(8)-C(9)	1.4157(14)		
C(9)-N(1)	1.3865(13)		
C(10)-P(1)	1.8347(12)		

2.3.2. Ligand Design: Bidentate *C^N* donor:

To obtain the proligands (**L7•**HBr, **L8•**HBr, and **L9•**HBr**)** I first synthesized 6-bromo/chlorophenanthridine via a one-step reaction between phenanthridinone with the appropriate phosphine oxide POX_3 (X = Cl and Br). Phenanthridinone itself was synthesized from 9-fluorenone following a published procedure from the patent literature.[25] 6-bromophenanthridine has been isolated as a light yellow solid in 72% yield. In the ^{1}H NMR of 6-bromophenanthridine, upfield shifts of the aromatic peaks was observed compared to 4-bromophenanthridine and the absence of 6-position singlet diagnostic peak was noted. 6-chlorophenanthridine was also synthesized following a published procedure,[26] a similarly coloured solid was isolated as product of 79% yield. ^{1}H NMR spectroscopy data matched the published values.[26] Reacting 6-bromophenanthridine with 1-methylimidazole, 1-(p-tolyl)-1H-imidazole and 1-mesityl-1H-imidazole, respectively, gave the bromide salts of **L7•**HBr, **L8•**HBr and **L9•**HBr (**Scheme 2.2**).

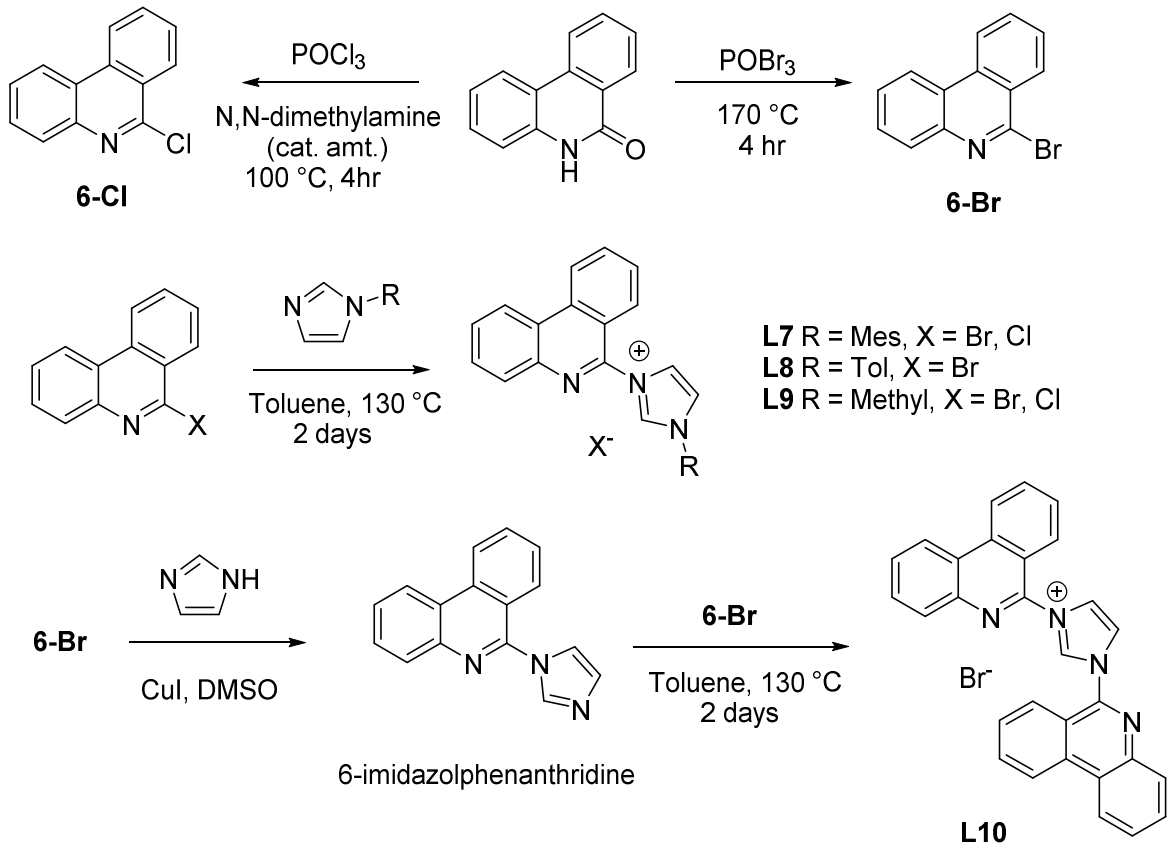

Scheme 2. 2: Synthesis of *C^N* ligand precursors **L7-L10•HX (X = Br, Cl)**

In these reactions, 6-bromophenanthridine was reacted with imidazole in toluene for 2 days at 130 °C to give an off-white solid, which was isolated by vacuum filtration and washed with Et_2O. For further purification the crude solid was recrystallized from DCM-Et_2O. The synthesis was accomplished by following the modified method of published procedure.[27] In the ^1H NMR spectrum, the acidic imidazolium proton was observed at ~10.6 ppm for both tolyl and mesityl in $CDCl_3$ and 9.69 for methyl in CD_3CN. A single crystal X-ray structure was obtained for **L7•**HBr salt from crystals grown in DCM-Et_2O by vapor diffusion (**Figure 2.3**) with bond distances and angles highlighted in (**Table 2.3**).

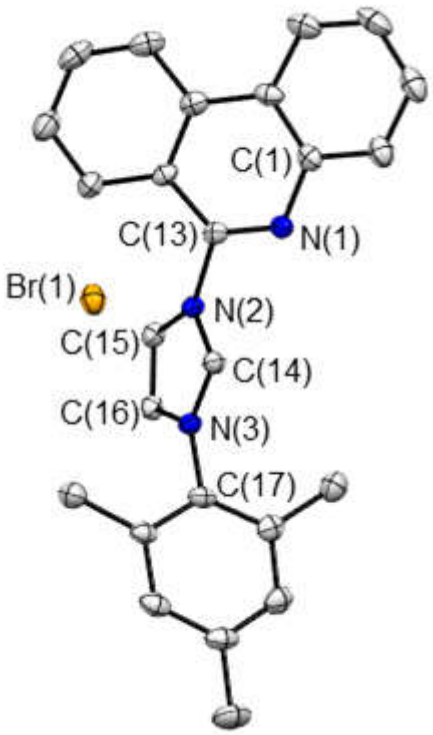

Figure 2. 3. ORTEP[24] of **L7•**HBr, all with thermal ellipsoids shown at 50% probability levels. Hydrogen atoms and labels on phosphine phenyl rings are omitted for clarity. Selected bond distances (Å) and angles (°).

Table 2. 3: Selected bond distances (Å) and angles (°) for **L7•**HBr:

Selected Bonds	**(Å)**	**Selected Angles**	**(°)**
C(1)-N(1)	1.376(4)	N(1)-C(13)-N(2)	113.9(3)
C(13)-N(1)	1.286(4)	N(3)-C(14)-N(2)	108.4(3)
C(14)-N(3)	1.321(4)	N(3)-C(14)-H(14)	125.8
C(14)-N(2)	1.338(4)	N(2)-C(14)-H(14)	125.8
C(15)-C(16)	1.341(4)	C(15)-C(16)-N(3)	107.2(3)
C(16)-N(3)	1.386(4)	C(14)-N(2)-C(15)	108.4(3)

The corresponding hydrochloride salts **L7•**HCl and **L9•**HCl were isolated from reaction of 6-chlorophenanthridine with 1-methylimidazole or 1-mesityl-1H-imidazole. I was unable to isolate the 3-(6-phenanthridinyl)-1-(4-methylphenyl)-1H-imidazolium chloride salt by our synthetic technique, for reasons that remain unclear. In the ^{1}H NMR spectra of the chloride salts, the tolyl imidazolium proton was observed around 9.91 ppm whereas the mesityl imidazolium proton was seen at 10.28 ppm in $(CD_3)_2SO$ solution.

The potentially tridentate ligand precursor **L10•**HBr was synthesized using 6-imidazolphenanthridine, which was synthesized by Cu(I) catalyzed Ullmann coupling. **L10•**HBr precursor was synthesized by the reaction between 6-imidazolphenanthridine and one more equivalent of 6-bromophenanthridine in toluene at 130 °C. A light yellow solid was isolated and washed with Et_2O. In the ^{1}H NMR spectra, the imidazolium peak was observed around 10.78 ppm in $(CD_3)_2SO$ solution. In the ^{1}H NMR, both the attached phenanthridine showed a symmetric chemical environment in **L10•**HBr, appearing as a single set of resonances with appropriate integration.

2.3.3. Ligand Design: Bidentate *N^N* donor:

To acquire **L11,** Buchwald-Hartwig coupling of **2**-Br and piperidine was performed (**Scheme 2.3**). A tertiary amine was obtained as a product from the reaction of aromatic halogen (**2**-Br) and secondary cyclic amine piperidine in presence of Pd^0 source and base (NaO^tBu) with supporting ligand *rac*-BINAP in toluene at 130 °C. A yellow solid was isolated after column chromatography, which was washed with Et_2O, giving a light yellow solid as product in 87% isolated yield of **L11** ligand.

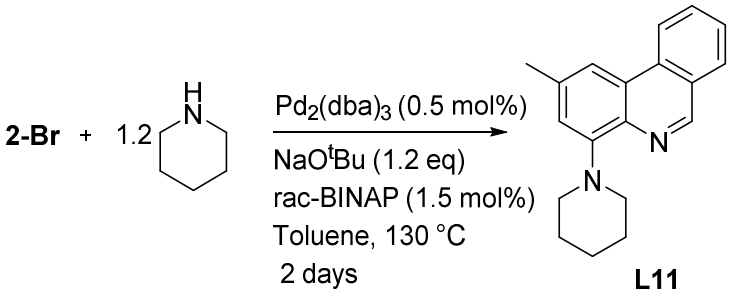

Scheme 2.3: Synthesis of bidentate *N^N* donor ligand

2.3.4. Coordination Chemistry:

2.3.4.1. Metal complexes of *P^N* Ligand:

To establish the coordinating ability of **L1** towards late transition metals, representative first row metal complexes of Ni and Zn were targeted (**Scheme 2.4**). These metals were chosen to allow characterization of complexes of **L1** with either redox-active Ni or redox-inactive metals (Zn). The chelating bifunctional ligand **L1** readily displaces weakly bound monodentate ligands such as PPh_3 from chloro(1-naphthyl)*bis*(triphenylphosphine)nickel at room temperature in CH_2Cl_2. This was evident by the disappearance of the resonance of **L1** and the appearance of a new singlet in the $^{31}P\{^1H\}$ NMR spectrum (δ = 30.6 ppm), consistent with formation of a single isomer with the strongly σ-donating napthyl group likely *trans* to the phenanthridinyl unit.

From this solution, complex (**L1**)Ni(Cl)(1-napthyl) could be isolated in high yield (92 %) as a crystalline red-orange solid. Inequivalent, sharp resonances for each phenyl ring in the -PPh_2 unit are evident in the ^1H NMR spectrum suggesting an orthogonal orientation of the napthyl and phenanthridinyl ring systems and limited rotation about the Ni-carbon bond across a range of temperatures (323-223 K). The signal for the diagnostic phenanthridine proton in the 6-position shifts drastically upon coordination to nickel (δ = 10.62 ppm), a shift of 1.5 ppm downfield

compared with (**L1**)Ni(Cl)(1-napthyl) In the crystal structure of (**L1**)Ni(Cl)(1-napthyl) (**Figure 2.4),** all bond angles are close to 90 °C which shows the crystal structure close to square planar geometry (**Table 2.4**).

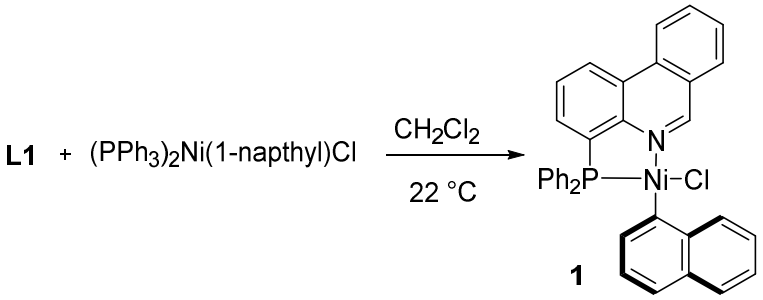

Scheme 2. 4: Synthesis of metal complex (**L1**)Ni(Cl)(1-napthyl)

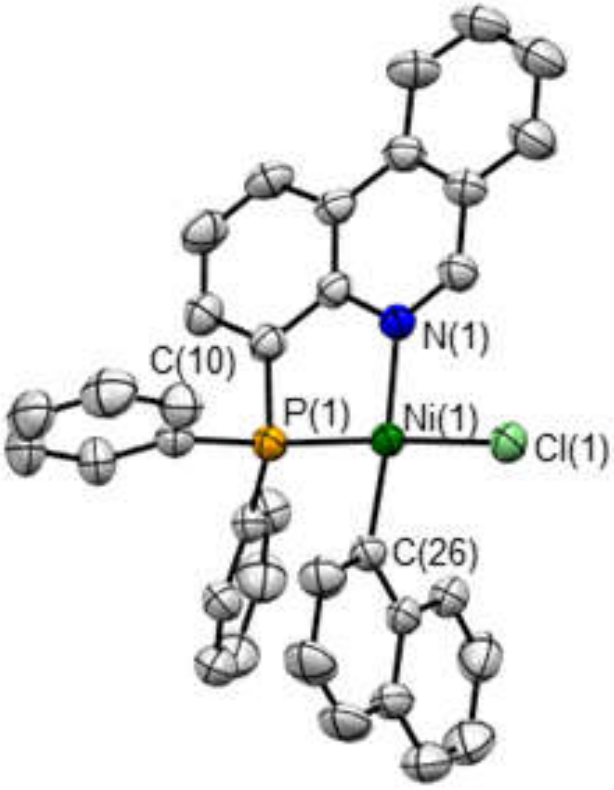

Figure 2. 4. ORTEP[24] of complex **(L1)Ni(Cl)(1-napthyl)**, all with thermal ellipsoids shown at 50% probability levels. Hydrogen atoms and labels on phosphine phenyl rings are omitted for clarity. Selected bond distances (Å) and angles (°).

Table 2. 4: Selected bond distances (Å) and angles (°) for (**L1**)Ni(Cl)(1-napthyl):

Selected Bonds	**(Å)**	**Selected Angles**	**(°)**
Ni(1)-C(26)	1.900(3)	N(1)-Ni(1)-P(1)	87.49(6)
Ni(1)-N(1)	1.996(2)	N(1)-Ni(1)-C(26)	95.88(7)
Ni(1)-P(1)	2.1053(9)	P(1)-Ni(1)-Cl(1)	86.08(8)
Ni(1)-Cl(1)	2.2162(9)	C(26)-Ni(1)-Cl(1)	90.61(8)
N(1)-C(1)	1.301(3)	N(1)-Ni(1)-Cl(1)	95.89(7)

To further study the coordination chemistry of **L1**, reaction of **L1** with $Ni(COD)_2$ was performed to obtain a Ni(0) complex. Ni complexes with lower oxidation (0 or +1) state are well known for performance as active catalyst, in small molecule bond activation chemistry.[28] Ni in higher oxidation states are also known to bind neutral *P^N* type ligands. To target a Ni(0) complex, a reaction was performed between **L1** and $Ni(COD)_2$ (COD = 1,5-cyclooctadiene) in THF at -35 °C, pumped dried to acquire a solid residue. The formation of complex (**L1**)Ni(COD) could be seen by comparing the diagnostic proton with that of free **L1**. In addition, in the ^{1}H NMR (**Figure 2.5**) of the crude, one equivalent of free COD was observed with a second equivalent still bound with the metal centre. Full consumption of the ^{31}P peak of **L1** was observed after the reaction and a new peak was observed at 41.7 ppm, consistent with binding of the phosphine arm of **L1** to Ni (**Figure 2.6**). The proposed structure of the product is shown in **Scheme 2.5**. Despite this solution NMR characterization, the proposed complex was found to decompose over time at room temperature. This may be due to dissociation of a labile cyclooctadiene ligand from Ni.

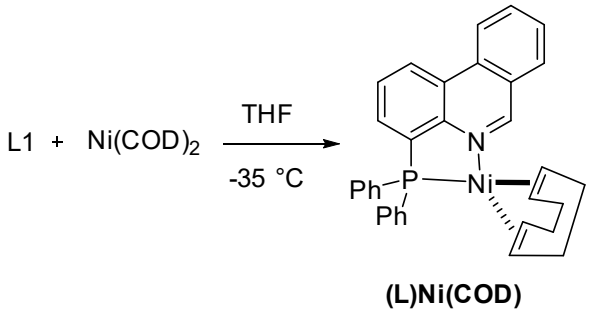

Scheme 2. 5: Synthesis of metal complex **(L1)Ni(COD)**

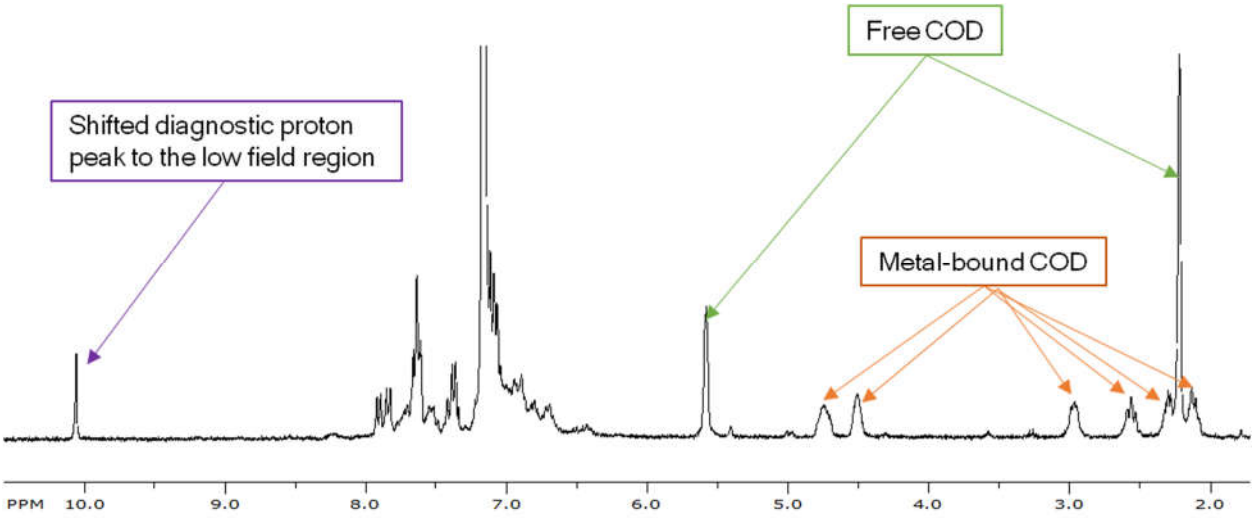

Figure 2. 5. ^{1}H NMR spectroscopic evidence for complex (**L1**)Ni(COD)

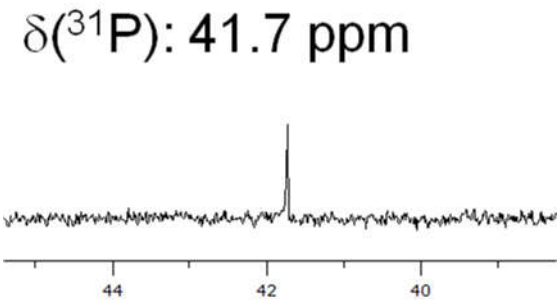

Figure 2. 6: ^{31}P NMR spectroscopic evidence for complex (**L1**)Ni(COD)

To make Ni(0) structurally stable, I attempted to install two additional (triphenyl)phosphine ligands at Ni in place of the weakly bound COD (**Scheme 2.6**). Two equivalents of triphenylphosphine were reacted with $Ni(COD)_2$ in Et_2O at 22 °C to generate

(COD)Ni(PPh_3)$_2$ which was then reacted with one equivalent **L1** to get the desired complex (**L1**)Ni(PPh_3)$_2$. Complex (**L1**)Ni(PPh_3)$_2$ was characterized by ^{1}H (**Figure 2.7**) and ^{31}P{^{1}H} spectroscopy (**Figure 2.8**). ^{31}P{^{1}H} NMR spectroscopy confirmed the construction of complex (**L1**)Ni(PPh_3)$_2$, with a doublet (~ 44 ppm) and triplet (~ 33 ppm) observed, with appropriate J_{AB} = 45.98 Hz coupling constant of two different phosphine environments (**Figure 2.8**). The addition of two monodentate PPh_3 ligands, however, did not seem improve the stability of (**L1**)Ni(PPh_3)$_2$, and decomposition was observed on storing at room temperature even under an N_2 atmosphere.

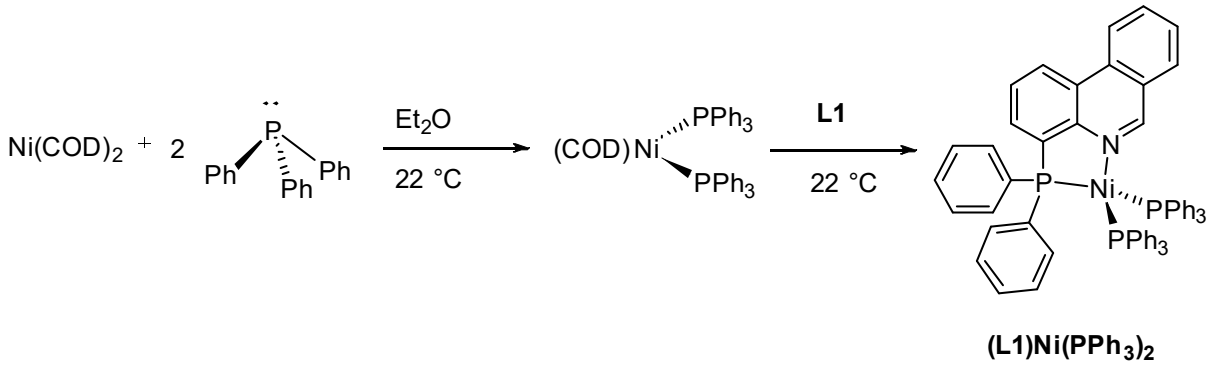

Scheme 2. 6: Synthesis of metal complex (**L1**)Ni(PPh_3)$_2$

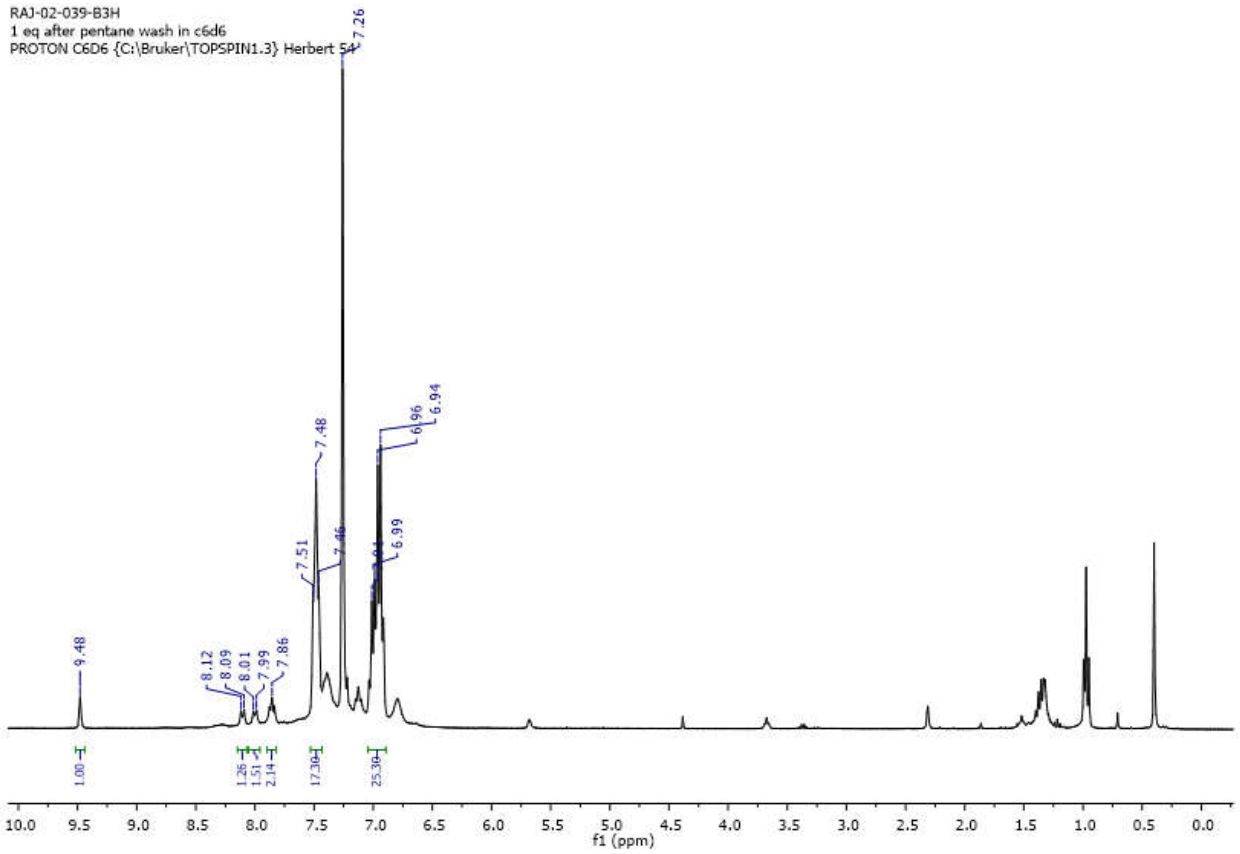

Figure 2. 7: ^{1}H NMR spectroscopic evidence for complex (**L1**)Ni(PPh_3)$_2$

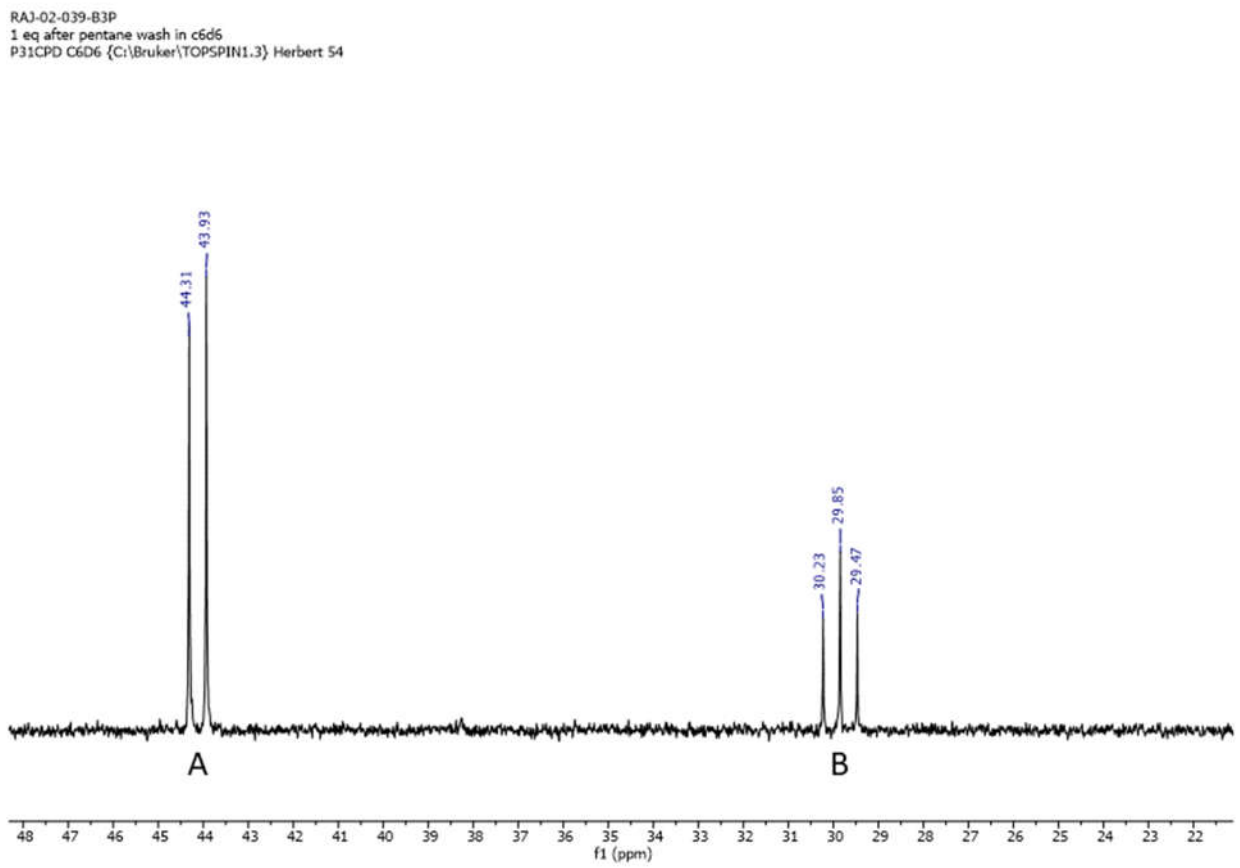

Figure 2. 8: ^{31}P NMR spectroscopic evidence for complex **(L1)Ni(PPh$_3$)$_2$**

Given that I was able to isolate complex (**L1**)Ni(Cl)(1-napthyl), I proceeded to simpler complexes of Ni(II). For these reactions, I turned to proligand **L2**, as the overall isolated yield of this proligands was higher than **L1**. A deep reddish pink suspension was obtained by reaction of **L2** with (DME)$NiCl_2$ at room temperature in THF solution (**Scheme 2.7**). The isolated solid however, was only weakly soluble in organic solvents. ^{1}H NMR was obtained from faintly soluble CD_2Cl_2 (**Figure 2.9**).

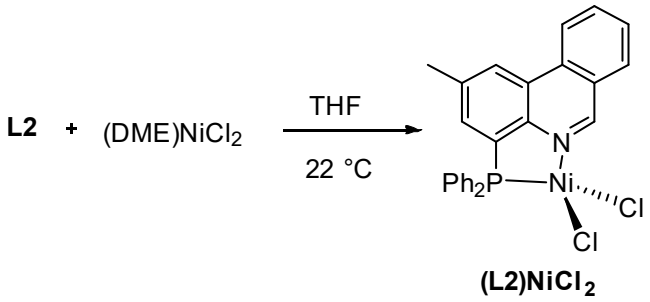

Scheme 2.7: Synthesis of metal complex (**L2**)$NiCl_2$

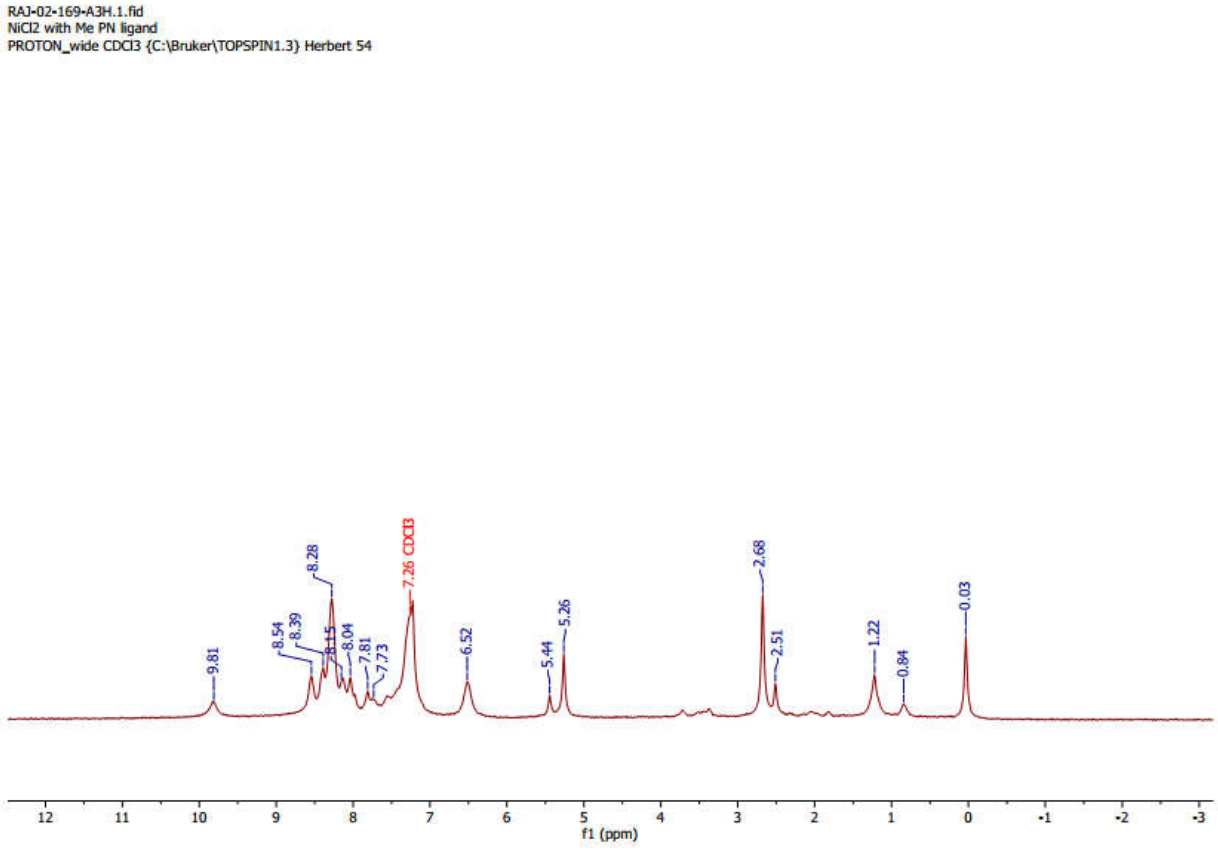

Figure 2. 9: ^1H NMR spectroscopic evidence for complex (**L2**)$NiCl_2$

L4 was used to perform the same reaction with (DME)$NiCl_2$ and complex **(L4)$NiCl_2$** was obtained (**Scheme 2.8**). Unlike complex (**L2**)$NiCl_2$, this compound was reddish pink in color, more soluble in common organic solvents, and diamagnetic. The diisopropylphosphine-

substituted ligand therefore provides both better solubility. This complex was characterized by ^{1}H and $^{31}P\{^{1}H\}$ NMR spectroscopy and single crystal X-ray diffraction (**Figure 2.10**). A diamagnetic environment was observed in ^{1}H NMR data with a downfield shift of diagnostic peak of phenanthridine ring. A combined electronegativity of Ni bound Cl^- ligands and 'N' atom provides extra deshielding effect at the carbon centre of 'imine' like carbon and connected H as well, which caused the downfield shift of diagnostic proton. Preliminary single crystal X-ray data supported the solution state characterization results by revealing a square planar geometry for Ni.

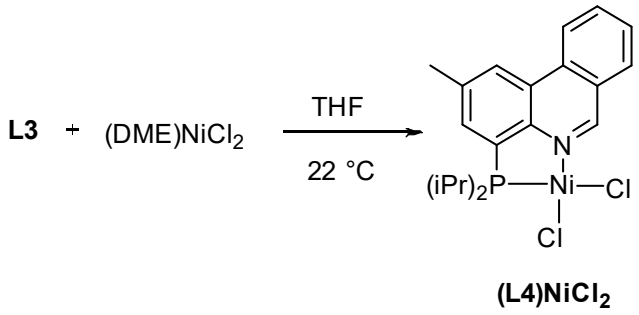

Scheme 2. 8: Synthesis of metal complex (**L4**)$NiCl_2$

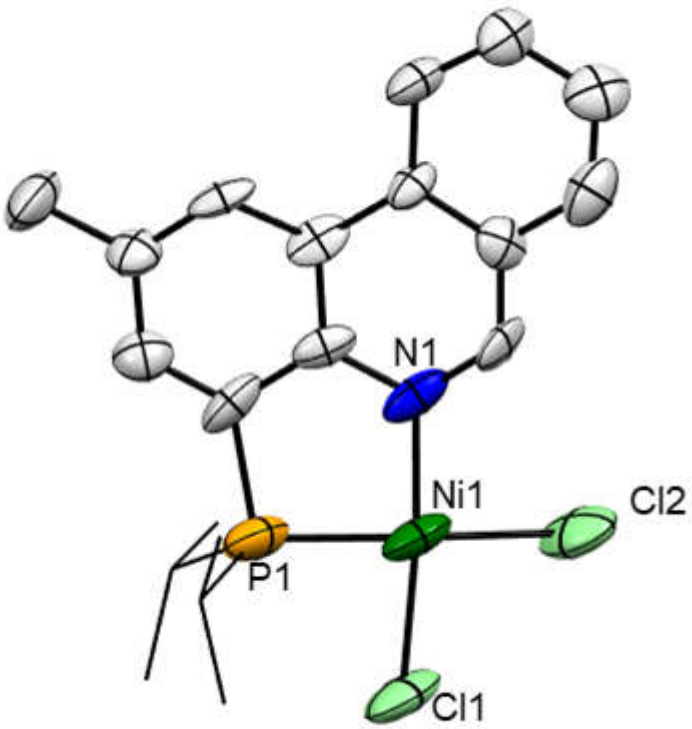

Figure 2. 10: Crystal structure of complex (**L4**)$NiCl_2$, Hydrogen atoms and labels on isopropyl group are omitted for clarity. A fully satisfactory crystal structure could not be obtained; nevertheless, preliminary data confirmed the proposed structure and connectivity.

Mixing a DCM solution of **L1** with a solution of $ZnCl_2$ in DCM led to the formation of a white precipitate after 3 h of stirring under ambient conditions. Isolation and re-crystallization from CH_2Cl_2/hexanes gave colorless crystals of **(L1)ZnCl₂** in good yield (83%; **Scheme 2.9**). Similar to complexes **(L1)Ni(Cl)(1-napthyl)**, **(L1)Ni(COD)** and **(L4)NiCl₂** the ^{1}H NMR of the Zn complex showed a downfield shift of the diagnostic proton of phenanthridine (δ_H = 9.57 ppm). In the solid state, the X-ray crystal structure showed tetrahedral geometry of complex **(L1)ZnCl₂** (**Figure 2.11**).

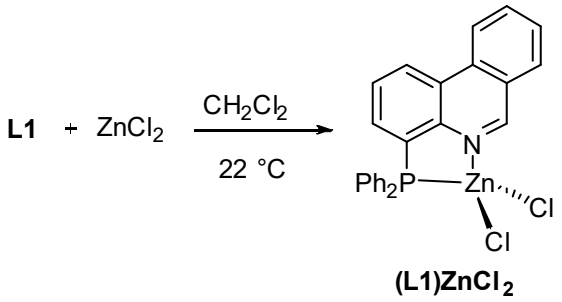

Scheme 2. 9: Synthesis of metal complex (**L1**)$ZnCl_2$

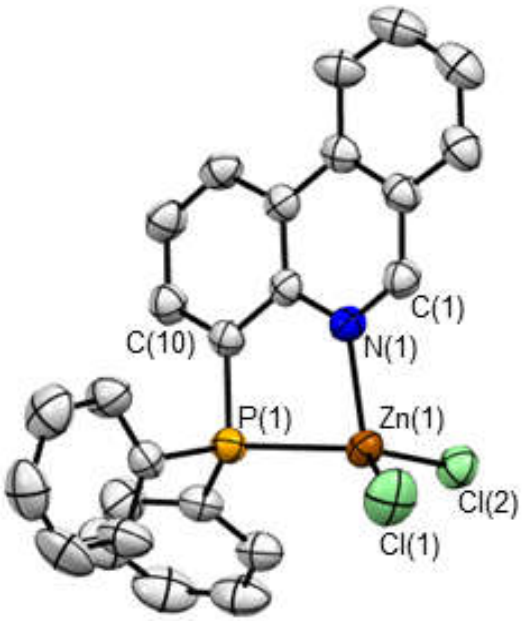

Figure 2. 11: ORTEP[24] of complex (**L1**)$ZnCl_2$ all with thermal ellipsoids shown at 50% probability levels. Hydrogen atoms and labels on phosphine phenyl rings are omitted for clarity. Selected bond distances (Å) and angles (°).

Table 2. 5: Selected bond distances (Å) and angles (°) for (**L1**)$ZnCl_2$:

Selected Bonds	(Å)	Selected Angles	(°)
Zn(1)-N(1)	2.091(2)	N(1)-Zn(1)-Cl(1)	110.51(7)
Zn(1)-Cl(1)	2.1896(10)	N(1)-Zn(1)-Cl(2)	105.16(6)
Zn(1)-Cl(2)	2.2230(8)	C(10)-P(1)-C(14)	102.73(5)
Zn(1)-P(1)	2.3854(8)	Cl(1)-Zn(1)-Cl(2)	118.08(4)
N(1)-C(1)	1.305(3)	N(1)-Zn(1)-P(1)	82.54(6)
N(1)-C(9)	1.396(3)	Cl(1)-Zn(1)-P(1)	121.01(3)
		Cl(2)-Zn(1)-P(1)	112.30(3)

2.3.4.2 Metal complexes of *C^N* ligand:

I next explored simple coordination complexes of our *C^N* ligands. The coinage metals bind carbene ligands well, especially silver, which could provide useful transmetallating reagents for formation of other transition metal complexes.[29] I therefore started with simple complexes of Ag(I). To access the PF_6 salt of precursor **L7** and **L8** I have synthesized the hexafluorosulphate salt of carbene precursors by reacting sodium hexafluorosulphate with the bromide salts of mesityl and tolyl precursor in water to obtain an off white precipitate after 2 days (**Scheme 2.10**). [**(L7)-H]PF_6** and [**(L8)-H]PF_6** collected by filtration. The precipitate was filtered and washed with water. Off white solid was collected after drying in high vacuum of 90% and 86% isolated yield as [**(L7)-H]PF_6** and **[(L8)-H]PF_6.** These have been characterized by ^1H, ^{19}F NMR spectroscopy and X-ray spectroscopy. Silver oxide is well known for deprotonating imidazolium salts and the metal binds easily to the *in situ* generated free carbene ligand. With one equivalent of mesityl hexafluorophosphate salt [**(L7)-H]PF_6**, 0.5 equivalent of Ag_2O was added in CH_3CN and stirred for 16 h at exactly 50 °C. A colorless solution has formed and all Ag_2O was

consumed. The solution was filtered through Celite and crystallized from diethyl ether at room temperature, giving faint yellow crystals. This complex has been characterized by ^{1}H NMR.

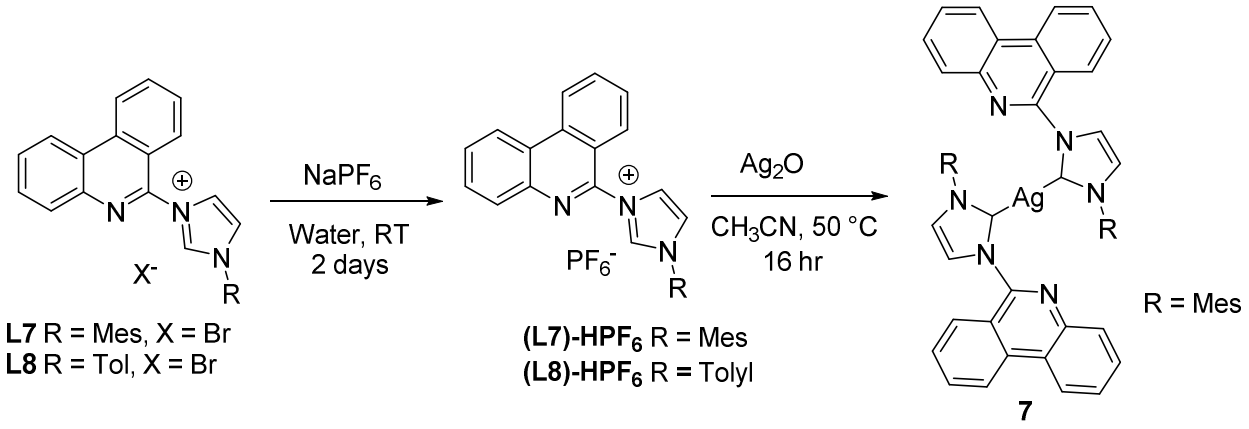

Scheme 2. 10: Synthesis of metal complex (**L7**)$_2$Ag(PF_6).

To validate the use of silver complexes to transmetallate our carbene/phenanthridine ligands, complex [(**L8**)$_2$Ir(CH_3CN)$_2$][PF_6]$_3$ was synthesized from 1.5 equivalent of bromide salt of (**L8)-HPF$_6$** with 0.5 equivalent of Ag_2O in acetonitrile at 50 °C for 24 h, followed by addition of 0.5 equivalent [Ir(COD)Cl]$_2$ in acetonitrile and continued stirring for 24 h at 50 °C with a slow increase to room temperature (**Scheme 2.11**). A faint orange solution was obtained after filtering. The isolated acetonitrile solution was used for crystallization with Et_2O. A yellow-orange crystals, suitable for X-ray crystallography were obtained after a week (**Figure 2.12**).

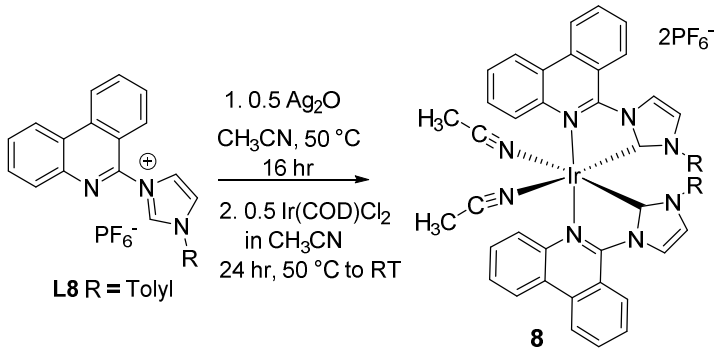

Scheme 2. 11: Synthesis of complex [(**L8**)$_2$Ir(CH_3CN)$_2$][PF_6]$_3$

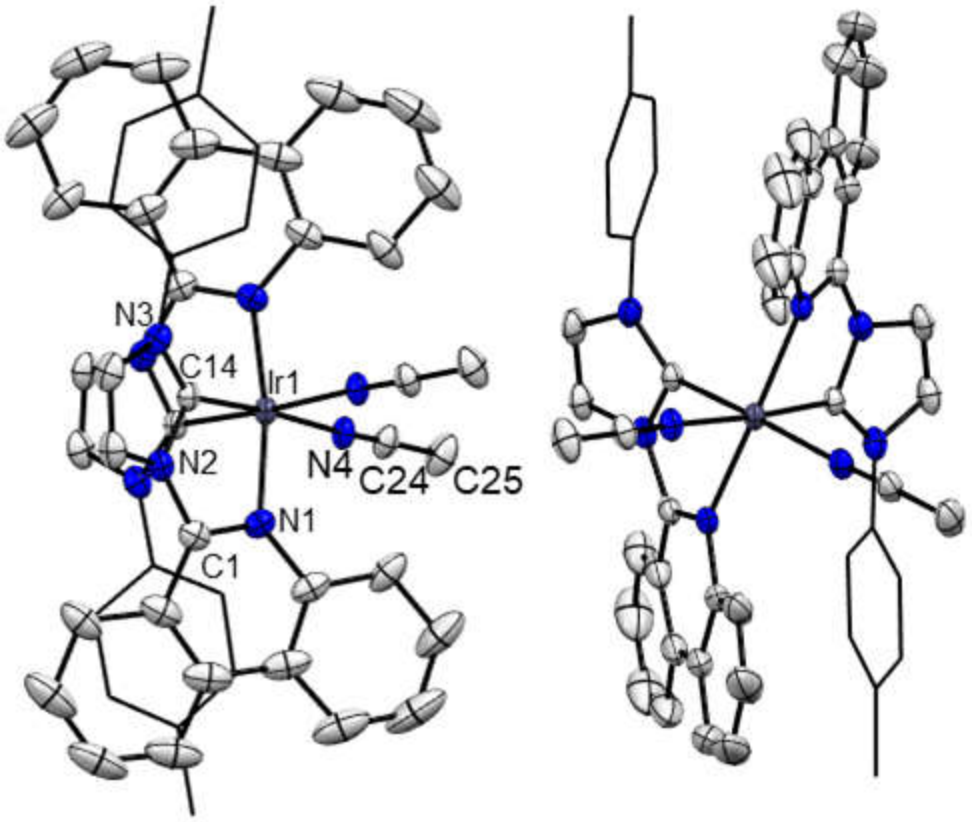

Figure 2. 12: ORTEP[24] of complex $[(\mathbf{L8})_2Ir(CH_3CN)_2][PF_6]_3$ all with thermal ellipsoids shown at 50% probability levels. Hydrogen atoms, labels on tolyl rings and counterions are omitted for clarity. Selected bond distances (Å) and angles (°).

Table 2. 6: Selected bond distances (Å) and angles (°) for $[(\mathbf{L8})_2Ir(CH_3CN)_2][PF_6]_3$:

Selected Bonds	**(Å)**	**Selected Angles**	**(°)**
Ir(1)-C(14)	1.984(3)	C(14)-Ir(1)-N(4)	176.36(13)
Ir(1)-N(4)	2.069(3)	C(14)-Ir(1)-N(1)	77.38(12)
Ir(1)-N(1)	2.088(3)	N(4)-Ir(1)-N(1)	99.48(11)

Complex $[(\mathbf{L8})_2Ru_2Cl_2](PF_6)_2$ was similarly synthesized by reaction between L8•HBr and half an equivalent of $RuCl_3.xH_2O$ in ethylene glycol at 200 °C for 12 hr (**Scheme 2.12**). The color of the solution changed to yellow. The solution was brought to room temperature and NH_4PF_6 solution in water was added to the reaction mixture. A yellow precipitate was isolated after filtration and washed with diethylether (3 x 5 mL). The precipitate was dried and dissolved in DCM and crystallized with Et_2O. A yellow blocked shaped crystal suitable for X-ray crystallography was obtained (**Figure 2.13**).

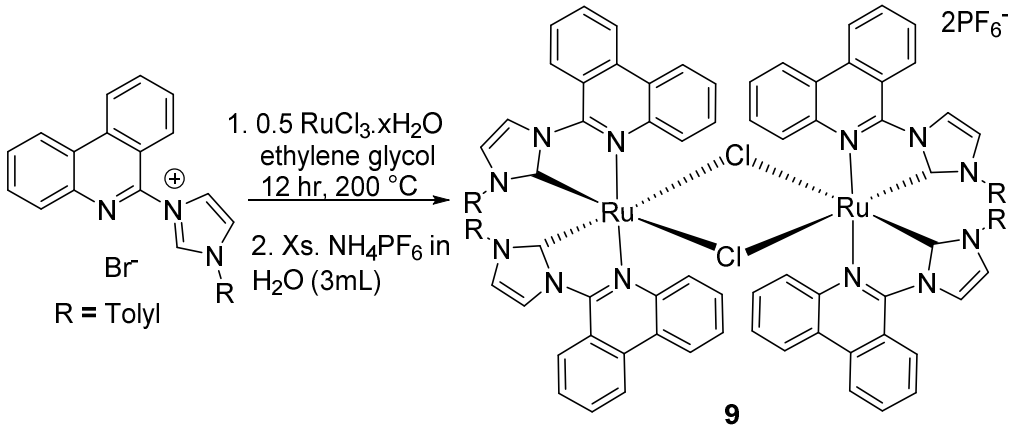

Scheme 2. 12: Synthesis of complex $[(\mathbf{L8})_2Ru_2Cl_2](PF_6)_2$

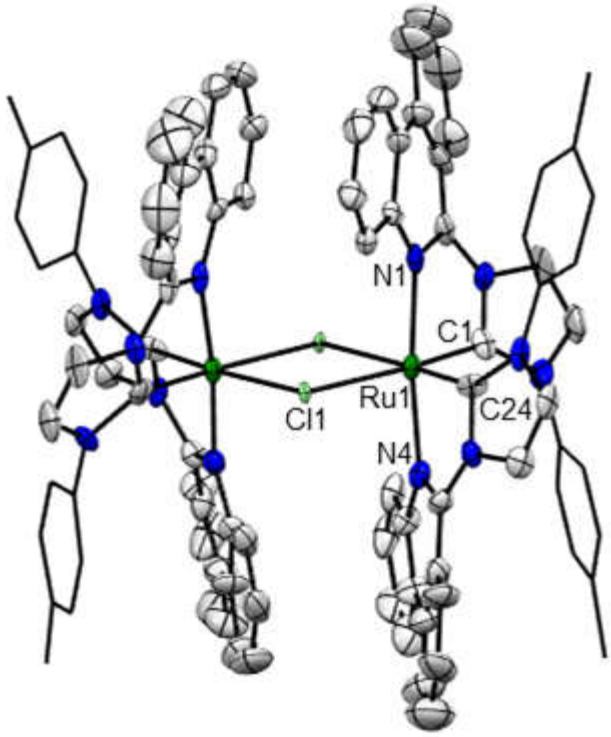

Figure 2. 13: Crystal structure of $[(\mathbf{L8})_2Ru_2Cl_2](PF_6)_2$. Hydrogen atoms and labels on tolyl rings, counter ions are omitted for clarity. A satisfactory crystal structure could not be obtained; nevertheless, preliminary data confirmed the proposed dimer structure and connectivity.

2.3.5. Electrochemistry of complexes (L1)Ni(Cl)(1-napthyl) and (L1)$ZnCl_2$:

The known redox activity of organic phenanthridine derivatives[30] suggested metal complexes containing phenanthridine-based ligands might exhibit both metal and ligand-based redox events. Cyclic voltammetry of (**L1**)Ni(Cl)(1-napthyl) and (**L1**)$ZnCl_2$ was performed in CH_2Cl_2 at ambient temperature (Figure 2.15). Both the complexes showed multiple irreversible events. An irreversible oxidation event at ~ 1.5 V vs Fc/Fc^+ (Fc = (η^5-$C_5H_5)_2Fe$) was common to the voltammograms of (**L1**)Ni(Cl)(1-napthyl) and (**L1**)$ZnCl_2$ [(Ni): 1.48; (Zn): 1.65 V]. An irreversible reduction wave at an onset potential negative of -1.5 V was also present in both the

voltammograms. Complex (**L1**)Ni(Cl)(1-napthyl) and (**L1**)$ZnCl_2$ exhibit oxidation and reduction events at comparable potentials is consistent with these particular redox events being ligand based.[31,32] This assignment is also supported by the presence of these waves in cyclic voltammograms of the zinc complex (**L1**)$ZnCl_2$, as metal-based redox events for zinc are inaccessible in the potential window investigated.[33] Besides, (4-diphenylphosphino)phenanthridine (**L1**) itself shows irreversible oxidation and reduction events at similar potentials along with an irreversible anodic peak attributed to oxidation of the free phosphine (E_p = 0.76 V vs Fc/Fc^+).

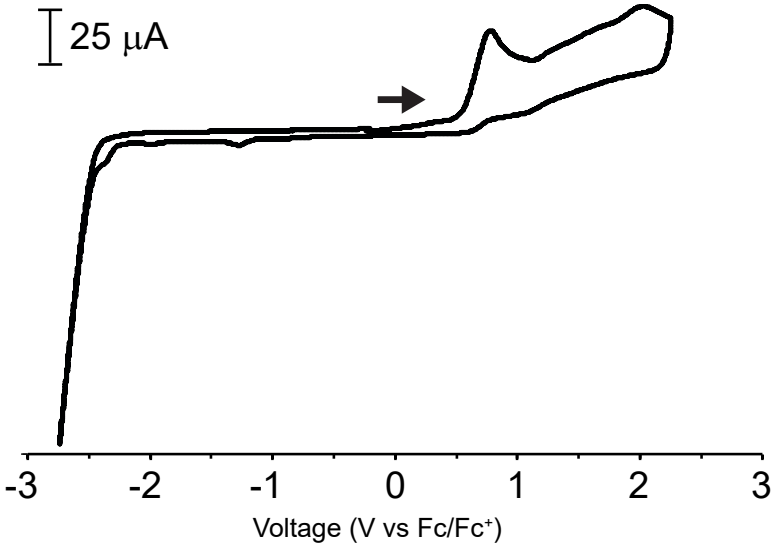

Figure 2. 14: Cyclic voltammogram of (4-diphenylphosphino)phenanthridine (**L1**) in CH_2Cl_2 at 22 °C at a scan rate of 100 mV/s. Arrow shows direction of initial scan. The concentration of analyte was $1.83x10^{-3}$ M, with 0.1 M nBu4NPF6 as supporting electrolyte.

Although the anodic electrochemistry of *mono*(8-diphenylphosphino)quinoline (Ph_2PNqn) complexes of Ni was not reported, the metal-based electrochemical reduction of [*bis*($Ph_2PNqn)_2Ni$][BF_4]$_2$ was observed at -0.66 V vs. Fc/Fc^+ in acetonitrile[34]. No reduction event for (**L1**)Ni(Cl)(1-napthyl) is observed at these potentials. For the metal complex (**L1**)Ni(Cl)(1-

napthyl) M^n/M^{n-1} reductions, additional cathodic events were observed [(**L1**)Ni(Cl)(1-napthyl) (Ni): -2.22]. The cyclic voltammograms of the nickel complex (**Figure 2.15**) contain further irreversible oxidation events (**L1**: 0.36, 0.88 V) that are assigned as metal-based, in accordance with their absence in the CV of (**L1**)$ZnCl_2$.

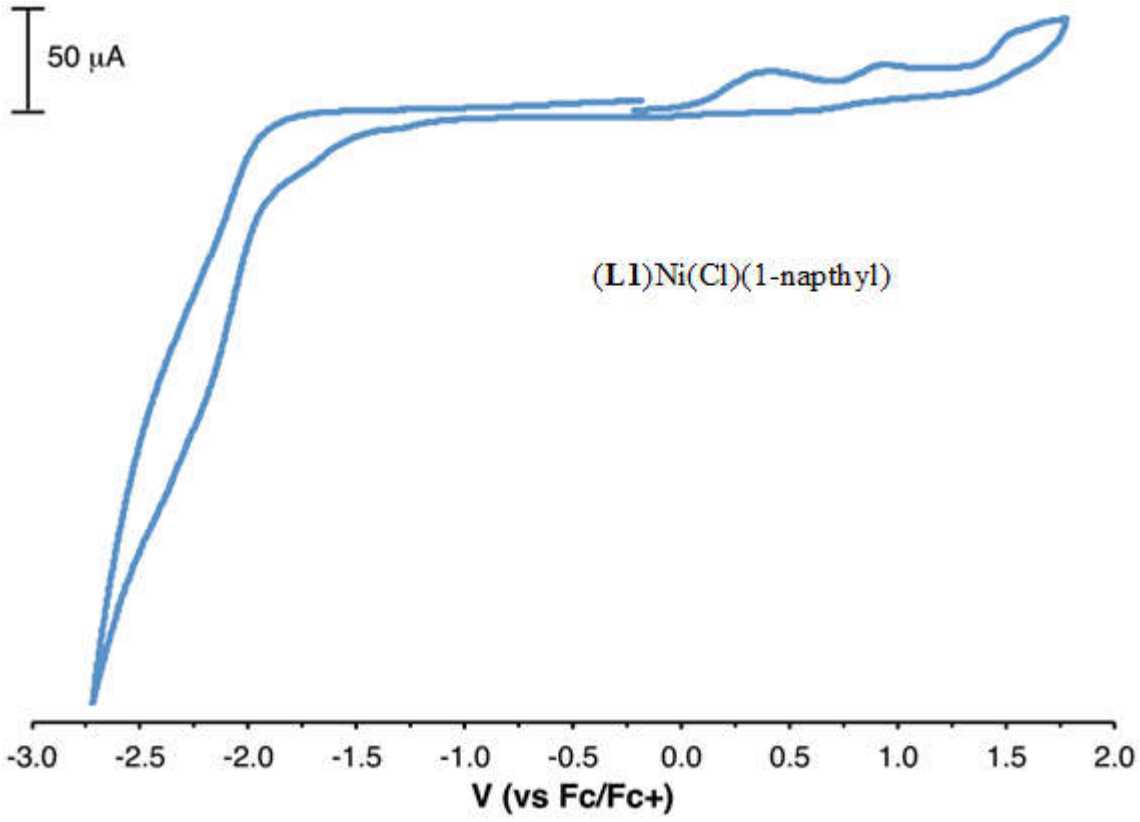

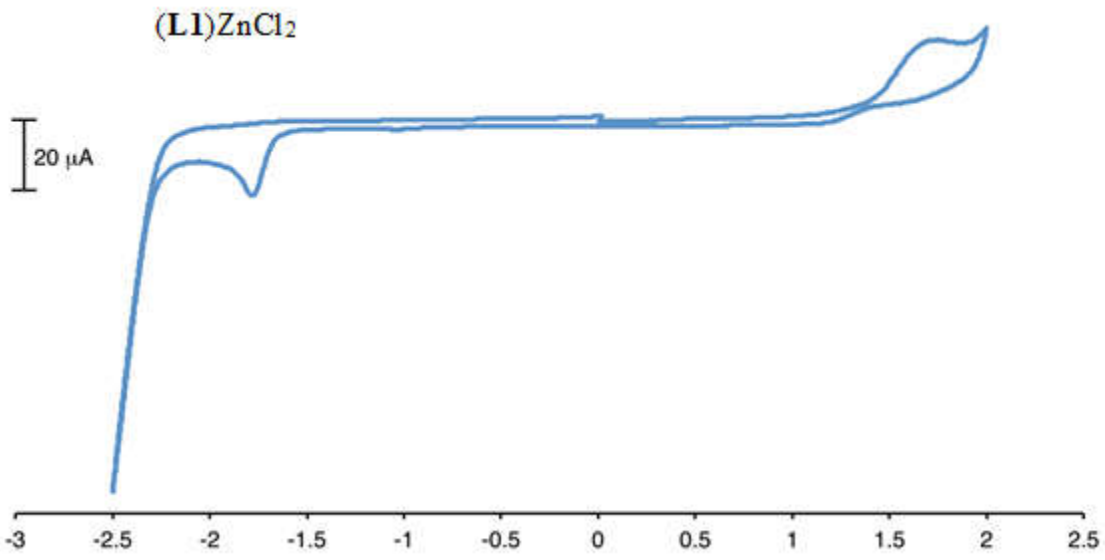

Figure 2. 15: Cyclic voltammograms of and in CH_2Cl_2 at 22 °C at a scan rate of 100 mV/s. Arrows show direction of initial scan. The concentration of analyte was (**L1**)Ni(Cl)(1-napthyl) = $1.14x10^{-3}$ M, (**L1**)$ZnCl_2$ = $1.33x10^{-3}$ M respectively, with 0.1 M *n*Bu_4NPF_6 as supporting electrolyte.

2.3.6. Absorption and Emisison Spectroscopy of complex (L1)Ni(Cl)(1-napthyl) and (L1)$ZnCl_2$:

Metal complexes (**L1**)Ni(Cl)(1-napthyl and (**L1**)$ZnCl_2$ display rich absorption spectra, with strong features in the UV (230-290 nm, ε = 20 000-90 000 M^{-1} cm^{-1}). Consistent with its orange-red colour, the nickel complex (**L1**)Ni(Cl)(1-napthyl) also absorbs in the visible end of the spectrum (λ_{max} = 397 nm). Due to solubility, luminescence spectra were collected in a relatively polar solvent (CH_2Cl_2), which typically attenuates luminescence efficiency.[35] Nevertheless, excitation of Zn complex into the lowest energy absorption bands (4: λexcitation = 360 nm) gives sharp emission peaks at 298 K (4: 382 nm) overlayed with broader features at both higher and lower wavelength (4: 371, 407, 421 nm; **Figure 2.16**). As has been observed with N-heterocycle-fused phenanthridines,[30] there is little overlap of the absorption and fluorescence spectra for phenathridine supported metal complex (**L1**)$ZnCl_2$, which could allow for suppression of Förster resonance energy transfer.

A.

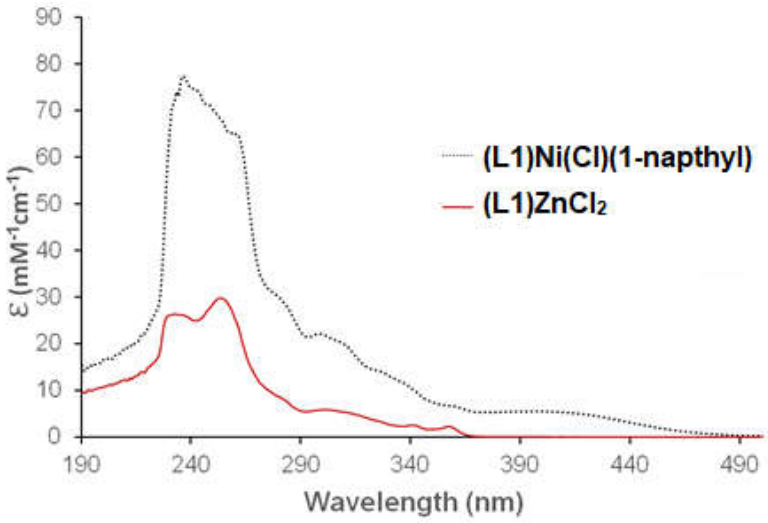

B.

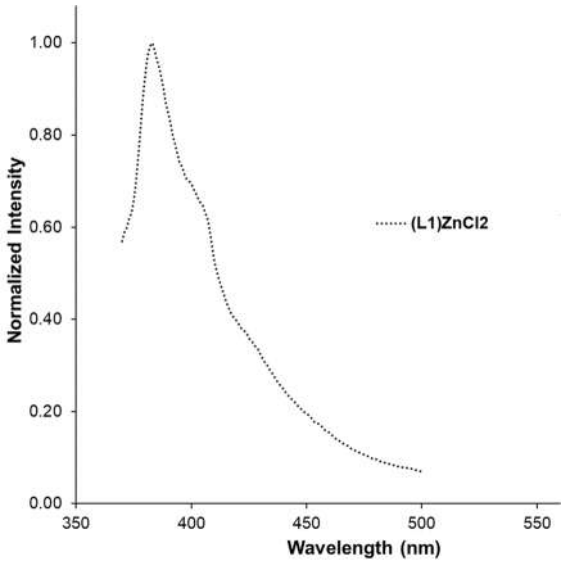

Figure 2. 16: A**.** UV-Vis absorption spectroscopy for complex (**L1**)Ni(Cl)(1-napthyl) and (**L1**)$ZnCl_2$ in DCM. B. Emission spectra of (**L1**)$ZnCl_2$ in DCM solution.

2.4. Conclusion:

Novel heteroleptic chelating ligands, phosphino-phenanthridine and N-heterocyclic carbene ligands, bearing a luminescent and electrochemically active phenanthridinyl unit, have been prepared and used to support complexes of first row transition metals. Cyclic voltammograms of complexes of redox-active (Ni) and redox-inactive metals (Zn) contain similar irreversible features, supporting the redox-active nature of the phenanthridinyl ligand. Zinc complex is emissive in CH_2Cl_2 solution, with emission maxima that range from the visible into the UV. X-ray solid-state structures confirmed the square planar geometry for Ni, tetrahedral for Zn and octahedral geometry for Ir, Ru complexes.

2.5. Experimental Section:

All air-sensitive manipulations were carried out either in a N_2-filled glove box or by using standard Schlenk techniques under Ar atmosphere. 2,6-dibromoaniline (AK Scientific), 2-formylphenyl boronic acid (Combi Blocks), $Pd(PPh_3)_4$ (Alfa Aesar), Na_2CO_3 (Alfa Aesar), chlorodiphenylphosphine (VWR), chloro(1-naphthyl)bis (triphenylphosphine)nickel(II) (Sigma Aldrich), $ZnCl_2$ (Alfa Aesar) and CuBr (Aldrich) were purchased and used without special purification. Solvents were dried and distilled by using appropriate drying agents and were oxygen free prior to use. 1,2-Dimethoxyethane was deoxygenated by three freeze–pump–thaw cycles prior to use in cross-coupling reactions but otherwise used as received. NMR spectra were recorded on a Bruker Avance 300 MHz or Bruker Avance-III 500 MHz spectrometer. ^{1}H and $^{13}C\{^{1}H\}$ NMR spectra were referenced to residual solvent peaks[36]. Electronic absorption spectra (750–190 nm) were recorded on a Thermo Scientific Genesys 10S UV–Vis spectrophotometer at room temperature. Steady-state fluorescence spectra were collected using a Fluorolog-3 Horiba

Jobin Yvon spectrofluorometer (Edison, NJ). Fluorescence spectra were collected using wavelengths set to 360 nm ($\lambda_{excitation}$ for emission spectrum) and 400 nm (observed for excitation spectrum) for (**L1**)$ZnCl_2$; excitation and emission slit was 2 nm ((**L1**)$ZnCl_2$) band pass resolution. All samples were measured at room temperature (22° C) and held in 10×10 mm2 quartz cuvettes. Elemental analyses were performed by Canadian Microanalytical Service Ltd., Delta, BC (Canada). Cyclic voltammetry was carried out using a CH Instruments 400C Series electrochemical analyzer/workstation in conjunction with a three-electrode cell. A BASi glassy carbon disk electrode (3.0 mm diameter) was used as the working electrode, a platinum wire the counter electrode, with a non-aqueous Ag/Ag+ quasi-reference electrode separated from the solution by a porous Teflon tip. All cyclic voltammetry (CV) measurements were conducted in CH_2Cl_2 with 0.1 M nBu_4NPF_6 as the supporting electrolyte, at scan rates ranging from 50 mV/s to 800 mV/s. Ferrocene was added to each solution as an internal reference, and potentials were referenced to the $Fe(\eta^5 –C_5H_5)_2/Fe(\eta^5 –C_5H_5)_2^+$ redox couple.

Preparation of 4-bromophenanthridine (1-Br):

Representative run: 2,6-dibromoaniline (1.01 g, 4.02 mmol) and $Pd(PPh_3)_4$ (0.09 g, 0.08 mmol) were added to a flask fitted with a condenser and charged with 1,2-dimethoxyethane (15 mL) under an Ar atmosphere. After ~15 min of stirring, 2-formylphenylboronic acid (0.66 g, 4.4 mmol) was added and stirring was continued for another 15 min. A deoxygenated solution of sodium carbonate (1.06 g, 0.01 mol) in 8 mL of distilled water was added. The reaction mixture was refluxed at 100 °C for 5 h with stirring. Then reaction mixture was cooled to room temperature and the volatiles were removed under reduced pressure. The remaining residue was extracted using dichloromethane (80 mL) and the extract was filtered and dried. 4-Bromophenanthridine was isolated as a light yellow solid following column chromatography on

activated neutral alumina using toluene as eluent (R_f = 0.21). Yield = 0.35 g (35 %). ^{1}H NMR ($CDCl_3$, 300 MHz, 25 °C): δ 9.39 (s, 1H, C_6-*H*), 8.59 (d - overlapped, J_{HH} = 8.4 Hz, 1H, C_{10}/C_1-*H*), 8.55 (d – overlapped, J_{HH} = 8.4 Hz, 1H, C_{10}/C_1-*H*), 8.08 (overlapped d, J_{HH} = 7.8 Hz, 2H, C_3/C_7-*H*), 7.89 (app t, J= 7.5 Hz, 1H, C_9-*H*), 7.75 (app t, J= 7.5 Hz, 1H, C_8-*H*), 7.52 ppm (dt, J_{HH} = 7.8, 1.2 Hz, 1H, C_2-*H*). ^{13}C{^{1}H} NMR ($CDCl_3$, 75 MHz, 25 °C): δ 154.5 (C_6=N), 141.8 (C_{4a}), 132.7 (C_3), 132.5 (C_{10a}), 131.7 (C_9), 129.2 (C_7), 128.3 (C_8), 127.6 (C_2), 126.6 (C_{6a}), 126.1 (C_4-Br), 125.9 (C_{10b}), 122.2 (C_1), 122.1 ppm (C_{10}).

Synthesis of 2,6-dimethyl-4-bromophenanthridine(3-Br):

2-bromo-6-iodo-*p*-toluidine (1.78 g, 5.70 mmol), 2-acetylphenylboronic acid (0.98 g, 6.00 mmol) and $Pd(PPh_3)_4$ (0.20 g, 0.17 mmol) were combined in a thick-walled, 500 mL Teflon-stoppered flask under N_2 atmosphere, followed addition of degassed 1,2-DME (100 mL) and a solution of Na_2CO_3 (1.8 g, 17.10 mmol) in 40 mL of degassed water. The flask was then sealed and vigorously stirred for overnight in an oil bath (130 °C). The flask was allowed to cool to room temperature and the mixture pumped dry. The crude was extracted with CH_2Cl_2 and excess $MgCl_2$ (0.5 g) was added and stirred overnight. The mixture was filtered through Celite, concentrated nearly to dryness and passed through a plug of neutral Al_2O_3. Drying *in vacuo* gave a pale yellow solid. Isolated yield = 1.42 g (87%). ^{1}H NMR (CD_2Cl_2, 500 MHz, 22 °C): δ 8.52 (d, J_{HH} = 5 Hz, 1H, C_7-*H*), 8.23 (s, 1H, C_3-*H*), 8.17 (d, J_{HH} = 5 Hz, 1H, C_{10}-*H*), 7.83 (br, 1H, C_1-*H*), 7.82-7.79 (overlapped m, 1H, C_9-*H*), 7.70-7.67 (overlapped m, 1H, C_8-*H*), 3.01 (s, 3H, $^{phen}C_6$Me-*H*), 2.55 ppm (s, 3H, $^{phen}C_2$Me-*H*). ^{13}C{^{1}H} NMR (CD_2Cl_2, 126 MHz, 22 °C): δ 159.4 (C_6=N), 139.4 (C_{4a}), 137.3 (C_3), 134.2 (C_1-*H*), 132.4 (C_{10a}), 131.0 (C_9-*H*), 128.2 (C_8-*H*), 127.0 (C_{10}-*H*), 126.4 (C_{6a}), 125.5 (C_4-Br), 125.2 (C_{10b}), 122.9 (C_7-*H*), 122.0 (C_3-*H*), 23.78 (s, $^{phen}C_{6,Me}$-*H*), 21.77 ppm (s, $^{phen}C_{2,Me}$-*H*).

Preparation of (4-diphenylphosphino)phenanthridine(L1)

A solution of *sec*-butyllithium (1.6 M, 3.2 mL, 4.0 mmol) in cyclohexane was added dropwise to a stirring solution of 4-bromophenanthridine (1.03 g, 4.00 mmol) in Et_2O (5 mL) at -78 °C over a period of 15 min. Stirring was then continued for additional 4 h while maintaining the same temperature. A solution of chlorodiphenylphosphine (0.88 g, 4 mmol) in Et_2O (2 mL) was added drop-wise and the reaction mixture was allowed to warm to room temperature. A white precipitate formed. The volatiles were removed under reduced pressure and the remnant dissolved in dichloromethane (40 mL) and filtered through a small plug of Celite. The filtrate was dried under vacuum to give a light yellow solid, which was then washed with degassed ethanol (50 mL). Yield = 1.05 g (72%). ^{1}H NMR ($CDCl_3$, 300 MHz, 25 °C): δ 9.23 (s, 1H, C_6-*H*), 8.64 (d - overlapped, J_{HH} = 8.4 Hz, 1H, C_{10}-*H*), 8.59 (d - overlapped, J_{HH} = 8.4 Hz, 1H, C_1-*H*), 8.02 (d, J_{HH} = 7.8 Hz, 1H, C_7-*H*), 7.87 (app t, *J* = 8 Hz, 1H), 7.71 (app t, *J* = 8 Hz, 1H), 7.57 (app t, *J* = 8 Hz, 1H), 7.33-7.30 (m, 10H), 7.37-7.28 (br, 10H), 7.13 ppm (dd, *J* = 7.2, 3.6 Hz, 1H). ^{13}C{^{1}H} NMR ($CDCl_3$, 75 MHz, 25 °C): δ 152.8 (C_6=N), 146.1 (d, J_{CP} = 17 Hz, C_{4a}), 139.1 (d, J_{CP} = 11 Hz, P-C_4), 138.0 (d, J_{CP} = 44 Hz, P-C_{11}), 134.3 (d, J_{CP} = 20 Hz, PC_{12}), 133.4 (C_3-H), 132.7 (C_{10a}), 131.1 (C_9-H), 129.0 (C_7-H), 128.5 (d, J_{CP} = 5 Hz, P-C_{13}), 128.4 (P-C_{14}), 127.7(C_8-H), 127.1 (C_2-H), 126.5 (C_{6a}), 123.8 (d, J_{CP} = 2 Hz, C_{10b}) 123.2 (C_1-H), 122.2 ppm (C_{10}-H). ^{31}P{^{1}H} NMR ($CDCl_3$, 121 MHz, 25 °C): δ -13.7 (s) ppm. Anal. Calc'd for $C_{25}H_{18}N_1P_1$: C, 82.63; H, 4.99. Found: C, 82.87; H, 5.39.

Single crystals of **1** suitable for X-ray diffraction were grown via diffusion of hexanes vapors into a CH_2Cl_2 solution. Crystal structure data for **1**: $C_{25}H_{18}NP$, 363.37 g/mol, monoclinic, space group $P2_1/c$; a = 12.800(3) Å, b = 9.4949(19) Å, c = 15.887(3) Å, β = 100.74(3)°, V = 1897.0(7) Å^3; Z = 4, ρ_{calcd} = 1.272 g cm^{-3}; crystal dimensions: 0.20 × 0.20 × 0.15 mm; diffractometer:

Bruker APEXII CCD; Mo Kα radiation, ω scans, 293(2) K, 2.511 ≤ θ ≤ 30.059°; 21514 reflections, 5550 independent (R_{int} = 0.0150), direct methods; absorption coeff (μ = 0.154 mm^{-1}), absorption correction: semi-empirical from equivalents; completeness to θ = 25.242°: 99.9%; refinement (against F^2) with SHELXL-2014/7, 244 parameters, 0 restraints, R_1 = 0.0439 ($I > 2\sigma$) and wR_2 = 0.1641 (all data), Goof = 1.357, residual electron density 0.267/−0.330 e $Å^{-3}$.

Synthesis of 4-diphenylphosphino-2-methylphenanthridine (L2)

4-Bromo-2-methylphenanthridine (2.18 g, 8.00 mmol) was dissolved in diethylether (6 mL) and cooled to -78 °C. A solution of *sec*-butyllithium in cyclohexane (1.6 M, 6.4 mL, 8.00 mmol) was added drop-wise over a period of 15 min. The mixture was stirred for additional 6 h at this temperature, following which a solution of chlorodiphenylphosphine (1.78 g, 8.00 mmol) in diethylether (6 mL) was added drop-wise. The reaction mixture was allowed to warm to room temperature overnight at which point a white precipitate was observed. The volatiles were removed under reduced pressure and the solid residue was dissolved in dichloromethane (40 mL) and filtered through a small plug of Celite. The filtrate was dried under vacuum to give a light brown solid, which was washed with degassed ethanol (50 mL). Yield = 1.91 g (63%). ^{1}H NMR ($CDCl_3$, 300 MHz, 22 °C): δ 9.19 (s, 1H, $^{phen}C_{Ar}$-*H*), 8.59 (d, J_{HH} = 9 Hz, 1H, $^{phen}C_{Ar}$-*H*), 8.37 (s, 1H, $^{phen}C_{Ar}$-*H*), 7.97 (d, 1H, J_{HH} = 6 Hz, $^{phen}C_{Ar}$-*H*), 7.81 (m, 1H, $^{phen}C_{Ar}$-*H*), 7.65 (m, 1H, $^{phen}C_{Ar}$-*H*), 7.41-7.32 (overlapped m, 10H, PC_{Ar}-*H*), 7.00 (br, 1H, $^{phen}C_{Ar}$-*H*), 2.48 ppm (s, 3H, C_{Me}-*H*). $^{13}C\{^1H\}$ NMR ($CDCl_3$, 75 MHz, 22 °C): δ 151.8 (br, J_{CP} = 2 Hz, ^{phen}C=N), 144.4 (d, J_{CP} = 17 Hz, $^{phen}C_{Ar}$), 138.6 (d, J_{CP} = 12 Hz, $^{phen}C_{Ar}$), 137.9 (d, J_{CP} = 11 Hz, PC_{Ar}), 136.8 ($^{phen}C_{Ar}$Me), 134.8 ($^{phen}C_{Ar}$H), 134.2 (d, J_{CP} = 20 Hz, PC_{Ar}H), 132.3 (d, J_{CP} = 2 Hz, $^{phen}C_{Ar}$), 130.7 ($^{phen}C_{Ar}$H), 128.8 ($^{phen}C_{Ar}$H), 128.4 (d, J_{CP} = 5 Hz, PC_{Ar}H), 128.3 (PC_{Ar}H), 127.5 ($^{phen}C_{Ar}$H), 126.5 (br,

$^{phen}C_{Ar}$), 123.6 (d, J_{CP} = 2 Hz, $^{phen}C_{Ar}$) 122.8 ($^{phen}C_{Ar}H$), 122.1 ($^{phen}C_{Ar}H$), 22.2 ppm (C_{Me}). $^{31}P\{^{1}H\}$ NMR ($CDCl_3$, 121 MHz, 22 °C): δ -13.6 ppm (s).

Synthesis of 4-diisoproplyphosphino-2-methylphenanthridine (L4)

Ligand (L3) has been synthesized following the same procedure used for L1 and L2. A 50 mL Schlenk flask was charged with 4-bromo-2-methylphenanthridine (0.54 g, 2.00 mmol) and Et2O (3 mL) and stirred for 15 min at -78 °C. sec-Butyllithium (1.6 M, 1.60 mL, 2.00 mmol) in cyclohexane was then added drop-wise and the reaction mixture stirred for 5 h at the same temperature. A solution of chlorodiisopropylphosphine (0.40 g, 2.00 mmol) in Et2O (4 mL) was then added drop-wise, followed by warming the reaction mixture to room temp by stirring overnight, at which point the solution color had changed to yellow. The reaction mixture was dried in vacuo to leave a gummy residue which was then dissolved in hexane (15 mL) and filtered through a small plug of silica. Then the filtrate was again filter through a small plug of silica and washed with more hexane (10 mL). The toluene (10 mL) was passed through the silica plug and collected and concentrated in vacuum to get a yellowish semi-solid as product. Yield = 0.38 g (63%). ^{1}H NMR ($CDCl_3$, 500 MHz, 25 °C): δ 9.29 (s, 1H, $^{Phen}C_{Ar}$-*H*), 8.59 (d, J_{HH} = 9 Hz, 1H, $^{Phen}C_{Ar}$-*H*), 8.37 (s, 1H, $^{Phen}C_{Ar}$-*H*), 8.02 (d, 1H, J_{HH} = 6 Hz, $^{Phen}C_{Ar}$-*H*), 7.81 (m, 1H, $^{Phen}C_{Ar}$-*H*), 7.69-7.66 (overlapped m, 2H, $^{Phen}C_1$), 2.65 (s, 3H, $^{phen}C_{Me}$-*H*), 2.41-2.35 (m, 2H, $^{Isopropyl}C_{methine}$-*H*), 1.16 (dd, 6H, $^{Isopropyl}C_{Me}$-*H),* 0.98 ppm (dd, 6H, $^{Isopropyl}C_{Me}$-*H*). $^{13}C\{^{1}H\}$ NMR ($CDCl_3$, 126 MHz, 25 °C): δ151.5 (s, C_6=N), 146.2 (d, J_{CP} = 17 Hz, C4a), 137.2 (d, J_{CP} = 12 Hz, P–C_4), 135.8 (d, J_{CP} = 11 Hz, C_1), 135.1 (C_2-C_{Me}), 132.7 (C_3-H), 130.6 (C_9–H), 128.7 (C_7–H), 127.4 (C_8–H), 126.4 (C_{6a}), 123.9 (br, J_{CP} = 2 Hz, C_{10b}), 122.6 (C_1–H), 122.1 (C_{10}–H), 23.5 (d, $^{phen}C_{Methine}$), 22.2 (s, $^{phen}C_{Me}$), 20.4 ($^{Isopropyl}C_{Me}$), 19.9 ppm ($^{Isopropyl}C_{Me}$). $^{31}P\{^{1}H\}$ NMR ($CDCl_3$, 121 MHz, 25 °C): δ -0.18 ppm (s).

Synthesis of 4-diphenylphosphino-2,6-dimethyl-phenanthridine (L5):

2,6-dimethyl-4-bromophenanthridine (0.268 g, 1.00 mmol) was dissolved in 5 mL of dry diethylether and cooled to -78 °C. A solution of *sec*-butyllithium in cyclohexane (1.6 M; 0.80 mL, 1.00 mmol) was added drop-wise over a period of 10 min. The reaction mixture was stirred for 6 h at -78 °C. A solution of chlorodiphenylphosphine (0.220 g, 1.00 mmol) in dry diethylether (6 mL) was added drop-wise to the reaction mixture and the mixture allowed to warm to room temperature overnight, at which point an off-white suspension was observed. The volatiles were removed under reduced pressure and the solid residue was dissolved in dichloromethane (10 mL) and filtered through a small plug of Celite. The filtrate was concentrated to ~2 mL under vacuum and 3 mL of pentane added. A precipitate formed overnight upon standing at -35° C. Isolated yield = 0.241 g (61%). ^{1}H NMR (CD_2Cl_2, 500 MHz, 22 °C): δ 8.63 (d, J_{HH} = 10 Hz, 1H, $^{Phen}C_{Ar}$-*H*), 8.35 (s, 1H, $^{Phen}C_{Ar}$-*H*), 8.16 (d, 1H, J_{HH} = 5, 10 Hz, $^{Phen}C_{Ar}$-*H*), 7.83 (t, 1H, J_{HH} =5, 10 Hz, $^{Phen}C_{Ar}$-*H*), 7.68 (t, 1H, J_{HH} =5, 10 Hz, $^{Phen}C_{Ar}$-*H*), 7.37-7.32 (overlapped m, 10H, PC_{Ar}-*H*), 6.98 (br, 1H, $^{phen}C_{Ar}$-*H*), 2.83 (s, 3H, $^{phen}C_{6}$Me-*H),* 2.46 ppm (s, 3H, $^{phen}C_{2}$Me-*H*). ^{13}C{^{1}H} NMR (CD_2Cl_2, 126 MHz, 22 °C): δ 157.3 ($^{Phen}C_{Ar}$-*H*), 143.8 (d, J_{CP} = 12 Hz, $^{Phen}C_{Ar}$), 139.1 (d, J_{CP} = 12 Hz, PC_{Ar}), 138.6 (d, J_{CP} = 11 Hz, PC_{Ar}), 136.5 ($^{Phen}C_{Ar}$-^{2}Me), 134.9 ($^{Phen}C_{Ar}$), 134.7 (d, J_{CP} = 20 Hz, PC_{12}–*H*), 132.8 (br, J_{CP} = 2 Hz, $^{Phen}C_{Ar}$), 130.7 ($^{Phen}C_{Ar}$-*H*), 128.8 ($^{Phen}C_{Ar}$-*H*), 128.7 (d, J_{CP} = 12 Hz, PC_{Ar}), 127.8 (PC_{Ar}), 127.0 ($^{Phen}C_{Ar}$-*H*), 126.4 (br, PC_{Ar}), 123.6 (br, J_{CP} = 2 Hz, $^{Phen}C_{Ar}$) 123.0 ($^{Phen}C_{Ar}$-*H*), 23.36 (C^{6}_{Me}), 22.32 ppm (C^{2}_{Me}). ^{31}P{^{1}H} NMR (CD_2Cl_2, 202 MHz, 22 °C): δ -12.97 ppm (s).

Synthesis of 8-diphenylphosphino-6-methylquinoline (L3)

This compound was synthesized following the procedure detailed for **L2**, using 8-bromo-6-methylquinoline (1.75 g, 8.00 mmol) and *sec*-butyllithium (1.6 M, 6.4 mL, 8.00 mmol) in Et_2O, followed by addition of chlorodiphenylphosphine (1.78 g, 8.00 mmol). The product was isolated as an off-white solid. Yield = 1.76 g (67%). ^{1}H NMR ($CDCl_3$, 300 MHz, 22 °C): δ 8.79 (m, 1H, $^{quin}C_{Ar}$-*H*), 8.06 (d, 1H, $^{quin}C_{Ar}$-H, J_{HH} = 9 Hz), 7.57 (s, 1H, $^{quin}C_{Ar}$-*H*), 7.36-7.27 (overlapped m, 11H, PC_{Ar}-*H* + $^{quin}C_{Ar}$-*H*), 6.93 (br, 1H, $^{quin}C_{Ar}$-*H*), 2.38 ppm (s, 3H, C_{Me}-*H*). $^{13}C\{^1H\}$ NMR ($CDCl_3$, 75 MHz, 22 °C): δ 149.0 (d, J_{CP} = 1.5 Hz, ^{quin}C=N), 148.4 (d, J_{CP} = 17 Hz, $^{quin}C_{Ar}$), 138.2 (d, J_{CP} = 13 Hz, $^{quin}C_{Ar}$), 137.7 (d, J_{CP} = 11 Hz, PC_{Ar}), 136.5 ($^{quin}C_{Ar}$H), 136.4 ($^{quin}C_{Ar}$Me), 135.5 (m, J_{CP} = 2 Hz, $^{quin}C_{Ar}$H), 134.3 (d, J_{CP} = 20 Hz, PC_{Ar}H), 128.5 (d, J_{CP} = 7 Hz, PC_{Ar}H), 128.4 (PC_{Ar}H), 128.1 (br, J_{CP} = 2 Hz, PC_{Ar}), 127.8 ($^{quin}C_{Ar}$H), 121.5 ($^{quin}C_{Ar}$H), 21.84 ppm (C_{Me}). $^{31}P\{^1H\}$ NMR ($CDCl_3$, 121 MHz, 22 °C): δ -14.9 ppm (s).

Synthesis of 8-diphenylphosphino-6-methyl-2-^{t}butylphenanthridine (L6)

This compound was synthesized following the procedure detailed for **L2**, using 4-bromo-6-methyl-2-terbutylpheanthridine (1.75 g, 8.00 mmol) and *sec*-butyllithium (1.6 M, 6.4 mL, 8.00 mmol) in Et_2O, followed by addition of chlorodiphenylphosphine (1.78 g, 8.00 mmol). The product was isolated as an off-white solid. Yield = 1.76 g (71%). ^{1}H NMR ($CDCl_3$, 300 MHz, 22 °C): δ 8. 67(d, 1H, $^{Phen}C_{Ar}$-*H*), 8.48 (s, 1H, $^{Phen}C_{Ar}$-H), 8.15 (m, 1H, $^{Phen}C_{Ar}$-*H),* 7.82 (m, 1H, $^{Phen}C_{Ar}$-*H*) 7.66 (m, 1H, $^{phen}C_{Ar}$-*H*), 7.35-7.32 (overlapped m, 9H, PC_{Ar}-*H*), 7.15-7.13 (br, 1H) 2.84 (s, 1H, $^{quin}C_{Ar}$-*H*), 1.27 ppm (s, 3H, C_{Me}-*H*).

Synthesis of NN donor ligand (L11):

4-bromo-2-methylphenanthridine (1.089 g, 4 mmol), piperidine (0.480 g, 5.6 mmol), sodium tert-butoxid (0.538 g, 5.6 mmol), bis(dibenzylidenacetone)palladium (0.018 g, 0.5 mol%), rac-BINAP (0.0374 g, 1.5 mol%) were taken in a 50 mL Teflon stoppered flask with 10 ml toluene. The mixture was stirred for 2 d at 130 °C. After that the mixture was taken to room and dried under reduced pressure and the product was purified by column chromatography ethyl acetate: hexane (10:2) The yellow solid was obtained with a yield of 0.98 g (89 %). ^{1}H NMR ($CDCl_3$, 500 MHz, 22 °C): 9.23 (s, 1H), 8.57 (d, 1H), 8.00 (m, 2H), 7.79 (m, 1H), 7.66 (m, 1H), 7.09 (br, 1H), 3.32 (br, 4H), 2.59 (s, 3H), 1.93 (br m, 4H) and 1.67 ppm (m, 2H). $^{13}C\{^{1}H\}$ NMR ($CDCl_3$, 126 MHz, 25 °C): 151.5, 150.2, 137.0, 136.9, 132.9, 130.4, 128.5, 127.2, 126.4, 125.2, 122.4, 118.4, 115.4, 54.2, 26.4, 24.8, 22.6 ppm.

Preparation of (L1)Ni(1-naphthyl)Cl.

A solution of (4-diphenylphosphino)phenanthridine (0.045 g, 0.125 mmol) in CH_2Cl_2 (2.5 mL) was added slowly to a solution of chloro(1-naphthyl)*bis*(triphenylphosphine)nickel(II) (0.093 g, 0.125 mmol) in CH_2Cl_2 (2.5 mL) to give an orange solution. The reaction mixture was stirred for 4 h, after which the volatiles were removed under reduced pressure. The solid residue was washed with diethyl ether (3 x 10 mL) and dried under vacuum to give a red-orange solid. Yield = 0.067 g (92%). ^{1}H NMR ($CDCl_3$, 500 MHz, 25 °C): δ 10.61 (s, 1H, $^{phen}C_{Ar}$-*H*), 9.13 (d, *J* = 8.3 Hz, 1H, $^{phen}C_{Ar}$-*H*), 8.70 (d, *J* = 7.7 Hz, 1H, $^{phen}C_{Ar}$-*H*), 8.60 (d, *J* = 8.3 Hz, 1H, $^{phen}C_{Ar}$-*H*), 8.28 (d, *J* = 7.9 Hz, 1H), 8.20 (d, *J* = 7.5 Hz, 1H, $^{phen}C_{Ar}$-*H* or PC_{Ar}-*H*), 8.17 (d, *J* = 7.5 Hz, 1H, $^{phen}C_{Ar}$-*H* or PC_{Ar}-*H*), 8.01 (app t, *J* = 7.7 Hz, 1H), 7.82 (app t, *J* = 7.5 Hz, 1H), 7.72 (dt, *J* = 18.7, 7.3 Hz, 2H, PC_{Ar}-*H*), 7.48 (dt, *J* = 7.4, 4.2 Hz, 1H, PC_{Ar}-*H*), 7.44 (td, *J* = 7.4, 7.0, 2.1 Hz, 2H, PC_{Ar}-*H*), 7.36 (d, *J* = 8.1 Hz, 1H, PC_{Ar}-*H*), 7.30 (d, *J* = 7.0 Hz, 1H, PC_{Ar}-*H*), 7.15 (d, *J* = 8.0

Hz, 1H, PC_{Ar}-*H*), 7.04 (overlapping m, 2H, C_{napth}-*H* and PC_{Ar}-*H*), 6.87 (overlapping dd, *J* = 7.5, 2.5 Hz, 2H, C_{napth}-*H*), 6.78 (overlapping dd, *J* = 8.0, 2.5 Hz, 2H, C_{napth}-*H*), 6.52 (d, *J* = 7.5 Hz, 1H, C_{napth}-*H*), 6.49 ppm (d, *J* = 7.5 Hz, 1H, C_{napth}-*H*). $^{13}C\{^1H\}$ NMR ($CDCl_3$, 126 MHz, 25 °C): δ 159.2 ($^{phen}C_{Ar}$-H), 147.7 (d, J_{CP} = 21 Hz, $^{phen}C_{Ar}$), 143.2 (d, J_{CP} = 48 Hz, C_{napth}), 140.2 (C_{napth}), 135.5 (d, J_{CP} = 4 Hz, PC_{Ar}-H), 134.0 (d, J_{CP} = 2 Hz, $^{phen}C_{Ar}$), 133.8 (PC_{Ar}-H), 133.7 ($^{phen}C_{Ar}$-H), 133.6 ($^{phen}C_{Ar}$-H), 133.4 (d, J_{CP} = 2 Hz, PC_{Ar}-H), 133.5 (d, J_{CP} = 34 Hz, $^{phen}C_{Ar}$), 132.9 ($^{phen}C_{Ar}$ - H), 132.5 (C_{napth}-H), 132.4 (C_{napth}-H), 132.2 ($^{phen}C_{Ar}$), 131.3 (d, J_{CP} = 2 Hz, PC_{Ar}-H), 130.9 ($^{phen}C_{Ar}$-*H*), 130.6 (d, J_{CP} = 56 Hz, PC_{Ar}), 130.0 (d, J_{CP} = 2 Hz, PC_{Ar}-H), 129.2 ($^{phen}C_{Ar}$-H), 129.0 (d, J_{CP} = 11 Hz, PC_{Ar}-H), 128.3 (d, J_{CP} = 6 Hz, C-H, PC_{Ar}-H), 127.8 (C_{napth}-H), 127.7 (C_{napth}-H), 127.5 (PC_{Ar}-H), 126.8 ($^{phen}C_{Ar}$), 126.6 (d, J_{CP} = 60 Hz, PC_{Ar}-H), 126.0 ($^{phen}C_{Ar}$-H), 125.9 ($^{phen}C_{Ar}$), 123.9 (C_{napth}-H), 123.8 (C_{napth}-H), 123.2 (C_{napth}-H), 122.6 (C_{napth}), 122.1 ppm ($^{phen}C_{Ar}$-*H*). $^{31}P\{^1H\}$ NMR ($CDCl_3$, 121 MHz, 25 °C): δ 30.6 ppm (s). UV-Vis: λ (ε) 298 (2.17 x 10^4), 306 (2.03 x 10^4), 325 (1.39 x 10^4), 335 (1.18 x 10^4), 358 (6.60 x 10^3), 397 nm (5.44 x 10^3 $M^{-1}cm^{-1}$). Anal. Calc'd for $C_{35}H_{25}N_1P_1Ni_1$: C, 71.90; H, 4.31. Found: C, 71.16; H, 4.67.

Single crystals of sufficient quality for X-ray diffraction were grown from dichloromethane/hexane at -35 °C. Crystal structure data for **2**: $C_{37}H_{29}Cl_5NNiP$, 754.54 g/mol, monoclinic, space group $P2_1/c$; a = 10.135(2) Å, b = 13.559(3) Å, c = 25.353(5) Å, β = 91.65(3)°, V = 3482.7(12) $Å^3$; Z = 4, ρ_{calcd} = 1.439 g cm^{-3}; crystal dimensions: 0.14 × 0.10 × 0.06 mm; diffractometer: Bruker APEXII CCD; Mo Kα radiation, ω scans, 298(2) K, 2.200 ≤ θ ≤ 27.477°; 20539 reflections, 7980 independent (R_{int} = 0.0296), direct methods; absorption coeff (μ = 1.015 mm^{-1}), absorption correction: semi-empirical from equivalents; completeness to θ = 26°: 99.9%; refinement (against F^2) with SHELXL-2014/7, 406 parameters, 0 restraints, R_1 =

0.0480 ($I > 2\sigma$) and wR_2 = 0.1458 (all data), Goof = 1.010, residual electron density 0.633/−0.834 e $Å^{-3}$.

Synthesis of complex (L1)Ni(COD):

Inside a glove box, a solution of L1 ligand (0.023 g, 0.063 mmol) was added dropowise over the period of 5 min to a stirring solution of $Ni(COD)_2$ (0.017 g, 0.063mmol) in THF (5 mL) at -35 °C. The color of the solution changed from faint green to deep colored. After 1 hr the solution was pumped dried under high vacuum to get a solid residue as product. ^1H NMR was taken in C_6D_6.

Synthesis of complex (L1)Ni(PPh_3)$_2$:

Inside a glove box, a solution of triphenyl phosphine (0.033 g, 0.125 mmol) in THF was added dropwise to a stirring suspension of $Ni(COD)_2$ (0.017 g, 0.063mmol) in THF. A deep dark solution was formed, which was stirred for 1 hr in room temp. After that a solution of **L1** in THF was added to the stirring solution of reaction mixture over the period of 5 mins and continued stirring for one more hour. The final solution was dried under vacuum and NMR was taken in C_6D_6.

Synthesis of complex (L2)$NiCl_2$:

Inside the glove box a solution **L2** solution of THF was dropwise added to the suspension of (DME)$NiCl_2$ in THF at room temp and continue stirring for overnight. After 16 hours of reaction a reddish pink suspension formed which was dried under vacuum and washed with Et_2O. Then the residue was dried under high vacuum to get the pink solid as product. NMR was taken in $CDCl_3$ solvent.

Synthesis of complex (L4)$NiCl_2$:

This complex was synthesized similarly as complex **(L2)$NiCl_2$**. After overnight stirring a reddish pink solution was formed which was then pumped to get a solid residue. The residue was washed with pentane and then dried under high vacuum to get the final product. The NMR was taken in $CDCl_3$.

Preparation of (L1)$ZnCl_2$.

A solution of (4-diphenylphosphino)phenanthridine (0.023 g, 0.063 mmol) in THF (2.5 mL) was added dropwise to a solution of $ZnCl_2$ (0.0085 g, 0.063 mmol) in THF (2.5 mL) with constant stirring. The mixture was stirred for additional 3 h, at which point the formation of a white suspension was noted. The reaction mixture was dried under reduced pressure and dissolved in the dichloromethane (5 mL) and filtered over Celite. Concentration and recrystallization from dichloromethane/hexane at room temperature gave colorless crystals. Yield = 0.026 g (83 %). ^{1}H NMR ($CDCl_3$, 300 MHz, 25 °C): δ 9.57 (s, 1H, N=C-*H*), 8.89-8.77 (m, 1H, $^{phen}C_{Ar}$-*H*), 8.67 (d, J_{HH} = 8.4 Hz, 1H, $^{phen}C_{Ar}$-*H*), 8.18 (dd, J_{HH} = 8.1, 1.2 Hz, 1H, $^{phen}C_{Ar}$-*H*), 8.05 (ddd, J = 8.4, 7.1, 1.3 Hz, 1H, $^{phen}C_{Ar}$-*H*), 7.95-7.81 (overlapped m, 3H, $^{phen}C_{Ar}$-*H*), 7.69 (overlapped m, 4H, PC_{Ar}-*H*), 7.52-7.43 ppm (overlapped m, 6H, PC_{Ar}-*H*). ^{13}C NMR ($CDCl_3$, 126 MHz, 25 °C): δ 156.7 (d, J_{CP} = 4 Hz, $^{phen}C_{Ar}H$), 142.8 (d, J_{CP} = 14 Hz, $^{phen}C_{Ar}$), 136.4 ($^{phen}C_{Ar}H$), 134.5 ($^{phen}C_{Ar}H$), 134.2 (d, J_{CP} = 14 Hz, $PC_{Ar}H$), 133.4 (d, J_{CP} = 2 Hz, $^{phen}C_{Ar}$),131.8 (d, J_{CP} = 2 Hz, $^{phen}C_{Ar}H$), 130.8 ($^{phen}C_{Ar}H$), 129.7 ($PC_{Ar}H$), 129.6 ($PC_{Ar}H$), 128.9 (d, J_{CP} = 34 Hz, $^{phen}C_{Ar}$), 128.6 (d, J_{CP} = 6 Hz, $^{phen}C_{Ar}H$), 126.9 (d, J_{CP} = 1 Hz, $^{phen}C_{Ar}H$), 126.3 (d, J_{CP} = 3 Hz, $^{phen}C_{Ar}$), 126.2 (d, J_{CP} = 39 Hz, PC_{Ar}), 125.9 (d, J_{CP} = 4 Hz, $^{phen}C_{Ar}$), 122.4 ($^{phen}C_{Ar}H$) ppm. $^{31}P\{^1H\}$ NMR ($CDCl_3$, 121 MHz, 25

°C): δ -32.4 (s) ppm. UV-Vis: λ (ε) 238 (2.60 x 10^4), 253 (2.89 x 10^4), 301 (5.68 x 10^3), 341 (2.49 x 10^3), 357 nm (2.13 x 10^3 $M^{-1}cm^{-1}$). Anal. Calc'd for $C_{25}H_{18}N_1P_1Zn_1Cl_2$•0.5($CH_2Cl_2$): C, 56.49; H, 3.53. Found: C, 56.69; H, 3.67. Half a molecule of CH_2Cl_2 (the crystallization solvent) was found in the asymmetric unit of the X-ray structure of (L1)$ZnCl_2$, and could also be seen by ^{1}H NMR spectroscopy upon dissolution of crystals of (L1)$ZnCl_2$.

Crystal structure data for (L1)$ZnCl_2$: $C_{51}H_{38}Cl_6N_2P_2Zn_2$, 1084.21 g/mol, monoclinic, space group *C*2/c; a = 17.297(4) Å, b = 8.0754(16) Å, c = 34.424(7) Å, β = 94.02(3)°, V = 4796.4(17) $Å^3$; Z = 4, ρ_{calcd} = 1.501 g cm^{-3}; crystal dimensions: 0.125 × 0.055 × 0.025 mm; diffractometer: Bruker APEXII CCD; Mo Kα radiation, ω scans, 293(2) K, 2.361 ≤ θ ≤ 27.511°; 21325 reflections, 5540 independent (R_{int} = 0.0237), direct methods; absorption coeff (μ = 1.439 mm^{-1}), absorption correction: semi-empirical from equivalents; completeness to θ = 26°: 100%; refinement (against F^2) with SHELXL-2014/7, 285 parameters, 0 restraints, R_1 = 0.0392 ($I > 2\sigma$) and wR_2 = 0.1181 (all data), Goof = 1.037, residual electron density 0.976/−0.665 e $Å^{-3}$.

General procedure of synthesis of L7-L10•HX (X = Br, Cl):

For the synthesis of bromo precursors, 6-Br (1 mmol) and corresponding imidazole (1.2 mmol) was taken into a 100 mL flask in 20 mL toluene. The mixture was refluxed for 48 hrs, a off white precipitate was filtered from the solution. The isolated solid was crystallized with DCM-Et_2O. The chloro precursors were synthesized using 6-chlorophenanthridine following same procedure.

Preparation of complex $(L7)_2Ag(PF_6)$.

L7•HPF_6 (1 mmol) was taken in a 50 mL Schlenk flask with Ag_2O (0.5 mmol) in CH_3CN (10 mL) at stir at 50 ° C until all the silver salt was consumes by around 12 hrs. The solution was cooled down to room temperature and filtered through the celite. The solution was pumped dry

and isolated from crystallization with CH_3CN-Et_2O mixture. A yellowish crystal was formed which isolated and washed with Et_2O.

Preparation of complex $[(L8)_2Ir(CH_3CN)_2][PF_6]_3$.

In a 50 mL Schlenk flask 1.5 equivalent L8•HPF_6 and 0.5 equivalent of Ag_2O was taken and stirred in CH_3CN at 50 ° C overnight. Then [Ir(COD)Cl] was taken 0.5 equivalent in CH_3CN (2 mL) solution and added to the reaction mixture under inert atmosphere. Then the reaction was taken to room temperature and stirred for 24 hrs before addition of 1 equivalent of $NaPF_6$ in CH_3CN (2 mL). The solution was pumped dried and washed with Et_2O and filtered through a filter paper. The isolated solid was crystallized with CH_3CN-Et_2O. X-ray quality crystal was isolated after 1 week.

Preparation of complex $[(L8)_2Ru_2Cl_2](PF_6)_2$.

In a 50 mL Schlenk flask **L8** bromide precursor and 0.5 equivalent of $RuCl_3.xH_2O$ were taken in ethylene glycol at 200 °C for 12 hr. The color of the solution changed to yellow. The solution was brought to room temperature and 0.5 equivalent of NH_4PF_6 solution in water was added to the reaction mixture. A yellow precipitate was isolated after filtration and washed with diethylether (3 x 5 mL). The yellow solid was crystallized with DCM-Et_2O.

2.6. References:

(1) Tang, C. W.; VanSlyke, S. A. Organic Electroluminescent Diodes. *Appl. Phys. Lett.* **1987**, *51*, 913–915.

(2) Accorsi, G.; Listorti, A.; Yoosaf, K.; Armaroli, Nicola. 1,10-Phenanthrolines: Versatile Building Blocks for Luminescent Molecules, Materials and Metal Complexes. *Chem. Soc. Rev.* **2009**, *38*, 1690–1700.

(3) Hancock, R. D. The Pyridyl Group in Ligand Design for Selective Metal Ion Complexation and Sensing. *Chem. Soc. Rev.* **2013**, *42*, 1500–1524.

(4) Bonnet, S.; Collin, J.-P.; Koizumi, M.; Mobian, P.; Sauvage, J.-Pierre. Transition-Metal-Complexed Molecular Machine Prototypes. *Adv. Mater.* **2006**, *18*, 1239–1250.

(5) Gunanathan, C.; Milstein, David. Metal-Ligand Cooperation by Aromatization-Dearomatization: A New Paradigm in Bond Activation and "Green" Catalysis. *Acc. Chem. Res.* **2011**, *44*, 588–602.

(6) Peng, H. M.; Webster, R. D.; Li, Xingwei. Quinoline-Tethered N-Heterocyclic Carbene Complexes of Rhodium and Iridium: Synthesis, Catalysis, and Electrochemical Properties. *Organometallics* **2008**, *27*, 4484–4493.

(7) Feltham, R. D.; Metzger, H. G. The Synthesis of Vicinal Bis(Dimethylarsino) Compounds. *J. Organomet. Chem.* **1971**, *33*, 347–355.

(8) Peters, J. C.; Harkins, S. B.; Brown, S. D.; Day, M. W. Pincer-like Amido Complexes of Platinum, Palladium, and Nickel. *Inorg. Chem.* **2001**, *40*, 5083–5091.

(9) Lee, C.-I.; Zhou, J.; Ozerov, O. V. Catalytic Dehydrogenative Borylation of Terminal Alkynes by a SiNN Pincer Complex of Iridium. *J. Am. Chem. Soc.* **2013**, *135*, 3560–3566.

(10) Park, G. Y.; Wilson, J. J.; Song, Y.; Lippard, S. J. *Proc. Natl. Acad. Sci. U.S.A*. **2012**, *109*, 11987.

(11) Fukase, A.; Kido, Junji. Organic Electroluminescent Devices Having Self-Doped Cathode Interface Layer. *Jpn. J. Appl. Phys.* **2002**, *41*, L334–L336.

(12) Kido, J.; Endo, Jun. A Novel Electroluminescent Metal Complex: Tris(4-Phenanthridinolato)Aluminum(III). *Chem. Lett.* **1997**, 593–594.

(13) Raszeja, L.; Maghnouj, A.; Hahn, S.; Metzler-Nolte, Nils. A Novel Organometallic ReI Complex with Favourable Properties for Bioimaging and Applicability in Solid-Phase Peptide Synthesis. *ChemBioChem* **2011**, *12*, 371–376.

(14) Lu, L.-Q.; Li, Y.; Junge, K.; Beller, Matthias. Iron-Catalyzed Hydrogenation for the In Situ Regeneration of an NAD(P)H Model: Biomimetic Reduction of α-Keto-/α-Iminoesters. *Angew. Chem. Int. Ed.* **2013**, *52*, 8382–8386.

(15) Lu, L.-Q.; Li, Y.; Junge, K.; Beller, Matthias. Relay Iron/Chiral Bronsted Acid Catalysis: Enantioselective Hydrogenation of Benzoxazinones. *J. Am. Chem. Soc.* **2015**, *137*, 2763–2768.

(16) Chen, Q.-A.; Gao, K.; Duan, Y.; Ye, Z.-S.; Shi, L.; Yang, Y.; Zhou, Y.-Gui. Dihydrophenanthridine: A New and Easily Regenerable NAD(P)H Model for Biomimetic Asymmetric Hydrogenation. *J. Am. Chem. Soc.* **2012**, *134*, 2442–2448.

(17) Tumir, L.-M. *Beilstein J. Org. Chem.* **2014**, *10*, 2930.

(18) Keller, P. A. *Sci Synth* **2005**, *15*, 1065.

(19) Dhara, S.; Ghosh, M.; Ray, J. K. Synthesis of Phenanthridines and Analogues via Suzuki Coupling and Condensation. *Synlett* **2013**, *24*, 2263–2265.

(20) Ghosh, M.; Ahmed, A.; Singha, R.; Ray, J. K. Domino Suzuki Coupling and Condensation Reaction: An Efficient Strategy towards Synthesis of Phenanthridines. *Tetrahedron Lett.* **2015**, *56*, 353–355.

(21) Mandapati, P.; Giesbrecht, P. K.; Davis, R. L.; Herbert, D. E. Phenanthridine-Containing Pincer-like Amido Complexes of Nickel, Palladium, and Platinum. *Inorg. Chem.* **2017**, *56*, 3674–3685.

(22) Nag, S.; Cibian, M.; Hanan, G. S. 8-(Diphenylphosphanyl)Quinoline. *Acta Crystallogr. Sect. E Struct. Rep. Online* **2010**, *66*, o2847.

(23) Brett, W. A.; Rademacher, P.; Boese, R. Redetermination of the Structure of Phenanthridine. *Acta Crystallogr. C* **1993**, *C49*, 1564–1566.

(24) Farrugia, L. J. ORTEP-3 for Windows - a Version of ORTEP-III with a Graphical User Interface (GUI). *J. Appl. Crystallogr.* **1997**, *30*, 565.

(25) Szabo, C.; Jagtap, P.; Southan, G.; Salzman, Andrew. Preparation of Phenanthridinones for Treatment of Neurodegeneration. U.S. Patent 6531464B1, March 11, 2003.

(26) Nagesh, H. N.; Suresh, N.; Prakash, G. V. S. B.; Gupta, S.; Rao, J. V.; Sekhar, K. V. G. C. Synthesis and Biological Evaluation of Novel Phenanthridinyl Piperazine Triazoles via Click Chemistry as Anti-Proliferative Agents. *Med. Chem. Res.* **2015**, *24*, 523–532.

(27) Liu, B.; Chen, C.; Zhang, Y.; Liu, X.; Chen, W. Dinuclear Copper(I) Complexes of Phenanthrolinyl-Functionalized NHC Ligands. *Organometallics* **2013**, *32*, 5451–5460.

(28) Standley, E. A.; Tasker, S. Z.; Jensen, K. L.; Jamison, T. F. Nickel Catalysis: Synergy between Method Development and Total Synthesis. *Acc. Chem. Res.* **2015**, *48*, 1503–1514.

(29) Danopoulos, A. A.; Simler, T.; Braunstein, P. N-Heterocyclic Carbene Complexes of Copper, Nickel, and Cobalt. *Chem. Rev.* **2019**, *119*, 3730–3961.

(30) Yan, L.; Zhao, D.; Lan, J.; Cheng, Y.; Guo, Q.; Li, X.; Wu, N.; You, Jingsong. Palladium-Catalyzed Tandem N-H/C-H Arylation: Regioselective Synthesis of N-Heterocycle-Fused

Phenanthridines as Versatile Blue-Emitting Luminophores. *Org. Biomol. Chem.* **2013**, *11*, 7966–7977.

(31) Herbert, D. E.; Ozerov, O. V. Binuclear Palladium Complexes Supported by Bridged Pincer Ligands. *Organometallics* **2011**, *30*, 6641–6654.

(32) Davidson, J. J.; DeMott, J. C.; Douvris, C.; Fafard, C. M.; Bhuvanesh, N.; Chen, C.-H.; Herbert, D. E.; Lee, C.-I.; McCulloch, B. J.; Foxman, B. M.; et al. Comparison of the Electronic Properties of Diarylamido-Based PNZ Pincer Ligands: Redox Activity at the Ligand and Donor Ability Toward the Metal. *Inorg. Chem.* **2015**, *54*, 2916–2935.

(33) Chang, M.-C.; Dann, T.; Day, D. P.; Lutz, M.; Wildgoose, G. G.; Otten, Edwin. The Formazanate Ligand as an Electron Reservoir: Bis(Formazanate) Zinc Complexes Isolated in Three Redox States. *Angew. Chem. Int. Ed.* **2014**, *53*, 4118–4122.

(34) Hashimoto, A.; Yamaguchi, H.; Suzuki, T.; Kashiwabara, K.; Kojima, M.; Takagi, H. D. Preparation, Crystal Structures, and Spectroscopic and Redox Properties of Nickel(II) Complexes Containing Phosphane-(Amine or Quinoline)-Type Hybrid Ligands and a Nickel(I) Complex Bearing 8-(Diphenylphosphanyl)Quinoline. *Eur. J. Inorg. Chem.* **2010**, 39–47.

(35) Choi, Y. W.; Lee, J. J.; Kim, Cheal. A Highly Selective Fluorescent Chemosensor Based on a Quinoline Derivative for Zinc Ions in Pure Water. *RSC Adv.* **2015**, *5*, 60796–60803.

(36) Fulmer, G. R.; Miller, A. J. M.; Sherden, N. H.; Gottlieb, H. E.; Nudelman, A.; Stoltz, B. M.; Bercaw, J. E.; Goldberg, K. I. NMR Chemical Shifts of Trace Impurities: Common Laboratory Solvents, Organics, and Gases in Deuterated Solvents Relevant to the Organometallic Chemist. *Organometallics* **2010**, *29*, 2176–2179.

Chapter 3:

3.1. Abstract:

The benzannulated bidentate pyridine/phosphine (*P^N*) ligands bearing quinoline or phenanthridine (3,4-benzoquinoline) units introduced in Chapter 2 are here discussed in the context of their halide-bridged, dimeric Cu(I) complexes, of the form $[(P\text{^}N)Cu]_2(\mu\text{-}X)_2$. The copper complexes are phosphorescent in the orange-red region of the spectrum in the solid state under ambient conditions. Structural characterization in solution and the solid-state reveals a flexible conformational landscape, with both diamond-like and butterfly motifs available to the Cu_2X_2 cores. Similarly, an alkyl functionalized phenanthridine/phosphine *P^N* ligand (**L5**) was used to construct an acetylide-bridged $[(P\text{^}N)Cu]_2(\mu\text{-acetylide})_2$ complex. A byproduct of this reaction, $(bis\text{-}P\text{^}N)_2Cu(I)$ acetylide complex with both κ^2- and η^1-P^N ligands was also isolated. These complexes were characterized by multi-nuclear NMR, elemental analysis and X-ray crystallography, which revealed the butterfly structure for the former set of compounds, and tetrahedral geometry for the latter, bearing a pendant phenanthridine moiety. Comparing the photophysical properties of complexes of (quinolinyl)phosphine ligands with those of π-extended (phenanthridinyl)phosphines has revealed a counter-intuitive impact of site-selective benzannulation. Contrary to conventional assumptions regarding π-extension and a bathochromic shift in the lowest energy absorption maxima, a blue shift of nearly 40 nm in the emission wavelength is observed for the complexes with larger ligand π-systems, which is assigned as phosphorescence on the basis of emission energies and lifetimes. Comparison of the ground-state and triplet excited state structures optimized from DFT and TD-DFT calculations allows attribution of this effect to a greater rigidity for the benzannulated complexes resulting in a

higher energy emissive triplet state, rather than significant perturbation of orbital energies. This chapter highlights how ligand structure can impact photophysical properties for emissive molecules by influencing their structural rigidity, in addition to their electronic structure.

3.2. Introduction:

Extending π-conjugation in a ligand system is a common strategy for adjusting photophysical properties in coordination complexes without significantly altering the parent ligand structure. This strategy introduces flexibility into the design of photosensitizers and emissive molecules, as properties can be tuned without substantial changes to the core coordination environment. Expanding conjugation typically induces bathochromic shifts of absorption and emission bands, as the frontier orbitals become progressively closer in energy with π-extension.[1,2,3,4] Recently, experimental systems[5,6] have begun to challenge the extent to which this conventional view is applicable and a theoretical framework[7] based on analysis of the site-dependent impact of π-extension on frontier molecular orbital energies has been developed. In this paradigm, the consequence of benzannulation is interpreted through the effect on HOMO/LUMO energies and the corresponding changes to the lowest lying singlet (S_1) and triplet (T_1) excited states.[6,7]

Curious as to the general applicability of this theoretical paradigm, this thesis and other work from the group has focused on developing synthetic routes to 2,4-disubstituted phenanthridines (phenanthridine = 3,4-benzoquinoline) that enable incorporation of this benzannulated aromatic *N*-heterocycle into multidentate ligand frameworks.[8,9] Surprisingly, within a series of pincer-type tridentate ligands, sequential quinoline-to-phenanthridine π-extension (e.g., from *bis*(8-quinolinyl)amido through (4-methylphenanthridinyl)(8-

quinolinyl)amido to *bis*(4-methylphenanthridinyl)amido ligand frameworks) was found to *not* significantly affect the energy of absorption of the corresponding Ni^{2+}, Pd^{2+} and Pt^{2+} complexes: the complexes showed isoenergetic λ_{max} values,[9] despite benzannulation leading to changes in the energies of the frontier orbitals, in line with the aforementioned theoretical models.[7] In that series of complexes, while stabilization of the lowest unoccupied molecular orbital (LUMO) was observed with π-extension, this was accompanied by a change in oscillator strength of the HOMO→LUMO and HOMO→LUMO+1 transitions, effectively shutting off the lower energy HOMO→LUMO transition in favor of the HOMO→LUMO+1. This resulted in near-identical UV-Vis absorption profiles despite the significant expansion of ligand conjugation.

In this chapter, a series of luminescent halide-bridged, dimeric Cu(I) complexes of phenanthridine-containing, *P^N*-coordinating ligands is presented (**Figure 3.1**; **$(L1)_2Cu_2X_2$**, **$(L2)_2Cu_2X_2$**: X = Cl, Br, I) and their photophysical properties are compared with those of quinoline analogs (**$(L3)_2Cu_2X_2$** : X = Cl, Br, I) comprising smaller π-systems. Cu(I) complexes are attracting increasing attention as low-cost luminescent materials, with applications in light-emitting devices, as photosensitizers, dyes and imaging agents.[10,11,12,13,14] Although the spin-orbit coupling (SOC) constant of copper is lower than that of 2nd and 3rd row elements like ruthenium, iridium and platinum, Cu(I) can nevertheless promote the formally forbidden phosphorescence from triplet states in some systems with π-acceptor ligands, owing to the efficiency of SOC pathways through coupling of the lowest triplet state with close-lying ^{1}MLCT states.[15] In some cases, meanwhile, a small S_1–T_1 energy gap can open up thermally activated delayed fluorescence (TADF) from T_1 to S_1 as another mechanism by which otherwise non-emissive triplet states can be harvested.[16] While the use of site-selective benzannulation in tuning emission has been reported for Pt[5,7] and Ir[6] emitters, such strategies have not, to our knowledge, been

explored in Cu(I) coordination complexes. Whilst the results reveal more pronounced lower energy absorption bands upon extending the π-system, a counter-intuitive blue shift in emission maximum is observed. This contrary behavior was not observed for Pt[5,7] or Ir,[6] where the direction of the shift was the same for both absorption and emission. A strong dependence of the luminescence efficiency on the identity of the halide bridge has also been discovered. Finally, an acetylide-bridged analog $[(P\text{^}N)Cu]_2(\mu\text{-}X)_2$ X = (4-*tert*-butylphenyl)acetylide is described. Acetylide substituted emitters based on Pt have been vastly studied, but are less commonly discussed as part of Cu complexes for photoemission.[17] As an anionic donor and strong field ligand, acetylides were considered to potentially boost emission properties.

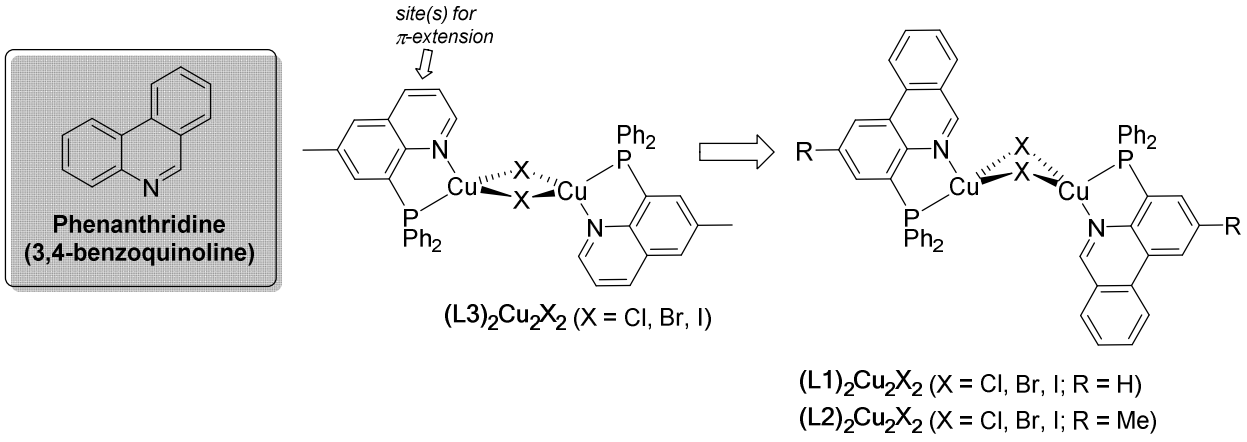

Figure 3. 1: Site-selective benzannulation of quinoline ligand frameworks in $[(P\text{^}N)Cu]_2(\mu\text{-}X)_2$ complexes.

3.3. Results and Discussion:

3.3.1. Synthesis:

Hybrid *P^N* donor proligands **L1** and **L2** were prepared from 4-bromophenanthridines as outlined in Chapter 2. The synthesis of **L1** and the dimeric Cu_2Br_2 compound **$(L1)_2Cu_2X_2$** was also discussed. Here, I found incorporating a methyl substituent in the 2-position allows higher yields of the 4-bromophenanthridine to be obtained compared with the unsubstituted analog (R = H),[9] thereby increasing the overall yields of **L2** compared with **L1**. Following lithium-halogen exchange with *sec*-BuLi and quenching with Ph_2PCl as an electrophilic source of phosphorus, 4-(diphenylphosphino)-2-methylphenanthridine (**L2**) was isolated in 63% yield. The corresponding 6-methylquinoline analog incorporating a less extended π-system (**L3**) could similarly be isolated in 67% yield by starting from 8-bromo-6-methylquinoline (**Scheme 3.1**).

The structure of the phenanthridine subunit in **L1** and **L2** is best described as an 'imine-bridged biphenyl' in accordance with Clar's postulate, wherein the dominant resonance contributor maximizes the number of aromatic sextets in the polycyclic aromatic system.[17] In the ^{1}H NMR spectra, the 'imine-like' hydrogen in the 6-position of the phenanthridine ring is consequently observed at a chemical shift unusually downfield for an aromatic *N*-heterocycle [δ(C_6-*H*) **L1**: 9.23 ppm, **L2**: 9.19 ppm], as is the 'imine-like' carbon in the $^{13}C\{^1H\}$ NMR spectra [δ(*C*$_6$-H) **L1**: 152.8 ppm, **L2**: 151.8 ppm]. In the quinoline-containing **L3**, the comparable C-H unit *ortho* to N is less deshielded [δ(*C*-*H*) 8.79 (m) and 149.0 ppm in the ^{1}H and $^{13}C\{^1H\}$ spectra respectively]. For each proligand, one sharp singlet is observed in the $^{31}P\{^1H\}$ NMR spectra (**L1**: –13.7 ppm, **L2**: –13.6 ppm, **L3**: –14.9 ppm).

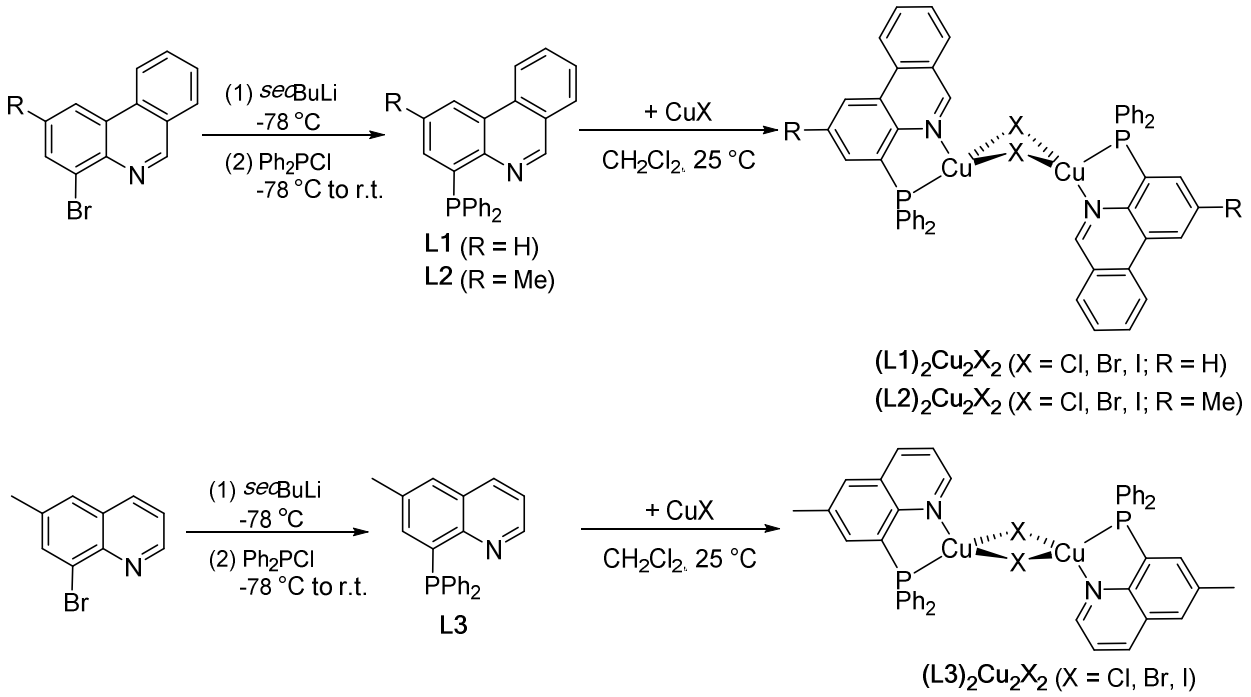

Scheme 3. 1: Synthesis of π-extended phenanthridine-based *P^N*-coordinating proligands **L1** and **L2**, the parent quinoline-based analog **L3**, and the corresponding halide-bridged Cu_2X_2 dimers $\mathbf{(L1)_2Cu_2X_2}$, $\mathbf{(L2)_2Cu_2X_2}$ and $\mathbf{(L3)_2Cu_2X_2}$ (X = Cl, Br, I).

Ligand **L6** was synthesized similarly to the other P^N ligands mentioned in this thesis (Chapter 2). 4-bromo-2-methyl-6-*tert*-butyl phenanthridine was isolated via Suzuki coupling reaction between 2-Iodo-6-bromo-4-tertbutyl aniline and 2-acetylphenylboronic acid, formation of 87% yield and proligand **L6** was then accessed as an off-white solid in 71 % yield via lithium-halogen exchange followed by addition of chlorodiphenylphosphine to install the phosphine group. The *tert*-butyl substituent makes **L6** very soluble in nonpolar solvents such as hexane, pentane, especially compared with the other ligands discussed here. **L6** was characterized by ^{1}H and ^{31}P NMR spectroscopy. In the ^{31}P NMR spectra, a singlet appears at -12.57 ppm. This is slightly downfield compared to **L2** (-13.61 ppm), possibly due to the electron-releasing alkyl group. The synthesis of Cu acetylide was based on a previously published procedure.[18] The Cu-

acetylide was found to be very insoluble in polar solvents in spite of the presence of *tert*-butyl group. The synthesis of (**L6**)$_2$Cu$_2$(acetylide)$_2$ was performed in DCM with ligand **L6** and Cu-acetylide at room temperature for 24 h (**Scheme 3.2**). A red solution indicates the formation of (**L6**)$_2$Cu$_2$(acetylide)$_2$ in reaction mixture.

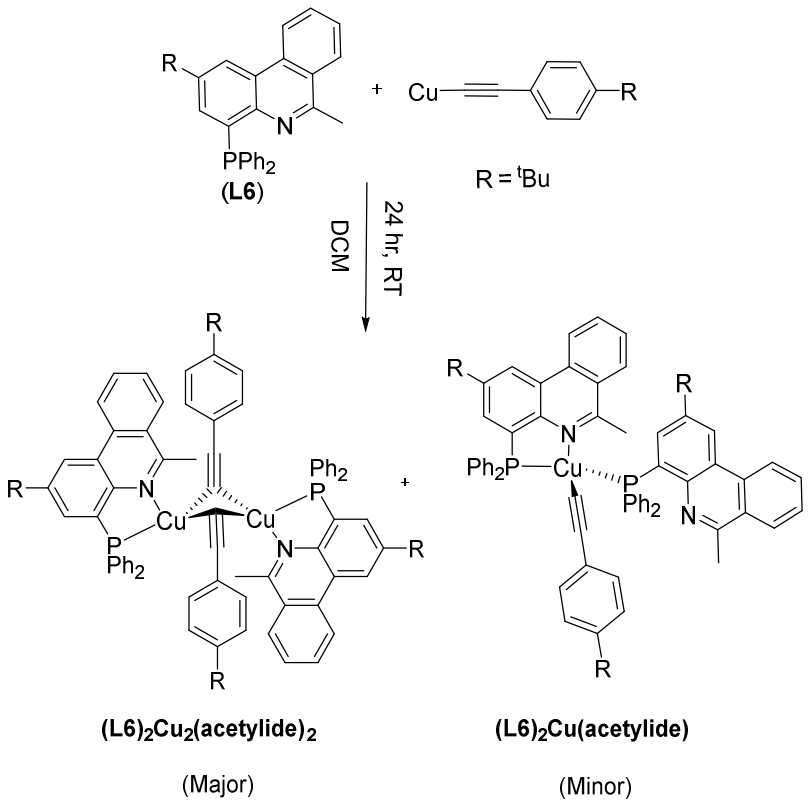

Scheme 3. 2: *P^N*-coordinating proligands **L6** (Chapter 2) and the corresponding acetylide-bridged dimers **(L6)$_2$Cu$_2$(acetylide)$_2$** and **(L6)$_2$Cu(acetylide).**

^{1}H NMR spectroscopy was performed in solution state in $CDCl_3$ and solid-state X-ray crystallography data was supported the solution state. In ^{1}H NMR spectroscopy, peak broadening has been observed possibly due to quadripolar coupling of Cu centre (**Figure 3.2**).

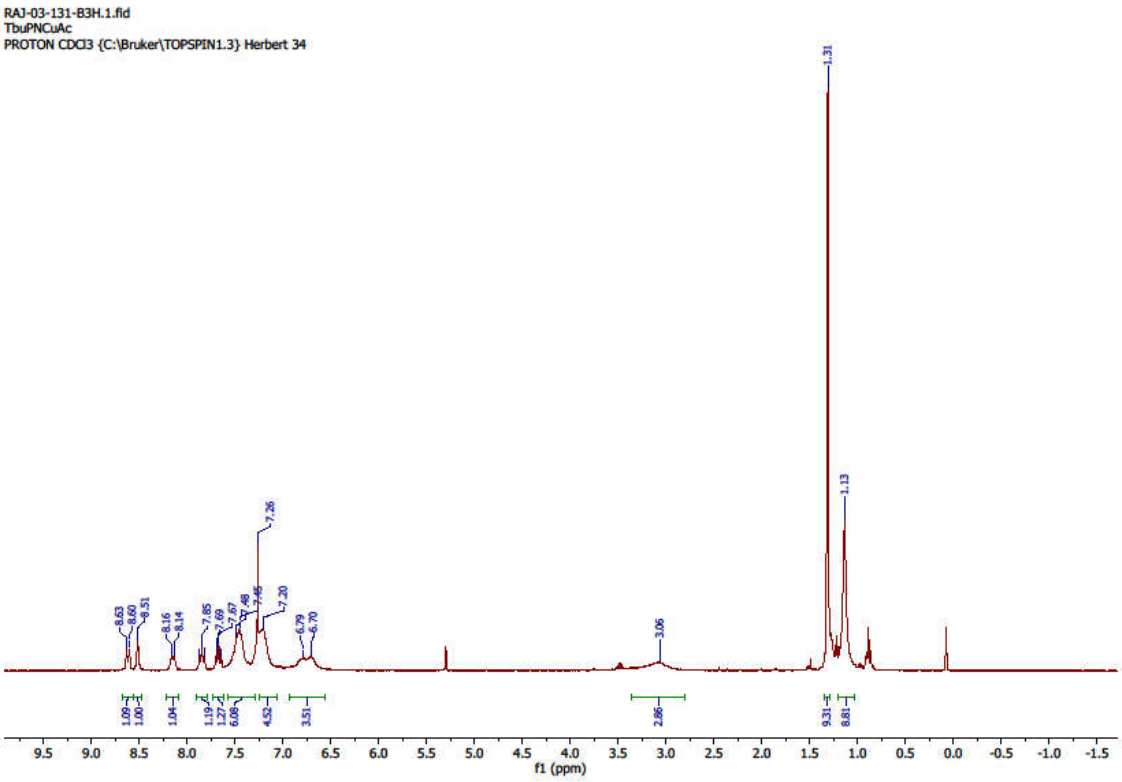

Figure 3. 2: ^{1}H NMR (300 MHz, 22°C) spectrum of **(L6)$_2$Cu$_2$(acetylide)$_2$** in $CDCl_3$.

The reaction mixture also indicates the presence of **(L6)$_2$Cu(acetylide)** as a minor product, which crystallizes together with **(L6)$_2$Cu$_2$(acetylide)$_2$**. The compound **(L6)$_2$Cu(acetylide)** has been characterized by solid-state X-ray crystallography (**Figure 3.13**). Similarly, addition of solutions of **L1**–**L3** in CH_2Cl_2 to suspensions of the appropriate CuX precursor (X = Cl, Br or I) led to the formation of yellow-orange solutions, which became increasingly homogeneous with conversion to the metallated products. Complexes **(L1)$_2$Cu$_2$X$_2$**, **(L2)$_2$Cu$_2$X$_2$** and **(L3)$_2$Cu$_2$X$_2$** were isolated following recrystallization. They were fully characterized in solution by multi-nuclear NMR spectroscopy and in the solid-state by elemental analysis and, for **(L2)$_2$Cu$_2$X$_2$** and **(L3)$_2$Cu$_2$X$_2$**, single-crystal X-ray diffraction. Quantitative

yields of **(L1)$_2$Cu$_2$X$_2$**, **(L2)$_2$Cu$_2$X$_2$** and **(L3)$_2$Cu$_2$X$_2$** were also obtained via simple solid-phase grinding[18] of the appropriate ligand (**L1-3**) with CuX, with identical solution NMR parameters observed for products from solution or solid-state synthesis as following (**Figure 3.3)**.

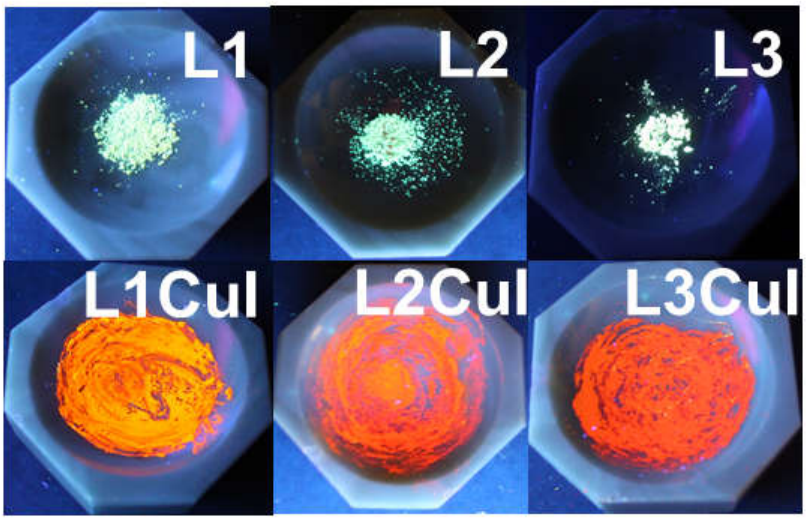

Figure 3. 3: Photographs taken under UV-light (λ = 365 nm) of solid-state samples of **L1, L2**, **L3** and **(L1)CuI, (L2)CuI, (L3)CuI** prepared by grinding the ligands with the appropriate CuX precursor and five drops of CH_3CN.

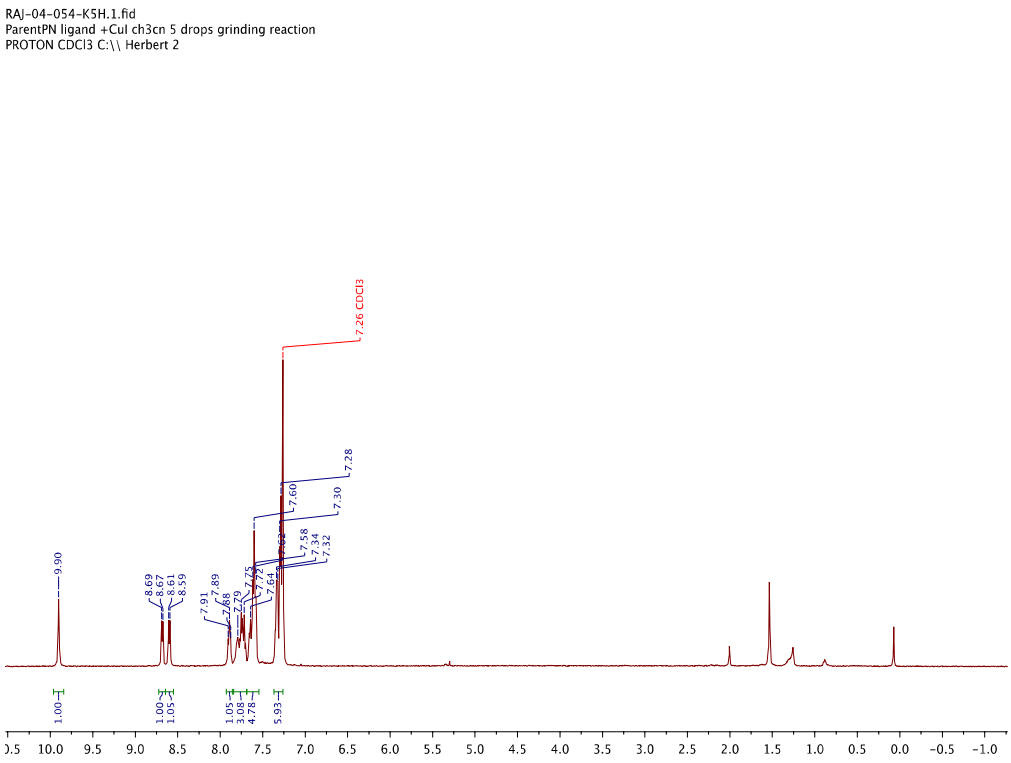

Figure 3. 4: ^{1}H NMR (500 MHz, 22°C) spectrum of (**L1)CuI** in $CDCl_3$ prepared by solid-state grinding.

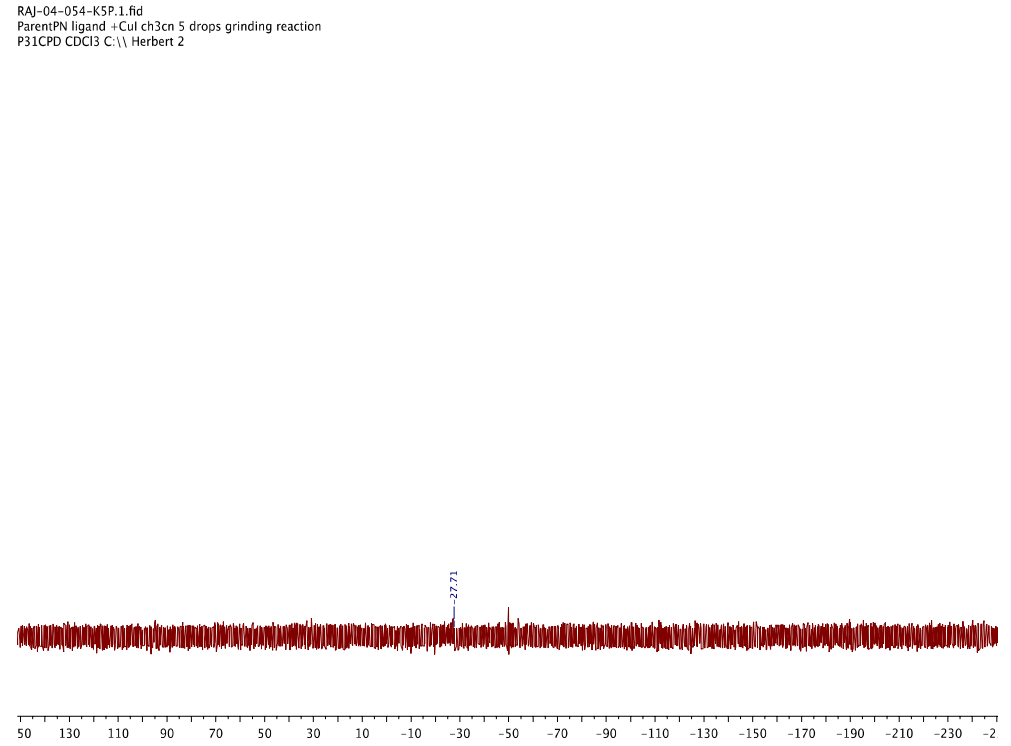

Figure 3. 5: ^{31}P{^{1}H} (121 MHz, 22°C) NMR spectrum of (**L1)CuI** in $CDCl_3$ prepared by solid-state grinding.

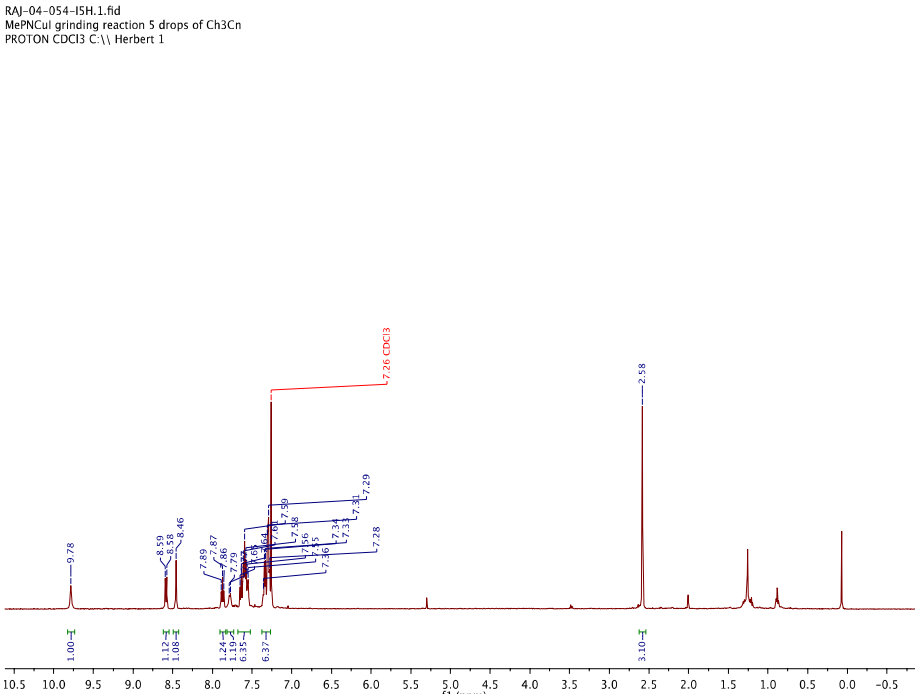

Figure 3. 6: ^{1}H NMR (500 MHz, 22°C) spectrum of **(L2)CuI** in $CDCl_3$ prepared by solid-state grinding.

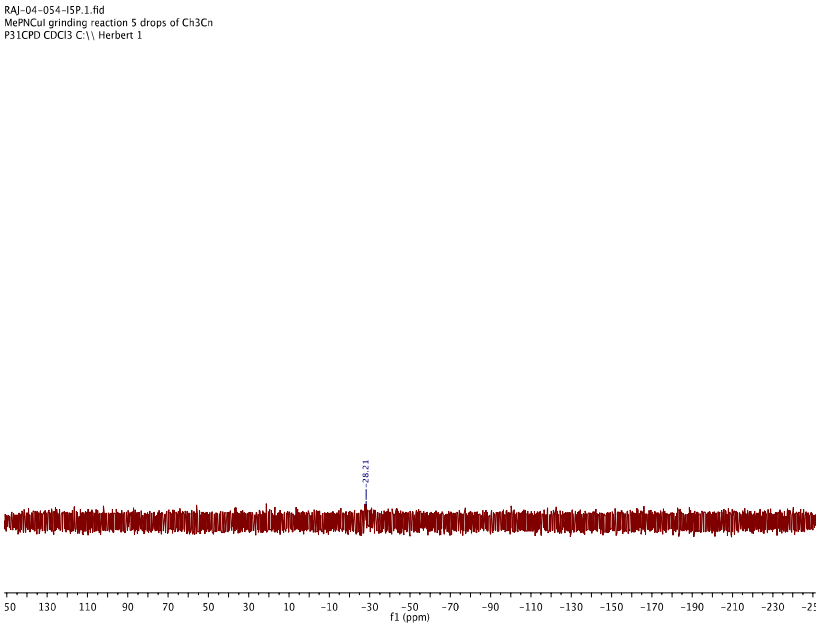

Figure 3. 7: ^{31}P{1H} (121 MHz, 22°C) NMR spectrum of **(L2)CuI** in $CDCl_3$ prepared by solid-state grinding.

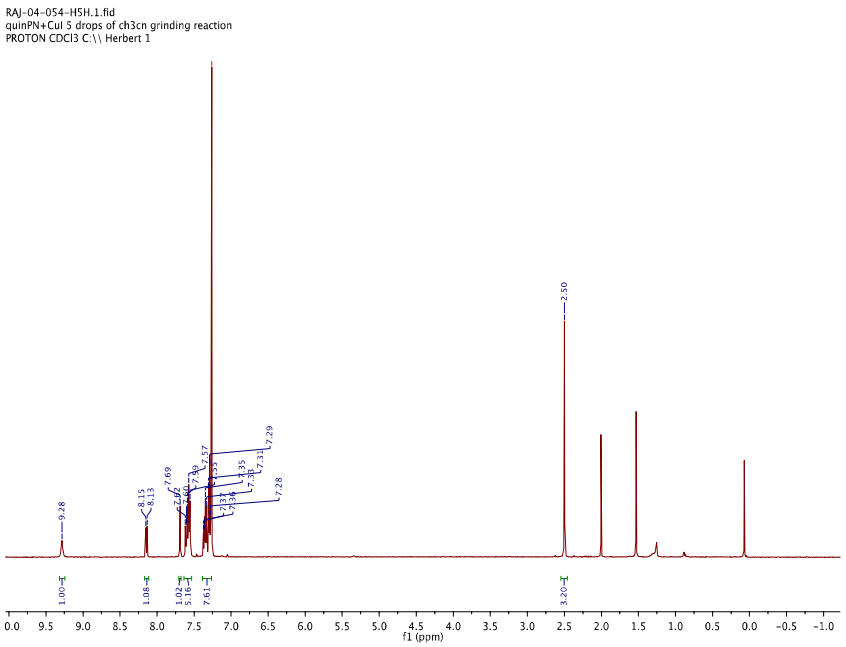

Figure 3. 8: ^{1}H NMR (500 MHz, 22°C) spectrum of **(L3)CuI** in $CDCl_3$ prepared by solid-state grinding.

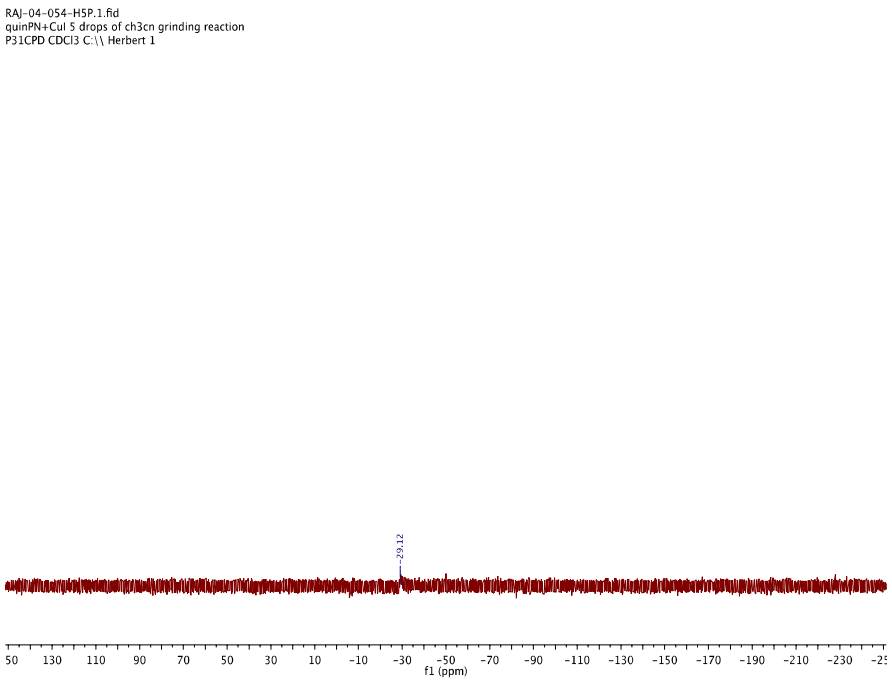

Figure 3. 9: $^{31}P\{^{1}H\}$ (121 MHz, 22°C) NMR spectrum of **(L3)CuI** in $CDCl_3$ prepared by solid-state grinding.

In the solid-state, most of the complexes adopt a 'diamond core'-like Cu_2X_2 motif, in which all four of the central atoms – the two copper ions and the two halides – are mutually coplanar (*vide supra* **Figure 3.1** and *vide infra* **Figure 3.11, 3.12**). In contrast, **(L2)CuI** and **(L1)CuBr**[8] adopt 'butterfly'-type structures, in which the two halides bend out of the plane towards one of the *P^N* ligands. In this structural motif, the molecule no longer bears a center of symmetry, but has two edge-sharing Cu–X–Cu triangles closer to one *P^N* ligand than the other (*vide infra* **Figure 3.11**). Both butterfly-type structures include a co-crystallized CH_2Cl_2 molecule in the lattice. In solution, only one set of ligand signals is evident by ^{1}H and $^{13}C\{^{1}H\}$ NMR spectroscopy for all compounds, suggesting fluxional structures that render the ligand environments equivalent on the NMR timescale, despite their inequivalence in the solid state in **(L2)CuI** and **(L1)CuBr**. In addition, for **(L2)CuBr** both types of structural motifs could be crystallized according to the crystallization conditions, with lattice-confined solvents favoring bent, butterfly-like structures, suggesting a soft energy landscape for the two geometries. A further possible isomer is a 'head-to-head' orientation of the two *P^N* ligands, where both phosphines are positioned on the same side of the Cu_2X_2 core. The formation of this isomer seems unlikely on steric grounds, as the two sets of phenyl rings of the PPh_2 units would clash more significantly than the phenanthridine/PPh_2 combination in the 'head-to-tail' orientation observed in the solid-state.

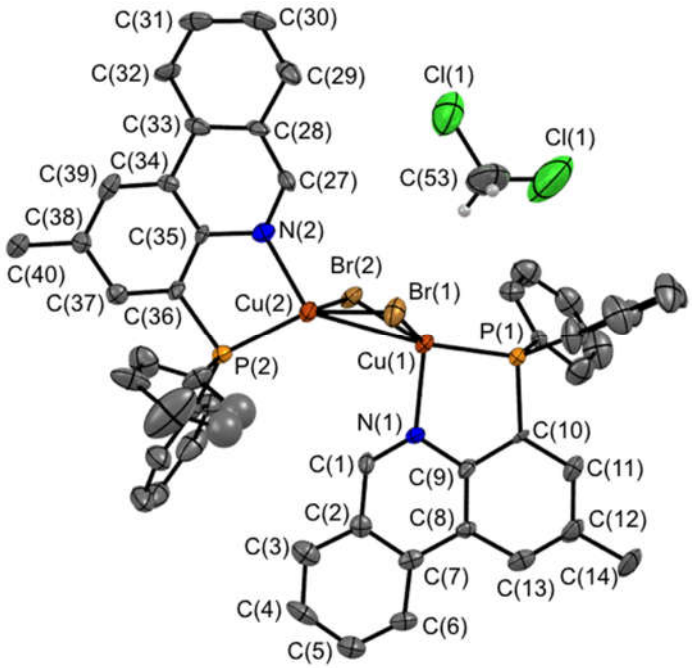

Figure 3. 10: ORTEPs[19] of the solid-state structure of **(L2)CuBr** crystallized in 'butterfly' conformation. Ellipsoids are shown at 50% probability levels with hydrogen atoms omitted for clarity. Selected bond distances (Å) and angles (°): Cu(1)-P(1) 2.204(3), Cu(2)-P(2) 2.201(4), Cu(1)-N(1) 2.100(9), Cu(2)-N(2) 2.085(10), Cu(1)-Br(1) 2.464(2), Cu(1)-Br(2) 2.4534(19), Cu(2)-Br(2) 2.506(2), Cu(2)-Br(1) 2.425(2), Cu(1)-Cu(2); P(1)-Cu(1)-N(1) 86.6(3), P(2)-Cu(2)-N(2) 86.5(3), Cu(1)-Br(1)-Cu(2) 71.84(6), Cu(1)-Br(2)-Cu(2) 70.65(6).

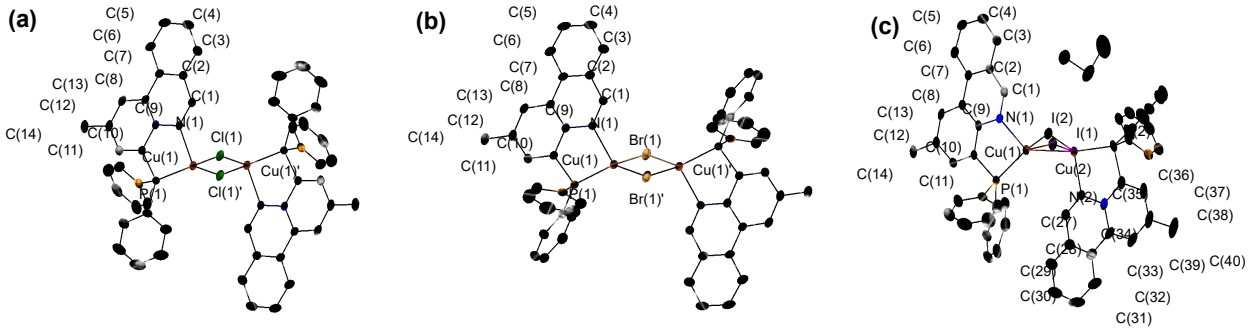

Figure 3. 11: ORTEPs[19] of the solid-state structures of (a) **(L2)CuCl**, (b) **(L2)CuBr** and (c) **(L2)CuI**. Ellipsoids are shown at 50% probability levels with hydrogen atoms, symmetry-generated and phenyl ring atom labels omitted for clarity in (a) and (b). In (c), an additional CH_2Cl_2 solvent molecule (beyond the one depicted) was found in the lattice but omitted here for clarity.

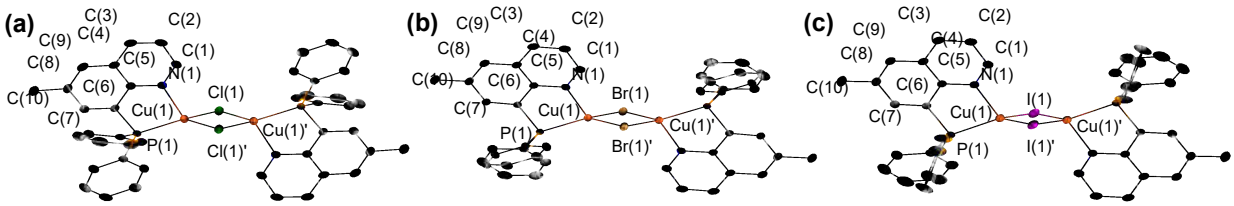

Figure 3. 12: ORTEPs[19] of the solid-state structures of (a) **(L3)CuCl**, (b) **(L3)CuBr** and (c) **(L3)CuI**. Ellipsoids are shown at 50% probability levels with hydrogen atoms, symmetry-generated and phenyl ring atom labels omitted for clarity.

Within each series of complexes, the Cu–X distances increase as expected with increasing ionic radius of the halide, as do the intramolecular Cu···Cu distances for the chloro- and bromo-containing 'diamond-core' structures; e.g., **(L2)CuCl** [2.9990(7) Å] compared with **(L2)CuBr** [3.3246(5) Å] (**Table 3.1**). In the bent butterfly geometry of **(L2)CuI**, the two metals are able to approach each other more closely, leading to a significantly shorter Cu···Cu distance of 2.7082(6) Å. The Cu···Cu distance in **(L3)CuI** [2.7227(4) Å] is similarly the shortest within the **(L3)$_2$Cu$_2$X$_2$** series [**(L3)CuCl**: 2.9802(5) Å; **(L3)CuBr** 3.0077(3) Å], even though a coplanar Cu_2X_2 arrangement is maintained in each case. In the structure of **(L3)CuI**, longer Cu-I bond distances [2.6071(2), 2.6259(3) Å; *cf.* ~ 2.3 Å (**(L3)CuCl**), ~2.4 Å (**(L3)CuBr**)] enable a considerably wider I–Cu–I angle [117.299(7)° compared to 105.068(6)° and 101.421(2)° for **(L3)CuBr** and **(L3)CuCl** respectively], allowing a closer approach of the two Cu centers. The Cu–P bond lengths increase with halide radius, whereas the Cu–N distances do not follow the same trend, decreasing with increasing halide radius within series **(L3)$_2$Cu$_2$X$_2$**.

Table 3. 1: Selected bond lengths (Å) and angles (°) of Cu_2X_2 complexes

	(L2)CuCl	(L2)CuBr	(L2)CuI [a]	(L3)CuCl	(L3)CuBr	(L3)CuI
Cu(1)-P(1)	2.1772(5)	2.2122(6)	2.2291(9), 2.2369(9)[b]	2.1934(6)	2.2088(3)	2.2365(4)
Cu(1)-N(1)	2.0969(11)	2.1386(16)	2.100(3), 2.102(3) [b]	2.1287(16)	2.1161(9)	2.1077(12)
Cu(1)-X(1)	2.3035(5)	2.4775(3)	2.5710(5)	2.3613(6)	2.4697(2)	2.6071(2)
Cu(1)-X(1)'	2.3795(7)	2.4862(3)	2.6854(5)[b]	2.3450(5)	2.47492(19)	2.6259(3)
Cu(1)-Cu(1)'	2.9990(7)	3.3246(5)	2.7082(6)	2.9802(5)	3.0077(3)	2.7227(4)
N(1)-Cu(1)-P(1)	86.09(3)	84.73(5)	84.77(8), 85.17(8)[b]	85.90(5)	86.28(2)	85.96(3)
X(1)-Cu(1)-X(1)'	100.376(18)	95.900(11)	111.995(16), 112.273(18)[b]	101.421(18)	105.068(6)	117.299(7)

[a] Structure has 'butterfly' Cu_2I_2 core and is a solvate with two molecules of CH_2Cl_2 located in the lattice.

[b] Cu(2)–P(2), Cu(2)–N(2), Cu(2)–I(2) lengths; N(2)-Cu(2)-P(2) and I(1)-Cu(2)-I(2) angles.

Interestingly, in the ^{1}H NMR spectra of the complexes in solution, the resonance assigned to the diagnostic proton in the 'imine-like' position of the phenanthridine-containing ligands is increasingly shifted downfield comparing the chloro to the bromo to the iodo member within each series **(L1)$_2$Cu$_2$X$_2$**, **(L2)$_2$Cu$_2$X$_2$** and **(L3)$_2$Cu$_2$X$_2$**. In the solid-state structures, the intramolecular distance between this proton (C_6-*H*) and the bridging halide decreases in the order of X = I > Br > Cl. The chloride in **(L1)CuCl** can be interpreted, therefore, as exhibiting the closest hydrogen-halide bonding, which manifests in a more significant shielding of the diagnostic proton nucleus and an upfield shift in the ^{1}H NMR spectrum. In the ^{31}P{^{1}H} NMR spectra of **(L1)$_2$Cu$_2$X$_2$**, the metal-bound phosphorus appears as a broad peak, shifted upfield from the proligand (**(L1)CuCl**: -17.9, **(L1)CuBr**: -24.0, (**L1)CuI**: -28.3 ppm; **(L2)CuCl**: -17.2, **(L2)CuBr**: -22.5, **(L2)CuI**: -27.8 ppm; and **(L3)CuCl**: -18.2, **(L3)CuBr**: -23.7, **(L3)CuI**: -29.9

ppm), with the size of the upfield shift corresponding to the size of the halide [δ_P(Cl) > δ_P(Br) > δ_P(I)].

The crystal structure of **(L6)$_2$Cu$_2$(acetylide)$_2$** shows the compound has a diamond core structure similar to the quinoline complexes (**(L3)$_2$Cu$_2$X$_2$**). In the crystal structure, the Cu-Cu distance is 2.3646 Å, closer than in the halide bridge Cu complexes described above. As explained, the butterfly geometry helps Cu-Cu to come close in **(L1)$_2$Cu$_2$X$_2$** and **(L2)$_2$Cu$_2$X$_2$,** while longer Cu-I bond and wider I-Cu-I angle provides the shorter Cu-Cu bond length in **(L3)$_2$Cu$_2$X$_2$**. In contrast, in the acetylide bridge Cu complex (L6)$_2$Cu$_2$(acetylide)$_2$, the carbon is smaller size than halogens and as a strong field ligand it holds two Cu center close to each other. Bond length dependency on size of molecule could also be seen in **(L3)$_2$Cu$_2$X$_2$** while changing the halogen size Cu-X: Cl<Br<I. In (L6)$_2$Cu$_2$(acetylide)$_2$ the Cu-C(31) bond length shows shorter 2.031(3) and 2.102(3) Å over (L3)CuCl. The metal-bound acetylene bond length at 1.193(5) Å is very close to free acetylene 1.208(4) Å.[20]

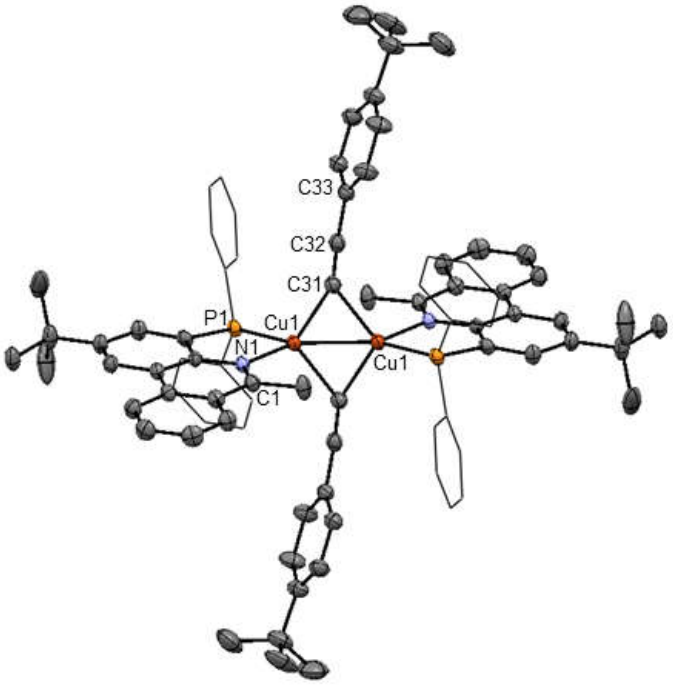

Figure 3. 13: ORTEPs[19] of the solid-state structures of **(L6)$_2$Cu$_2$(acetylide)$_2$**. Ellipsoids are shown at 50% probability levels with hydrogen atoms, symmetry-generated and phenyl ring atom labels omitted for clarity.

Table 3. 2: Selected bond distances (Å) and angles (°) for **(L6)$_2$Cu$_2$(acetylide)$_2$**:

Selected Bonds	**(Å)**	**Selected Angles**	**(°)**
C(31)-Cu(1)	2.031(3)	N(1)-Cu(1)-P(1)	87.19(7)
Cu(1)-Cu(1)*	2.3646(7)	C(1)-N(1)-Cu(1)	124.8(2)
C(31)-Cu(1)*	2.102(3)	Cu(1)-C(31)-Cu(1)*	69.76(11)
C(31)-C(32)	1.193(5)	C(32)-C(31)-Cu(1)	152.3(3)
C(1)-N(1)	1.313(4)	C(31)-Cu(1)-C(31)*	110.24(11)
Cu(1)-N(1)	2.129(3)	C(31)-Cu(1)-Cu(1)*	56.53(10)
Cu(1)-P(1)	2.2001(9)	C(31)*-Cu(1)-Cu(1)	53.70(9)

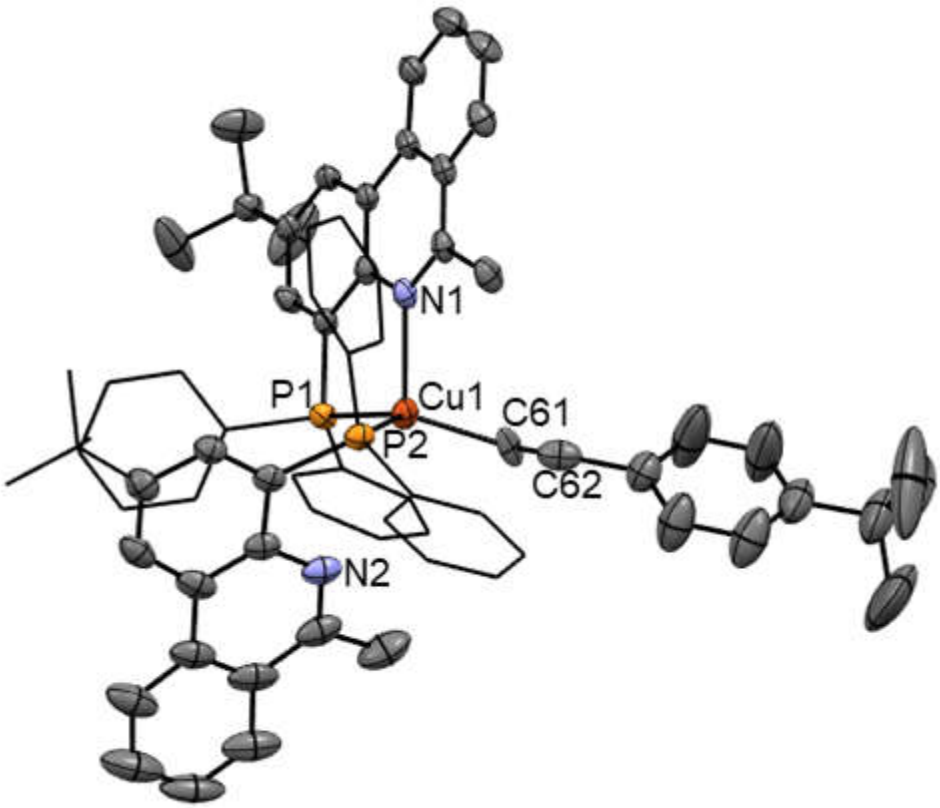

Figure 3. 14: Crystal structure of complex **(*P*^*N*)$_2$Cu(acetylide).** Hydrogen atoms and labels on phosphine, acetylide and phenanthridine are omitted for clarity. A satisfactory crystal structure could not be obtained; nevertheless, preliminary data confirmed the proposed dimer structure and connectivity.

3.3.2. Electronic Absorption and Photoluminescence:

UV-Vis absorption spectra were collected for all nine complexes in solution in CH_2Cl_2 at ambient temperature. As expected from their orange color, the complexes absorb strongly in the UV with a tail into the visible region (**Figure 3.16**). The spectra of the phenanthridine-containing compounds (**(L1)$_2$Cu$_2$X$_2$** and **(L2)$_2$Cu$_2$X$_2$**) contain additional low energy features compared with the quinoline derivatives **(L3)$_2$Cu$_2$X$_2$**, with a well-resolved maximum at 353 nm (**(L1)$_2$Cu$_2$X$_2$**),

slightly red-shifted for the methyl derivatives (**(L2)$_2$Cu$_2$X$_2$**: λ_{max} = 355 nm), and a peak/shoulder at 340 nm. In comparison, the quinoline-containing complexes all show lower molar absorptivities and absorption spectra shifted firmly into the UV and edge of the visible. Comparison with the UV-visible spectra of the corresponding ligands is informative. **L1** and **L2** show bands around 350 and 335 nm that resemble those in the spectra of the corresponding copper complexes.

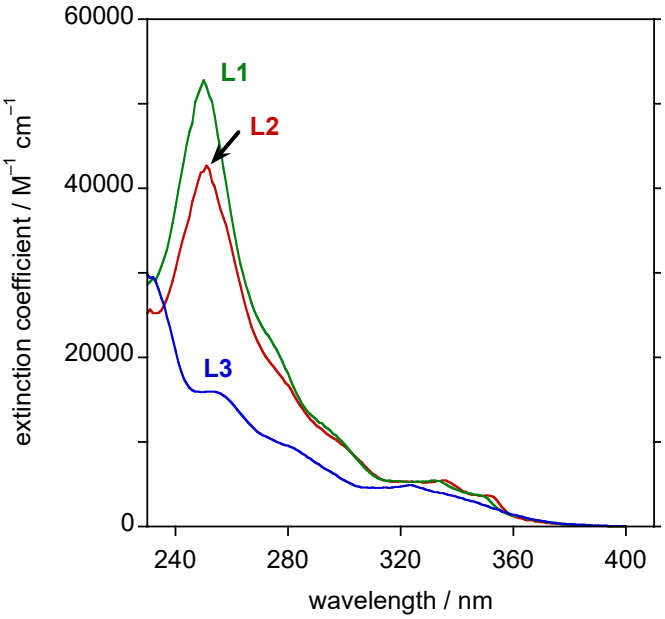

Figure 3. 15: Absorption spectra of **L1** – **L3** in DCM at 298 ± 3 K.

A series of bands in this region, albeit a little sharper, is in fact, characteristic of phenanthridine itself and typical also of many of its derivatives.[21] On the other hand, the quinoline ligand **L3** displays a blue-shifted absorption spectrum relative to its phenanthridine analogues, with a broad band centered at 323 nm. The lower energy of absorption of the phenanthridine compared to the quinoline ligands is consistent with the intuitive expectation that a more conjugated system will

typically have lower energy transitions associated with it. The main difference between the spectra of the three ligands and their copper(I) complexes is the presence of the long-wavelength tail in the complexes. These tails can reasonably be attributed to relatively weak, spin-allowed charge-transfer transitions (^{1}CT), in which the acceptor in the CT process is the heterocycle, based on assignments of Cu(I) complexes with related nitrogenous heterocyclic ligands. Whilst such transitions in homoleptic $[Cu(N\text{^}N)_2]^+$ complexes have clear-cut ^{1}MLCT assignments (i.e., with the donor orbitals being of predominantly metal-based *d* character),[11] in the present heteroleptic complexes featuring relatively electron-rich halide ligands, the donor orbitals in the CT process would be more likely to comprise of molecular orbitals spanning both the metal and the halide; i.e., $^1\{d_{Cu} / p_X \rightarrow \pi^*_{N\text{^}P}\}$ or alternatively denoted ^{1}(M+X)LCT. Calculations using time-dependent density functional theory (TD-DFT) support this assignment (*vide infra*). Such conclusions have been deduced previously for related *P^N* ligand-supported Cu_2X_2 dimers bearing both diphenylphosphino and pyridinyl donors.[22,23] In these complexes, the lowest-energy transitions involve significant contributions from the frontier orbitals and are assigned as mainly HOMO-LUMO transitions, contributing significantly to the first excited singlet (S_1) and triplet (T_1) states of the complexes.[22,23]

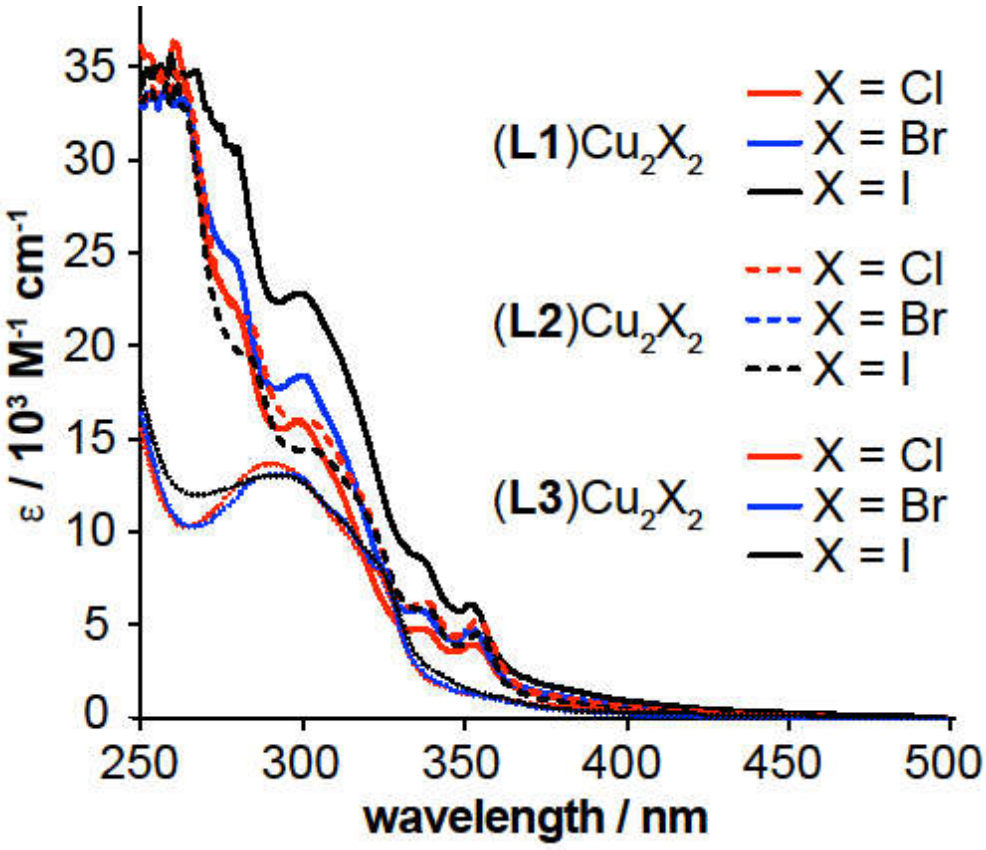

Figure 3. 16: UV-Vis absorption spectra of **$(L1)_2Cu_2X_2$**, **$(L2)_2Cu_2X_2$** and **$(L3)_2Cu_2X_2$** in CH_2Cl_2 solution at room temperature.

As already discussed early in this chapter, the three iodo complexes appear quite brightly luminescent to the eye when observed as powdered samples under long-wavelength UV irradiation, glowing orange/red (*vide supra* **Figure 3.3**). The bromo complexes are also visibly red luminescent, whilst for the chloro complexes, the emission is at best faint. The emission of the samples was studied in the solid state at ambient temperature using an integrating sphere to estimate photoluminescence quantum yields (Φ_{lum}) under continuous-wave excitation, whilst pulsed laser diode excitation was used to measure the luminescence lifetimes (τ) of the samples. The emission in dilute glassy solution at 77 K was also studied. Representative spectra are shown in Figures 17–19 with data summarized in **Table 3.3**. At room temperature in solution, only very weak emission is observed, at similar wavelengths to the free ligand. This weak emission is

therefore attributed to free ligand resulting from dissociation, in amounts barely perceptible by emission spectroscopy and unobservable by NMR spectroscopy.

Table 3. 3: Summary of photophysical data for **$(L1)_2Cu_2X_2$**, **$(L2)_2Cu_2X_2$** and **$(L3)_2Cu_2X_2$** [a]

Compound	Emission[b] λ_{max} / nm	Φ_{lum} x 10^2	τ / ns [c]	k_r / 10^3 s^{-1} [d]	k_{nr} / 10^5 s^{-1} [d]	Emission 77 K[e]	
						λ_{max} / nm	τ / ns
(L1)CuCl	682[f]	--[f]	150	--	--	[h]	[h]
(L1)CuBr	655	0.42	630	6.7	16	[h]	[h]
(L1)CuI	606	2.4	3200	7.5	3.1	622	81000
(L2)CuCl	679	0.14	240	5.8	42	636	91000
(L2)CuBr	655	0.70	810	8.6	12	660	38000
(L2)CuI	630	1.2	1000	12.0	9.9	656	34000
(L3)CuCl	--[g]	--[g]	--[g]	--	--	667	18000, 110000[i]
(L3)CuBr	691	0.05	250	2.0	40	690	15000
(L3)CuI	674	0.62	1000	6.2	9.9	687	18000

[a] Data are for solid state (powdered) samples except for 77 K data. [b] Room temperature, recorded using an integrating sphere and CCD detector; λ_{ex} = 425 nm. [c] λ_{ex} = 405 nm. [d] Radiative k_r and non-radiative k_{nr} rate constants as estimated from quantum yield and lifetime (see text). [e] In a glass of composition diethyl ether / isopentane / ethanol (2:2:1 v/v). [f] The intensity is weak and the spectrum of too poor quality to determine a reliable quantum yield. [g] Too weak for reliable spectra or lifetimes to be determined. [h] A good quality spectrum at 77 K could not be obtained for these samples, possibly due to poor solubility at low temperatures. [i] This sample showed biexponential decay kinetics, with relative weightings of 30:70.

A number of common features within the series, as well as several trends, emerge from these results:

(i) The emission maxima are in the red region of the spectrum, in the range 600–700 nm (**Figure 3.17**), much lower in energy than the lowest-energy absorption maxima. They have similar values in EPA glass at 77 K (**Figure 3.18**).

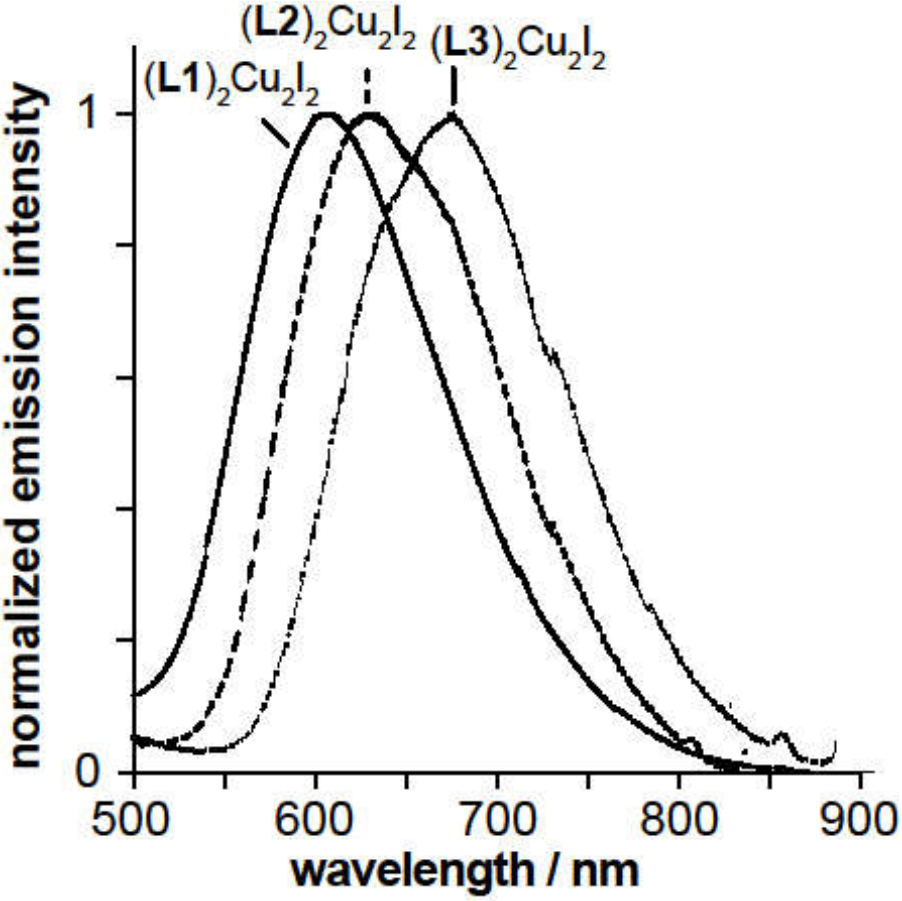

Figure 3. 17: Emission spectra of **(L1)CuI**, **(L2)CuI** and **(L3)CuI** in the solid state at 298 ± 3 K, λ_{ex} = 425 nm.

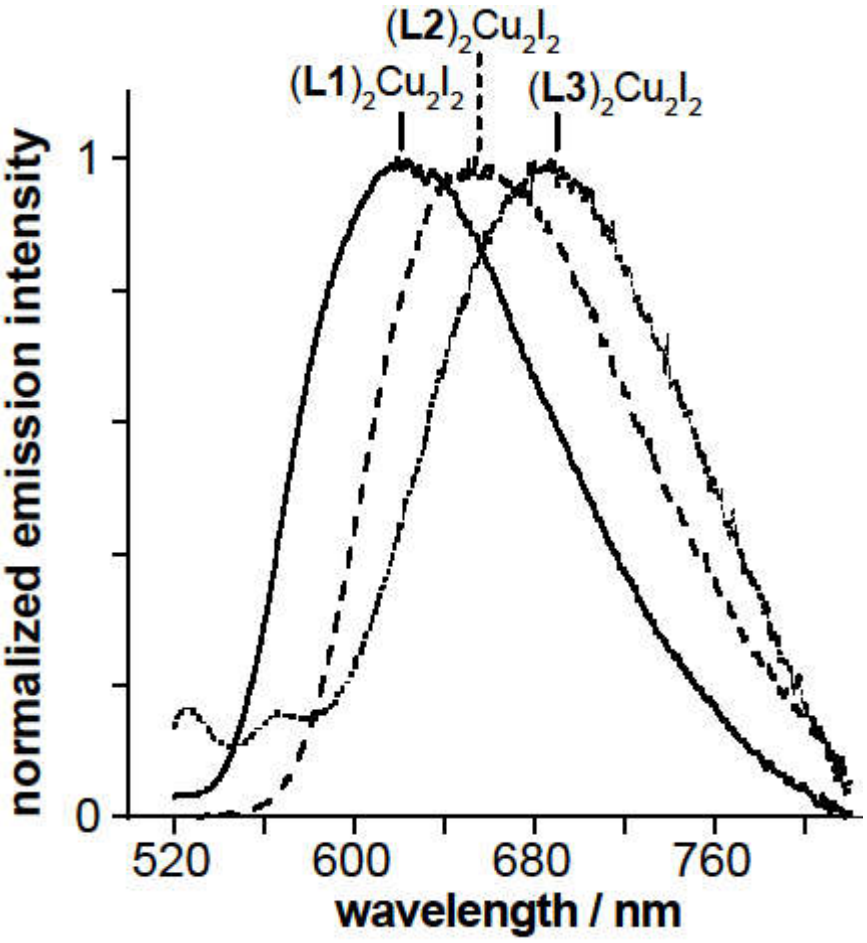

Figure 3. 18: Emission spectra of **(L1)CuI**, **(L2)CuI** and **(L3)CuI** in EPA glass at 77 K, λ_{ex} = 425 nm. EPA = diethyl ether / isopentane / ethanol (2:2:1 v/v).

(ii) The luminescence lifetimes are of the order of hundreds of nanoseconds to a few microseconds at room temperature, increasing to tens of microseconds in glassy solution at 77 K. Within each of the three series of complexes (**$(L1)_2Cu_2X_2$**, **$(L2)_2Cu_2X_2$** and **$(L3)_2Cu_2X_2$**), the emission energy decreases in the order I > Br > Cl (e.g., as shown for series **$(L2)_2Cu_2X_2$** in **Figure 3.19**).

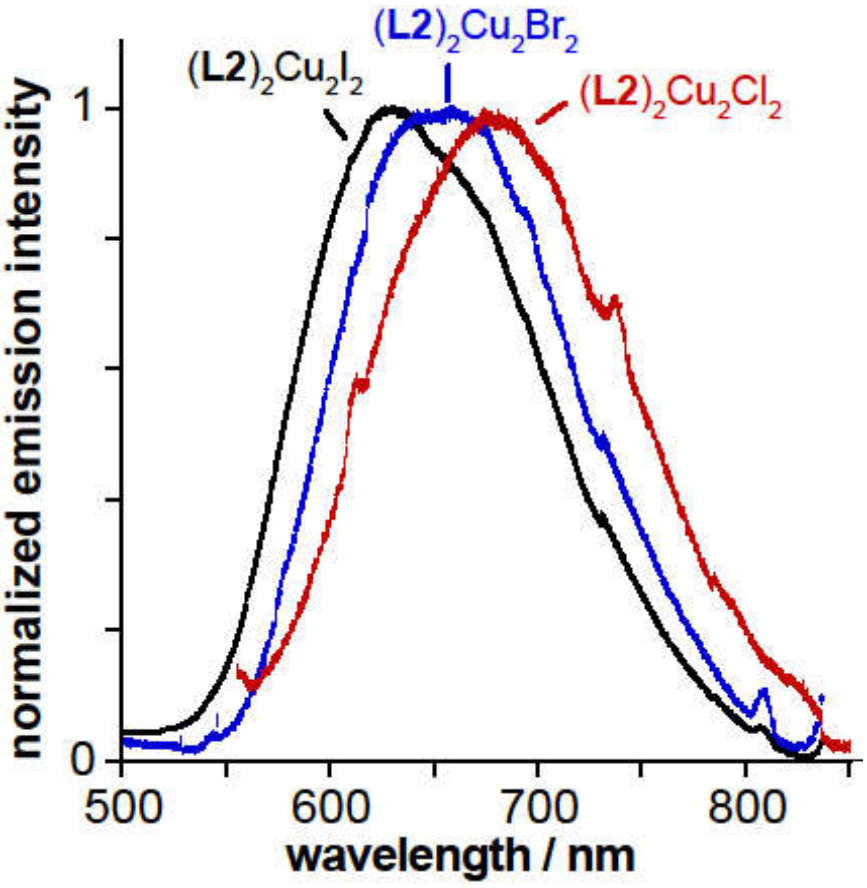

Figure 3. 19: Emission spectra of **(L2)CuCl**, **(L2)CuBr** and **(L2)CuI** in the solid state at 298 ± 3 K, λ_{ex} = 425 nm.

(iii) Within each of these three series of complexes, the iodo complexes are the brightest emitters in the solid state and the chloro the weakest; i.e., Φ_{lum} values decrease in the order I > Br > Cl. The values for the iodo complexes are of the order of 10^{-2}.

(iv) Similarly, within each of the three series of complexes, the luminescence lifetimes (τ) decrease in the order I > Br > Cl.

(v) Considering the effect of benzannulation, it can be seen from the series **(L1)CuI**, **(L2)CuI** and **(L3)CuI** that *a red shift is observed on going from the phenanthridine complexes to the corresponding quinoline complex, despite the more extended conjugation in the former* (**Figures**

3.17 and 3.18). The same is true for the series **(L1)CuBr**, **(L2)CuBr** and **(L3)CuBr** (and probably also for the chloro complexes, although the weakness of their emission and resulting poor spectra make the analysis unreliable).

Taken together, points (i) and (ii) strongly suggest that the emission emanates from an excited state of triplet character. The very large difference in energy between the lowest-energy absorption band and the emission band is typical of phosphorescence from a triplet state, formed indirectly following initial population of a spin-allowed singlet state through light absorption. The emission lifetimes are too long to be prompt fluorescence, but are typical of phosphorescence in which the spin selection rule has been somewhat relaxed through the effect of spin-orbit coupling. On the other hand, it is also possible that there is a thermally activated delayed fluorescence (TADF) component to the emission. As discussed in the introduction, some related Cu(I) complexes have small S_1–T_1 energy gaps, which allows thermal repopulation of the singlet state, leading to fluorescence but with a lifetime determined by that of the triplet state.[16] A shift in the emission maximum to lower energies upon cooling is typically a signature of TADF. For the current set of complexes, the lack of room temperature emission in solution prohibits a direct comparison of λ_{em} with that in the low-temperature glass. Use of the solid-state room temperature data has to be treated with caution, since packing effects can significantly influence the emission properties. Notwithstanding, it can be seen that the emission maxima of, for example, the iodo complexes are displaced to longer wavelengths at 77K, suggesting that TADF may possibly be involved at room temperature.

The observed decrease in the emission energy in the order I > Br > Cl, noted in point (iii), is consistent with the proposed $^3\{d_{Cu}/p_X \rightarrow \pi^*_{N\wedge P}\}$, or ^{3}(M+X)LCT, charge-transfer assignment: the HOMO will be highest in energy for X = Cl and lowest for X = I, according to the order of

ligand-field strengths of the halogens, Cl > Br > I. Such a trend has been observed previously in related halide-containing Cu(I) complexes.[24,25]

The observation that the most intense emitters (the iodo member of each family) are also the longest-lived suggests that differing rates of non-radiative decay processes may be key to the halide-dependent trends (iv) and (v). If one makes the assumption that the emitting state is formed with unitary efficiency, and therefore that the radiative rate constant $k_r = \Phi / \tau$, the values of k_r can be estimated from the experimentally-measured parameters, and hence also the rate constant of non-radiative decay processes $k_{nr} = (\tau^{-1} - k_r)$. The values thus calculated, where possible (**Table 3.3**), suggest that the trend to decreasing lifetimes and lower efficiencies in the order I > Br > Cl is due primarily to an increase in the rate of non-radiative decay k_{nr} in the order I < Br < Cl. Such an effect may in part be due to the decreasing excited state energy (lowest for chloro), in line with the so-called 'energy gap law'. Typically, for compounds with a common type of excited state and in the absence of deactivation processes involving higher-lying states, k_{nr} should increase as the excited state energy decreases, owing to the increased probability of intramolecular energy transfer into high-energy vibrational modes within the molecule. Detailed quantitative treatments indicate that a logarithmic dependence may be anticipated,[26] as observed in some classic studies with Ru(II) and Pt(II) complexes, for example.[27, 27, 28, 29, 30] In the present instance, a plot of $\{\ln k_{nr}\}$ versus the excited-state energy (estimated from λ_{max}) reveals a quite convincing linear relationship (**Figure 3.20**).

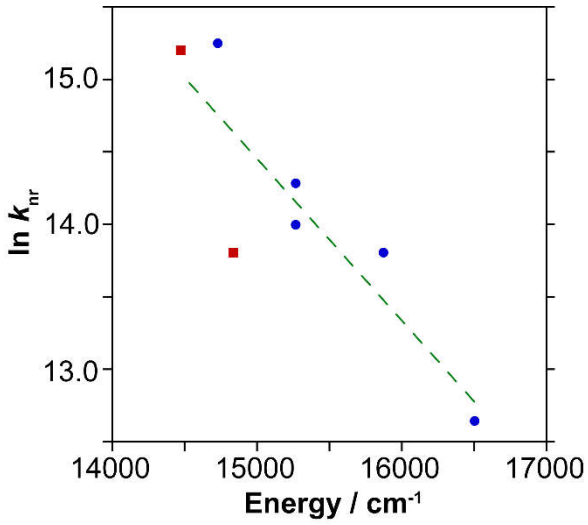

Figure 3. 20: Plot of ln k_{nr} versus the emission energy as estimated from λ_{max} in the solid-state spectra. Data points for phenanthridine complexes are shown as blue circles; quinoline complexes as red squares. The dashed green line is the best linear fit using *all* data points.

The rate constant data suggest that an additional contribution to the trend of more efficient emission for the iodo complexes arises from an increase in the k_r value in the order Cl < Br < I. Such a trend may be a reflection of the increasing spin-orbit coupling (SOC) constants in the same order. One caveat to this analysis is that I assume, as noted above, that the emitting state is formed with unitary efficiency in each case. This assumption relies on the rate constant of intersystem crossing (ISC) from the singlet manifold to the emissive triplet state being much faster than other deactivation pathways of the singlet. There is no evidence of any higher energy fluorescence emission in the spectra, and so the assumption may be a good approximation, but the higher SOC of iodine should also facilitate ISC. Previous work with dicopper(I)-NHC-picolyl complexes has indicated the potential importance of cuprophilic interactions in promoting phosphorescence through enhanced SOC.[30] However, the crystal structures of **(L2)CuI** and **(L3)CuI** have $d_{Cu–Cu}$ of 2.708 and 2.723 Å, respectively,

approximately 0.2 Å longer than in the dicopper(I)-NHC-picolyl complexes, and so such an effect is unlikely to play a significant role in the present complexes.

Finally, I turn to point (vi), namely the counter-intuitive observation that the quinoline complexes emit at lower energy than the phenanthridine analogues, despite the less extended π system, and contrary to the trend observed in absorption. Some insight into this trend can be gleaned from the corresponding ligands. As mentioned earlier, **L1** and **L2** display a series of lower-energy absorption bands than **L3**, indicating that the energy E_S of the lowest-lying *singlet* state of the phenanthridine ligands is lower than for the quinoline analog. This is reproduced in TD-DFT calculations of **(L2)CuI** and **(L3)CuI** (*vide infra*). The opposite conclusion, however, applies to the lowest-lying *triplet* states, again reproduced by TD-DFT. Inspection of the well-defined (0, 0) bands in the phosphorescence spectra of **L1** and 8-bromoquinoline (as a model for **L3**, which gave a less well-resolved spectrum) at 77 K reveals that their triplet energies E_T are approximately 21460 and 20940 cm^{-1} respectively (**Figure 3.21**).

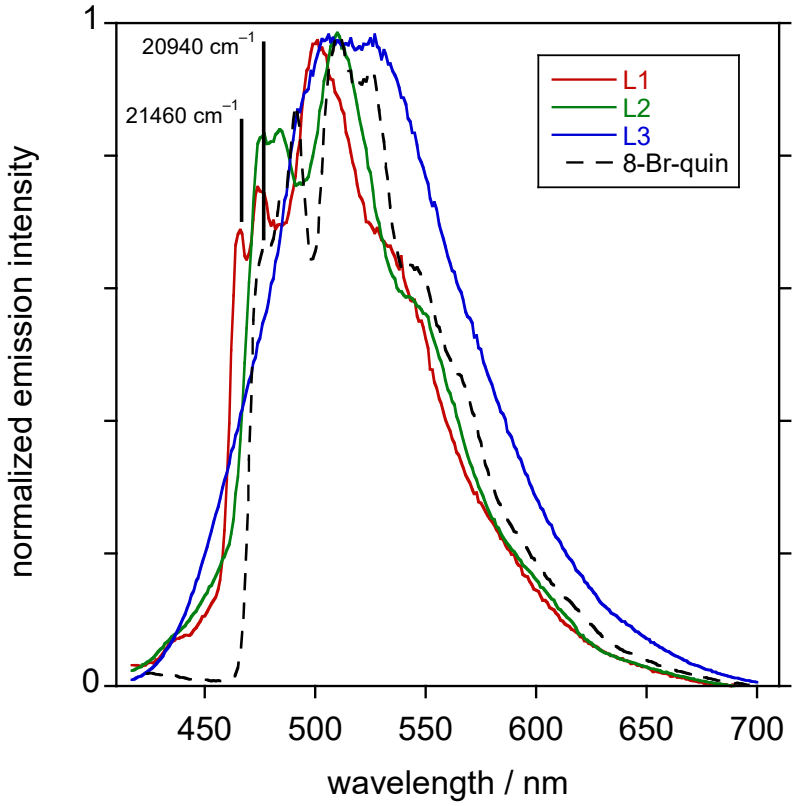

Figure 3. 21: Normalized phosphorescence spectra of **L1, L2** and **L3** in EPA at 77 K. Since **L3** does not give a well-resolved spectrum under these conditions, the spectrum of 8-bromoquinoline (as a model for an 8-substituted quinoline with no methyl groups) is also included to offer a direct comparison with **L1**. The vertical black lines indicate the respective positions of the (0,0) bands of L1 and 8-bromoquinoline, highlighting the lower energy of the quinoline phosphorescence.

Indeed, the same trend is observed in unsubstituted phenanthridine and quinoline: $E_T = 22050$ and 21850 cm^{-1} respectively; *cf.* $E_S = 28590$ and 31850 cm^{-1} respectively.[31, 32] Although I am not aware of any detailed theoretical studies into the trend in E_T versus E_S for such aromatics, there is some consensus in the literature that formation of the triplet state of arenes is accompanied by considerable distortion, for example in benzene, leading to D_{2h} symmetry where two C–C bonds are significantly lengthened relative to the ground state and four are shortened.[33,34,35,36] It then

becomes clear why benzannulation (as in phenanthridine versus quinoline) might *destabilize* the triplet state, since the electronically desirable distortion may be inhibited.

3.3.3. Density Functional Theory (DFT) and Time-Dependent (TD-DFT) calculations

To gain further insight into the electronic structure of the Cu_2X_2 complexes, DFT calculations were carried out at the B3LYP level of theory, focusing on the iodo complexes from which emission was observed to be strongest. As emission is only observed in the solid-state, the basis set was selected based on optimization of the calculated geometries to match the solid-state structures, focusing on bond lengths, angles and the conformation of the $Cu_2(\mu\text{-}I)_2$ core (diamond core vs. butterfly). The two conformers (diamond core vs. butterfly) of **(L3)CuI** are very close in energy, with the butterfly motif more stable by 1.4 kJ mol^{-1}. This suggests that both conformers can exist at room temperature in equilibrium. The extra stability in the butterfly structure could result from Cu···Cu orbital (d_z^2 and p_z) interactions modulated by several factors such as the nature of the *P^N* ligands, the bridging halides,[37,38] and also possibly from solvent interactions, as seen in the preference for butterfly structures upon solvent inclusion in the crystal lattice (see **Figure 3.10**). To directly elucidate the impact of benzannulation, I were most curious to compare complexes **(L2)CuI** and **(L3)CuI**, which differ by formal addition of a butadiene fragment at the 2,3-position of the quinolinyl moiety in **(L3)CuI**. Basis sets 6-31G(d,p) on H, C, N, P; m6-31G(d) on Cu; and LANL2DZ on halides were found to most closely reproduce parameters from the solid-structure of **(L3)CuI** (Table S1) and **(L2)CuI** (Table S2). MOs of both complexes were calculated, with isosurfaces of the frontier orbitals shown in **Figure 3.22**.

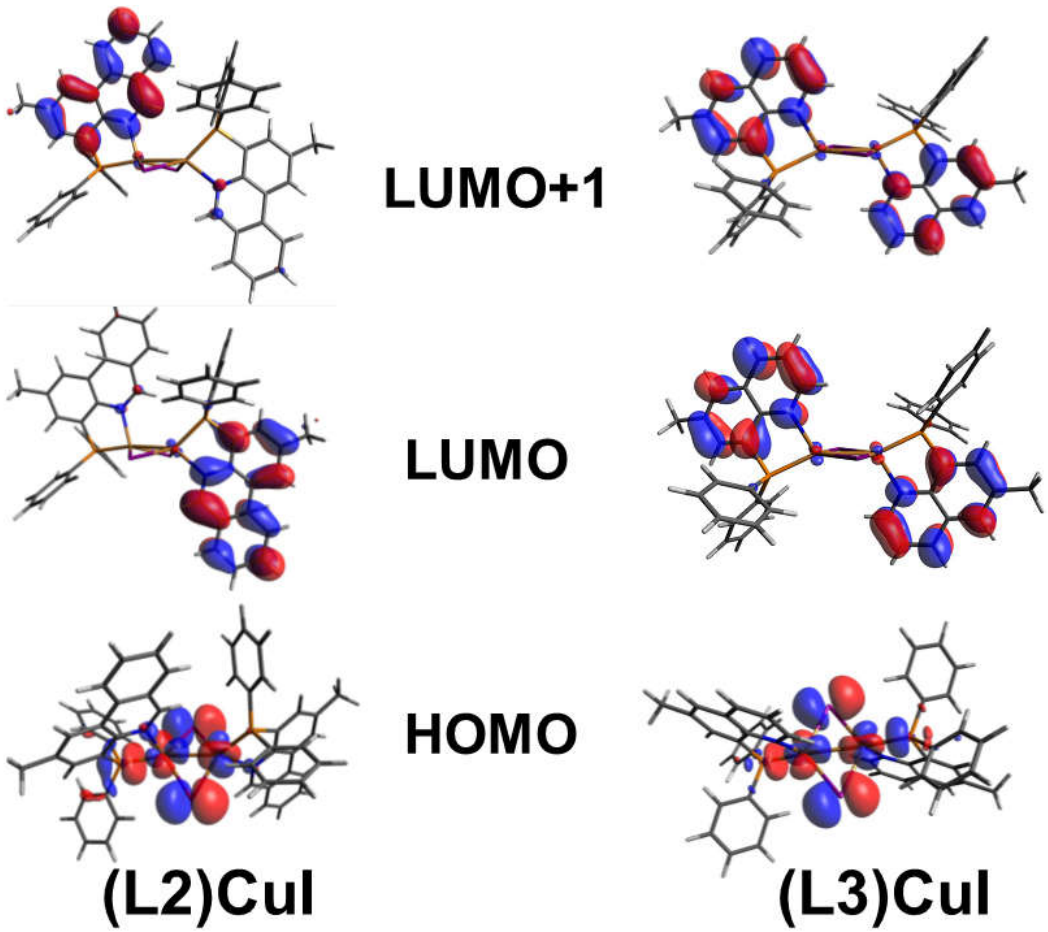

Figure 3. 22: HOMO, LUMO and LUMO+1 diagrams for **(L2)CuI** and **(L3)CuI** (isovalue = 0.03).

Contour curves of the frontier MOs for the optimized ground state geometry are consistent with related *P^N* supported Cu_2X_2 dimers.[22,23,39] The HOMOs of both **(L2)CuI** and **(L3)CuI** are composed mainly of metal and halide orbital contributions, with minor contributions from the phosphorus (**Table 3.4-3.6**). In the case of the planar diamond core of **(L3)CuI**, the Cu(I) centers equally contribute ~25% to the HOMO, while the iodides only contribute ~15% each. Minor contributions (~6% each) are also observed from both phosphorus centers. This is not the case for **(L2)CuI**, where for the asymmetric butterfly structure, one phosphorus contributes significantly more than the other to the HOMO (~1% vs 11%). Contributions from the two Cu atoms are also not the same (~20% vs. 33%).

Table 3. 4: Atomic contributions (Mulliken) to the HOMO of **(L2)CuI** and (L3)CuI (S_0).

	Cu1	**Cu2**	**I1**	**I2**	**P1**	**P2**	**Ph1**	**Ph2**	**N-hc1**[a]	**N-hc2**[a]
(L2)CuI	20.14	33.19	12.82	11.56	0.66	11.08	0.63	4.94	1.78	3.19
(L3)CuI	24.57	24.57	15.11	15.11	6.31	6.31	3.21	3.21	0.80	0.80

[a] *N*-hc = *N*-heterocyclic ligand backbone (i.e. Me-phen for **(L2)CuI** or Me-quin for **(L3)CuI**).

Table 3. 5: Atomic contributions (Mulliken) to the LUMO (TD-DFT) of **(L2)CuI** (S_1 state) and **(L3)CuI** (S_2 state) from the first allowed excited state.

	Cu1	**Cu2**	**I1**	**I2**	**P1**	**P2**	**Ph1**	**Ph2**	**N-hc1**[a]	**N-hc2**[a]
(L2)CuI (S_1)	1.45	0.89	0.02	0.13	0.53	0.13	2.88	0.13	89.33	4.50
(L3)CuI (S_2)	0.54	0.54	0.09	0.09	0.98	0.98	2.44	2.44	45.94	45.97

[a] *N*-hc = *N*-heterocyclic ligand backbone (i.e. Me-phen for **(L2)CuI** or Me-quin for **(L3)CuI**).

Table 3. 6: Atomic contributions (Mulliken) to the LUMO+1 (TD-DFT) of **(L2)CuI** (S_1 state) and **(L3)CuI** (S_2 state) from the first allowed excited state.

	Cu1	**Cu2**	**I1**	**I2**	**P1**	**P2**	**Ph1**	**Ph2**	**N-hc1**[a]	**N-hc2**[a]
(L2)CuI (S_1)	4.87	3.94	0.19	0.01	0.27	0.62	2.88	0.13	0.13	83.09
(L3)CuI (S_2)	2.52	2.52	0.12	0.12	0.76	0.76	2.26	2.26	44.35	44.32

[a] *N*-hc = N-heterocyclic ligand backbone (i.e. Me-Phenan for **(L2)CuI** or Me-quin for **(L3)CuI**).

The asymmetry in the atomic contributions likely results from the puckering of the molecule to the butterfly structure that is observed in the solid state. Similar to pyridinyl

analogs,[22,23,39] the LUMO/LUMO+1 of **(L2)CuI** and **(L3)CuI** are both localized on the aromatic *N*-heterocyclic quinoline or phenanthridine moieties. For **(L3)CuI**, these two virtual orbitals are the in-phase and out-of-phase combinations of the π* orbital framework of the two quinoline arms. In the non-centrosymmetric **(L2)CuI**, the LUMO is calculated to represent one phenanthridine ligand arm π* orbital framework and the LUMO+1 the other, with the LUMO-containing phenanthridine ligand arm closer to the Cu_2I_2 core.

TD-DFT calculations for both **(L2)CuI** and **(L3)CuI** reveal that the transitions with the largest oscillator strengths in the low-energy region of the calculated absorption spectra have either LUMO←HOMO (**(L2)CuI**: transition 3, 69%) or LUMO+1←HOMO (**(L3)CuI**: transition 2, 49%) character. The calculated HOMOs for both **(L2)CuI** and **(L3)CuI** are localized almost entirely on the Cu_2X_2 cores, while the LUMO for **(L2)CuI** and LUMO+1 for **(L3)CuI** are composed of the *N*-heterocycle π* orbitals of either the phenanthridinyl or quinolinyl moieties, supporting the (d_{Cu}+p_{halide})-to-π* charge-transfer assignment to the low energy transitions.

Comparing the frontier MO energies (**Table 3.7**), the HOMO and LUMO of **(L2)CuI** are both destabilized from their positions in the smaller **(L3)CuI**, but the occupied MO only to a small extent. The LUMO destabilization is mirrored in the electrochemistry of **$(L2)_2Cu_2X_2$** and **$(L3)_2Cu_2X_2$** . While the reduction of these compounds is irreversible, the LUMO energy can be estimated by the relative peak on-set ($E_{red,onset}$) which, for example, is shifted cathodically for **(L2)CuBr** ($E_{red,onset}$ ~ -2.1 V vs $FcH^{0/+}$) compared with **(L3)CuBr** ($E_{red,onset}$ ~ -2.0 V; **Figure 3.23**).

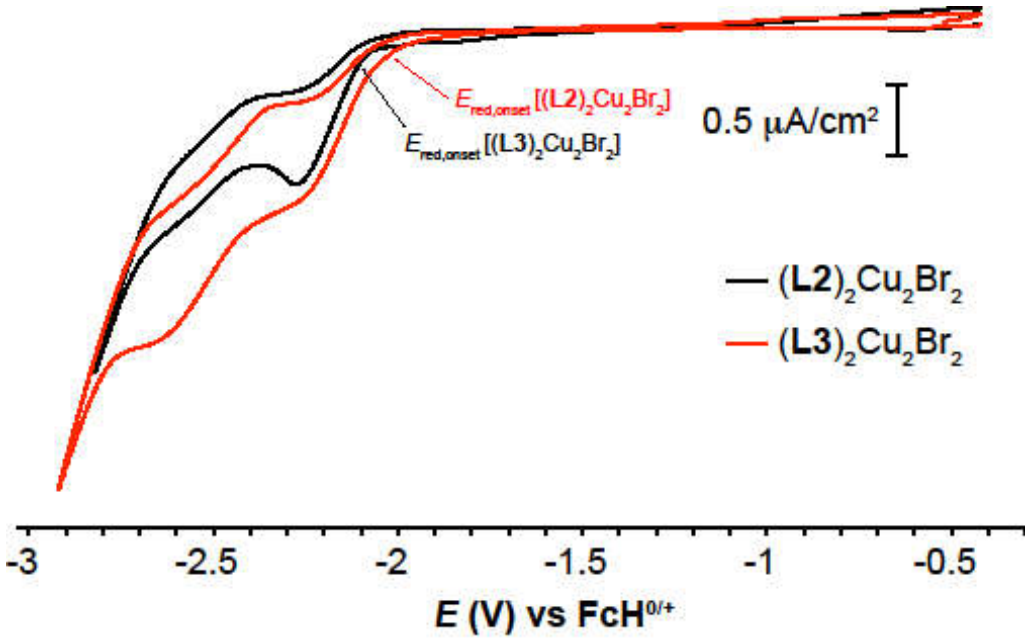

Figure 3. 23: Cyclic voltammograms showing reduction of **(L2)CuBr** and **(L3)CuBr** ([analyte] = 1.1 mM; 0.076 M [*n*Bu$_4$N][PF$_6$], 100 mV/s scan rate).

In their analysis of Pt(II) complexes with bis(2-pyridylimino)isoindole (BPI) and benzannulated ligand analogs, Hanson *et al.* noted that the HOMO of a 1,3-butadiene fragment has appropriate symmetry to act as an effective electron-donating group to the LUMO of the isoindole of BPI, and that the destabilization is due largely to this effect on the LUMO, as opposed to a significant influence on the HOMO.[7] The orbital contributions to the frontier orbitals of **(L3)CuI** (**Figure 3.22**) similarly reveal that the LUMO/LUMO+1 (but not the HOMO) present lobal density of the appropriate symmetry at the site of benzannulation to interact with the HOMO of a 1,3-butadiene moiety.

This results in an increase in the calculated HOMO-LUMO gap, which does not by itself explain the appearance of additional low energy absorptions in the experimental UV-Vis spectrum. As noted earlier, the additional low energy bands in the phenanthridine-containing systems are associated with the phenanthridine unit itself. The lowest-energy bands that

contribute to the long wavelength tail are presumably CT bands, with orbital parentage. However, as these bands form a long, unresolved tail, I hesitate to precisely compare the band positions of these lowest energy absorptions. Comparing the energies of the lowest lying singlet states obtained from the TD-DFT calculations, as predicted from the absorption spectra, the energy of the lowest lying singlet state, $E(S_1)$, for **(L2)CuI**, which boasts a larger π system, was calculated to be *lower* than the corresponding $E(S_1)$ for the quinoline congener **(L3)CuI**. The geometry of each ground state was then re-optimized as a triplet to give the geometry and free energy of the lowest lying triplet states (T_1). As observed in the emission spectra, the energy of the lowest-lying triplet states, $E(T_1)$, was found to be lower for **(L3)CuI**, in contradiction to the ordering of $E(S_1)$ (**Figure 3.24**).

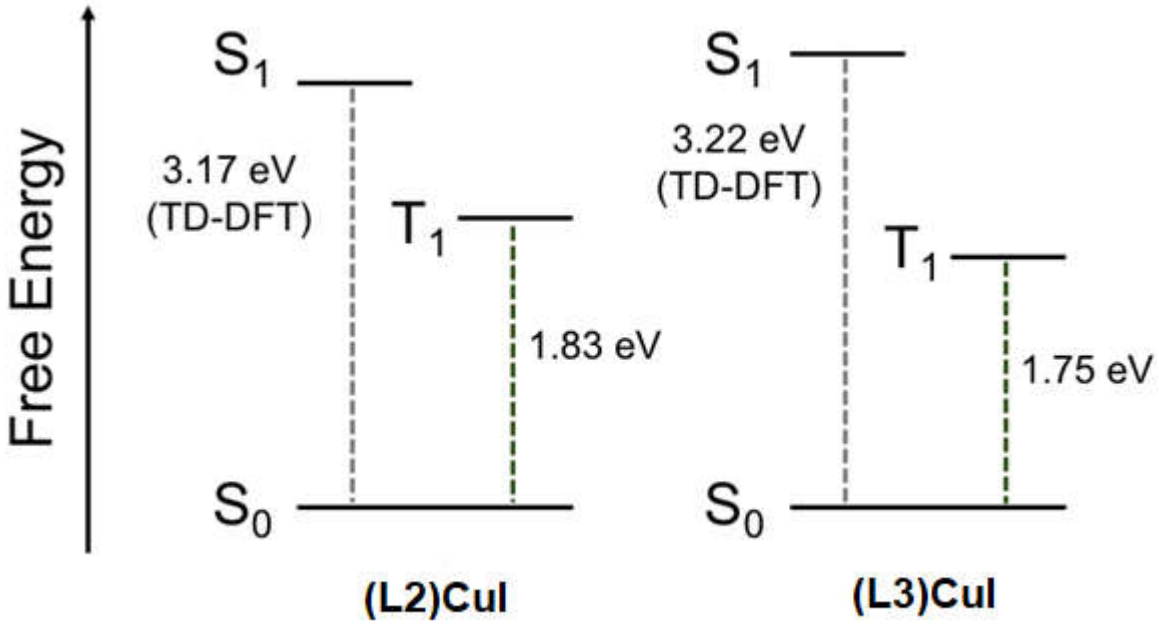

Figure 3. 24: Comparison of the relative energies of the first triplet excited states of **(L2)CuI** and **(L3)CuI**. The $S_0 \rightarrow S_1$ energies were obtained from TD-DFT calculations, while $T_1 \rightarrow S_0$ energies were estimated from the difference of the sum of electronic and thermal free energies (frequency calculation) of the T_1 and S_0 states.

Table 3. 7: Calculated orbital energies for **(L2)CuI** and **(L3)CuI**[a]

Complex	E(HOMO)/eV	E(LUMO)/eV	E(LUMO+1)/eV	$\Delta E_{HOMO-LUMO}$ /eV	$\Delta E_{HOMO-LUMO+1}$ /eV
(L2)CuI	-5.828	-0.530	-0.523	5.298	5.305
(L3)CuI	-5.828	-0.513	-0.480	5.315	5.348

[a] TD-DFT: CAM-B3LYP/6-31G(d,p) on H, C, N, P; m6-31G(d) on Cu; and LANL2DZ on I

While it is not possible to say whether the trend of an increasing gap between the frontier orbitals is reflected in the absorption spectra, owing to the weak and broad nature of the long wavelength absorption tails to which the CT bands probably contribute, it is clear that the calculated trend *is* reproduced in the emission maxima of the complexes (*vide supra,* **Figure 3.18**). TD-DFT analysis revealed that, as observed for the proligands **L2** and **L3**, while the lowest lying singlet state of the phenanthridine-containing complex **(L2)CuI** is lower in energy than for the more compact π-system of the quinoline-containing **(L3)CuI**, the opposite is true for the lowest lying *triplet* states (**Figure 3.24**). Thus, **(L2)CuI** is calculated to have a larger singlet-triplet gap and a higher energy emission maximum, despite an increase in conjugation compared with **(L3)CuI**.

Comparing the optimized geometries of the ground state (S_0) and first excited triplet state (T_1) of **(L2)CuI** and **(L3)CuI** reveals structural changes that accompany emission (**Figure 3.27**). The root-mean-squared deviations, calculated from overlaying the optimized S_0 and T_1 structures (**(L2)CuI**: 1.321 Å, **(L3)CuI**: 1.551; **Figure 3.25**), are consistent with bigger structural differences for the smaller quinolinyl-based system. In both ground-state structures, the two Cu centers are found in approximate trigonal pyramidal environments, with nearly identical τ_4 indices (a useful geometric parameter for evaluating the geometry of four-coordinate complexes[40]) of 0.86/0.87 (**(L2)CuI**) and 0.86/0.86 (**(L3)CuI**) representative of tetrahedral

geometries distorted towards trigonal pyramidal environments; a τ_4 value of 1.00 represents an ideal tetrahedral geometry, while 0.00 represents a square-planar environment and 0.85 a trigonal pyramidal (C_{3v}) setting.[40] In their T_1 excited states, the Cu centers in both complexes experience nearly identical "rocking" distortions[41] towards see-saw-like (C_{2v}) geometries as the Cu_2I_2 core becomes increasingly bent (τ_4 in T_1 geometries **(L2)CuI**: 0.66/0.80; **(L3)CuI**: 0.66/0.80). Thus, the more significant ground-state/excited-state (GS-ES) geometrical distortion for **(L3)CuI** is not rooted in changes to the bond angles and coordination geometry around copper. Changes observed in the Cu-Cu and I-I bond distances are different, with a contraction of 0.08 Å and 0.38 Å, respectively, as **(L3)CuI** puckers into a butterfly structure in the T_1 state, with significant canting of the *P^N* ligand units with respect to one another. In comparison, the Cu-Cu and I-I distances in **(L2)CuI** contract to a smaller degree (0.04 Å and 0.32 Å, respectively), as the optimized ground-state geometry of **(L2)CuI** is already bent into a butterfly-type structure.

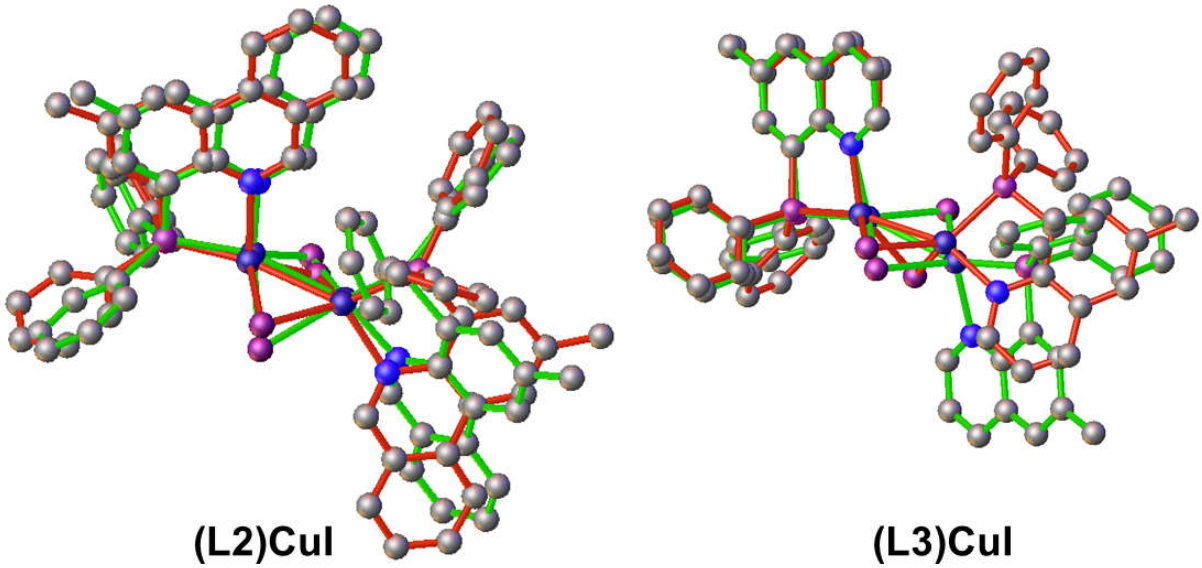

Figure 3. 25: Overlay of optimized ground state (S_0, green) and excited state (T_1, red) geometries of **(L2)CuI** and **(L3)CuI**.

The different extent of change to the relative orientation of the two *P^N* ligands in **(L3)CuI** vs **(L2)CuI** can be quantified by comparing the bond angles P1-Cu1-Cu2/Cu1-Cu2-P2 (S_0: 153.9/153.9; T_1: 163.3/116.0) and N1-Cu1-Cu2/Cu1-Cu2-N2 (S_0: 122.5/122.5; T_1: 111.0/156.2); these change by 38°/9° and 34°/13°, respectively, which represent significant GS-ES perturbations for **(L3)CuI**. In comparison, the same angles in **(L2)CuI** are distorted to a much smaller extent, 19°/6° and 14°/5°, respectively (P1-Cu1-Cu2/Cu1-Cu2-P2 S_0: 169.5/134.4; T_1: 163.1/115.1 and N1-Cu1-Cu2/Cu1-Cu2-N2 S_0: 142.2/106.9; T_1: 112.2/156.6). Thus, the ability of the phenanthridinyl *P^N* ligand to resist reorientation in **(L2)CuI** compared to **(L3)CuI** appears to play a role in limiting distortion in the excited state. Looking more closely at the *N*-heterocyclic moieties, the C_5N sub-unit in the quinolinyl moiety in **(L3)CuI** is observed to distort significantly compared with the benzannulated C_5N sub-unit in the phenanthridinyl moiety of the ligand in **(L2)CuI** (**Figure 3.26**).

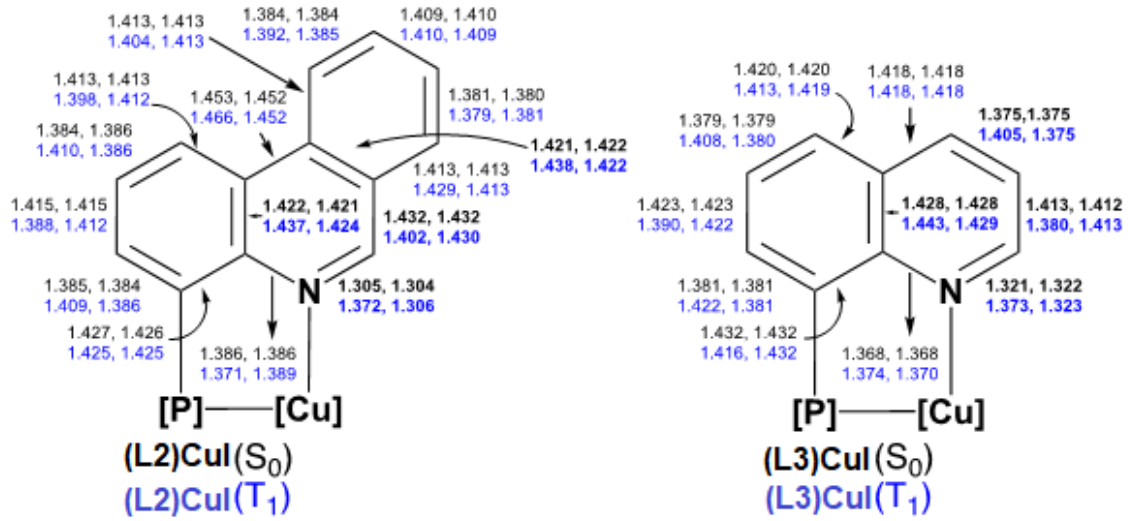

Figure 3. 26: Comparison of bond distances within the quinolinyl and phenanthridinyl moieties of (L2)CuI and (L3)CuI in the DFT-optimized ground state (S_0) and first excited triplet state (T_1) structures. The pyridine sub-units are highlighted in bold.

As noted for the aromatic *N*-heterocycles themselves, the higher energy triplet state of **(L2)CuI** is also likely due to inhibition of the electronically desirable distortion for **(L2)CuI** compared with **(L3)CuI**. A similar observation has been made for cyclometallated Pt complexes with extended π-systems.[5] In that work, the extent of π-conjugation in aromatic *C^N* ligand was found to also *not* correspond with the observed trends in emission energies, and was rationalized in terms of structural distortions that occur upon cyclometalation matching distortions that stabilized the molecules' triplet states. While the energy cost of geometry relaxation of the T_1 state to the S_0 state has been previously estimated by calculating the corresponding relaxation energy (λ_T),[42] the λ_T values calculated for **(L2)CuI** (0.390 eV) and **(L3)CuI** (0.391 eV), are very similar. Nevertheless, the observed and measurable geometric changes are consistent with the phenanthridinyl *P^N* ligands enforcing an excited state geometry more similar to the ground state geometry in **(L2)CuI** than for the smaller quinolinyl analogs **(L3)CuI**, with a commensurately smaller resulting apparent Stokes shift.

Table 3. 8: Calculated photophysical parameters for **(L2)CuI** and **(L3)CuI**.

E (eV)	**(L2)CuI**	**(L3)CuI**
E^{adia}	1.909	1.801
$E^{vert\text{-}abs}$	3.166	3.218
$E^{vert\text{-}phos}$	1.519	1.410
λ_T	0.390	0.391

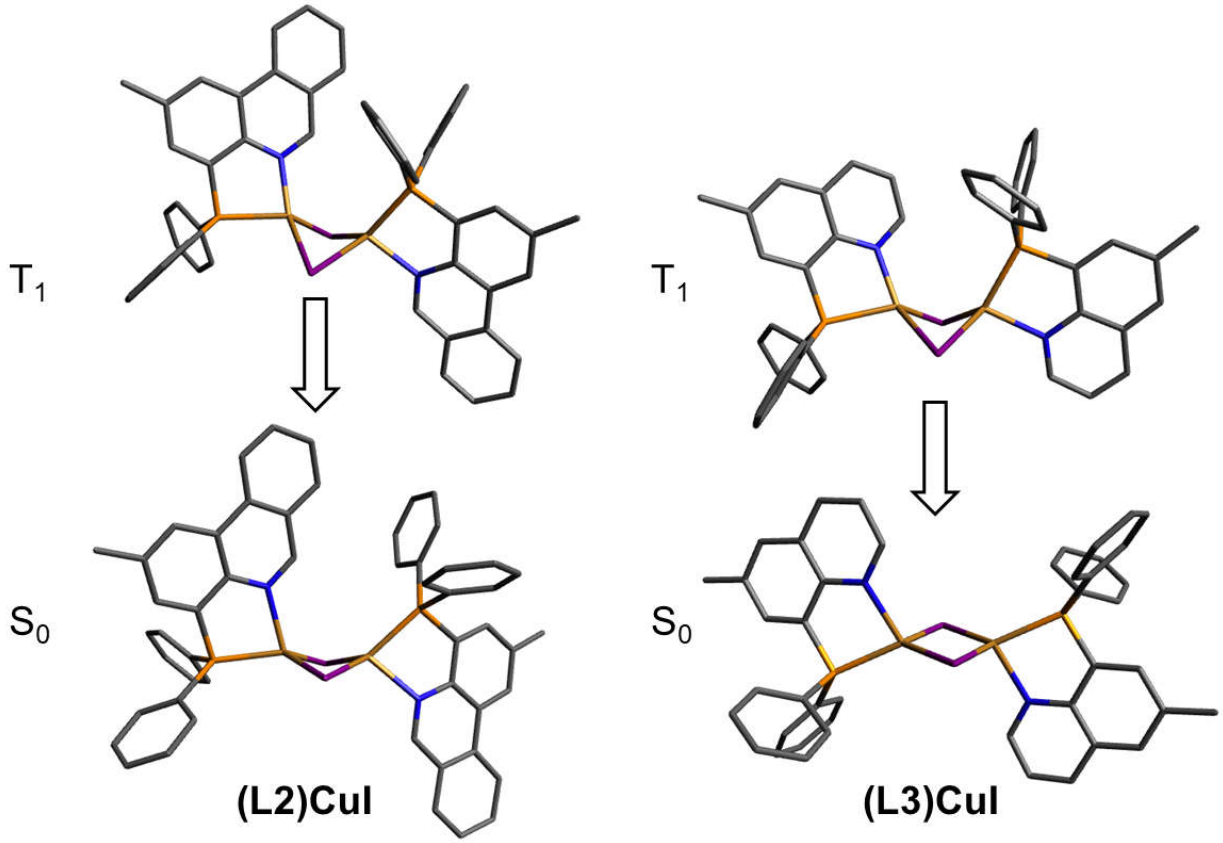

Figure 3. 27: Comparison of optimized structures for T_1 and S_0 states of **(L2)CuI** and **(L3)CuI**.

3.4. Conclusion

The design of new emissive molecules based on relatively low-cost copper is an important target in sustainable materials chemistry.[43,44,45,46] To fully realize the potential of luminescent Cu coordination complexes, the ability to tune emission wavelengths based on molecular structure is critical. While ligand benzannulation and the resulting extension of a molecule's π-system is often used to red-shift absorption and emission,[6] understanding the mechanism underlying changes in a molecule's electronic structure both in the ground state and excited (emissive) states can allow for both red and blue shifts.[5,7] Despite appearing to represent a simple extension of a quinoline π system, the incorporation of phenanthridine (3,4-

benzoquinoline) into ligand frameworks results in a counter-intuitive blue shift of emission maximum, assigned as phosphorescence from metal-affected, ligand-centered triplet states. The asymmetry of benzannulation in phenanthridine both renders it a more potent and less sterically encumbered donor, and in this case, results in a destabilization of the emissive triplet state relative to the more compact π system of the quinoline derivative that can be traced back to the reluctance of the phenanthridinyl *P^N* ligand to undergo as sizeable a ground-state/excited-state distortion compared with the smaller quinoline analogs.

3.5. Experimental Section:

Unless otherwise stated, all air sensitive manipulations were carried out inside an inert-atmosphere glove box (N_2) or using standard Schlenk techniques (Ar). 2,6-Dibromoaniline (AK Scientific), *N*-iodosuccinimide (AK Scientific), *p*-toluidine (Alfa Aesar), *N*-bromosuccinimide (Alpha Aesar), 2-formylphenyl boronic acid (Combi Blocks), $Pd(PPh_3)_4$ (Alfa Aesar), Na_2CO_3 (Alfa Aesar), chlorodiphenylphosphine (VWR), CuBr (Aldrich), CuI (Aldrich) and CuCl (Acros) were purchased from commercial suppliers and used as received. (L2)CuBromo-4-methylaniline,[47] 6-bromo-(L2)CuIodo-4-methylaniline,[9] 4-bromo-2-methylphenanthridine,[9] 8-bromo-6-methylquinoline,[47] and 4-diphenylphosphinophenanthridine[8] (**L1**) were synthesized following published procedures. Organic solvents were dried over appropriate reagents and deoxygenated prior to use, with the exception of 1,2-dimethoxyethane and water, which were simply degassed. NMR spectra were recorded on a Bruker Avance 300 MHz or Bruker Avance-III 500 MHz spectrometer as noted. Elemental analyses were performed by Canadian Microanalytical Service Ltd., Delta, BC (Canada).

General synthesis of Cu_2X_2 complexes:

All halide-bridged Cu(I) complexes were prepared via an analogous procedure : a solution of **L1**, **L2** or **L3** (0.063 mmol) in DCM (3 mL) was added drop-wise to a stirring suspension of CuX (0.063 mmol) in DCM (3mL). The reaction mixture was stirred overnight at room temperature. The solution was then filtered through a small plug of Celite and solid material was obtained via crystallization following slow diffusion of hexane into a dichloromethane solution. For **$(L3)_2Cu_2X_2$** , single crystals suitable for X-ray diffraction were obtained via slow diffusion of diethylether into CH_2Cl_2 solutions of the complexes.

Complexes (**L1)CuI**, **(L2)CuI** and **(L3)CuI** were also prepared by grinding together the appropriate ligand and CuX precursor together with five drops of CH_3CN in a porcelain mortar and pestle, following a published procedure.[18] Specifically, solid **L1**, **L2** or **L3** (0.063 mmol) and CuI (0.063 mmol) were placed in the mortar and five drops of CH_3CN were added and the mixture was thoroughly ground with a pestle for 5 min, at which time the color of the mixture could be clearly seen to change (**Figure 3.3**). The solid was scraped from the mortar, dried under vacuum and ^1H and ^{31}P NMR spectra were collected. The NMR spectra were identical to those obtained from solution state reactions (see **Figures 3.4-3.9**).

(L1)CuCl: Orange-red crystals. Yield = 0.026 g (89%). ^1H NMR ($CDCl_3$, 500 MHz, 22 °C): δ 9.05 (v br, 1H, $^{phen}C_{Ar}$-*H*), 8.83 (br, J_{HH}= 5 Hz, 1H, $^{phen}C_{Ar}$-*H*), 8.69 (br, J_{HH}= 10 Hz, 1H, $^{phen}C_{Ar}$-*H*), 7.99 (m, 1H, $^{phen}C_{Ar}$-*H*), 7.87 (m, 2H, $^{phen}C_{Ar}$-*H*), 7.76-7.71 (m, 2H, $^{phen}C_{Ar}$-*H*), 7.52-7.49 (overlapped m, 4H, PC_{Ar}-*H*), 7.44-7.41 (m, 2H, PC_{Ar}-*H*), 7.36-7.33 ppm (overlapped m, 4H, PC_{Ar}-*H*). ^{13}C NMR ($CDCl_3$, 126 MHz, 22 °C): δ 156.9 ($^{phen}C_{Ar}$H), 145.3 (d, J_{CP} = 16 Hz,

$^{phen}C_{Ar}$), 135.9 ($^{phen}C_{Ar}H$), 133.5 (d, J_{CP} = 15 Hz, P$C_{Ar}H$), 133.3 ($^{phen}C_{Ar}$), 132.8 ($^{phen}C_{Ar}H$), 131.6 (d, J_{CP} = 31 Hz, PC_{Ar}), 130.4 (P$C_{Ar}H$), 129.9 ($^{phen}C_{Ar}H$), 129.3 (br, J_{CP} = 10 Hz, P$C_{Ar}H$), 129.0 ($^{phen}C_{Ar}H$), 128.3 (br, J_{CP} = 5 Hz, $^{phen}C_{Ar}H$), 126.6 ($^{phen}C_{Ar}$), 125.9 ($^{phen}C_{Ar}H$), 125.6 ($^{phen}C_{Ar}$), 122.4 ppm ($^{phen}C_{Ar}H$). $^{31}P\{^{1}H\}$ NMR ($CDCl_3$, 202 MHz, 22 °C): δ -17.9 ppm (br, s). Anal. Calc. for $C_{50}H_{36}N_2P_2Cu_2Cl_2$**.**(0.5 CH_2Cl_2): C, 60.67; H, 3.79. Found: C, 60.90; H, 3.90.

(L1)CuI: Yellow crystals. Yield = 0.029 g (84%). ^{1}H NMR ($CDCl_3$, 500 MHz, 22 °C): δ 9.88 (s, 1H, $^{phen}C_{Ar}$-*H*), 8.68 (d, J_{HH} = 10 Hz, 1H, $^{phen}C_{Ar}$-*H*), 8.60 (d, J_{HH} = 10 Hz, 1H, $^{phen}C_{Ar}$-*H*), 7.89 (m, 1H, $^{phen}C_{Ar}$-*H*), 7.77-7.70 (overlapped m, 3H, $^{phen}C_{Ar}$-*H*), 7.66-7.61 (overlapped m, 5H, $^{phen}C_{Ar}$-*H*, PC_{Ar}-*H*), 7.36-7.28 ppm (overlapped m, 6H, PC_{Ar}-*H*). $^{13}C\{^{1}H\}$ NMR ($CDCl_3$, 126 MHz, 22 °C): δ 156.3 (d, J_{CP} = 4 Hz, $^{phen}C_{Ar}H$), 145.2 (d, J_{CP} = 18 Hz, $^{phen}C_{Ar}$), 135.8 ($^{phen}C_{Ar}H$), 134.1 (d, J_{CP} = 16 Hz, P$C_{Ar}H$), 133.4 ($^{phen}C_{Ar}$), 133.2 ($^{phen}C_{Ar}$), 132.8 ($^{phen}C_{Ar}$), 132.3 ($^{phen}C_{Ar}H$), 129.7 (P$C_{Ar}H$), 129.6 ($^{phen}C_{Ar}H$), 128.7 (d, J_{CP} = 10 Hz, P$C_{Ar}H$), 128.4 ($^{phen}C_{Ar}H$), 127.4 (d, J_{CP} = 4 Hz, $^{phen}C_{Ar}H$), 127.0 (br, J_{CP} = 3 Hz, $^{phen}C_{Ar}$), 125.2 (br, J_{CP} = 4 Hz, $^{phen}C_{Ar}H$), 124.9 ($^{phen}C_{Ar}$), 122.1 ppm ($^{phen}C_{Ar}H$). $^{31}P\{^{1}H\}$ NMR ($CDCl_3$, 202 MHz, 22 °C): δ -28.3 ppm (br, s). Anal. Calc. for $C_{50}H_{36}N_2P_2Cu_2I_2$•($CH_2Cl_2$): C, 51.36; H, 3.21. Found: C, 51.70; H, 2.85.

(L2)CuCl: Orange-red crystals. Yield = 0.022 g (74%). ^{1}H NMR ($CDCl_3$, 300 MHz, 22 °C): δ 8.83 (br, 1H, $^{phen}C_{Ar}$-H C_6-*H*), 8.69 (d, J_{HH} = 8.3 Hz, 1H, $^{phen}C_{Ar}$-*H*), 8.63 (s, 1H, $^{phen}C_{Ar}$-*H*), 8.01-7.96 (m, 1H, $^{phen}C_{Ar}$-*H*), 7.75 -7.66 (m, J_{HH} = 5.5, 4.5 Hz, 3H, $^{phen}C_{Ar}$-*H*), 7.50 – 7.42 (overlapped m, 6H, PC_{Ar}-*H*), 7.38 – 7.33 (overlapped m, 4H, PC_{Ar}-*H*), 2.66 ppm (s, 3H, C_{Me}-*H*). $^{13}C\{^{1}H\}$ NMR ($CDCl_3$, 126 MHz, 22 °C): δ 155.1 ($^{phen}C_{Ar}H$), 143.8 (d, J_{CP} = 17 Hz, $^{phen}C_{Ar}$), 138.8 ($^{phen}C_{Ar}H$), 137.2 ($^{phen}C_{Ar}$), 133.4 (br, J_{CP} = 15 Hz, P$C_{Ar}H$), 133.2 ($^{phen}C_{Ar}$), 132.5 ($^{phen}C_{Ar}H$), 131.4 (d, J_{CP} = 30 Hz, PC_{Ar}), 130.5 (P$C_{Ar}H$), 129.7 ($^{phen}C_{Ar}H$), 129.2 (d, J_{CP} = 8 Hz,

PC_{Ar}H), 128.9 ($^{phen}C_{Ar}$H), 126.5 ($^{phen}C_{Ar}$H), 125.9 ($^{phen}C_{Ar}$), 125.5 ($^{phen}C_{Ar}$H), 122.4 ($^{phen}C_{Ar}$H), 22.2 ppm (C_{Me}). $^{31}P\{^{1}H\}$ NMR ($CDCl_3$, 121 MHz, 22 °C): δ -17.2 ppm (br, s). Anal. Calc. for $C_{52}H_{40}N_2P_2Cu_2Cl_2$: C, 65.55; H, 4.23. Found: C, 65.02; H, 4.27.

(L2)CuBr: Orange crystals. Yield = 0.026 g (81%). ^{1}H NMR ($CDCl_3$, 500 MHz, 22 °C): δ 9.36 (br s, 1H, $^{phen}C_{Ar}$-H), 8.61 (d, J_{HH} = 8.6 Hz, 1H, $^{phen}C_{Ar}$-*H*), 8.52 (s, 1H, $^{phen}C_{Ar}$-*H*), 7.92-7.89 (m, 1H, $^{phen}C_{Ar}$-*H*), 7.73 (d, J_{HH} = 7.8 Hz, 1H, $^{phen}C_{Ar}$-*H*), 7.67 – 7.55 (overlapped m, 6H, $^{phen}C_{Ar}$-*H,* PC_{Ar}-*H*), 7.41 – 7.32 (overlapped m, 6H, PC_{Ar}-*H*), 2.62 ppm (s, 3H, C_{Me}-*H*). $^{13}C\{^{1}H\}$ NMR ($CDCl_3$, 126 MHz, 22 °C): δ 154.9 ($^{phen}C_{Ar}$H), 143.7 (d, J_{CP} = 17 Hz, $^{phen}C_{Ar}$), 137.9 (br, $^{phen}C_{Ar}$H), 136.9 ($^{phen}C_{Ar}$), 133.8 (d, J_{CP} = 15 Hz, PC_{Ar}H), 132.5 (d, J_{CP} = 5 Hz, $^{phen}C_{Ar}$H), 132.3 (br, $^{phen}C_{Ar}$), 130.1 (PC_{Ar}H), 129.8 ($^{phen}C_{Ar}$H), 129.0 (br, J_{CP} = 10 Hz, PC_{Ar}H), 128.6 ($^{phen}C_{Ar}$H), 126.8 ($^{phen}C_{Ar}$), 125.3 ($^{phen}C_{Ar}$), 125.2 (d, J_{CP} = 4 Hz, $^{phen}C_{Ar}$H), 122.2 ($^{phen}C_{Ar}$H), 22.2 ppm (C_{Me}). $^{31}P\{^{1}H\}$ NMR ($CDCl_3$, 121 MHz, 22 °C): δ -22.5 ppm (br, s). Anal. Calc. for $C_{52}H_{40}N_2P_2Cu_2Br_2$: C, 59.95; H, 3.87. Found: C, 59.92; H, 3.90.

(L2)CuI: Yellow crystals. Yield = 0.024 g (68%). ^{1}H NMR ($CDCl_3$, 300 MHz, 22 °C): δ 9.75 (s, 1H, $^{phen}C_{Ar}$-*H*), 8.60 (d, J_{HH} = 9 Hz, 1H, $^{phen}C_{Ar}$-*H*), 8.47 (s, 1H, $^{phen}C_{Ar}$-*H*), 7.91-7.86 (m, 1H, $^{phen}C_{Ar}$-*H*), 7.75 (d, J_{HH} = 6 Hz, 1H, $^{phen}C_{Ar}$-*H*), 7.67-7.55 (overlapping m, 6H, $^{phen}C_{Ar}$-*H*, PC_{Ph}-*H*), 7.39-7.28 (overlapping m, 6H, $^{phen}C_{Ar}$-*H*, PC_{Ph}-*H*), 2.59 ppm (s, 3H, C_{Me}-*H*). $^{13}C\{^{1}H\}$ NMR ($CDCl_3$, 126 MHz, 22 °C): δ 155.4 ($^{phen}C_{Ar}$-*H*), 143.7 (d, J_{CP} = 18 Hz, $^{phen}C_{Ar}$), 137.5 ($^{phen}C_{Ar}$), 137.0 ($^{phen}C_{Ar}$-*H*), 134.1 (d, J_{CP} = 16 Hz, PC_{Ar}-*H*), 133.2 ($^{phen}C_{Ar}$), 132.5 ($^{phen}C_{Ar}$-*H*), 132.0 (PC_{Ar}), 129.7 ($^{phen}C_{Ar}$), 129.6 ($^{phen}C_{Ar}$-*H*), 128.7 (d, J_{CP} = 9 Hz, PC_{Ar}-*H*), 128.2 (PC_{Ar}-*H*), 127.1 ($^{phen}C_{Ar}$-*H*), 125.1 ($^{phen}C_{Ar}$), 125.0 ($^{phen}C_{Ar}$), 124.9 ($^{phen}C_{Ar}$), 122.0 ($^{phen}C_{Ar}$-*H*), 22.1 ppm (C_{Me}).

$^{31}P\{^{1}H\}$ NMR ($CDCl_3$, 202 MHz, 22 °C): δ -27.8 ppm (br, s). Anal. Calc. for $C_{52}H_{40}N_2P_2Cu_2I_2$•($CH_2Cl_2$): C, 54.99; H, 3.55. Found: C, 54.45; H, 3.60.

(L3)CuCl: Red crystals. Yield = 0.019 g (70%). ^{1}H NMR ($CDCl_3$, 300 MHz, 25 °C): 8.38 (m-overlapped, J_{HH} = 9, 3 Hz, 1H, $^{quin}C_{Ar}$-*H*), 8.33 (br s - overlapped, 1H, $^{quin}C_{Ar}$-*H*), 7.91 (s, 1H, $^{quin}C_{Ar}$-*H*), 7.73 (br, J_{HH} = 3 Hz, 1H, $^{quin}C_{Ar}$-*H*), 7.45 – 7.31 (overlapping m, 11 H, $^{quin}C_{Ar}$-*H*, PC_{Ph}-*H*), 2.57 ppm (s, 3H, C_{Me}-*H*). $^{13}C\{^{1}H\}$ NMR ($CDCl_3$, 75 MHz, 22 °C): δ 151.3 ($^{quin}C_{Ar}$-*H*), 147.8 (d, J_{CP} = 18 Hz, $^{quin}C_{Ar}$), 139.9 ($^{quin}C_{Ar}$-*H*), 138.5 ($^{quin}C_{Ar}$-*H*), 138.3 ($^{quin}C_{Ar}$-*H*), 133.2 (br, J_{CP} = 14 Hz, PC_{Ar}-*H*), 131.3 (d, J_{CP} = 32 Hz, PC_{Ar}), 130.9 ($^{quin}C_{Ar}$), 130.5 ($^{quin}C_{Ar}$-*H*), 129.3 (PC_{Ar}-*H*), 129.2 (PC_{Ar}-*H*), 123.0 (PC_{Ar}-*H*), 21.8 ppm (C_{Me}). $^{31}P\{^{1}H\}$ NMR ($CDCl_3$, 121 MHz, 22 °C): δ -18.2 ppm (br, s). Anal. Calc. for $C_{44}H_{36}N_2P_2Cu_2Cl_2$: C, 61.98; H, 4.26. Found: C, 61.55; H, 4.01.

(L3)CuBr: Orange crystals. Yield = 0.023 g (79%). ^{1}H NMR ($CDCl_3$, 300 MHz, 25 °C): δ 8.94 (br, s, 1H, $^{quin}C_{Ar}$-*H*), 8.24 (d, J_{HH} = 6 Hz, 1H, $^{quin}C_{Ar}$-*H*), 7.78 (s, 1H, $^{quin}C_{Ar}$-*H*), 7.67 (m, J_{HH} = 9, 3 Hz, 1H, $^{quin}C_{Ar}$-*H*) 7.54-7.48 (overlapping m, 4H, $^{quin}C_{Ar}$-*H*, PC_{Ar}-*H*), 7.44-7.29 (overlapping m, 7H, PC_{Ar}-*H*), 2.53 ppm (s, 3H, C_{Me}-*H*). $^{13}C\{^{1}H\}$ NMR ($CDCl_3$, 75 MHz, 22 °C): δ 151.3 (d, J_{CP} = 4 Hz, $^{quin}C_{Ar}$-*H*), 147.5 (d, J_{CP} = 17 Hz, $^{quin}C_{Ar}$), 139.3 ($^{quin}C_{Ar}$-*H*), 137.6 ($^{quin}C_{Ar}$-*H*), 137.5 ($^{quin}C_{Ar}$-*H*), 133.7 (d, J_{CP} = 17 Hz, PC_{Ar}-*H*), 132.1 (d, J_{CP} = 30 Hz, PC_{Ar}), 130.2 ($^{quin}C_{Ar}$), 130.1 ($^{quin}C_{Ar}$), 129.0 (PC_{Ar}-*H*), 128.9 (PC_{Ar}-*H*), 122.9 (d, J_{CP} = 3 Hz, PC_{Ar}-*H*), 21.8 ppm (C_{Me}). $^{31}P\{^{1}H\}$ NMR ($CDCl_3$, 121 MHz, 22 °C): δ -23.7 ppm (br, s). Anal. Calc. for $C_{44}H_{36}N_2P_2Cu_2Br_2$: C, 56.12 H, 3.85. Found: C, 55.71 H, 3.84.

(L3)CuI: Orange-red crystals. Yield = 0.022 g (69%). ^{1}H NMR ($CDCl_3$, 300 MHz, 22 °C): δ 9.28 (br, 1H, $^{quin}C_{Ar}$-*H*), 8.14 (d, J_{HH} = 9 Hz, 1H, $^{quin}C_{Ar}$-*H*), 7.69 (s, 1H, $^{quin}C_{Ar}$-*H*), 7.61 – 7.56 (overlapping m, 5H, $^{quin}C_{Ar}$-*H*, PC_{Ph}-*H*), 7.37 – 7.28 (overlapping m, 7H, $^{quin}C_{Ar}$-*H*, PC_{Ph}-*H*), 2.50 ppm (s, 3H, C_{Me}-*H*). $^{13}C\{^{1}H\}$ NMR ($CDCl_3$, 75 MHz, 22 °C): δ 151.8 (d, J_{CP} = 5 Hz, $^{quin}C_{Ar}$-*H*), 147.3 (d, J_{CP} = 18 Hz, $^{quin}C_{Ar}$), 139.2 (d, J_{CP} = 3 Hz, $^{quin}C_{Ar}$-*H*), 137.1 (d, J_{CP} = 4 Hz, $^{quin}C_{Ar}$), 136.9 (d, J_{CP} = 2.2 Hz, $^{quin}C_{Ar}$-*H*), 135.5 (d, J_{CP} = 17 Hz, $^{quin}C_{Ar}$), 134.0 (d, J_{CP} = 15.7 Hz, PC_{Ph}-*H*), 133.1 (PC_{Ar}), 129.6 ($^{quin}C_{Ar}$), 128.8 ($^{quin}C_{Ph}$), 128.7 (d, J_{CP} = 15 Hz, PC_{Ar}-*H*), 122.8 (d, J_{CP} = 3 Hz, $PC_{Ar}H$), 21.7 ppm (C_{Me}). $^{31}P\{^{1}H\}$ NMR ($CDCl_3$, 121 MHz, 22 °C): δ -29.9 ppm (br, s). Anal. Calc. for $C_{44}H_{36}N_2P_2Cu_2I_2$: C, 51.03; H, 3.50. Found: C, 50.63; H, 3.48.

Synthesis of (L6*)*$_2$Cu$_2$(acetylide)$_2$ and (L6*)*$_2$Cu(acetylide):

Inside the glove box, **L6** (1 mmol) and Cu-acetylide (1 mmol) was mixed in a 20 mL vial in 10 mL DCM solvent. A yellow-orange solution was formed which was then stirred for 24 hrs. Then the solution was pumped dried and washed with hexane and re-dried under high vacuum. The isolated orange solid was crystallized with DCM-Et_2O. (L6)$_2$Cu$_2$(acetylide)$_2$ was isolated as orange solid. A very small amount of (L6*)*$_2$Cu(acetylide) was co-crystallized as deep red crystal. (L6*)*$_2$Cu$_2$(acetylide)$_2$ was characterized by 1H NMR and solid state X-ray structure and (L6*)*$_2$Cu(acetylide) characterized by X-ray structure.^{1}H NMR ($CDCl_3$, 300 MHz, 22 °C): δ 8.61 (m, 1H), 8.51 (s, 1H), 8.15 (br m, 1H), 7.85 (m, 1H), 7.67 (m, 1H), 7.45 (v br, 6H), 7.20 (v br, 5H), 6.74 (v br, 4H), 3.06 (v br, 3H), 1.31 (s, 9H), 1.13 ppm (s, 9H).

X-Ray Crystallography Experimental Details:

X-ray crystal structure data was using collected from multi-faceted crystals of suitable size and quality selected from a representative sample of crystals of the same habit using an optical microscope. In each case, crystals were mounted on MiTiGen loops with data collection carried out in a cold stream of nitrogen (150 K; Bruker D8 QUEST ECO). All diffractometer manipulations were carried out using Bruker APEX3 software. Structure solution and refinement was carried out using XS, XT and XL software, embedded within the Bruker SHELXTL suite.[48] For each structure, the absence of additional symmetry was confirmed using ADDSYM incorporated in the PLATON program.[49] CCDC Nos. 1811419-1811424 contain the supplementary crystallographic data for this chapter. The data can be obtained free of charge from The Cambridge Crystallographic Data Centre via www.ccdc.cam.ac.uk/structures.

Crystal structure data for **(L2)CuCl**: X-ray quality crystals were grown following diffusion of diethylether vapor into CH_2Cl_2 at room temperature. Crystal structure parameters: $C_{52}H_{40}Cl_2Cu_2N_2P_2$ 952.80 g/mol, triclinic, space group *P*-1; a = 9.1636(17) Å, b = 10.448(2) Å, c = 12.101(2) Å, α = 96.098(14)°, β = 99.601(13)°, γ = 109.077(17)°, V = 1063.4(4) Å^3; Z = 1, ρ_{calcd} = 1.488 g cm^{-3}; crystal dimensions 0.310 x 0.270 x 0.100 mm; diffractometer Bruker D8 QUEST ECO CMOS; Mo K_α radiation, 150(2) K, $2\theta_{max}$ = 34.463°; 78831 reflections, 8169 independent (R_{int} = 0.0288), direct methods; absorption coeff (μ = 1.241 mm^{-1}), absorption correction semi-empirical from equivalents (SADABS); refinement (against F_o^2) with SHELXTL V6.1, 272 parameters, 0 restraints, R_1 = 0.0297 ($I > 2\sigma$) and wR_2 = 0.0759 (all data), Goof = 1.024, residual electron density 0.592/−0.404 e Å^{-3}.

Crystal structure data for **(L2)CuBr**: X-ray quality crystals were grown following diffusion of diethylether vapor into CH_2Cl_2 at room temperature. Crystal structure parameters: $C_{52}H_{40}Br_2Cu_2N_2P_2$ 1041.70 g/mol, monoclinic, space group *C*2/c; a = 18.8357(10) Å, b = 14.1568(7) Å, c = 16.0421(8) Å, β = 90.953(2)°, V = 4277.1(4) Å^3; Z = 4, ρ_{calcd} = 1.618 g cm^{-3}; crystal dimensions 0.310 x 0.180 x 0.100 mm; diffractometer Bruker D8 QUEST ECO CMOS; Mo K$_\alpha$ radiation, 150(2) K, $2\theta_{max}$ = 33.213°; 82121 reflections, 8185 independent (R_{int} = 0.0588), direct methods; absorption coeff (μ = 2.978 mm^{-1}), absorption correction semi-empirical from equivalents (SADABS); refinement (against F_o^2) with SHELXTL V6.1, 272 parameters, 0 restraints, R_1 = 0.0376 ($I > 2\sigma$) and wR_2 = 0.0738 (all data), Goof = 1.079, residual electron density 0.882/−0.752 e Å^{-3}.

Crystal structure data for **(L2)CuI**: X-ray quality crystals were grown following diffusion of hexanes into CH_2Cl_2 at room temperature. Crystal structure parameters: $C_{52}H_{40}I_2Cu_2N_2P_2(CH_2Cl_2)_2$ 1305.53 g/mol, monoclinic, space group *P*2/n; a = 21.0960(18) Å, b = 10.6127(8) Å, c = 24.0691(19) Å, β = 108.277(4)°, V = 5116.9(7) Å^3; Z = 4, ρ_{calcd} = 1.695 g cm^{-3}; crystal dimensions 0.170 x 0.080 x 0.050 mm; diffractometer Bruker D8 QUEST ECO CMOS; Mo K$_\alpha$ radiation, 150(2) K, $2\theta_{max}$ = 27.582°; 108133 reflections, 11817 independent (R_{int} = 0.0926), direct methods; absorption coeff (μ = 2.348 mm^{-1}), absorption correction semi-empirical from equivalents (SADABS); refinement (against F_o^2) with SHELXTL V6.1, 649 parameters, 0 restraints, R_1 = 0.0378 ($I > 2\sigma$) and wR_2 = 0.0749 (all data), Goof = 1.017, residual electron density 0.762/−0.937 e Å^{-3}.

Crystal structure data for **(L3)CuCl**: X-ray quality crystals were grown following diffusion of diethylether vapor into CH_2Cl_2 at room temperature. Crystal structure parameters: $C_{44}H_{36}Cl_2Cu_2N_2P_2$ 852.67 g/mol, monoclinic, space group $P2_1/n$; a = 9.7430(6) Å, b = 15.2568(9) Å, c = 12.7931(8) Å, β = 96.112(3)°, V = 1890.8(2) Å^3; Z = 2, ρ_{calcd} = 1.498 g cm^{-3}; crystal dimensions 0.080 x 0.080 x 0.050 mm; diffractometer Bruker D8 QUEST ECO CMOS; Mo K$_\alpha$ radiation, 150(2) K, $2\theta_{max}$ = 27.557°; 65040 reflections, 4350 independent (R_{int} = 0.0523), direct methods; absorption coeff (μ = 1.386 mm^{-1}), absorption correction semi-empirical from equivalents (SADABS); refinement (against F_o^2) with SHELXTL V6.1, 236 parameters, 0 restraints, R_1 = 0.0328 ($I > 2\sigma$) and wR_2 = 0.0641 (all data), Goof = 1.050, residual electron density 0.380/−0.524 e Å^{-3}.

Crystal structure data for **(L3)CuBr**: X-ray quality crystals were grown following diffusion of diethylether vapor into CH_2Cl_2 at room temperature. Crystal structure parameters: $C_{44}H_{36}Br_2Cu_2N_2P_2$ 941.59 g/mol, monoclinic, space group $P2_1/n$; a = 9.8884(5) Å, b = 15.3309(8) Å, c = 12.6587(8) Å, β = 95.466(2)°, V = 1910.31(18) Å^3; Z = 2, ρ_{calcd} = 1.637 g cm^{-3}; crystal dimensions 0.330 x 0.260 x 0.220 mm; diffractometer Bruker D8 QUEST ECO CMOS; Mo K$_\alpha$ radiation, 150(2) K, $2\theta_{max}$ = 42.248°; 126369 reflections, 13474 independent (R_{int} = 0.0495), direct methods; absorption coeff (μ = 3.324 mm^{-1}), absorption correction semi-empirical from equivalents (SADABS); refinement (against F_o^2) with SHELXTL V6.1, 236 parameters, 0 restraints, R_1 = 0.0315 ($I > 2\sigma$) and wR_2 = 0.0730 (all data), Goof = 1.074, residual electron density 0.731/−0.802 e Å^{-3}.

Crystal structure data for **(L3)CuI**: X-ray quality crystals were grown following diffusion of diethylether vapor into CH_2Cl_2 at room temperature. Crystal structure parameters: $C_{44}H_{36}I_2Cu_2N_2P_2$ 1035.59 g/mol, monoclinic, space group $P2_1/n$; a = 10.0569(6) Å, b = 15.2785(10) Å, c = 13.3126(9) Å, β = 103.807(2)°, V = 1986.4(2) Å^3; Z = 4, ρ_{calcd} = 1.731 g cm^{-3}; crystal dimensions 0.400 x 0.220 x 0.190 mm; diffractometer Bruker D8 QUEST ECO CMOS; Mo K$_\alpha$ radiation, 150(2) K, $2\theta_{max}$ = 40.350°; 111652 reflections, 12535 independent (R_{int} = 0.0331), direct methods; absorption coeff (μ = 2.739 mm^{-1}), absorption correction semi-empirical from equivalents (SADABS); refinement (against F_o^2) with SHELXTL V6.1, 236 parameters, 0 restraints, R_1 = 0.0318 ($I > 2\sigma$) and wR_2 = 0.0733 (all data), Goof = 1.143, residual electron density 1.542/−1.106 e Å^{-3}.

Optical Spectroscopy Measurements:

The absorption spectra of the complexes were measured in solution in CH_2Cl_2 in 1 cm quartz cuvettes using a Thermo Scientific Genesys UV-vis spectrometer at room temperature. Emission spectra at 77 K were recorded in 4 mm diameter tubes held within a liquid-nitrogen-cooled quartz dewar, using a Jobin Yvon Fluoromax-2 spectrometer equipped with a Hamamatsu R928 photomultiplier tube (PMT). The spectra in the solid state were recorded by means of an integrating sphere attached to a Jobin Yvon Fluorolog instrument through optical fibres. Finely powdered samples were contained within Spectralon sample holders of 10 mm diameter. Quantum yields were determined using a sample of finely powdered $BaSO_4$ as a non-emissive blank. Scattered light at λ_{ex} = 425 nm for sample and blank was measured using a neutral density filter of O.D. = 2, whilst the emission region was monitored in the absence of the filter. A Synapse CCD detector was used for detection of the emitted light, which offers better sensitivity

in the red / NIR region compared to the R928 PMT. Luminescence lifetimes at ambient temperature were measured by time-correlated single-photon counting (TCSPC) following excitation using a pulsed laser diode at 405 nm and using an R928 PMT for detection. The same detector operating in multi-channel scaling (MCS) mode was used to measure the longer lifetimes at 77 K, following excitation with a pulsed xenon flashlamp.

3.6. References:

(1) Li, Z.; Sun, W. Synthesis, Photophysics, and Reverse Saturable Absorption of Platinum Complexes Bearing Extended π-Conjugated C^N^N Ligands. *Dalton Trans* **2013**, *42*, 14021–14029.

(2) Sicilia, V.; Fuertes, S.; Martin, A.; Palacios, Adrian. N-Assisted CPh-H Activation in 3,8-Dinitro-6-Phenylphenanthridine. New C,N-Cyclometalated Compounds of Platinum(II): Synthesis, Structure, and Luminescence Studies. *Organometallics* **2013**, *32*, 4092–4102.

(3) Li, Z.; Cui, P.; Wang, C.; Kilina, S.; Sun, Wenfang. Nonlinear Absorbing Cationic Bipyridyl Iridium(III) Complexes Bearing Cyclometalating Ligands with Different Degrees of π-Conjugation: Synthesis, Photophysics, and Reverse Saturable Absorption. *J. Phys. Chem. C* **2014**, *118*, 28764–28775.

(4) Jiang, B.; Gu, Y.; Qin, J.; Ning, X.; Gong, S.; Xie, G.; Yang, Chuluo. Deep-Red Iridium(III) Complexes Cyclometalated by Phenanthridine Derivatives for Highly Efficient Solution-Processed Organic Light-Emitting Diodes. *J. Mater. Chem. C* **2016**, *4*, 3492–3498.

(5) Bossi, A.; Rausch, A. F.; Leitl, M. J.; Czerwieniec, R.; Whited, M. T.; Djurovich, P. I.; Yersin, H.; Thompson, M. E. Photophysical Properties of Cyclometalated Pt(II)

Complexes: Counterintuitive Blue Shift in Emission with an Expanded Ligand π System. *Inorg. Chem.* **2013**, *52*, 12403–12415.

(6) Liu, B.; Lystrom, L.; Kilina, S.; Sun, Wenfang. Tuning the Ground State and Excited State Properties of Monocationic Iridium(III) Complexes by Varying the Site of Benzannulation on Diimine Ligand. *Inorg. Chem.* **2017**, *56*, 5361–5370.

(7) Hanson, K.; Roskop, L.; Djurovich, P. I.; Zahariev, F.; Gordon, M. S.; Thompson, M. E. A Paradigm for Blue- or Red-Shifted Absorption of Small Molecules Depending on the Site of π-Extension. *J. Am. Chem. Soc.* **2010**, *132*, 16247–16255.

(8) Mondal, R.; Giesbrecht, P. K.; Herbert, D. E. Nickel(II), Copper(I) and Zinc(II) Complexes Supported by a (4-Diphenylphosphino)Phenanthridine Ligand. *Polyhedron* **2016**, *108*, 156–162.

(9) Mandapati, P.; Giesbrecht, P. K.; Davis, R. L.; Herbert, D. E. Phenanthridine-Containing Pincer-like Amido Complexes of Nickel, Palladium, and Platinum. *Inorg. Chem.* **2017**, *56*, 3674–3685.

(10) Ford, P. C.; Cariati, E.; Bourassa, James. Photoluminescence Properties of Multinuclear Copper(I) Compounds. *Chem. Rev. Wash. C* **1999**, *99*, 3625–3647.

(11) Armaroli, N.; Accorsi, G.; Cardinali, F.; Listorti, Andrea. Photochemistry and Photophysics of Coordination Compounds: Copper. *Top. Curr. Chem.* **2007**, *280*, 69–115.

(12) Peng, R.; Li, M.; Li, Dan. Copper(I) Halides: A Versatile Family in Coordination Chemistry and Crystal Engineering. *Coord. Chem. Rev.* **2010**, *254*, 1–18.

(13) Tsuge, K.; Chishina, Y.; Hashiguchi, H.; Sasaki, Y.; Kato, M.; Ishizaka, S.; Kitamura, Noboru. Luminescent Copper(I) Complexes with Halogenido-Bridged Dimeric Core. *Coord. Chem. Rev.* **2016**, *306*, 636–651.

(14) Cariati, E.; Lucenti, E.; Botta, C.; Giovanella, U.; Marinotto, D.; Righetto, Stefania. Cu(I) Hybrid Inorganic-Organic Materials with Intriguing Stimuli Responsive and Optoelectronic Properties. *Coord. Chem. Rev.* **2016**, *306*, 566–614.

(15) Yersin, H.; Rausch, A. F.; Czerwieniec, R.; Hofbeck, T.; Fischer, Tobias. The Triplet State of Organo-Transition Metal Compounds. Triplet Harvesting and Singlet Harvesting for Efficient OLEDs. *Coord. Chem. Rev.* **2011**, *255*, 2622–2652.

(16) Czerwieniec, R.; Leitl, M. J.; Homeier, H. H. H.; Yersin, Hartmut. Cu(I) Complexes - Thermally Activated Delayed Fluorescence. Photophysical Approach and Material Design. *Coord. Chem. Rev.* **2016**, *325*, 2–28.

(17) Maksic, Z. B.; Baric, D.; Mueller, Thomas. Clar's Sextet Rule Is a Consequence of the σ-Electron Framework. *J. Phys. Chem. A* **2006**, *110*, 10135–10147.

(18) Belyaev, A.; Dau, T. M.; Jänis, J.; Grachova, E. V.; Tunik, S. P.; Koshevoy, I. O. Low-Nuclearity Alkynyl D10 Clusters Supported by Chelating Multidentate Phosphines. *Organometallics* **2016**, *35*, 3763–3774.

(19) Macrae, C. F.; Bruno, I. J.; Chisholm, J. A.; Edgington, P. R.; McCabe, P.; Pidcock, E.; Rodriguez-Monge, L.; Taylor, R.; van de Streek, J.; Wood, P. A. Mercury CSD 2.0 - New Features for the Visualization and Investigation of Crystal Structures. *J. Appl. Crystallogr.* **2008**, *41*, 466–470.

(20) Overend, J. The Equilibrium Bond Lengths in Acetylene and HCN. *Trans Faraday Soc* **1960**, *56*, 310–314.

(21) Montalti, Marco. *Handbook of Photochemistry*; Taylor & Francis: Boca Raton Fla., 2006.

(22) Zeng, C.; Wang, N.; Peng, T.; Wang, Suning. Copper(I) Complexes Bearing 1,2-Phenyl-Bridged P^N, P^N^P, and N^P^N Chelate Ligands: Structures and Phosphorescence. *Inorg. Chem.* **2017**, *56*, 1616–1625.

(23) Leitl, M. J.; Kuechle, F.-R.; Mayer, H. A.; Wesemann, L.; Yersin, Hartmut. Brightly Blue and Green Emitting Cu(I) Dimers for Singlet Harvesting in OLEDs. *J. Phys. Chem. A* **2013**, *117*, 11823–11836.

(24) Araki, H.; Tsuge, K.; Sasaki, Y.; Ishizaka, S.; Kitamura, Noboru. Luminescence Ranging from Red to Blue: A Series of Copper(I)-Halide Complexes Having Rhombic $\{Cu_2(\mu\text{-}X)_2\}$ (X = Br and I) Units with N-Heteroaromatic Ligands. *Inorg. Chem.* **2005**, *44*, 9667–9675.

(25) Zink, D. M.; Baechle, M.; Baumann, T.; Nieger, M.; Kuehn, M.; Wang, C.; Klopper, W.; Monkowius, U.; Hofbeck, T.; Yersin, H.; et al. Synthesis, Structure, and Characterization of Dinuclear Copper(I) Halide Complexes with P^N Ligands Featuring Exciting Photoluminescence Properties. *Inorg. Chem.* **2013**, *52*, 2292–2305.

(26) Englman, R.; Jortner, Joshua. Energy Gap Law for Radiationless Transitions in Large Molecules. *Mol. Phys.* **1970**, *18*, 145–164.

(27) Caspar, J. V.; Meyer, T. J. Application of the Energy Gap Law to Nonradiative, Excited-State Decay. *J. Phys. Chem.* **1983**, *87*, 952–957.

(28) Kober, E. M.; Caspar, J. V.; Lumpkin, R. S.; Meyer, T. J. Application of the Energy Gap Law to Excited-State Decay of Osmium(II)-Polypyridine Complexes: Calculation of Relative Nonradiative Decay Rates from Emission Spectral Profiles. *J. Phys. Chem.* **1986**, *90*, 3722–3734.

(29) Whittle, C. E.; Weinstein, J. A.; George, M. W.; Schanze, K. S. Photophysics of Diimine Platinum(II) Bis-Acetylide Complexes. *Inorg. Chem.* **2001**, *40*, 4053–4062.

(30) Wilson, J. S.; Chawdhury, N.; Al-Mandhary, M. R. A.; Younus, M.; Khan, M. S.; Raithby, P. R.; Koehler, A.; Friend, R. H. The Energy Gap Law for Triplet States in Pt-Containing Conjugated Polymers and Monomers. *J. Am. Chem. Soc.* **2001**, *123*, 9412–9417.

(31) Zander, M. The Significance of Donor-Acceptor Interactions in the External Heavy Atom Effect of Silver Nitrate on the Luminescence Behavior of Aza-Aromatic Systems and Carbazoles. *Z. Fuer Naturforschung Teil Astrophys. Phys. Phys. Chem.* **1978**, *33A*, 998–1000.

(32) Najbar, J.; Jarzeba, W.; Urbanek, Z. H. Internal Heavy-Atom Effect on the T1 States of Monochloroquinolines and Monochloronaphthalenes. *Chem. Phys.* **1983**, *79*, 245–253.

(33) de Groot, M. S.; van der Waals, J. H. Paramagnetic Resonance in Phosphorescent Aromatic Hydrocarbons. III. Conformational Isomerism in Benzene and Triptycene. *Mol. Phys.* **1963**, *6*, 545–562.

(34) de Groot, M. S.; Hesselmann, I. A. M.; van der Waals, J. H. Electron Resonance of Phosphorescent Mesitylene. *Mol. Phys.* **1965**, *10*, 91–93.

(35) Rabalais, J. W.; Maria, H. J.; McGlynn, S. P. Phosphorescence Decay of Benzene and Methylbenzene Derivatives. *J. Chem. Phys.* **1969**, *51*, 2259–2273.

(36) Buma, W. J.; Van der Waals, J. H.; Van Hemert, M. C. Conformational Instability of the Lowest Triplet State of Benzene: The Result of Ab Initio Calculations. *J. Am. Chem. Soc.* **1989**, *111*, 86–87.

(37) Summerville, R. H.; Hoffmann, Roald. Tetrahedral and Other M2L6 Transition Metal Dimers. *J. Am. Chem. Soc.* **1976**, *98*, 7240–7254.

(38) Aullon, G.; Ujaque, G.; Lledos, A.; Alvarez, S.; Alemany, Pere. To Bend or Not To Bend: Dilemma of the Edge-Sharing Binuclear Square Planar Complexes of D8 Transition Metal Ions. *Inorg. Chem.* **1998**, *37*, 804–813.

(39) Wei, F.; Liu, X.; Liu, Z.; Bian, Z.; Zhao, Y.; Huang, Chunhui. Structural and Photophysical Study of Copper Iodide Complex with P^N or P^N^P Ligand. *CrystEngComm* **2014**, *16*, 5338–5344.

(40) Yang, L.; Powell, D. R.; Houser, R. P. Structural Variation in Copper(I) Complexes with Pyridylmethylamide Ligands: Structural Analysis with a New Four-Coordinate Geometry Index, T4. *Dalton Trans.* **2007**, 955–964.

(41) Cunningham, C. T.; Moore, J. J.; Cunningham, K. L. H.; Fanwick, P. E.; McMillin, D. R. Structural and Photophysical Studies of Cu(NN)2+ Systems in the Solid State. Emission at Last from Complexes with Simple 1,10-Phenanthroline Ligands. *Inorg. Chem.* **2000**, *39*, 3638–3644.

(42) Uoyama, H.; Goushi, K.; Shizu, K.; Nomura, H.; Adachi, Chihaya. Highly Efficient Organic Light-Emitting Diodes from Delayed Fluorescence. *Nature* **2012**, *492*, 234–238.

(43) Hamze, R.; Jazzar, R.; Soleilhavoup, M.; Djurovich, P. I.; Bertrand, G.; Thompson, M. E. Phosphorescent 2-, 3- and 4-Coordinate Cyclic (Alkyl)(Amino)Carbene (CAAC) Cu(I) Complexes. *Chem. Commun.* **2017**, *53*, 9008–9011.

(44) He, L.-H.; Luo, Y.-S.; Di, B.-S.; Chen, J.-L.; Ho, C.-L.; Wen, H.-R.; Liu, S.-J.; Wang, J.-Y.; Wong, W.-Yeung. Luminescent Three- and Four-Coordinate Dinuclear Copper(I) Complexes Triply Bridged by Bis(Diphenylphosphino)Methane and Functionalized 3-(2'-Pyridyl)-1,2,4-Triazole Ligands. *Inorg. Chem.* **2017**, *56*, 10311–10324.

(45) Hupp, B.; Nitsch, J.; Schmitt, T.; Bertermann, R.; Edkins, K.; Hirsch, F.; Fischer, I.; Auth, M.; Sperlich, A.; Steffen, Andreas. Stimulus-Triggered Formation of an Anion-Cation Exciplex in Copper(I) Complexes as a Mechanism for Mechanochromic Phosphorescence. *Angew. Chem. Int. Ed.* **2018**, *57*, 13671–13675.

(46) Kim, Y.-E.; Kim, J.; Park, J. W.; Park, K.; Lee, Yunho. σ-Complexation as a Strategy for Designing Copper-Based Light Emitters. *Chem. Commun.* **2017**, *53*, 2858–2861.

(47) Lee, C.-I.; Zhou, J.; Ozerov, O. V. Catalytic Dehydrogenative Borylation of Terminal Alkynes by a SiNN Pincer Complex of Iridium. *J. Am. Chem. Soc.* **2013**, *135*, 3560–3566.

(48) Sheldrick, G. M. A Short History of SHELX. *Acta Crystallogr. A* **2008**, *64*, 112–122.

(49) Spek, A. L. Structure Validation in Chemical Crystallography. *Acta Crystallogr. D Biol. Crystallogr.* **2009**, *65*, 148–155.

Chapter 4:

4.1. Abstract:

The structural and photophysical properties of three sets of yellow-orange emitting Cu(I) complexes of the form [(*P^N*)$_2$Cu]X are presented. Here, *P^N* represents a bidentate neutral donor ligand based on phenanthridine (3,4-benzoquinoline) incorporating a phosphine unit at the 4-position, of which three ligands are investigated, namely (4-diphenylphosphino)phenanthridine (**L1**), (4-diphenylphosphino)(2-methyl)phenanthridine (**L2**) and (2,6-dimethyl)(4-diphenylphosphino)phenanthridine (**L5**). For each *P^N*-coordinating ligand, the corresponding homoleptic copper(I) complex (**(L1)$_2$Cu$_2$X$_2$**, **(L2)$_2$Cu$_2$X$_2$**, **(L5)$_2$Cu$_2$X$_2$**) has been prepared as both the hexafluorophosphate and tetraphenylboronate salt (X = PF_6^- or BPh_4^-). The identity of the counterion was found to have an intense and unexpected impact on the emission properties of the solid-state powder form, amplifying the effects of *P^N* ligand modification and enabling emission wavelength tuning from orange to yellow. These effects can be attributed to differences in molecular packing, and the impact of ligand structure and inter-ionic interactions on distortions in the excited state relative to the ground state. The experimental results have been interpreted theoretically with the help of density functional theory (DFT) and time-dependent DFT (TD-DFT) calculations.

4.2. Introduction:

As I discussed in the previous chapter design of new emissive molecules based low-cost and abundant metals like copper which is essential for increasing sustainability[1] of light-emitting devices, photosensitizers, dyes and imaging agents.[2,3] While 2nd and 3rd row elements like ruthenium, iridium and platinum have higher spin-orbit coupling (SOC) constants, Cu(I) can nonetheless facilitate formally forbidden phosphorescence from triplet states when efficient SOC pathways are available via coupling of the lowest triplet excited state with close-lying ^{1}MLCT states.[4] In addition, a small S_1–T_1 energy gap can enable thermally activated delayed fluorescence (TADF) via thermal repopulation of the S_1 from the lower energy T_1 state, which presents another mechanism by which otherwise non-emissive triplet states can be harvested.[5] In this case, emission is essentially via the singlet S_1 state and in this way, the "singlet harvesting effect" enables utilization of all injected excitons for the generation of light in electroluminescent devices,[6] presenting similar advantages as triplet light-harvesters based on heavier, more precious transition metals.[7]

To fully understand the potential of luminescent Cu(I) coordination complexes, the development of molecular design approach to tune emission wavelengths and optimise photophysical properties, such as lifetimes and quantum yields, is crucial. One eminent strategy is to apply ligand design to prevent molecular distortions of tetrahedral Cu(I) complexes in the excited state that can lead to competitive non-radiative decay. For instance, methylation *ortho* to the nitrogen donors in bidentate *N^N* phenanthroline frameworks has been shown to boost quantum yields of Cu(I) complexes containing such ligands, accompanied by extension of the emission lifetimes. These outcomes are associated with the impact of the methyl groups in restricting the flattening of the structure away from D_{2d} symmetry towards D_{2h}.[8] This effect is not

universal, however; the impact of ligand *ortho* methylation in related Cu(I) complexes supported by (8-diphenylphosphino)(2-methyl/hydro)quinoline ligands is minimal.[9] Complimentary tactics to enhance the effect of ligand modifications could therefore potentially expand the reach of these design strategies. In this chapter, I report examples of homoleptic Cu(I) complexes of bidentate *P^N*-coordinating ligands based on a phenanthridine unit substituted at the 4-position with a diphenylphosphine moiety: L**1**[X] (L**1** = $[(\mathbf{L1})_2Cu]^+$), **L2**[X] (**2** = $[(\mathbf{L2})_2Cu]^+$), L**5**[X] (L**5** = $[(\mathbf{L5})_2Cu]^+$) where X = PF_6^- or BPh_4^- in each case. The *P^N* ligand **L1** is the parent (4-diphenylphosphino)phenanthridine described in Chapter 1; **L2** is (4-diphenylphosphino)(2-methyl)phenanthridine, incorporating a methyl substituent para to the nitrogen atom; and **L5** is (2,6-dimethyl)(4-diphenylphosphino)phenanthridine, which in addition incorporates a methyl substituent at the position *ortho* to the nitrogen atom, reminiscent of the *ortho*-methylated phenanthrolines mentioned above.[8,9] The complexes all show moderately intense photoluminescence in the solid-state, in the orange-yellow region of the spectrum. In investigating the photophysical properties of powder samples of these complexes, a strong effect of the counterion on the emission properties was discovered, in which changing the counterion can amplify the impact of otherwise subtle changes to ligand architecture.

4.3. Results and Discussion:

4.3.1. Synthesis:

The π-extended hybrid *P^N* donor **L5** has been synthesized following the same procedure to the preparation of **L1**[10] and **L2**.[11] As discussed in Chapter 2, the tricyclic frame of the phenanthridine moiety was prepared via a one-pot, Pd-catalyzed cross-coupling/condensation of

the appropriately substituted aniline with 2-acetylphenylboronic acid (**Scheme 4.1**). 4-Bromo-2,6-dimethylphenanthridine could be isolated in this way in 87% yield following column chromatography by using DCM as eluent. The proligand **L5** was then accessed as an off-white solid in 61% yield after crystallization, via lithium-halogen exchange using *sec*-butyllithium in Et_2O, followed by quenching with Ph_2PCl. Evidence for the formation of phenanthridine core could be perceived in the downfield shift of the "imine-like" C_6 carbon observed by $^{13}C\{^1H\}$ NMR spectroscopy at 157.3 ppm (*cf.* **L1**: 152.8 ppm; **L2**: 151.8 ppm). All three proligands exhibit similar ^{31}P NMR shifts (**L1**: –13.7 ppm; **L2**: –13.6 ppm; **L5**: –12.9 ppm).

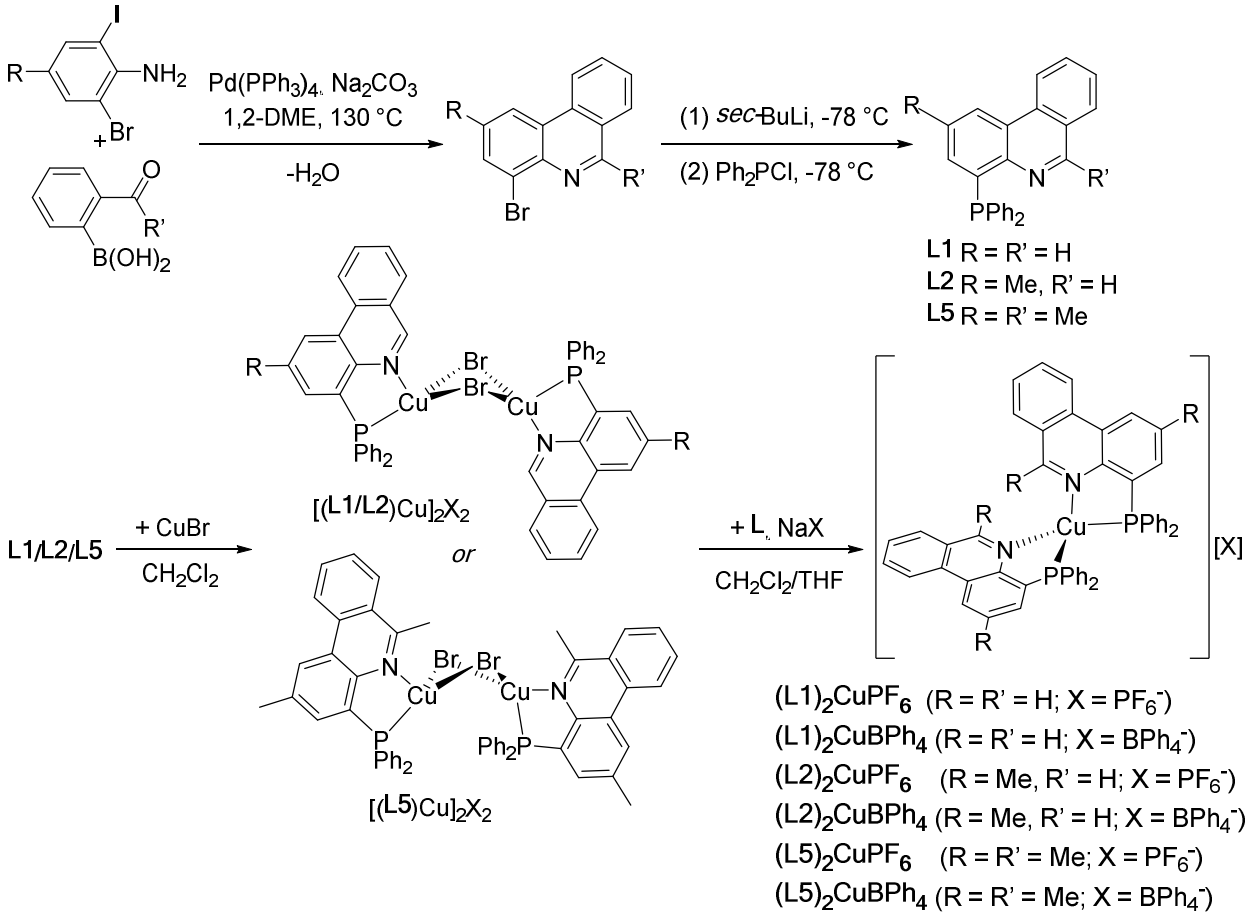

Scheme 4. 1: Synthesis of proligands **L1**,[10] **L2**[11] and **L5** (this work) and their Cu(I) complexes.

DCM solutions of the proligands was added to the suspensions of CuBr which gave increasingly homogeneous orange solutions of halide-bridged [(**L**)Cu]$_2$(μ-Br)$_2$ dimers. I have previously reported the isolation and properties of [(**L**)Cu]$_2$(μ-Br)$_2$ complexes of **L1**[10] and **L2**.[11] Full characterization details of [(**L5**)Cu]$_2$(μ-Br)$_2$ are provided in the experimental section. The solid-state structure of [(**L5**)Cu]$_2$(μ-Br)$_2$ shows a bent, butterfly-like orientation to the Cu_2Br_2 sub-unit with an intermetallic distance of 2.6793(4) Å and a 'head-to-head' orientation of the two *P^N* ligands in which the nitrogen donors are on the same side of the Cu_2Br_2 core (**Figure 4.1**).

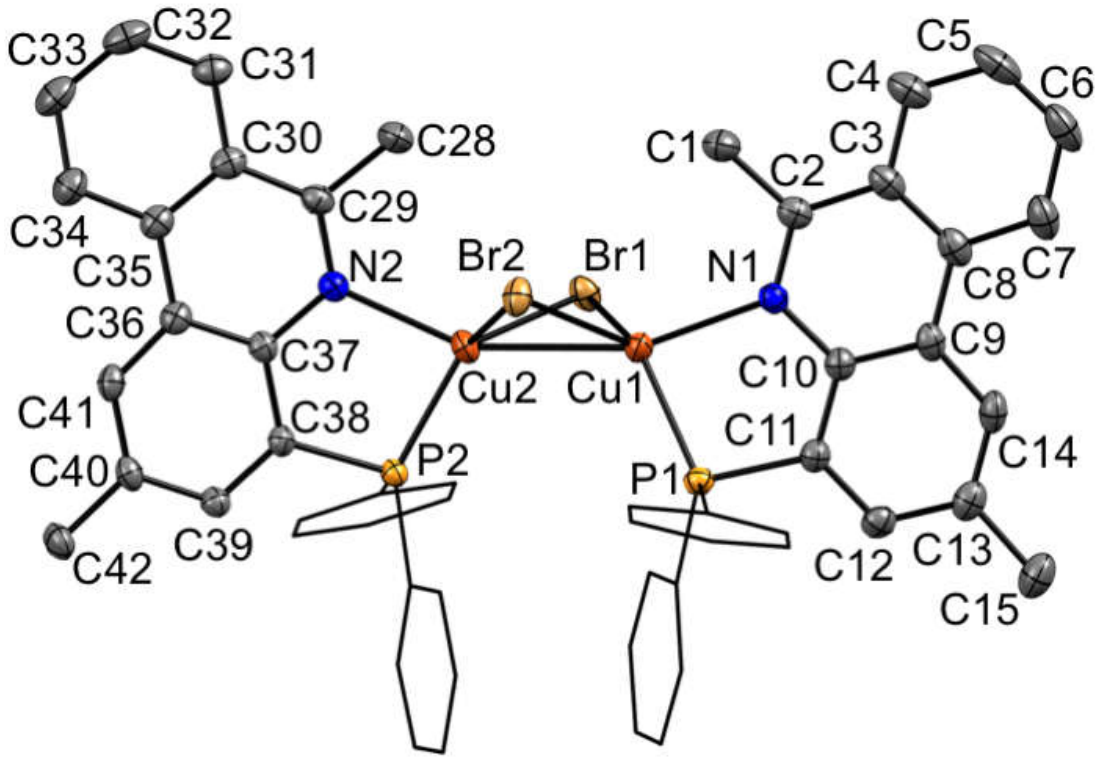

Figure 4. 1: Solid-state X-ray structures of **(L5)$_2$Cu$_2$Br$_2$** with thermal ellipsoids (where shown at 50% probability levels). Hydrogen atoms and a molecule of the solvent of crystallization (CH_2Cl_2) are omitted for clarity

In comparison, the other equivalent halide-bridged dimers of [(**L1-L2**)Cu]$_2$(μ-X)$_2$ (X = Cl, Br, I) are all 'head-to-tail', with longer Cu-Cu intrametallic distances (see Chapter 3).[10,11] The presence of *ortho* methyl groups adjacent to the phenanthridine nitrogens thus appears to override the steric preferences for [(**L5**)Cu]$_2$(μ-Br)$_2$ of the PPh_2 units to avoid each other in the solid-state.

Addition of a second equivalent of the *P^N* ligand, followed by metathesis with sodium hexafluorophosphate or sodium tetraphenylborate salt dissolved in tetrahydrofuran, gave bright yellow/green suspensions, from which the targeted [(**L**)$_2$Cu]X salts could be isolated as light yellow solids. The Cu(I) complexes are soluble in most polar organic solvents, and were fully characterized in solution by multi-nuclear NMR spectroscopy, and in the solid-state by elemental analysis and single-crystal X-ray diffraction. A symmetric ligand environment of both the bound ligands for all six Cu(I) complexes was observed by NMR spectroscopy.

An asymmetric ligand centre has also been created by using mixed ligand environment around Cu centre. So, ligand **L1** was reacted with copper bromide in dichloromethane to synthesize halide bridge Cu complex[10] while an equivalent of ligand **L2** was added in situ and continued stirring before addition of $NaBPh_4$ (**Scheme 4.2**). The solution was dried and washed with ether to obtain the product as faint yellowish white solid. The NMR of the solid was taken in $CDCl_3$ (**Figure 4.2**). In the ^{1}H NMR spectrum the diagnostic singlet proton of phenanthridine of 'imine' like carbon (C=N bond) showed two broad distinguished peaks around 8.25-8.27 ppm for two different phenanthridine. The broadening could be evident of quardripolar coupling of Cu(I) in an asymmetric environment.[12] However, the phosphorus signal showed indistinguishable singlet for both phosphine signals (**Figure 4.3**).

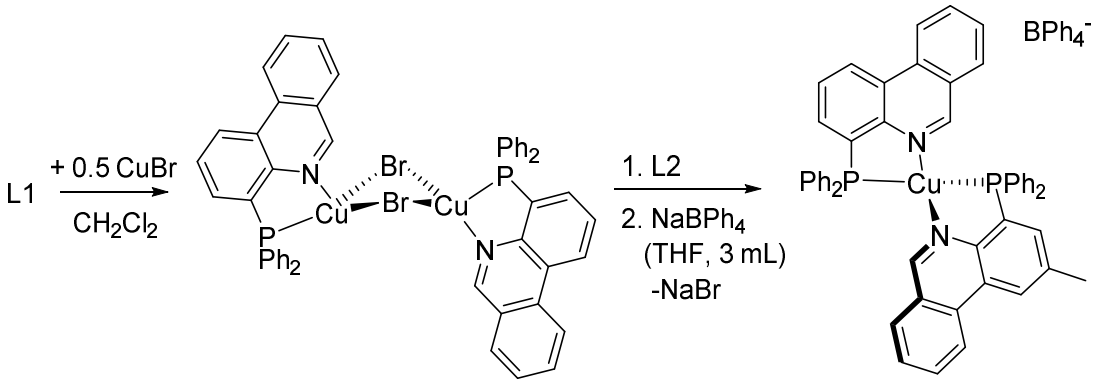

Scheme 4. 2: Synthesis of asymmetric Cu(I) complexes using proligands **L1**[10] and **L2**[11].

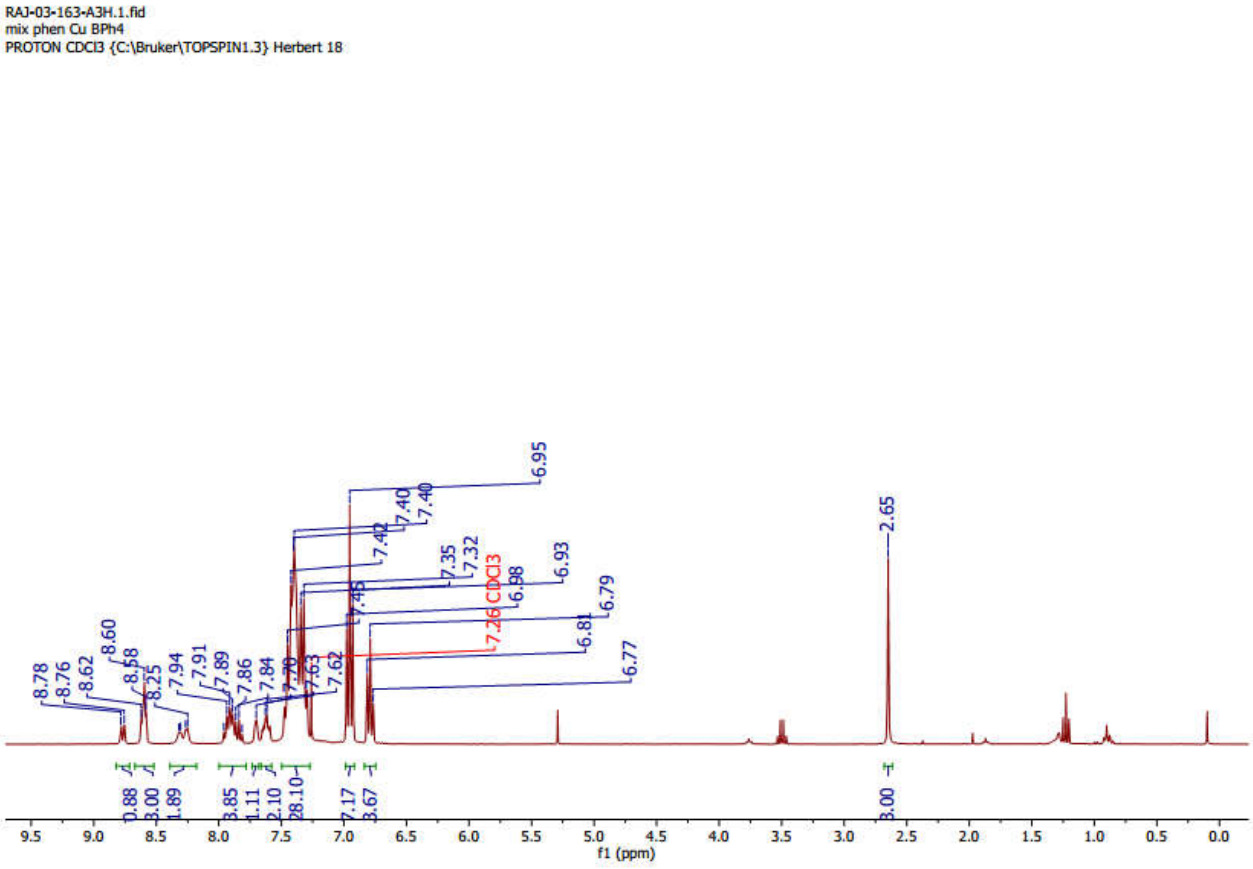

Figure 4. 2: ^{1}**H NMR** spectroscopy of complex **(L1)(L2)CuBPh$_4$**

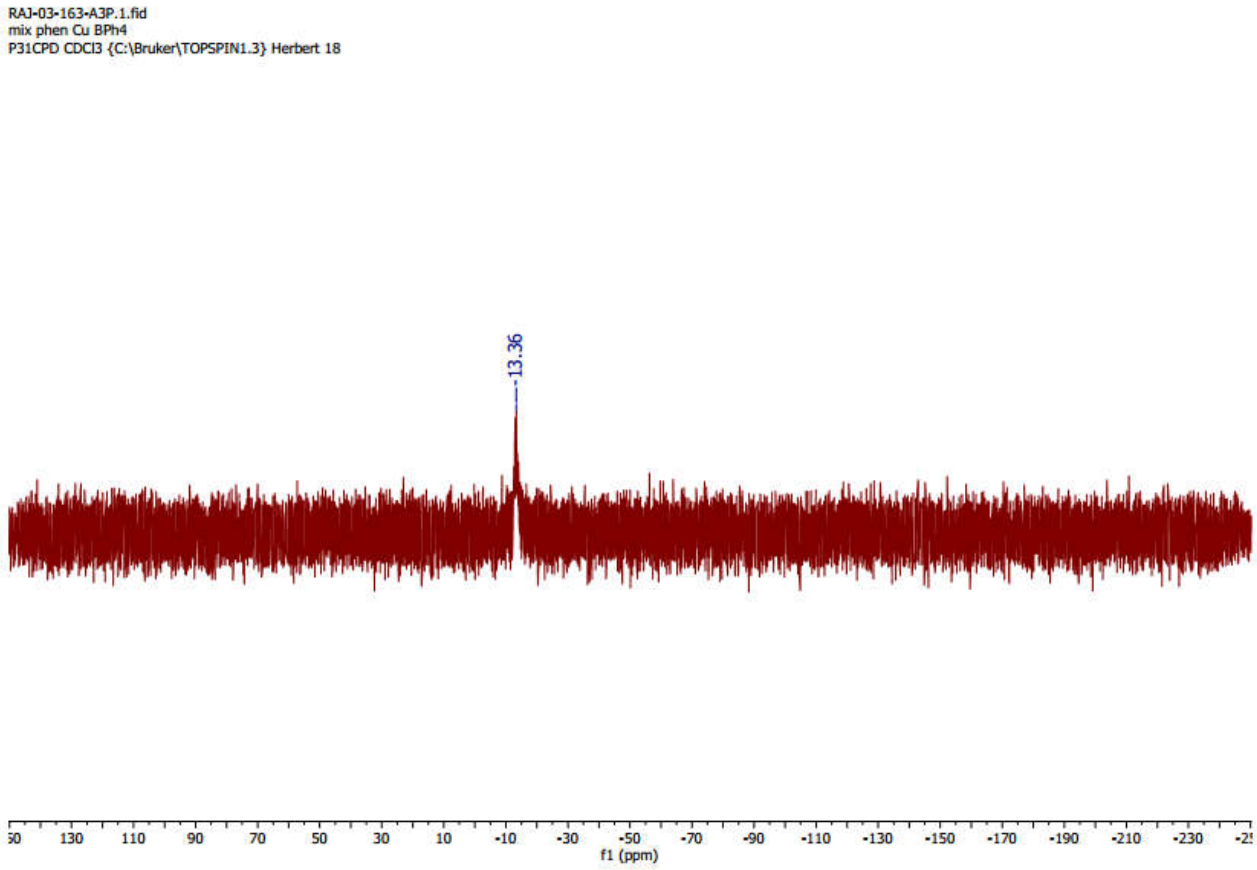

Figure 4. 3: $^{31}P\{^{1}H\}$ NMR spectroscopy of complex **(L1)(L2)CuBPh$_4$**

Single crystals suitable for X-ray diffraction were obtained for the entire series by slow diffusion of hexanes vapour into dichloromethane solutions or layering technique of hexane and DCM. In the solid-state, all six complexes adopt the distorted tetrahedral geometry expected of four-coordinate Cu(I) with bulky ligand sets (exemplified by the BPh_4^- and PF_6^- salts series in **Figure 4.4**). Comparing bond lengths, all six complexes show very similar metal-ligand interactions (**Table 4.1**). In examining the bond angles, the differences observed by relatively small changes in ligand sterics (replacing H with CH_3) become evident. While the bite angles (N1-Cu1-P1, for example) remain unchanged as a result of the rigid sp^2 aromatic ligand backbone of the π-extended conjugated system, the interligand angles are significantly perturbed

in moving from **(L1)Cu**$^{+}$ to **(L5)Cu**$^{+}$. However, it is very interesting that, these differences are exacerbated in changing from PF_6^- to BPh_4^-. Thus, τ_δ metrics (**Table 4.1** and footnote *a*) measured for each crystallographically independent molecule suggest that **L1** and **L2**, bearing no sterically imposing substitutents, favour a distorted sawhorse geometry in their Cu(I) complexes ($\tau_\delta \sim 0.55$) when paired with a PF_6^- counterion, but enforce more distortion for tetrahedral ligand arrangement ($\tau_\delta \sim 0.63$-0.69) as a BPh_4^- salt. These distortions of structure are caused by unequal P-Cu-P vs N-Cu-N angles (**Table 4.1**), and larger dihedral angles between the Cu-P1 vectors and the plane formed by the Cu-P2-N2 sub-unit of the second *P^N* ligand compared with the equivalent dihedral angle formed by the Cu1-N1 bond/Cu-P2-N2 plane (**Table 4.2**).

The inequivalence of these angles is smallest in **(L5)$_2$Cu$_2$X$_2$** structure. Particularly, in **(L5)$_2$Cu$_2$X$_2$** the N-Cu-N angles are much larger, resulting from *ortho*-methylation. Increasing sterics close to the donor nitrogen by methyl substituent in **L5** favours even less distortion from idealized tetrahedral geometry for both BPh_4 and PF_6 salts. Comparing **(L5)$_2$CuBPh$_4$** and **(L5)$_2$CuPF$_6$**, the N-Cu-N angles are quite similar; even though, the P-Cu-P angles are much smaller in **(L5)$_2$CuBPh$_4$**. The space-filling diagrams exlain that these geometric constraints arise from more intimate inter-ion contacts for the tetraarylborate salt (**Figure 4.6**). Cu(I) complexes of (8-diphenylphosphino)quinoline have been reported to crystallize independently in different solvent mixture as *syn* and *anti-clinal* 'distortion' isomers which, remarkably, are different colors in the solid-state.[13] In the case of our phenanthridinyl-based *P^N* ligated Cu(I) cations, slight flattening distortions are seen and the observed geometries are best described as *anti*-clinal isomers (**Figure 4.4**).

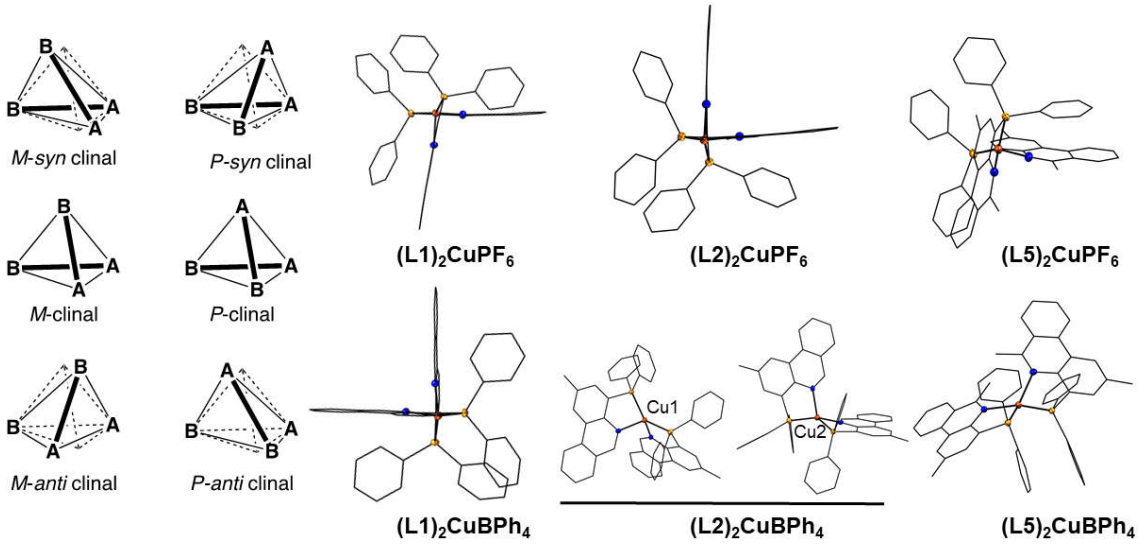

Figure 4.4: Schematic views of cations of **$(L1)_2CuX$**, $(L2)_2X$ (X = BPh_4, two crystallographically distinct molecules in asymmetric unit) and **$(L5)_2CuX$** (X = BPh_4, PF_6) illustrating geometric isomers resulting from ligand-induced distortions from tetrahedral geometry.[13]

More pronounced are the significant rocking distortions[8] that can be seen in **Figure 4.5**. It is also evident in the solid-state structures is the pronounced bending of the Cu-N bond out of plane with the phenanthridine ligand in the **$(L5)_2Cu_2X_2$** complex. The dihedral angle of the Cu-N vector with the plane formed by the tricyclic phenanthridine moiety reaches 21° in **$(L5)_2Cu_2X_2$** , compared with the much more coplanar arrangement in **$(L1)_2Cu_2X_2$/$(L2)_2Cu_2X_2$** (~0-5°; explained in the table following **Table 4.2**).

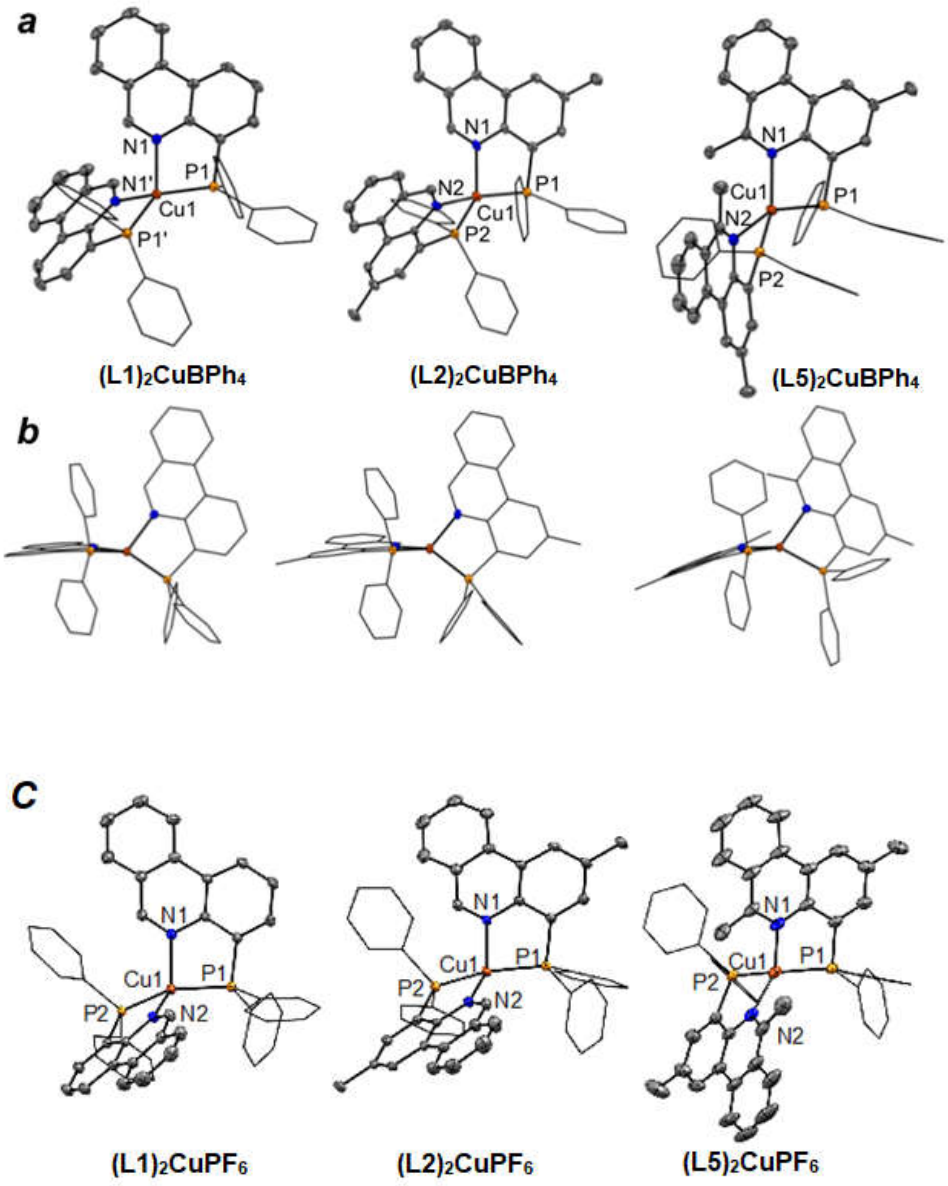

Figure 4. 5: (a) Solid-state X-ray structures of the cationic fragments of **(L1)$_2$CuBPh$_4$**, **(L2)$_2$CuBPh$_4$** and **(L5)$_2$CuBPh$_4$**. Hydrogen atoms, counterions and lattice-confined solvent molecules **(L2)$_2$CuBPh$_4$** are omitted for clarity. (b) View highlighting rocking distortions from idealized tetrahedral geometry and bending of the Cu-N bond out of the phenanthridine ligand plane (c) Solid-state X-ray structures of the cationic fragments of **(L1)$_2$CuPF$_6$**, **(L2)$_2$CuPF$_6$** and **(L5)$_2$CuPF$_6$** with thermal ellipsoids (where shown at 50% probability levels). Hydrogen atoms, counterions and lattice-confined solvent molecules are omitted for clarity.

Table 4. 1: Selected bond lengths (Å) and angles (°) for **$(L1)_2X$**, **$(L2)_2X$** and **$(L5)_2X$**.

	$(L1)_2CuBPh_4$	**$(L2)_2CuBPh_4$**	**$(L5)_2CuBPh_4$**	**$(L1)_2CuPF_6$**	**$(L2)_2CuPF_6$**	**$(L5)_2CuPF_6$**
Cu1-N1/ Cu2-N3	2.0669(16)	2.094(3) 2.066(3)	2.0740(18)	2.0538(16)	2.0578(18)	2.1251(18)
Cu1-N2/ Cu2-N4		2.061(3) 2.094(3)	2.1222(18)	2.0837(15)		2.0951(19)
Cu1-P1/ Cu2-P3	2.2328(5)	2.2041(10) 2.2229(10)	2.2527(6)	2.2195(5)	2.2016(6)	2.2162(6)
Cu1-P2/ Cu2-P4		2.2222(10) 2.2197(10)	2.2251(6)	2.2115(5)		2.2265(6)
N1-Cu1-N2/ N3-Cu2-N4	105.46(9)	101.40(11) 105.94(11)	123.78(7)	109.20(6)	100.19(10)	118.93(7)
P1-Cu1-P2/ P3-Cu2-P4	136.73(3)	131.49(4) 137.17(4)	126.15(2)	145.49(2)	146.99(4)	133.23(2)
N1-Cu1-P1/ N3-Cu2-P3	87.04(5)	86.70(8) 86.14(8)	87.92(5)	87.31(5)	86.83(5)	85.63(5)
N2-Cu1-P2 N4-Cu2-P4		86.59(8) 86.79(8)	85.02(5)	86.34(4)		86.65(5)
N1-Cu1-P2/ N3-Cu2-P4	119.87(5)	117.95(8) 116.76(8)	129.20(5)	116.41(5)	114.83(5)	114.67(5)
N2-Cu1-P1/ N4-Cu2-P3		131.48(8) 123.11(8)	106.63(5)	110.26(5)		121.21(5)
τ_δ[a]	0.64	0.69, 0.63	0.72	0.56	0.54	0.68

[a] $\tau_\delta = \delta*[360-(\alpha+\beta)]/141$, where $\delta = \beta/\alpha$, the ratio of the second largest (β) to largest (α) angle.

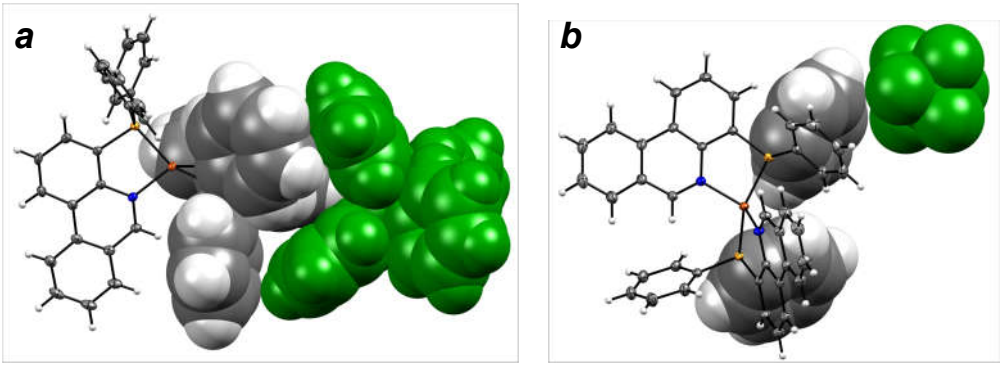

Figure 4. 6: Partial space-filling diagrams for (a) **(L1)$_2$CuBPh$_4$** and (b) **(L1)$_2$CuPF$_6$**.

Table 4. 2: Dihedral angles (°) from solid-state X-ray structures (**(L1)$_2$X**, **(L2)$_2$X** and **(L5)$_2$X**.; X = PF_6, BPh_4) and DFT optimized structures (**L1Cu$^+$**, **L2Cu$^+$** and **L5Cu$^+$**).

	θ_{Cu}[a]	θ_{Phen}[b]	α_P[c]	α_N[d]	P-Cu-P	N-Cu-N	β_N[e]	β_P[f]
(L**1**)$_2$**CuBPh$_4$**	86.9	88.3	144.27(6)	106.41(7)	136.73(3)	105.46(9)	5.71(6)	6.56(3)
(L**1**)$_2$**CuPF$_6$**	83.3	79.3	156.77(5), 151.05(5)	117.82(6), 122.49(6)	145.49(2)	109.20(6)	2.53(5), 5.94(5)	1.34(7), 2.92(6)
(L**2**)$_2$**CuBPh$_4$**[g]	79.6	70.45	142.23(9), 155.53(9)	132.95(12), 119.91(12)	131.49(4)	101.40(11)	0.21(10), 3.91(10)	3.05(14), 7.52(11)
	87.4	89.6	146.74(9), 153.00(10)	126.57(12), 120.98(13)	137.17(4)	105.94(11)	11.90(10), 8.12(10)	0.15(14), 3.31(14)
(L**2**)$_2$**CuPF$_6$**	88.4	84.1	154.16(6)	100.27(8)	146.99(4)	100.19(10)	5.58(6)	--
(L5)$_2$CuBPh$_4$	81.5	89.4	148.14(6), 129.44(6)	128.05(7), 143.88(6)	126.15(2)	123.78(7)	20.29(6), 15.22(6)	4.99(7), 5.37(7)
(L5)$_2$CuPF$_6$	83.4	83.6	140.96(8), 146.71(6)	133.11(9), 128.41(8)	133.23(2)	118.93(7)	21.09(6), 17.45(7)	8.92(10), 1.10(11)
1$^+$ (S_0)	85.3	82.3			144.24	109.17		
1$^+$ (T_1)	73.0	71.9			108.72	105.63		
2$^+$ (S_0)	85.3	82.6			144.14	109.18		
2$^+$ (T_1)	72.1	73.6			108.61	105.78		
3$^+$ (S_0)	85.5	86.2			130.56	118.55		
3$^+$ (T_1)	**80.3**	**79.0**			107.68	120.89		

[a] dihedral angle between planes formed by P1-Cu1-N1/P2-Cu1-N2
[b] dihedral angle between planes formed by carbon/nitrogen atoms of the two phenanthridine moieties
[c] angle formed by (P-Cu) bond vector with P-Cu-N plane of second ligand calculated as (180 – β), where β is the acute angle between a line through the bond and the perpendicular projection of that bond on the plane.
[d] angle formed by (N-Cu) bond vector with P-Cu-N plane of second ligand.
[e] dihedral angle between (N-Cu) bond vector and phenanthridine plane of same ligand.
[f] dihedral angle between (P-Cu) bond vector and phenanthridine plane of same ligand.
[g] two crystallographically distinct molecules in the asymmetric unit

4.3.2. Electronic Absorption and Photoluminescence:

Absorption spectra of all the Cu(I) complexes were recorded in DCM solution at room temperature (**Figure 4.7**).

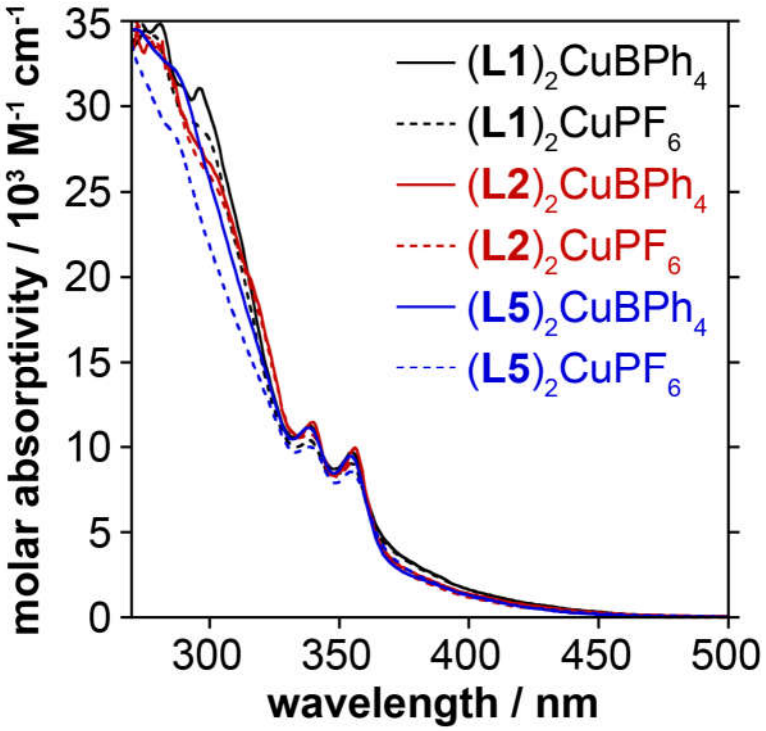

Figure 4. 7: UV-Vis absorption spectra of **(L1)$_2$CuX, (L2)$_2$CuX** and **(L5)$_2$CuX** recorded in CH_2Cl_2 at room temperature.

All show strong absorption features in the UV region (250-300 nm; ε ~ 35 × 10^3 $M^{-1}cm^{-1}$), with two distinct but weaker bands at ~340 nm and a weak tail into the visible region. The intense absorption bands in the UV are assigned to ligand-centered (LC) π-π* transitions of the diphenylphosphino and phenanthridine units. The two distinct maxima evident at ~338 and ~355 nm also appear in the spectra of the proligands.

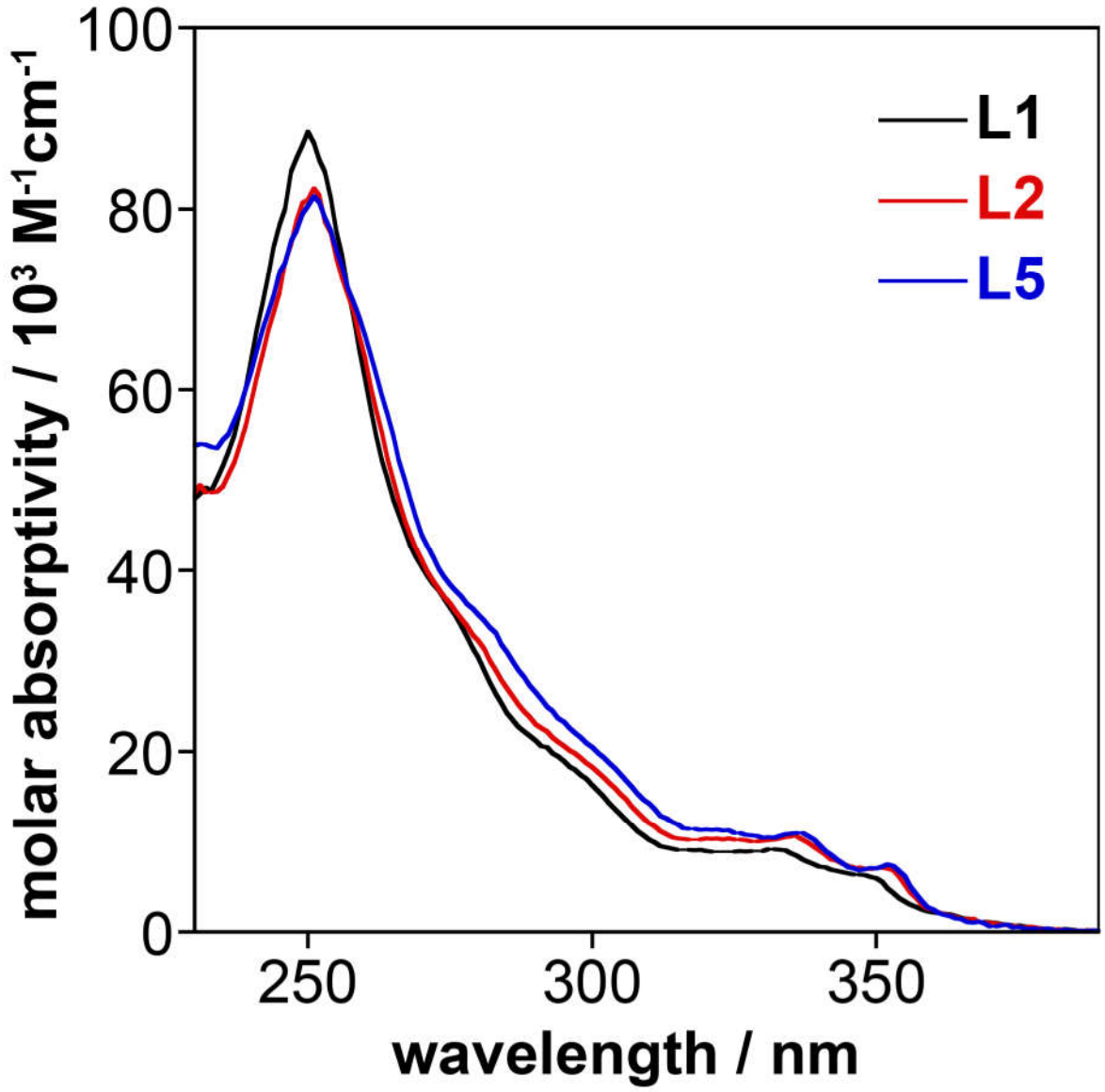

Figure 4. 8: Absorption spectra of L1, L2, and L5 in CH_2Cl_2 at 298 ± 3 K.

Bands in this region are in fact characteristic of phenanthridine itself and also of many of its derivatives[14], including in the dimeric $(\mathbf{L})_2Cu_2X_2$ precursors.[11] In contrast, the absorption spectra of related $(P\text{^}N)_2$Cu(I) complexes of bidentate quinolinylphosphine ligands, *bis*((8-diphenylphosphino)quinoline)Cu(I) and *bis*((8-diphenylphosphino)-2-methylquinoline)Cu(I), are

broad and featureless in this region.[9] The major difference between the absorption spectra of the ligands and their Cu(I) complexes is the longer wavelength tail in the visible region of those complexes, attributable to relatively weak spin-allowed charge-transfer transitions (^{1}CT), in which the phenanthridine heterocycle serves as the CT acceptor. By analogy to homoleptic $[Cu(N\text{^}N)_2]^+$ complexes,[15] I assign these as metal-to-ligand ^{1}MLCT in character, the donor orbitals being of metal-based *d* character with participation from the phosphine-metal bonding pairs. Close examination of the peaks around ~341 nm and ~357 nm revealed only slight bathochromic shift for all BPh_4^- complexes, with the sets of spectra otherwise indistinguishable. Thus, the different ligand geometries observed in the solid-state are likely brought to equilibrium in solution, yielding virtually isoenergetic spectral profiles. This is supported by TD-DFT calculated vertical absorption energies and DFT-determined frontier orbital energies, which are similar for the three cations **(L1)Cu$^+$**, **(L2)Cu$^+$** and **(L5)Cu$^+$**.

Table 4. 3: Calculated photophysical parameters for **(L1)Cu$^+$**, **(L2)Cu$^+$** and **(L5)Cu$^+$** complexes.

E **(eV)**	**(L1)Cu$^+$**	**(L2)Cu$^+$**	**(L5)Cu$^+$**
Δ*E* (S_1-TD)	3.110	3.172	3.158
Δ*E* (S_1-T_1)	0.863	0.901	0.721
Δ*E*(adiab)	2.247	2.272	2.436
Δ*E*(phos)	1.444	1.477	1.691
λ_T	0.803	0.795	0.745

In addition, all three complexes showed irreversible redox events at similar potentials vs $FcH^{0/+}$ (FcH = $(\eta^5\text{-}C_5H_5)_2Fe$; oxidation: **$(L1)_2CuPF_6$** ~0.755 V, **$(L2)_2CuPF_6$** ~0.741 and **$(L5)_2CuPF_6$**

~0.690; reduction: **(L1)$_2$CuPF$_6$** ~ -2.142 V, **(L2)$_2$CuPF$_6$** ~ -2.216 and **(L5)$_2$CuPF$_6$** ~ -2.355; see **Figure 4.9**).

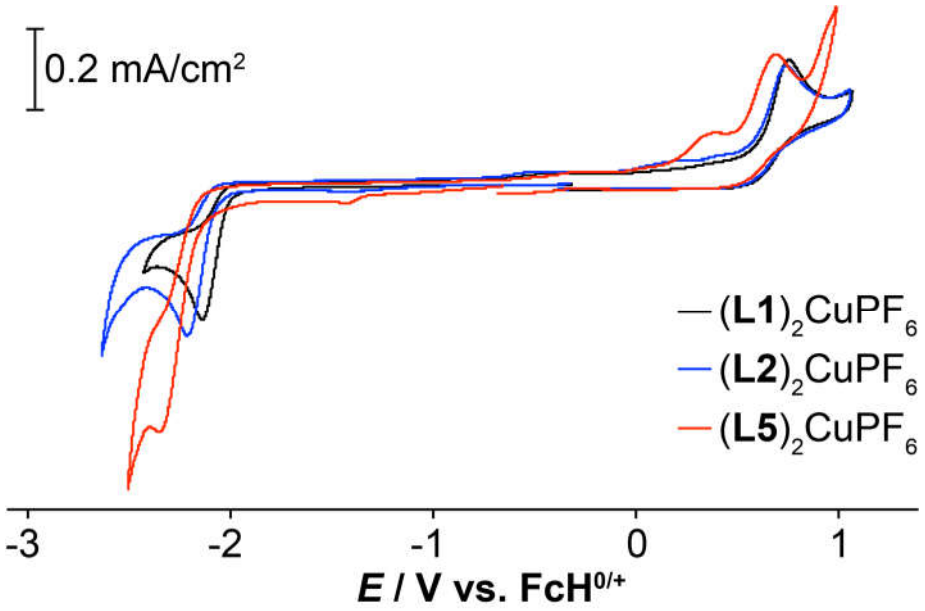

Figure 4. 9: Cyclic voltammograms of **(L1)$_2$X**, (L**2**)$_2$**X** and (L**5**)$_2$**X**.; X = PF_6 ([analyte] = 1.1 mM; 0.1 M [*n*Bu$_4$N][PF_6], 100 mV/s scan rate).

While a slight cathodic shift is observed with increased alkylation of the phenanthridinyl unit, making it harder to reduce, a corresponding shift to the oxidation potential is also observed with methylation. The electrochemically estimated HOMO-LUMO gaps for the series of complexes fall within a relatively narrow spread of 150 mV (**Table 4.4**), consistent with their isoenergetic absorption spectra.[16]

Table 4. 4: Tabulated potentials vs. $FcH^{0/+}$ of irreversible redox events for $(L1)_2X$, $(L2)_2X$ and $(L5)_2X$.; X = PF_6 ([analyte] = 1.1 mM; 0.1 mM [nBu$_4$N][PF_6], 100 mV/s scan rate)

	$E_{peak,\ cathodic}$	$E_{peak,}$ anodic	$\Delta E_{cathodic-anodic}$
(L1)CuPF$_6$	-2.142	0.755	2.897
(L2)CuPF$_6$	-2.216	0.741	2.957
(L3)CuPF$_6$	-2.355	0.690, 0.335[a]	3.045

[a] Minor anodic peak observable in Figure 4.9.

In DCM solution, the complexes are not emissive at ambient temperature, even with rigorous exclusion of oxygen. But, powdered samples of all six complexes are brightly luminescent to the eye when observed under long-wavelength UV irradiation, glowing bright yellow to orange in colour (**Figure 4.10**). The emission of Cu(I) complexes were therefore studied in the solid state at ambient temperature, using an integrating sphere to evaluate photoluminescence quantum yields (Φ_{lum}) under continuous-wave excitation, and with pulsed laser diode excitation to measure the corresponding luminescence lifetimes (τ) (**Table 4.5; Figure 4.11**).

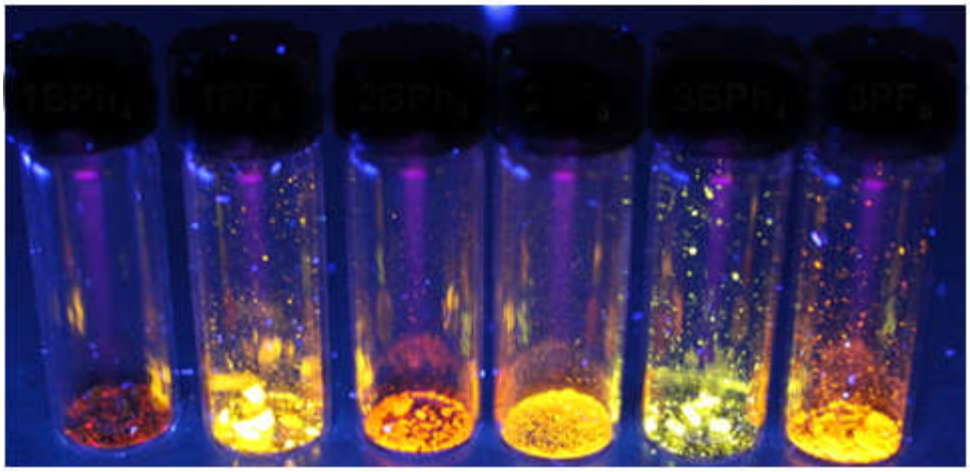

Figure 4. 10: Optical photographs of **(L1)$_2$CuX**, **(L2)$_2$CuX** and **(L5)$_2$CuX** ; X = PF_6, BPh_4 under UV light (long-wave radiation).

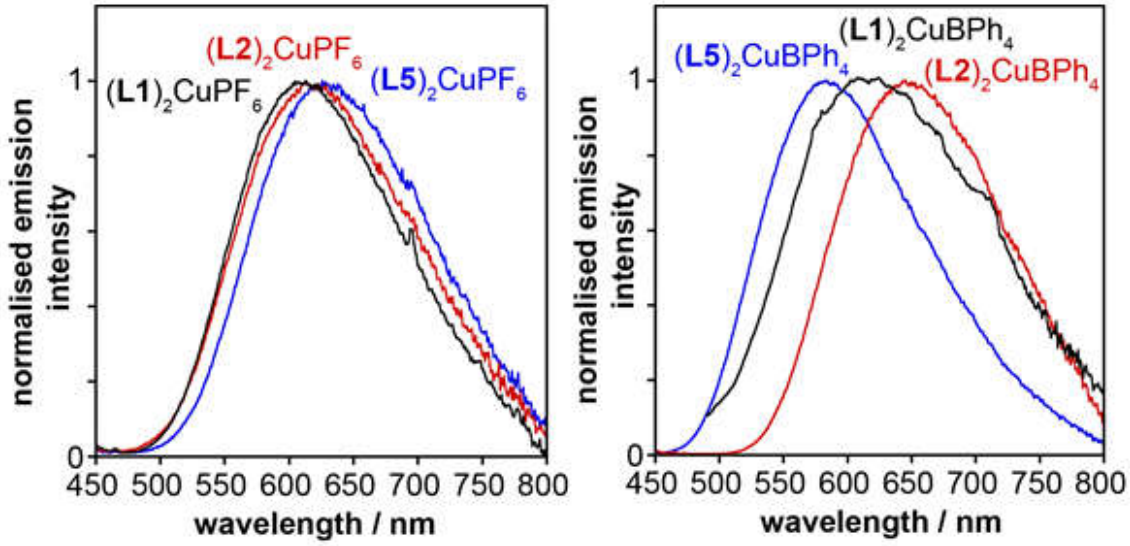

Figure 4. 11: Emission spectra of **(L1)$_2$CuX, (L2)$_2$CuX** and **(L5)$_2$CuX**. in the solid-state at 298 ± 3 K λ_{ex} = 425 nm, where X = *(a)* PF_6^- or *(b)* BPh_4^-.

Table 4. 5: Emission data for **(L1)$_2$CuX**, (L**2)$_2$CuX** and (L**5)$_2$CuX**. in the solid state at 298 ± 1 K and in dilute EPA glass at 77 K. (Lifetimes for the former are quoted in ns and for the latter in μs).

Compound	Emission in the solid state at 298 ± 1 K			Emission in EPA glass at 77 K[(c)]	
	λ_{max} / nm[(a)]	$\Phi_{lum} \times 10^2$ [(a)]	τ / ns [(b)]	λ_{max} / nm	τ / μs [(d)]
(L1)CuPF$_6$	607	2.4	2100	615	51, 144 (43/56)
(L2)$_2$CuPF$_6$	619	0.80	1900	611	39, 150 (28/72)
(L5)$_2$CuPF$_6$	629	1.7	1300	564	740
(L1)$_2$CuBPh$_4$	618	2.9	710	615	47, 134 (35/65)
(L2)$_2$CuBPh$_4$	647	2.0	840	611	48, 160 (28/72)
(L5)$_2$CuBPh$_4$	584	8.9	7400	564	730

(a) Values from spectra recorded using an integrating sphere, λ_{ex} = 425 nm. *(b)* Measured by time-correlated single-photon counting, λ_{ex} = 425 nm. *(c)* EPA = diethyl ether / isopentane / ethanol (2:2:1 v/v). *(d)* Measured by multichannel scaling, λ_{ex} = 370 nm. Where two values are given, the decay follows biexponential kinetics with relative magnitudes of the two components in parenthesis.

For all six complexes in powdered form, broad, featureless emission peaks are observed, consistent with MLCT character to the emissive state. [15,5] All show maxima in the orange-to-red region of the spectrum, between 584 and 647 nm, with quantum yields mostly around 2%, but complex **(L5)$_2$CuBPh$_4$** has a significantly higher quantum yield. The lifetimes are roughly around of the order of a microsecond, with some variation (**Table 4.5**); **(L5)$_2$CuBPh$_4$** is again notable in that it displays a significantly longer lifetime than the other complexes. Hexafluorophosphate salts of Cu(I) complexes of bidentate *P^N* ligands incorporating smaller quinolinyl π-systems *bis*((8-diphenylphosphino)quinoline)Cu(I), and **(L5)$_2$CuPF$_6$**, *bis*((8-diphenylphosphino)-2-methylquinoline)Cu(I), but that are otherwise directly analogous to **(L1)$_2$CuPF$_6$** and (L**5)$_2$CuPF$_6$** respectively, show broad emission centred at 640 nm, with

lifetimes of 0.33 and ~ 1.0 μs, respectively.[9] In comparison, the emission maxima (λ_{max}) of **(L1)$_2$CuPF$_6$** is blue-shifted by 22 nm compared to that of **(L5)$_2$CuPF$_6$**.

In a frozen glass of EPA at 77 K, complexes L**1CuX** and L**2CuX** display orange/red luminescence while the brighter luminescence of L**5CuX** is green-yellow to the eye (EPA = diethyl ether / isopentane / ethanol, 2:2:1 v/v). The corresponding emission spectra are broad and structureless (**Figure 4.10**), and highlight a substantial blue-shift of **L5CuX** compared to **L1CuX** and **L2CuX** (whose emission maxima are very close to one another) by not considering the counterion. The timescale of luminescence is long: complexes **(L5)$_2$CuPF$_6$** and **(L5)$_2$CuBPh$_4$** have emission lifetimes of 740 and 730 μs respectively (the same, within the uncertainty on the measurement). The emission data of the **(L1)$_2$CuX** and **(L2)$_2$CuX** complexes is shorter, showing biexponential decay, fitting to a major component of about 150 μs and a minor of around 50 μs in each case. The long lifetimes are indicative of phosphorescence from a triplet state via intersystem crossing. The formally forbidden $T_1 \rightarrow S_0$ emission is evidently promoted by the Cu(I) centre, however, since the phosphorescence lifetimes of the corresponding free *P^N* ligands are of the order of hundreds of *milliseconds* (τ = 240, 310, and 530 ms for **L1**, **L2**, and **L5**, respectively).The temporal decay of the emission from ligands are easily visible to the naked eye.

The substantial blue-shift of the phosphorescence of L**5CuX** relative to the other complexes (reproducible by TD-DFT) – despite the absorption spectra being so similar for all six complexes – may be indicative of inhibition of attainment of a geometry that most stabilises the triplet state, probably as a result of the steric influence of the *ortho* methyl groups (see below). In Cu(I) complexes of phenanthroline *N^N* ligands, the steric impact of *ortho*-positioned methyl groups typically boosts quantum yields and leads to longer emission lifetimes, as noted in the

Introduction.[8] In the case of our *P^N* ligands, an extraordinary effect of the counterion could be seen in the room temperature spectra. In frozen glass at 77 K, the impact of ligand modification is evident in the particularly blue-shifted of emission from **L5CuX** compared to **L1CuX/L2CuX**. At low temperature, *ortho* methylation of nitrogen clearly has a large impact on structural reorganization, whereas methylation *para* to nitrogen (i.e., in **L2**) does not. At room temperature, this same structural modification of the *P^N* ligand has rather little effect on the emission maxima for the PF_6^- salts, while a much bigger variation is seen in emission wavelength according to *P^N* ligand for the BPh_4^- salts.

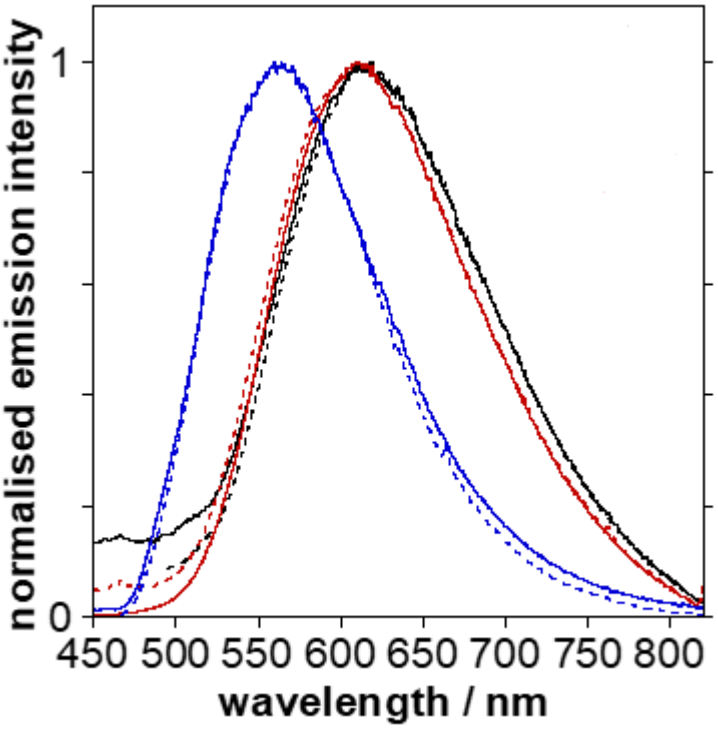

Figure 4. 12: Emission spectra of ('–,---'**(L1)$_2$CuX**, '–,---'(L**2**)$_2$**CuX** and '–,---'(L**5**)$_2$**CuX**; X = PF_6, BPh_4) in dilute EPA glass at 77 K, λ_{ex} = 370 nm.

To examine if this counterion amplification of ligand design effects is due to closer inter-ion interactions observed in the solid state (**Figure 4.6**), I compared the DFT-optimized (gas-phase) geometries of the cations in both the ground state (S_0) and first triplet excited state (T_1), and investigated the electronic structure and nature of the optical transitions with TD-DFT. In the T_1 excited state, all three cations show elongation of Cu-P distances, which is most pronounced for (L**1**)**Cu**$^+$.

Table 4. 6: Selected bond distances [Å] and angles [°] for the DFT-optimized S_0 and T_1 state structures of $(L1)_2Cu^+$, $(L2)_2Cu^+$, and $(L5)_2Cu^+$.

	$(L1)_2Cu^+$		**$(L2)_2Cu^+$**		**$(L5)_2Cu^+$**	
Bond (Å)	**S_0**	**T_1**	**S_0**	**T_1**	**S_0**	**T_1**
Cu-N1	2.104	1.921	2.102	2.097	2.146	2.185
Cu-N2	2.104	2.098	2.102	1.920	2.121	1.945
Cu-P1	2.238	2.297	2.238	2.299	2.244	2.262
Cu-P2	2.237	2.271	2.238	2.272	2.257	2.290
Angle (°)	**S_0**	**T_1**	**S_0**	**T_1**	**S_0**	**T_1**
N1-Cu-N2	109.2	105.6	109.2	105.8	118.5	120.9
N1-Cu-P1	85.7	84.4	115.5	114.7	86.0	84.1
N1-Cu-P2	115.5	159.0	85.8	84.2	114.5	113.2
N2-Cu-P1	115.4	115.0	85.8	84.4	124.2	144.9
N2-Cu-P2	85.7	84.1	115.5	159.0	86.4	85.9
P1-Cu-P2	144.3	108.7	144.1	108.6	130.6	107.7

This is consistent with participation of filled Cu-P σ-bonding orbitals in the MLCT excitation to vacant phenanthridine-based π* acceptor orbitals, supported by population analysis

of the frontier and next-nearest-in-energy orbitals, and TD-DFT enabled assignment of the lowest energy excitation as HOMO→LUMO/HOMO-1→LUMO+1 in character. The most noticeable structural change is to the coordination geometry of the four-coordinate Cu centre. The three optimized S_0 structures have τ_δ metrics of 0.57 (L**1**)$_2$**Cu**$^+$, 0.57 (L**2**)$_2$**Cu**$^+$ and 0.71 (L**5**)$_2$**Cu**$^+$, which align well with the τ_δ metrics and distorted sawhorse geometries of all the PF_6 salts (**Table 4.1**). In the triplet excited state (T_1) state, a distinct distortion towards true sawhorse geometry is accompanied by a reduction in τ_δ to 0.44 (L**1**)$_2$**Cu**$^+$, 0.44 (L**2**)$_2$**Cu**$^+$ and 0.56 (L**5**)$_2$**Cu**$^+$; **Table 4.7**).

Table 4. 7: Geometric indices (τ_δ)[17] of **(L1)$_2$CuX**, (L**2**)$_2$**CuX** and (L**5**)$_2$**CuX**; X = PF_6, BPh_4) crystal structures, and DFT optimized S_0 and T_1 structures of $L1^+$, $L2^+$ and $L5^+$.

τ_δ	**PF_6**	**BPh_4**	**S_0**	**T_1**
(L1)$_2$CuX	0.56	0.64	0.57	0.44
(L2)$_2$CuX	0.54	0.64	0.57	0.44
(L5)$_2$CuX	0.70	0.72	0.71	0.56

In addition, for (L**1**)$_2$**Cu**$^+$/(L**2**)$_2$**Cu**$^+$ the P-Cu-P angles compress notably from 144° in the ground state to 109° in the first excited triplet state. The same angle in the more sterically encumbered $(L5)_2Cu^+$ is also made more acute in the excited state (S_0: 131° vs. T_1: 108°), but as this angle is tighter in the ground state already, the change is small. The N-Cu-N angles are comparatively invariant for all three complexes, constricting by only a few degrees for (L**1**)$_2$**Cu**$^+$/(L**2**)$_2$**Cu**$^+$ (S_0: 109° vs. T_1: 106°) and relaxingly slightly for $(L5)_2Cu^+$ (S_0: 119° vs. T_1: 121°).

Thus, inclusion of 6-position methyl groups in the phenanthridine on its own is not enough to prevent significant reorganization in the emissive excited states at room temperature. As a result, emission from **(L1)$_2$CuPF$_6$**, (**L2)$_2$CuPF$_6$** and **(L5)$_2$CuPF$_6$** is relatively close to each other even in the solid-state, under ambient conditions. At 77K, there is sufficient scope for slight reorganisation in the emissive state for (L**1)$_2$CuX** and (L**2)$_2$CuX** and emission wavelengths are isoenergetic, while (L**5)$_2$CuX** shows blue-shifted emission for both ion pairs, highlighting the impact of *ortho*-methylation. At room temperature, replacing PF_6^- counterion with BPh_4^- leads to closer inter-ion contacts in the solid-state, evident in the space-filling diagrams shown above. As we can see in **Figure 4.12**, to minimize the structural reorganization of the large phenanthrindinyl moiety, in the T_1 geometry, the PPh_2 fragment twists substantially, which would be hampered by the presence of the BPh_4^- ion. The inhibition of this twisting of geometry probably leads to the observed boost in quantum yield of **(L5)$_2$CuBPh$_4$** via reduction of non-radiative decay rates excited state and also accounts for the substantial blue-shift in the wavelength of emission from this complex even at ambient temperature. While packing effects have been previously investigated and reported,[18,19] including counterion-dependent emission,[20,21] this is the first study explaining how close inter-ion interactions can amplify the impact of ligand design in a synergistic fashion.

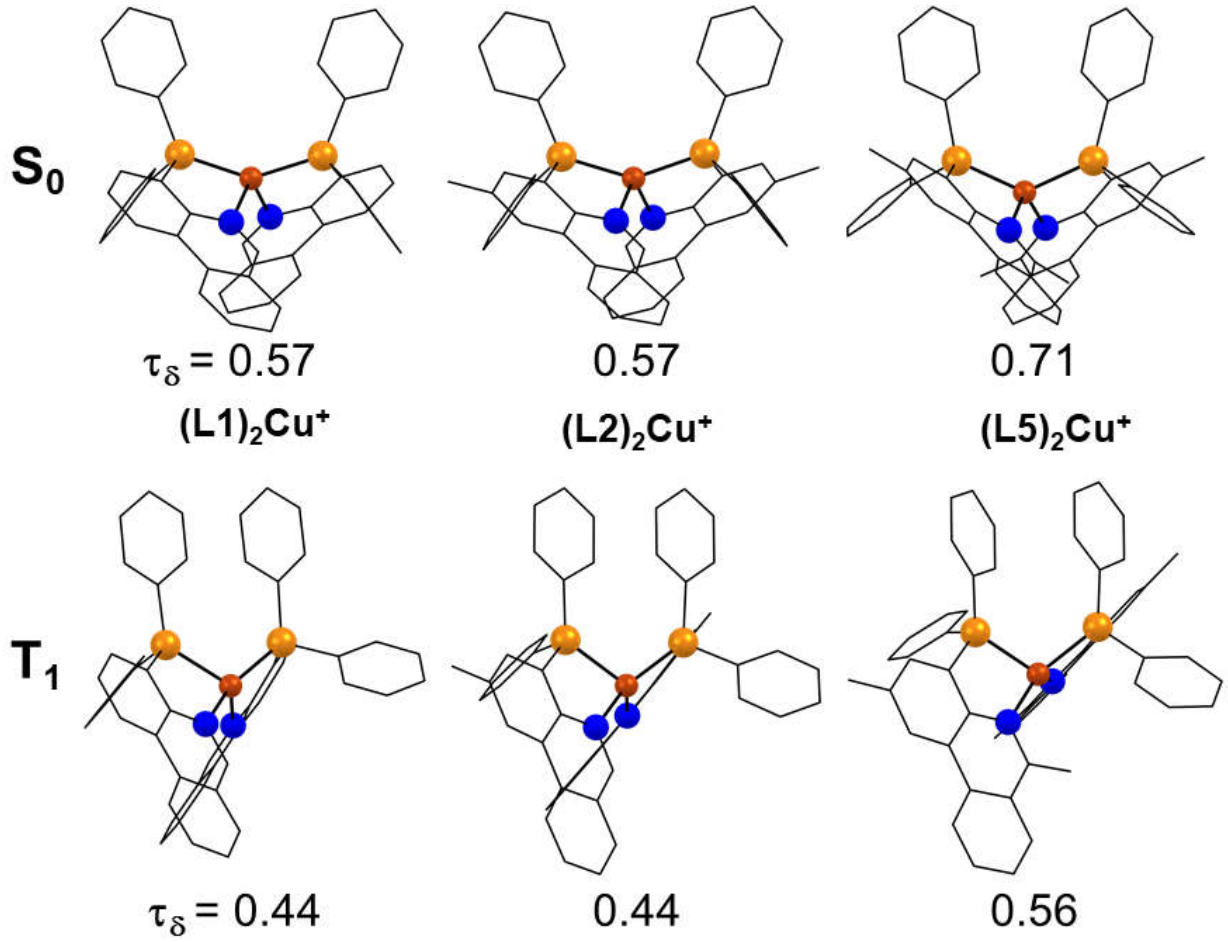

Figure 4. 13: Optimized geometries and τ_δ[17] metrics of the ground-state (S_0) and first excited triplet state (T_1) of **(L1)$_2$Cu$^+$**, **(L2)$_2$Cu$^+$** and **(L5)$_2$Cu$^+$**.

4.4. Conclusion:

While ligand design could be used to tune emission from phosphorescent transition metal complexes, the effect of changes to one ligand architecture may or may not translate to another. Herein, I have found that changing the counterion in [(*P*^*N*)$_2$Cu]X complexes has an intense impact on emission from solid samples. For complexes of PF_6^- anions where inter-ion interactions are restricted, changes to ligand architecture do not have a notable impact on emission properties at room temperature. Introducing a BPh_4^- counterion results in an

amplification of these changes, and emission wavelengths can be tuned to higher energy with an associated boost to quantum yields, unchanging with an increased rigidity to the excited state. This is both an outcome of a bulkier counterion and incorporation of a large, tricyclic phenanthridine moiety on the *P^N* ligand backbone. As a result, I have been able to tune phosphorescence from Cu(I) complexes with closely related supporting ligands from orange-red (647 nm) to quite bright, yellow emission (584 nm), by making use of the synergy between *P^N* ligand *ortho* methylation and inter-ion interactions. Yellow light emitting Cu(I) complexes are relatively rare,[22,23,24,25,26,27] despite yellow being a key component for achieving white light emission in organometallic light emitting diodes (OLEDs).[28] The applicability of this technique for amplifying ligand effects through choice of counterion to other phosphorescent emitters is currently underway.

4.5. Experimental Section:

Unless otherwise stated, all air sensitive experiments were carried out inside an inert-atmosphere glove box (N_2) or using standard Schlenk techniques (Ar). 2,6-Dibromoaniline (AK Scientific), *N*-iodosuccinimide (AK Scientific), *p*-toluidine (Alfa Aesar), *N*-bromosuccinimide (Alpha Aesar), 2-formylphenyl boronic acid (Combi Blocks), 2-acetylphenyl boronic acid (Combi blocks), $Pd(PPh_3)_4$ (Alfa Aesar), Na_2CO_3 (Alfa Aesar), chlorodiphenylphosphine (VWR), CuBr (Aldrich), sodium hexafluorophosphate (Alfa Aesar) and sodium tetraphenylborate (Aldrich) were purchased from commercial suppliers and used as received. 2-Bromo-4-methylaniline,[29] 6-bromo-2-iodo-4-methylaniline,[30] 4-bromo-2-methylphenanthridine,[30] 8-bromo-6-methylquinoline,[29] (4-diphenylphosphino)phenanthridine[10] (**L1**) and (4-diphenylphosphino)-2-methylphenanthridine[11] (**L2**) were synthesized following

published procedures. Organic solvents were dried over appropriate reagents and deoxygenated prior to use, with the exception of 1,2-dimethoxyethane (1,2-DME) and water, which were simply degassed. NMR spectra were recorded on a Bruker Avance 300 MHz or Bruker Avance-III 500 MHz spectrometer as noted. Electronic absorption spectra (750–190 nm) were recorded on a Thermo Scientific Helios Zeta UV-VIS spectrophotometer at room temperature and concentrations on the order of 1.0×10^{-4} mol L^{-1}. Elemental analyses were performed by Canadian Microanalytical Service Ltd., Delta, BC and at the University of Manitoba on a Perkin Elmer EA2400 CHN Analyzer.

Synthesis of $(L1)_2CuBPh_4$: A solution of (4-diphenylphosphino)phenanthridine (0.023 g, 0.063 mmol) in CH_2Cl_2 (3 mL) was added drop-wise to a suspension of CuBr (0.009 g, 0.063 mmol) in CH_2Cl_2 (3 mL) with constant stirring. The reaction mixture was stirred overnight at room temperature. An orange suspension formed, which was filtered through celite and drop-wise added to a solution of one more equivalent of (4-diphenylphosphino)phenanthridine (0.023 g, 0.063 mmol) in CH_2Cl_2 (2 mL). After one hour, a solution of sodium tetraphenylborate (0.021 g, 0.063 mmol) in THF (3 mL) was added. The color changed to yellowish green. Stirring was continued overnight and the reaction mixture then filtered through small plug of celite and dried under vacuum to give a greenish solid, which was washed with Et_2O (50 mL) and dried in vacuum to give an off-white product. X-ray quality single crystals were grown by slow diffusion of hexane into a DCM solution of the product. Yield = 0.044 g (64%). ^{1}H NMR (CDCL5, 500 MHz, 22 °C): δ 8.77 (m, J_{HH} = 10 Hz, 2H, $^{phen}C_{Ar}$-*H*), 8.61 (m, J_{HH} = 10 Hz, 2H, $^{phen}C_{Ar}$-*H*), 8.31 (s, 2H, $^{phen}C_{Ar}$-*H*), 7.95-7.89 (m, 4H, $^{phen}C_{Ar}$-*H*), 7.84 (m, J_{HH} = 10, 5 Hz, 4H, $^{phen}C_{Ar}$-*H*), 7.62 (m, J_{HH} = 10, 5 Hz, 2H, PC_{Ar}-*H*), 7.46-7.36 ppm (overlapped m, 21H, PC_{Ar}-*H*), 7.33-7.30

(overlapped m, 8H, PC_{Ar}-*H,* PC_{BPh4}-*H*), 6.96-6.39 (br, 8H, PC_{BPh4}-*H*), 6.80-6.77 ppm (br, 4H, PC_{BPh4}-*H*). $^{13}C\{^{1}H\}$ NMR (CDCL5, 126 MHz, 22 °C): δ 164.4 (q, J_{CB} = 49 Hz, $^{phen}C_{Ar}$), 156.5 ($^{phen}C_{Ar}$), 145.5 (br, $^{phen}C_{Ar}$-*H*), 136.4 (br, PC_{Ar}-*H*), 136.3 (s, $^{phen}C_{Ar}$), 133.8 ($^{phen}C_{Ar}$-*H*), 133.2 (v br, J_{CP} = 31 Hz, PC_{Ar}), 132.7 (s, PC_{Ar}-*H*), 130.7 (t, $^{phen}C_{Ar}$-*H*), 129.6 (PC_{Ar}-*H*), 129.4 (br, $^{phen}C_{Ar}$-*H*), 129.3 ($^{phen}C_{Ar}$-*H*), 128.9 ($^{phen}C_{Ar}$), 126.4 ($^{phen}C_{Ar}$-*H*), 126.2 ($^{phen}C_{Ar}$), 125.7 (br, $^{phen}C_{Ar}$), 125.5 (br, J_{CB} = 4, PC_{BPh4}), 122.5($^{phen}C_{Ar}$-*H*), 121.5 ppm ($^{phen}C_{Ar}$-*H*). $^{31}P\{^{1}H\}$ NMR (CDCL5, 121 MHz, 22 °C): δ -13.3 ppm (br, s). Anal. Calc. for $C_{74}H_{56}N_2P_2BCu$: C, 80.10; H, 5.09 %. Found: C, 80.26, H, 5.35 %.

Synthesis of (L1)$_2$CuPF$_6$: (L1)$_2$CuPF$_6$ was prepared by a similar procedure to **(L1)$_2$CuBPh$_4$** using (4-diphenylphosphino)phenanthridine (0.023 g, 0.063 mmol) in CH_2Cl_2 (3 mL) and CuBr (0.009 g, 0.063 mmol) in CH_2Cl_2 (3 mL) and followed by addition of one more equivalent (4-diphenylphosphino)phenanthridine (0.023 g, 0.063 mmol) and sodium hexafluorophosphate (0.021 g, 0.063 mmol) in THF (3 mL); solid off white product. X-ray quality single crystals were grown by slow diffusion of Et_2O in DCM solution of the product. Yield = 0.046 g (78%). ^{1}H NMR (CDCL5, 300 MHz, 22 °C): δ 8.93 (br m, *J* = 5 Hz, 2H, $^{phen}C_{Ar}$-*H*), 8.75 (m, *J* = 5 Hz, 2H, $^{phen}C_{Ar}$-*H*), 8.36 (v br, 2H, $^{phen}C_{Ar}$-*H*), 8.04-8.01 (br, 2H, $^{phen}C_{Ar}$-*H*), 7.97-7.93 (overlapped m, 4H, $^{phen}C_{Ar}$-*H*), 7.74-7.71 (m, 2H, PC_{Ar}-*H*), 7.53-7.33 ppm (overlapped m, 22H, PC_{Ar}-*H*). $^{13}C\{^{1}H\}$ NMR (CDCL5, 75 MHz, 22 °C): δ 156.5 ($^{phen}C_{Ar}$H), 145.6 (br, J_{CP} = 16 Hz, $^{phen}C_{Ar}$), 136.3 ($^{phen}C_{Ar}$-*H*), 133.8 (s, PC_{Ar}-*H*), 133.2 (v br, $^{phen}C_{Ar}$), 133.0 (br, PC_{Ar}), 132.8 ($^{phen}C_{Ar}$H), 131.1 (v br, PC_{Ar}), 130.6 (PC_{Ar}H), 129.7 ($^{phen}C_{Ar}$H), 129.4 (br, PC_{Ar}H), 129.3 ($^{phen}C_{Ar}$H), 128.8 ($^{phen}C_{Ar}$), 126.4 ($^{phen}C_{Ar}$), 126.3 ($^{phen}C_{Ar}$H), 125.8 ($^{phen}C_{Ar}$), 122.5 ppm ($^{phen}C_{Ar}$H). $^{31}P\{^{1}H\}$ NMR (CDCL5, 121 MHz, 22 °C): δ -13.1 (br, s), 144.3 ppm (sep). ^{19}F NMR (CDCL5, 121 MHz, 25

°C): -73.89 ppm (d, J_{PF} = 755 Hz). Anal. Calc'd for: $C_{50}H_{36}N_2P_3F_6Cu$•$0.5CH_2Cl_2$: C, 62.14, H, 3.99 %. Found: C, 60.20; H, 4.00 %.

Synthesis of (L2)$_2$CuBPh$_4$: Following the similar procedure of (L**1)$_2$CuBPh$_4$,** (2-methyl,4-diphenylphosphino)phenanthridine (0.024 g, 0.063 mmol) was added drop-wise to CuBr (0.009 g, 0.063 mmol) in CH_2Cl_2 (6 mL). Then one more equivalent (2-methyl,4-diphenylphosphino)phenanthridine (0.024 g, 0.063 mmol) was added before sodium tetraphenylborate (0.021 g, 0.063 mmol) in THF (3 mL) was added to give an orange solid. X-ray quality single crystals were grown by slow diffusion of Et_2O into a DCM solution of the product. Yield = 0.065 g (91%). ^{1}H NMR (CDCL5, 500 MHz, 22 °C): δ 8.60 (br, 4H, $^{phen}C_{Ar}$-*H*), 8.25 (s, 2H, $^{phen}C_{Ar}$-*H*), 7.91 (m, J_{HH} = 15, 10 Hz, 2H, $^{phen}C_{Ar}$-*H*), 7.70 (br, J_{HH}= 10 Hz, 2H, $^{phen}C_{Ar}$-*H*), 7.61 (m, J_{HH} = 10, 15 Hz, 4H, $^{phen}C_{Ar}$-*H*), 7.46-7.32 (overlapped m, 30H, PC_{Ar}-*H,* PC_{BPh4}-*H*), 6.96 (overlapped m, 8H, PC_{BPh4}-*H*), 6.79 (overlapped m, 4H, PC_{BPh4}-*H*), 2.65 ppm (s, 3H, $^{Phen}C_{Me}$-*H*). ^{13}C{^{1}H} NMR (CDCL5, 126 MHz, 22 °C): δ 164.4 (q, J_{CB} = 49 Hz, PC_{BPh4}), 155.5 (br, $^{phen}C_{Ar}$-*H*), 144.0 (t, J_{CP} = 10, 11 Hz, $^{phen}C_{Ar}$), 139.2 (s, PC_{Ar}), 137.5 (s, $^{phen}C_{Ar}$-*H*), 133.5 ($^{phen}C_{Ar}$-*H*), 133.2 (v br, PC_{Ar}), 132.9 (t, J_{CP} = 16, 17 Hz, PC_{Ar}), 132.4 ($^{phen}C_{Ar}$), 131.1 (v br, PC_{Ar}), 130.6 (PC_{Ar}-*H*), 129.5 (PC_{Ar}-*H*), 129.4 (br, $^{phen}C_{Ar}$-*H*), 129.1 (PC_{Ar}H), 126.3 ($^{phen}C_{Ar}$H), 126.1 (s, $^{phen}C_{Ar}$), 125.6(t, $^{phen}C_{Ar}$), 125.5 (br, J_{CB} = 3 Hz, PC_{BPh4}-*H*), 122.4 (s, $^{phen}C_{Ar}$), 121.5 (s, PC_{BPh4}-*H*), 22.15 ppm ($^{Phen}C_{Me}$-*H*). ^{31}P{^{1}H} NMR (CDCL5, 202 MHz, 22 °C): δ -13.1 ppm (br, s). Anal. Calc'd for: $C_{78}H_{60}BCuN_2P_2$: C, 80.24; H, 5.32 %. Found: C: 80.41, H: 5.32 %.

Synthesis of (L2)$_2$CuPF$_6$: Complex **(L2)$_2$CuPF$_6$** was synthesized in a similar way to **(L1)$_2$CuBPh$_4$** using **L2** (0.024 g, 0.063 mmol) and CuBr (0.089 g, 0.063 mmol). Then one more equivalent (2-methyl,4-diphenylphosphino)phenanthridine (0.024 g, 0.063 mmol) was added to the reaction mixture, before adding a solution of sodium hexafluorophosphate (0.021 g, 0.063

mmol) in THF (3 mL); solid yellowish-green product. X-ray quality single crystals were grown by slow diffusion of hexane into a DCM solution of the product. Yield = 0.49 g (80%). ^{1}H NMR (CDCL5, 300 MHz, 22 °C): δ 8.71 (m, J = 5 Hz, 2H, $^{phen}C_{Ar}$-*H*), 8.68 (br, 2H, $^{phen}C_{Ar}$-*H*), 8.27 (br, 2H, $^{phen}C_{Ar}$-*H*), 8.00 (m, 2H, $^{phen}C_{Ar}$-*H*), 7.72-7.69 (overlapped m, 4H, $^{phen}C_{Ar}$-*H*), 7.51-7.34 (overlapped m, 22H, $^{phen}C_{Ar}$-*H*, PC_{Ar}-*H*), 2.68 ppm (s, 6H, $^{Phen}C_{Me}$-H). ^{13}C{^{1}H} NMR (CDCL5, 75 MHz, 22 °C): δ 155.6 ($^{phen}C_{Ar}$-*H*), 144.0 (br, J_{CP} = 9,11 Hz, $^{phen}C_{Ar}$), 139.2 ($^{phen}C_{Ar}$-*H*), 137.4 (PC_{Ar}-*H*), 133.5 ($^{phen}C_{Ar}$), 133.2 (v br, $^{phen}C_{Ar}$-*H*), 132.8 (PC_{Ar}), 132.5 (PC_{Ar}), 131.1 (v br, PC_{Ar}), 130.6 (PC_{Ar}-*H*), 129.7 ($^{phen}C_{Ar}$), 129.4 (br, PC_{Ar}-*H*), 129.1 ($^{phen}C_{Ar}$-*H*), 126.4 ($^{phen}C_{Ar}$), 126.1 ($^{phen}C_{Ar}$), 125.6 ($^{phen}C_{Ar}$), 122.4 ($^{phen}C_{Ar}$-*H*), 22.14 ppm ($^{Phen}C_{Me}$-*H*). ^{31}P{^{1}H} NMR (CDCL5, 121 MHz, 22 °C): δ -13.06 (br, s), 144.3 ppm (sep). ^{19}F NMR (CDCL5, 282 MHz, 22 °C): -73.9 ppm (d, J_{PF} = 755 Hz). Anal. Calc'd for: $C_{52}H_{40}N_2P_3F_6Cu$: C, 60.73, H, 4.04 %. Found: C, 60.16; H, 4.14 %.

Synthesis of ((2,6-dimethyl)(4-diphenylphosphino)phenanthridine)$_2$Cu$_2$Br$_2$: This complex was synthesized via a procedure analogus to that described previously[31]. **L5** (0.024 g, 0.063 mmol) in CH_2Cl_2 (3 mL) was drop-wise added to a stirring suspension of CuBr (0.009 g, 0.063 mmol) in CH_2Cl_2 (3 mL). The reaction mixture was stirred overnight at room temperature, giving a yellow suspension which was filtered through a small plug of Celite and recrystallized following slow diffusion of hexane into a dichloromethane solution. Orange-yellow crystals. Yield = 0.026 g (81%). ^{1}H NMR (CDCL5, 300 MHz, 22 °C): δ 8.71 (br, J_{HH} = 15 Hz, 1H, $^{phen}C_{Ar}$-*H*), 8.58 (s, 1H, $^{phen}C_{Ar}$-*H*), 8.07 (br, 1H, $^{Phen}C_{Ar}$-*H*), 7.97 (m, J_{HH} = 10, 15 Hz, 1H, $^{phen}C_{Ar}$-*H*), 7.74 (m, J_{HH} = 10, 15 Hz, 1H, $^{phen}C_{Ar}$-*H*), 7.50 (s, 1H, $^{Phen}C_{Ar}$-*H*), 7.37 – 7.28 (overlapped m, 5H, PC_{Ar}-*H*), 7.23 – 7.18 (overlapped m, 5H, PC_{Ar}-*H*), 2.59 ppm (s, 6H, $^{phen}C^{2}_{Me}$-*H,* $^{phen}C^{6}_{Me}$-*H*). ^{13}C{^{1}H} NMR (CDCL5, 126 MHz, 22 °C): δ 162.1 (s, $^{phen}C_{Ar}$-*H*), 143.6 (s,

$^{phen}C_{Ar}$), 137.7 (br, $^{phen}C_{Ar}$-*H*), 133.2 ($^{phen}C_{Ar}$), 132.5 (d, PC_{Ar}-*H*), 132.3 (d, $^{phen}C_{Ar}$-*H*), 129.9 ($^{phen}C_{Ar}$-*H*), 128.9 ($^{phen}C_{Ar}$-*H*), 127.8 ($^{phen}C_{Ar}$-*H*), 126.4 ($^{phen}C_{Ar}$), 125.7 (br, $^{phen}C_{Ar}$), 125.2 (d, $^{phen}C_{Ar}$), 122.8 ($^{phen}C_{Ar}$-*H*), 25.7 (C_{Me}), 21.9 ppm (C_{Me}). $^{31}P\{^{1}H\}$ NMR (CDCL5, 121 MHz, 22 °C): δ -28.6 ppm (br, s).

Synthesis of (L5)$_2$CuBPh$_4$: L5 (0.025 g, 0.063 mmol) and CuBr (0.009 g, 0.063 mmol) were first combined in THF (3 mL) to give a yellow suspension. An second equivalent of **L5** (0.025 g, 0.063 mmol) and sodium tetraphenylborate (0.011 g, 0.063 mmol) in THF (3 mL) were then added. The resulting yellow-green solution was filtered through Celite and dried, and X-ray quality single crystals were grown by slow diffusion of hexane into a CH_2Cl_2 solution of the product. Yield = 0.041 (56%). ^{1}H NMR (CD_2Cl_2, 500 MHz, 22 °C): δ 8.77 (m, J_{HH}= 15 Hz , 2H, $^{phen}C_{Ar}$-*H*), 8.71 (s, 2H, $^{phen}C_{Ar}$-*H*), 8.02 (m, J_{HH} = 15, 10 Hz, 2H, $^{phen}C_{Ar}$-*H*), 7.97 (br, J_{HH}= 10 Hz, 2H, $^{phen}C_{Ar}$-*H*), 7.75 (m, J_{HH} = 10, 15 Hz, 4H, $^{phen}C_{Ar}$-*H*), 7.65 (v br, 2H, PC_{Ar}-*H*), 7.39-7.37 (overlapped m, 4H, $^{phen}C_{Ar}$-*H,* PC_{Ar}-*H*), 7.33 (overlapped m, 8H, PC_{Ar}-*H*), 7.23-7.16 (overlapped m, 16H, PC_{Ar}-*H,* PC_{BPh4}-*H*), 7.02-7.00 (overlapped m, 8H, PC_{BPh4}-*H*), 6.87-6.84 (overlapped m, 4H, PC_{BPh4}-*H*), 2.64 (s, 3H, $^{Phen}C_6$Me-*H*), 2.43 ppm (s, 3H, $^{Phen}C_2$Me-*H*). $^{13}C\{^{1}H\}$ NMR (CD_2Cl_2, 126 MHz, 22 °C): δ 164.6 (q, J_{CB} = 49 Hz, PC_{BPh4}), 162.8 (br, $^{phen}C_{Ar}$), 144.2 (t, J_{CP} = 8,10 Hz, $^{phen}C_{Ar}$), 138.9 (PC_{Ar}-*H*), 138.6 ($^{phen}C_{Ar}$-*H*), 136.4 ($^{phen}C_{Ar}$-*H*), 133.3 (br, PC_{Ar}-*H*), 132.8 (PC_{Ar}), 132.6 (t, J_{CP} = 16,16 Hz, $^{phen}C_{Ar}$), 132.2 (br, PC_{Ar}), 130.6 ($^{phen}C_{Ar}$-*H*), 129.4 (br, $^{phen}C_{Ar}$-*H*), 129.2 (PC_{Ar}),128.8 ($^{phen}C_{Ar}$), 128.1 ($^{phen}C_{Ar}$H), 126.7 ($^{phen}C_{Ar}$), 126.4 ($^{phen}C_{Ar}$-*H*), 126.1 (br, J_{CB} = 3 Hz, PC_{BPh4}-*H*), 125.9 (br, $^{phen}C_{Ar}$), 123.2 ($^{phen}C_{Ar}$), 122.2 ($^{phen}C_{Ar}$-*H*), 26.10 ($^{Phen}C^{2}_{Me}$-*H*), 22.04 ppm ($^{Phen}C^{6}_{Me}$-*H*). $^{31}P\{^{1}H\}$ NMR (CDCL5, 121 MHz, 22 °C): δ -17.7 ppm (br, s). Anal. Calc'd for: $C_{78}H_{64}BCuN_2P_2$. CH_2Cl_2: C, 75.87; H, 5.32 %. Found: C, 75.57; H, 5.43 %.

Synthesis of $(L5)_2CuPF_6$: This complex was prepared by a similar procedure using **L5** (0.025 g, 0.063 mmol) and CuBr (0.089 g, 0.063 mmol) in CH_2Cl_2 (6 mL). A yellow suspension formed. Addition of one more equivalent of **L5** (0.025 g, 0.063 mmol) and sodium hexafluorophosphate (0.021 g, 0.063 mmol) in THF (3 mL) gave the product; yellow solid. X-ray quality single crystals were grown by slow diffusion of diethylether into a CH_2Cl_2 solution. Yield = 0.041 g (66%). ^{1}H NMR (CDCL5, 500 MHz, 22 °C): δ 8.78 (d, J = 10 Hz, $^{phen}C_{Ar}$-*H*), 8.69 (br, 1H, $^{phen}C_{Ar}$-*H*), 8.03 (m, J = 5, 10 Hz, 1H, $^{phen}C_{Ar}$-*H*), 7.98 (d, J = 5 Hz, 2H, $^{phen}C_{Ar}$-*H*), 7.77 (t, J = 10, 15 Hz, 2H, $^{phen}C_{Ar}$-*H*), 7.54 (v br, 2H, PC_{Ar}-*H*), 7.39-7.36 (overlapped m, 4H, PC_{Ar}-*H*), 7.16 (overlapped m, 16H, PC_{Ar}-*H*), 2.63 (s, 3H, $^{Phen}C^2_{Me}$-*H*), 2.40 ppm (s, 3H, $^{Phen}C^2_{Me}$-*H*). ^{13}C{^{1}H} NMR (CDCL5, 126 MHz, 22 °C): δ 162.5 ($^{phen}C_{Ar}$-*H*), 143.7 (t, J_{CP} = 16 Hz, $^{phen}C_{Ar}$), 138.4 ($^{phen}C_{Ar}$-*H*), 138.1 (br, J_{CP} = 15 Hz, PC_{Ar}H), 133.1 ($^{phen}C_{Ar}$), 132.8 (v br, $^{phen}C_{Ar}$-*H*), 132.4 (br, PC_{Ar}), 132.0 (t, J_{CP} = 31 Hz, PC_{Ar}-*H*), 130.5 ($^{phen}C_{Ar}$-*H*), 129.9 (br, PC_{Ar}), 129.2 (PC_{Ar}-*H*), 129.0 (br, $^{phen}C_{Ar}$), 127.8 ($^{phen}C_{Ar}$-*H*), 126.2 ($^{phen}C_{Ar}$), 125.5 (br, $^{phen}C_{Ar}$-*H*), 122.9 ($^{phen}C_{Ar}$), 25.70 ($^{Phen}C^2_{Me}$), 21.93 ppm ($^{Phen}C^6_{Me}$). ^{31}P{^{1}H} NMR (CDCL5, 121 MHz, 22 °C): δ -17.7 (br, s), -144.3 ppm (sep, J_{PF} = 755 Hz). ^{19}F NMR (CDCL5, 500 MHz, 22 °C): -73.9 ppm (d, J_{PF} = 755 Hz). Anal. Calc'd for $C_{54}H_{44}CuF_6N_2P_3 \bullet CH_2Cl_2$: C, 61.37; H, 4.34 %. Found: C, 61.61; H, 4.46 %.

4.5.1. X-Ray Crystallography Experimental Details:

X-ray crystal structure data was collected from multi-faceted crystals of suitable size and quality selected from a representative sample of crystals of the same habit using an optical microscope. In each case, crystals were mounted on MiTiGen loops with data collection carried out in a cold stream of nitrogen (150 K; Bruker D8 QUEST ECO). All diffractometer manipulations were carried out using Bruker APEX3 software.[32] Structure solution and refinement was carried out

using XS, XT and XL software, embedded within the Bruker SHELXTL suite.[33] For each structure, the absence of additional symmetry was confirmed using ADDSYM incorporated in the PLATON program.[34] CCDC 1872863-1872869 contain the supplementary crystallographic data for this chapter. The data can be obtained free of charge from The Cambridge Crystallographic Data Centre via www.ccdc.cam.ac.uk/structures.

Crystal structure data for (L**1**)$_2$**CuPF$_6$**: X-ray quality crystals were grown following diffusion of diethylether vapor into CH_2Cl_2 at room temperature. Crystal structure parameters: $C_{51}H_{38}Cl_2$ $CuF_6N_2P_3$ 1020.18 g/mol, triclinic, space group *P*-1; a = 9.1636(17) Å, b = 10.448(2) Å, c = 12.101(2) Å, α = 96.098(14)°, β = 99.601(13)°, γ = 109.077(17)°, V = 1063.4(4) Å^3; Z = 1, ρ_{calcd} = 1.488 g cm^{-3}; crystal dimensions 0.310 x 0.270 x 0.100 mm; diffractometer Bruker D8 QUEST ECO CMOS; Mo K$_\alpha$ radiation, 150(2) K, θ_{max} = 34.463°; 78831 reflections, 8169 independent (R_{int} = 0.0288), direct methods; absorption coeff (μ = 1.241 mm^{-1}), absorption correction semi-empirical from equivalents (SADABS); refinement (against F_o^2) with SHELXTL V6.1, 272 parameters, 0 restraints, R_1 = 0.0297 ($I > 2\sigma$) and wR_2 = 0.0759 (all data), Goof = 1.024, residual electron density 0.592/−0.404 e Å^{-3}.

Crystal structure data for (L**1**)$_2$**CuBPh$_4$**: X-ray quality crystals were grown following diffusion of hexanes vapor into CH_2Cl_2 at room temperature. Crystal structure parameters: $C_{74}H_{56}B$ CuN_2P_2 1109.49 g/mol, Monoclinic, space group C2/c; a = 18.204(7) Å, b = 18.807(7) Å, c = 18.109(6) Å, α = 90°, β = 116.99(13)°, γ = 90°, V = 5524.5(4) Å^3; Z = 4, ρ_{calcd} = 1.334 Mg/m^3; crystal dimensions 0.250 x 0.120 x 0.120 mm; diffractometer Bruker D8 QUEST ECO CMOS; Mo K$_\alpha$ radiation, 150(2) K, θ_{max} = 30.622°; 91982 reflections, 8513 independent (R_{int} = 0.0722), direct methods; absorption coeff (μ = 0.502 mm^{-1}), absorption correction semi-

empirical from equivalents (SADABS); refinement (against F_o^2) with SHELXTL V6.1, 362 parameters, 0 restraints, R_1 = 0.0490 ($I > 2\sigma$) and wR_2 = 0.1559 (all data), Goof = 1.005, residual electron density 0.556/−0.477 e Å^{-3}.

Crystal structure data for (L**2**)$_2$**CuPF$_6$**: X-ray quality crystals were grown following diffusion of hexanes vapor into CH_2Cl_2 at room temperature. Crystal structure parameters: $C_{104}H_{80}Cu_2F_{12}N_4P_6$ 1926.62 g/mol, Monoclinic, space group C2/c; a = 24.047(7) Å, b = 9.432(3) Å, c = 20.640(6) Å, α = 90°, β = 93.49(16)°, γ = 90°, V = 4672.9(2) Å^3; Z = 2, ρ_{calcd} = 1.369 Mg/m^3; crystal dimensions 0.280 x 0.090 x 0.080 mm; diffractometer Bruker D8 QUEST ECO CMOS; Mo K$_\alpha$ radiation, 150(2) K, θ_{max} = 30.614°; 87059 reflections, 7202 independent (R_{int} = 0.0836), direct methods; absorption coeff (μ = 0.632 mm^{-1}), absorption correction semi-empirical from equivalents (SADABS); refinement (against F_o^2) with SHELXTL V6.1, 292 parameters, 0 restraints, R_1 = 0.0540 ($I > 2\sigma$) and wR_2 = 0.1144 (all data), Goof = 1.012, residual electron density 0.606/−0.683 e Å^{-3}.

Crystal structure data for **(L2)$_2$CuBPh$_4$**: X-ray quality crystals were grown following diffusion of diethylether vapor into CH_2Cl_2 at room temperature. Crystal structure parameters: $C_{76.50}H_{61}B\,ClCuN_2P_2$ 1180.01 g/mol, Triclinic, space group P-1; a = 13.929(6) Å, b = 18.462(8) Å, c = 25.833(12) Å, α = 107.47(3)°, β = 95.17(3)°, γ = 107.16(3)°, V = 5937.2(5) Å^3; Z = 4, ρ_{calcd} = 1.320 Mg/m^3; crystal dimensions 0.100 x 0.100 x 0.050 mm; diffractometer Bruker D8 QUEST ECO CMOS; Mo K$_\alpha$ radiation, 150(2) K, θ_{max} = 27.603°; 134866 reflections, 27407 independent (R_{int} = 0.1484), direct methods; absorption coeff (μ = 0.515 mm^{-1}), absorption correction semi-empirical from equivalents (SADABS); refinement (against F_o^2) with SHELXTL V6.1, 1508 parameters, 0 restraints, R_1 = 0.0596 ($I > 2\sigma$) and wR_2 = 0.1528 (all data), Goof = 1.005, residual electron density 0.411/−0.629 e Å^{-3}.

Crystal structure data for (**L5)CuPF$_6$**: X-ray quality crystals were grown following diffusion of diethylether vapor into CH_2Cl_2 at room temperature. Crystal structure parameters: $C_{109}H_{88Cl2}Cu_2$ $F_{12}N_4P_6$ 2065.63 g/mol, Monoclinic, space group C2/c; a = 27.339(7) Å, b = 25.087(11) Å, c = 17.994(9) Å, α = 90°, β = 128.56(10)°, γ = 90°, V = 9651.0(8) Å^3; Z = 4, ρ_{calcd} = 1.422 Mg/m^3; crystal dimensions 0.320 x 0.200 x 0.090 mm; diffractometer Bruker D8 QUEST ECO CMOS; Mo Kα radiation, 150(2) K, θ_{max} = 34.390°; 158133 reflections, 18551 independent (R_{int} = 0.0602), direct methods; absorption coeff (μ = 0.671 mm^{-1}), absorption correction semi-empirical from equivalents (SADABS); refinement (against F_o^2) with SHELXTL V6.1, 645 parameters, 0 restraints, R_1 = 0.0580 ($I > 2\sigma$) and wR_2 = 0.1706 (all data), Goof = 1.000, residual electron density 1.075/−1.409 e Å^{-3}.

Crystal structure data for (**L5)$_2$CuBPh$_4$**: X-ray quality crystals were grown following diffusion of hexanes vapor into CH_2Cl_2 at room temperature. Crystal structure parameters: $C_{39}H_{32}B_{0.50}Cu_{0.50}NP$ 582.80 g/mol, Triclinic, space group P-1; a = 11.749(4) Å, b = 16.295(6) Å, c = 17.841(6) Å, α = 66.52(19)°, β = 87.83(2)°, γ = 88.68(2)°, V = 3130.62(19) Å^3; Z = 4, ρ_{calcd} = 1.237 Mg/m^3; crystal dimensions 0.200 x 0.100 x 0.050 mm; diffractometer Bruker D8 QUEST ECO CMOS; Mo Kα radiation, 150(2) K, θ_{max} = 29.718°; 144753 reflections, 17714 independent (R_{int} = 0.0814), direct methods; absorption coeff (μ = 0.446 mm^{-1}), absorption correction semi-empirical from equivalents (SADABS); refinement (against F_o^2) with SHELXTL V6.1, 761 parameters, 0 restraints, R_1 = 0.0501 ($I > 2\sigma$) and wR_2 = 0.1400 (all data), Goof = 1.062, residual electron density 0.489/−0.795 e Å^{-3}.

Crystal structure data for [(**L5**)Cu]$_2$(μ-Br)$_2$: X-ray quality crystals were grown following diffusion of diethylether vapor into CH_2Cl_2 at room temperature. Crystal structure parameters: $C_{55}H_{46}Br_2Cl_2Cu_2N_2P_2$ 1154.68 g/mol, triclinic, space group *P*-1; a = 12.3597(8) Å, b =

13.5264(9) Å, c = 14.5021(9) Å, α = 80.780(3)°, β = 89.069(3)°, γ = 88.363(3)°, V = 2392.0(3) Å^3; Z = 2, ρ_{calcd} = 1.603 g cm^{-3}; crystal dimensions 0.587 x 0.208 x 0.205 mm; diffractometer Bruker D8 QUEST ECO CMOS; Mo K$_\alpha$ radiation, 150(2) K, θ_{max} = 27.565°; 79926 reflections, 11013 independent (R_{int} = 0.0325), direct methods; absorption coeff (μ = 2.779 mm^{-1}), absorption correction semi-empirical from equivalents (SADABS); refinement (against F_o^2) with SHELXTL V6.1, 272 parameters, 0 restraints, R_1 = 0.0291 ($I > 2\sigma$) and wR_2 = 0.0650 (all data), Goof = 1.033, residual electron density 0.700/−0.691 e Å^{-3}.

4.5.2. Optical Spectroscopy Measurements:

The absorption spectra of the complexes were measured in solution in CH_2Cl_2 in 1 cm quartz cuvettes using a Thermo Scientific Genesys UV−vis spectrometer at room temperature. Emission spectra at 77 K were recorded in 4 mm diameter tubes held within a liquid-nitrogen-cooled quartz dewar, using a Jobin Yvon Fluoromax-2 spectrometer equipped with a Hamamatsu R928 photomultiplier tube (PMT). The spectra in the solid state were recorded by means of an integrating sphere attached to a Jobin Yvon Fluorolog instrument through optical fibers. Finely powdered samples were contained within Spectralon sample holders of 10 mm diameter. Quantum yields were determined using a sample of finely powdered $BaSO_4$ as a non-emissive blank. Scattered light at λ_{ex} = 425 nm for sample and blank was measured using a neutral density filter of O.D. = 2, while the emission region was monitored in the absence of the filter. The detector for this set-up was also a Hamamatsu R928 PMT. Luminescence lifetimes at ambient temperature were measured by time-correlated single-photon counting (TCSPC) following excitation using a pulsed laser diode at 405 nm and using an R928 PMT for detection. The same detector operating in multichannel scaling (MCS) mode was used to measure the

longer lifetimes at 77 K, following excitation with a microsecond-pulsed xenon lamp.

4.5.3. Theoretical Calculations:

All calculations were carried out using the Gaussian 16 B.01 software package.[35] Optimization of the ground state geometries (S_0) was carried out in the gas phase with the dispersion-corrected CAM-B3LYP functional[36]using Grimme's D3 dispersion and Becke-Johnson damping,[37]and the def2-svp basis set[38] on all atoms. Crystal structure coordinates obtained for the [Cu(*P^N*)$_2$][PF_6] analogues were used as starting input. Subsequently, the T_1 state geometries were optimized at the same level of theory with CAM-B3LYP-D3(BJ)/def2-svp, using the optimized S_0 geometries as starting input. Frequency analyses on all optimized structures were performed at the same level of theory to confirm that these are at a minimum on the potential energy surface. All single point calculations, including time-dependent DFT (TDDFT), were carried out with the M06 functional[39] and def2-svp basis set on all atoms. TDDFT analyses on L**1CuX**, L**2CuX**, and **L5CuX** were carried out with the GaussSum software[40]All structures presented and MOs were generated using the Avogadro molecular editing software,[41] and the fragment contributions to the MOs were analyzed with the QMForge software.[42] The photophysical parameters: adiabatic energy, ΔE(adiab); phosphorescence energy, ΔE(phos); and reorganization energy, λ_T, were calculated as previously reported.[11] The ΔE(S_1-T_1) gap is estimated from the difference between the TDDFT energy of the S_1 state, ΔE(S_1-TD); and the single point energy obtained for the optimized T_1 geometry.

4.6. References:

(1) Bozic-Weber, B.; Constable, E. C.; Housecroft, C. E. Light Harvesting with Earth Abundant D-Block Metals: Development of Sensitizers in Dye-Sensitized Solar Cells (DSCs). *Coord. Chem. Rev.* **2013**, *257*, 3089–3106.

(2) Housecroft, C. E.; Constable, E. C. The Emergence of Copper(I)-Based Dye Sensitized Solar Cells. *Chem. Soc. Rev.* **2015**, *44*, 8386–8398.

(3) Cariati, E.; Lucenti, E.; Botta, C.; Giovanella, U.; Marinotto, D.; Righetto, Stefania. Cu(I) Hybrid Inorganic-Organic Materials with Intriguing Stimuli Responsive and Optoelectronic Properties. *Coord. Chem. Rev.* **2016**, *306*, 566–614.

(4) Yersin, H.; Rausch, A. F.; Czerwieniec, R.; Hofbeck, T.; Fischer, Tobias. The Triplet State of Organo-Transition Metal Compounds. Triplet Harvesting and Singlet Harvesting for Efficient OLEDs. *Coord. Chem. Rev.* **2011**, *255*, 2622–2652.

(5) Czerwieniec, R.; Leitl, M. J.; Homeier, H. H. H.; Yersin, Hartmut. Cu(I) Complexes - Thermally Activated Delayed Fluorescence. Photophysical Approach and Material Design. *Coord. Chem. Rev.* **2016**, *325*, 2–28.

(6) Bizzarri, C.; Hundemer, F.; Busch, J.; Bräse, S. Triplet Emitters versus TADF Emitters in OLEDs: A Comparative Study. *Polyhedron* **2018**, *140*, 51–66.

(7) Zhao, J.; Ji, S.; Wu, W.; Wu, W.; Guo, H.; Sun, J.; Sun, H.; Liu, Y.; Li, Q.; Huang, L. Transition Metal Complexes with Strong Absorption of Visible Light and Long-Lived Triplet Excited States: From Molecular Design to Applications. *RSC Adv.* **2012**, *2*, 1712–1728.

(8) Cunningham, C. T.; Moore, J. J.; Cunningham, K. L. H.; Fanwick, P. E.; McMillin, D. R. Structural and Photophysical Studies of $Cu(NN)_2^+$ Systems in the Solid State. Emission at Last from Complexes with Simple 1,10-Phenanthroline Ligands. *Inorg. Chem.* **2000**, *39*, 3638–3644.

(9) Tsukuda, T.; Nishigata, C.; Arai, K.; Tsubomura, Taro. Photophysical Properties of Copper(I) and Zinc(II) Complexes Containing Phosphinoquinoline Ligands. *Polyhedron* **2009**, *28*, 7–12.

(10) Mondal, R.; Giesbrecht, P. K.; Herbert, D. E. Nickel(II), Copper(I) and Zinc(II) Complexes Supported by a (4-Diphenylphosphino)Phenanthridine Ligand. *Polyhedron* **2016**, *108*, 156–162.

(11) Mondal, R.; Lozada, I. B.; Davis, R. L.; Williams, J. A. G.; Herbert, D. E. Site-Selective Benzannulation of N-Heterocycles in Bidentate Ligands Leads to Blue-Shifted Emission from [(P^N)Cu]2(μ-X)2 Dimers. *Inorg. Chem.* **2018**, *57*, 4966–4978.

(12) Gschwind, R. M. Organocuprates and Diamagnetic Copper Complexes: Structures and NMR Spectroscopic Structure Elucidation in Solution. *Chem. Rev.* **2008**, *108*, 3029–3053.

(13) Suzuki, T.; Yamaguchi, H.; Hashimoto, A.; Nozaki, K.; Doi, M.; Inazumi, N.; Ikeda, N.; Kawata, S.; Kojima, M.; Takagi, H. D. Orange and Yellow Crystals of Copper(I) Complexes Bearing 8-(Diphenylphosphino)Quinoline: A Pair of Distortion Isomers of an Intrinsic Tetrahedral Complex. *Inorg. Chem.* **2011**, *50*, 3981–3987.

(14) Farruggia, G.; Iotti, S.; Prodi, L.; Montalti, M.; Zaccheroni, N.; Savage, P. B.; Trapani, V.; Sale, P.; Wolf, F. I. 8-Hydroxyquinoline Derivatives as Fluorescent Sensors for Magnesium in Living Cells. *J. Am. Chem. Soc.* **2006**, *128*, 344–350.

(15) Armaroli, N.; Accorsi, G.; Cardinali, F.; Listorti, Andrea. Photochemistry and Photophysics of Coordination Compounds: Copper. *Top. Curr. Chem.* **2007**, *280*, 69–115.

(16) D'Andrade, B. W.; Datta, S.; Forrest, S. R.; Djurovich, P.; Polikarpov, E.; Thompson, M. E. Relationship between the Ionization and Oxidation Potentials of Molecular Organic Semiconductors. *Org. Electron.* **2005**, *6*, 11–20.

(17) Reineke, M. H.; Sampson, M. D.; Rheingold, A. L.; Kubiak, C. P. Synthesis and Structural Studies of Nickel(0) Tetracarbene Complexes with the Introduction of a New Four-Coordinate Geometric Index, Tδ. *Inorg. Chem.* **2015**, *54*, 3211–3217.

(18) Zhang, L.; Li, B.; Su, Zhongmin. Phosphorescence Enhancement Triggered by Π Stacking in Solid-State [Cu(N-N)(P-P)]BF4 Complexes. *Langmuir* **2009**, *25*, 2068–2074.

(19) Volz, D.; Nieger, M.; Friedrichs, J.; Baumann, T.; Brase, Stefan. How the Quantum Efficiency of a Highly Emissive Binuclear Copper Complex Is Enhanced by Changing the Processing Solvent. *Langmuir* **2013**, *29*, 3034–3044.

(20) Yersin, H.; Otto, H.; Gliemann, Guenter. Emission, Emission Lifetime, and Absorption of [Hexaureachromium]X3 Single Crystals. *Theor. Chim. Acta* **1974**, *33*, 63–78.

(21) Gneuss, T.; Leitl, M. J.; Finger, L. H.; Yersin, H.; Sundermeyer, Joerg. A New Class of Deep-Blue Emitting Cu(I) Compounds - Effects of Counter Ions on the Emission Behavior. *Dalton Trans.* **2015**, *44*, 20045–20055.

(22) Benito, Q.; Le Goff, X. F.; Maron, S.; Fargues, A.; Garcia, A.; Martineau, C.; Taulelle, F.; Kahlal, S.; Gacoin, T.; Boilot, J.-P.; et al. Polymorphic Copper Iodide Clusters: Insights into the Mechanochromic Luminescence Properties. *J. Am. Chem. Soc.* **2014**, *136*, 11311–11320.

(23) Bai, S.-Q.; Kai, D.; Ke, K. L.; Lin, M.; Jiang, L.; Jiang, Y.; Young, D. J.; Loh, X. J.; Li, X.; Hor, T. S. Andy. A Triazolyl-Pyridine-Supported CuI Dimer: Tunable Luminescence and Fabrication of Composite Fibers. *ChemPlusChem* **2015**, *80*, 1235–1240.

(24) Chai, H.; Wang, L.; Liu, T.; Yu, Z. A Versatile Ru(II)-NNP Complex Catalyst for the Synthesis of Multisubstituted Pyrroles and Pyridines. *Organometallics* **2017**, *36*, 4936–4942.

(25) Wang, Z.; Chen, X.; Liu, B.; Liu, Q.; Solan, G. A.; Yang, X.; Sun, W.-H. Cooperative Interplay between a Flexible PNN-Ru(II) Complex and a NaBH4 Additive in the Efficient Catalytic Hydrogenation of Esters. *Catalysis Science & Technology* **2017**, *7*, 1297–1304.

(26) Attilio Ardizzoia, G.; Brenna, S.; Civati, F.; Colombo, V.; Sironi, Angelo. A Phosphorescent Copper(I) Coordination Polymer with Sodium 3,5-Dimethyl-4-Sulfonate Pyrazolate. *CrystEngComm* **2017**, *19*, 6020–6027.

(27) Feng, J.; Chen, Y.; Han, Y.; Liu, J.; Ma, S.; Zhang, H.; Chen, Xingguo. PH-Regulated Synthesis of Trypsin-Templated Copper Nanoclusters with Blue and Yellow Fluorescent Emission. *ACS Omega* **2017**, *2*, 9109–9117.

(28) Wong, M. Y.; Zysman-Colman, E. Purely Organic Thermally Activated Delayed Fluorescence Materials for Organic Light-Emitting Diodes. *Advanced Materials* **2017**, *29*, 1605444.

(29) Lee, C.-I.; Zhou, J.; Ozerov, O. V. Catalytic Dehydrogenative Borylation of Terminal Alkynes by a SiNN Pincer Complex of Iridium. *J. Am. Chem. Soc.* **2013**, *135*, 3560–3566.

(30) Mandapati, P.; Giesbrecht, P. K.; Davis, R. L.; Herbert, D. E. Phenanthridine-Containing Pincer-like Amido Complexes of Nickel, Palladium, and Platinum. *Inorg. Chem.* **2017**, *56*, 3674–3685.

(31) Mondal, R.; Lozada, I. B.; Davis, R. L.; Williams, J. A. G.; Herbert, D. E. Site-Selective Benzannulation of N-Heterocycles in Bidentate Ligands Leads to Blue-Shifted Emission from [(P^N)Cu]2(μ-X)$_2$ Dimers. *Inorg. Chem.* **2018**, *57*, 4966–4978.

(32) Bruker-AXS. *APEX3 V2016.1-0*; Madison, Wisconsin, USA, 2016.

(33) Sheldrick, G. M. A Short History of SHELX. *Acta Crystallogr., Sect. A: Found. Crystallogr.* **2008**, *64*, 112–122.

(34) Spek, A. L. Structure Validation in Chemical Crystallography. *Acta Crystallogr., Sect. D: Biol. Crystallogr.* **2009**, *65*, 148–155.

(35) Frisch, M. J.; Trucks, G. W.; Schlegel, H. B.; Scuseria, G. E.; Robb, M. A.; Cheeseman, J. R.; Scalmani, G.; Barone, V.; Petersson, G. A.; Nakatsuji, H.; et al. *Gaussian 16, Revision B.01*; Gaussian 16, Revision B.01, Gaussian, Inc., Wallingford CT; Gaussian, Inc.: Wallingford CT, 2016.

(36) Yanai, T.; Tew, D. P.; Handy, N. C. A New Hybrid Exchange-Correlation Functional Using the Coulomb-Attenuating Method (CAM-B3LYP). *Chem. Phys. Lett.* **2004**, *393*, 51–57.

(37) Grimme, S.; Ehrlich, S.; Goerigk, L. Effect of the Damping Function in Dispersion Corrected Density Functional Theory. *J. Comput. Chem.* **2011**, *32*, 1456–1465.

(38) Weigend, F. Accurate Coulomb-Fitting Basis Sets for H to Rn. *Phys. Chem. Chem. Phys.* **2006**, *8*, 1057–1065.

(39) Zhao, Y.; Truhlar, D. G. The M06 Suite of Density Functionals for Main Group Thermochemistry, Thermochemical Kinetics, Noncovalent Interactions, Excited States, and Transition Elements: Two New Functionals and Systematic Testing of Four M06-Class Functionals and 12 Other Functionals. *Theor. Chem. Acc.* **2008**, *120*, 215–241.

(40) O'Boyle, N. M.; Tenderholt, A. L.; Langner, K. M. Software News and Updates Cclib: A Library for Package-Independent Computational Chemistry Algorithms. *J. Comput. Chem.* **2008**, *29*, 839–845.

(41) Hanwell, M. D.; Curtis, D. E.; Lonie, D. C.; Vandermeersch, T.; Zurek, E.; Hutchison, G. R. Avogadro: An Advanced Semantic Chemical Editor, Visualization, and Analysis Platform. *J. Cheminf.* **2012**, *4*, 17.

(42) Tenderholt, A. L. *QMForge: A Program to Analyze Quantum Chemistry Calculations*.

Chapter 5:

5.1. Abstract:

A series of Group VIII transition metal (Fe and Ru) complexes bearing bidentate *N*-heterocycle-based *P^N* and *C^N* ligands have been synthesized and fully characterized. The (*P^N*)$FeBr_2$ complexes (**L1/L2/L4**)$FeBr_2$ are characterized as high spin paramagnets, while octahedral $[(P^N)_3Fe]^{2+}$ were found to be low spin and diamagnetic. Solid samples of all three paramagnetic complexes (**L1/L2/L4**)$FeBr_2$ showed magnetic moments of ~4.5 μ_B by solid-state magnetometry, representing four unpaired electrons of the high spin Fe(II) centres. The magnetic moments were confirmed in solution using Evans' method. The electronic environment about the Fe centre was further characterized by solid-state Mössbauer spectroscopy. Octahedral $[(P^N/C^N)_3Fe]^{2+}$ complexes synthesized using phenanthridinyl phosphine (**L2**) were also compared with analogs prepared using less π-extended quinolinyl phosphine (**L3**) ligands. The octahedral complexes were characterized in the solution state using NMR and UV-Vis spectroscopy, and in the solid-state by X-ray spectroscopy and elemental analysis. A site-selective effect of π-extension can been observed when comparing the lowest energy absorption bands in the UV-Vis spectra. Contrary to the conventional assumptions regarding π-extension, a hypsochromic shift was observed for π-extended (phenanthridinyl) phosphine Fe(II) complex. *N*-heterocyclic carbene ligand based Fe(II) and Ru(II) also showed interesting metal to ligand (MLCT) excited state properties, evident from broad peaks in the visible region of UV-Vis spectroscopy. Spectroelectrochemistry of octahedral Fe complexes were performed to further explore the effect of π-extension.

5.2. Introduction:

As discussed in the previous chapters, π-extended bifunctional ligands are of interest owing to the potential for strong bonding to metal ions of a ligand bearing an accessible conjugated π-system. π-Extended conjugated ligand systems bound to Group VIII metals such as Ru often show long-lived metal-to-ligand charge transfer (MLCT) excited state character, important for designing small molecule photosensitizers.[1] Small molecule photosensitizer are of interest for applications such as dye-sensitized solar cell (DSSCs), where transition metal coordination complexes are attached to mesoporous semiconductor surfaces, such as titanium dioxide (TiO_2), to act as sensitizer. Sensitization of the surface occurs as a result of photoexcitation of the complex, following which electron injection from complex to semiconductor conduction band occurs thanks to long-live charge-transfer excited states. Such processes require long-lived ^{1}MLCT or ^{3}MLCT, and typically need to avoid unproductive decay via ^{3}MC states back to the ground state.

Increasing attention is also being paid to Fe complexes in this respect, to address sustainability in photosensitizer design. In this chapter, I have disclosed the coordination chemistry of π-extended bifunctional phosphine and carbene-phenanthridine ligands with Group VIII metals. Bidentate *P^N* donor ligands have been found to be very interesting in last decades in different fields of chemistry, and happens to be quiet different coordination property over bidentate homoleptic *P^P* or *N^N* type ligands.[2] For example, *P^N* donor ligands have been prominently applied for asymmetric catalysis[3] and photo-emissive material synthesis[4]. Group VIII metals are well-known for binding with simple bidentate *P^N* donor ligand under mild conditions. The coordination geometry of d^8 metal complex with bidentate ligands can range

from tetrahedral, to pyramidal and octahedral, depending on the number of ligands bound, their donor properties and steric constraints.[5]

The use of π-extension is a common strategy for tuning the photophysical properties of small molecule coordination complexes. This approach provides flexibility for the design of photo-emissive materials,[6,7] photosensitizers,[1] and solar cells by maintaining the molecular core while tuning molecular properties.[8] Typically, π-extension leads to bathochromic shift of both absorption and emission spectra, as the HOMO and LUMO become energetically closer.[6] However, surprisingly, the effect of π-extension did not seem to play role in absorption spectra of Ni(II), Pd(II) and Pt(II) while comparing quinoline to phenanthridine π-extension in a *N^N^N* pincer type ligand: the lowest energy absorption band was not significantly changed and showed isoenergetic λ_{max} values.[9] In our previous study with (diphenylphosphine)phenanthridine (**L2**) and quinoline (**L3**) ligands in the context of Cu(I) halide bridge complexes, I observed red shifted absorption as a result of phenanthridine π-extension but blue shifted emission.[7] In that case, theoretical modelling explained that rigidity caused by π-extension provided extra stability to the Cu centre, diminishing the excited state structural orientation.[7]

Continuing with this theme, I explored Group VIII metal ion coordination chemistry with phosphine/phenanthridine ligands **L1**, **L2**, **L3** and **L4**. The characterization and coordination chemistry of **L1** and **L2** with late transition metals such as Ni, Zn and Cu is discussed in Chapters **2**, **3** and **4**.[10] In this chapter, I discuss the synthesis of high-spin Fe(II) complexes of phosphino-phenanthridine ligands, generally [Fe(*P^N*)Br_2], and low-spin octahedral [Fe(*P^N*)$_3$][PF_6]$_2$. Changes in the observed structural geometry of [Fe(*P^N*)Br_2] complexes resulting from changes in the ligand structure are noted. As well, a hypsochromic shift has been observed from quinoline to phenanthridine in the UV-Vis spectra of lowest energy spectra of

octahedral Fe(II) complexes. Similarly, octahedral Ru(II) complex with **L2** was synthesized. Octahedral Ru complexes are well known for their photoemissive properties,[11] enabling applications as photosensitizers[12] and photocatalysts for synthesis.[13] All complexes were characterized by solution state NMR spectroscopy and solid state X-ray spectroscopy and elemental analysis. Similarly, precursor **L8•**HBr (Chapter 2, Scheme 2.2) was used to synthesize octahedral Fe(II) and Ru (II) complexes by *in situ* generation of *N*-heterocyclic carbene containing *C^N* proligands. Carbene ligands are strong σ-donor and weak π-acceptor strongly binds with metal ions, and similarly anticipated to enable applications in designing photosensitizers with extended long charge-transfer excited state lifetimes.[1]

5.3. Results and Discussion:

The synthesis of proligands **L1** and **L2** from 4-bromophenanthridines and their characterization is discussed in preceding chapters (Scheme 2.2).[10,7] The corresponding di-isopropyl (**L4**) analog was synthesized in similar fashion to that outlined in Chapter 2. The proligand **L4** was prepared from 2-methyl-4-bromophenanthridine by lithium halogen exchange using *sec*-BuLi and followed by quenching the lithiated product with (chloro)diisopropylphosphine. The ligand **L4** can be isolated as a yellow semi-solid in 63% yield after passing through a short plug of silica using DCM as eluent.

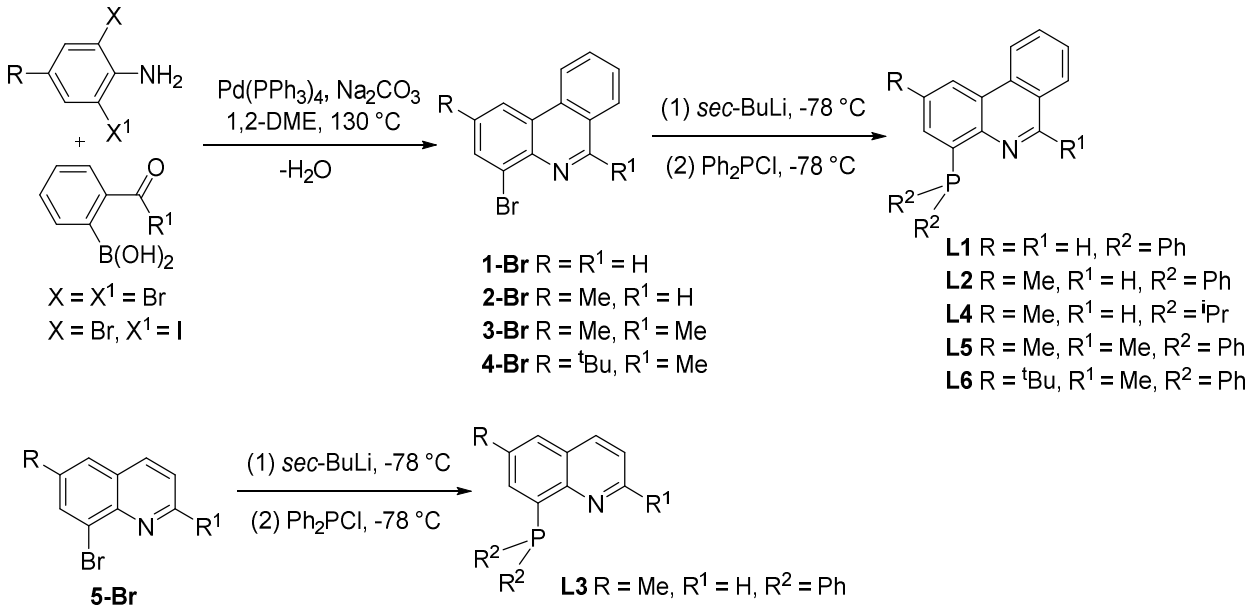

Scheme 5. 1: Bidentate *P^N* proligand synthesis via lithium-halogen exchange

Having the same structural phenanthridine subunit of **L1** and **L2**, proligand **L4** also shows 'imine bridge biphenyl' character in accordance with Clar's rule.[14] **L4** has been characterized by 1- and 2D ^{1}H, ^{13}C and ^{31}P{^{1}H} NMR spectroscopy. The 'imine-like' hydrogen of 6-position of **L4** has a chemical shift in ^{1}H NMR spectra δ(C_6-*H*) of 9.29 ppm, compared to δ(C_6-*H*) **L1**: 9.23 and **L2**: 9.19 ppm. In the ^{13}C{^{1}H} NMR spectra, the corresponding carbon nucleus resonates at **L3**: 151.53 ppm, compared to **L1**: 152.8 and **L2**: 151.8 ppm. In the ^{31}P{^{1}H} NMR spectrum, a sharp singlet was observed for **L4**: δ -0.07 ppm, significantly downfield shift compared to **L1**: δ -13.7 and **L2**: δ -13.6 ppm as a result of exchanging phenyl substituents for alkyl groups. The (*P^N*)$FeBr_2$ complexes were synthesized by drop-wise addition of THF solutions of **L1**, **L2** and **L4** into suspensions of $FeBr_2$ in THF, generating a brown suspension of metal-bound P^N ligand. Complexes **(L1)$FeBr_2$**, **(L2)$FeBr_2$** and **(L4)$FeBr_2$** were isolated

following recrystallization and fully characterized by the single crystal X-ray and elemental analysis.

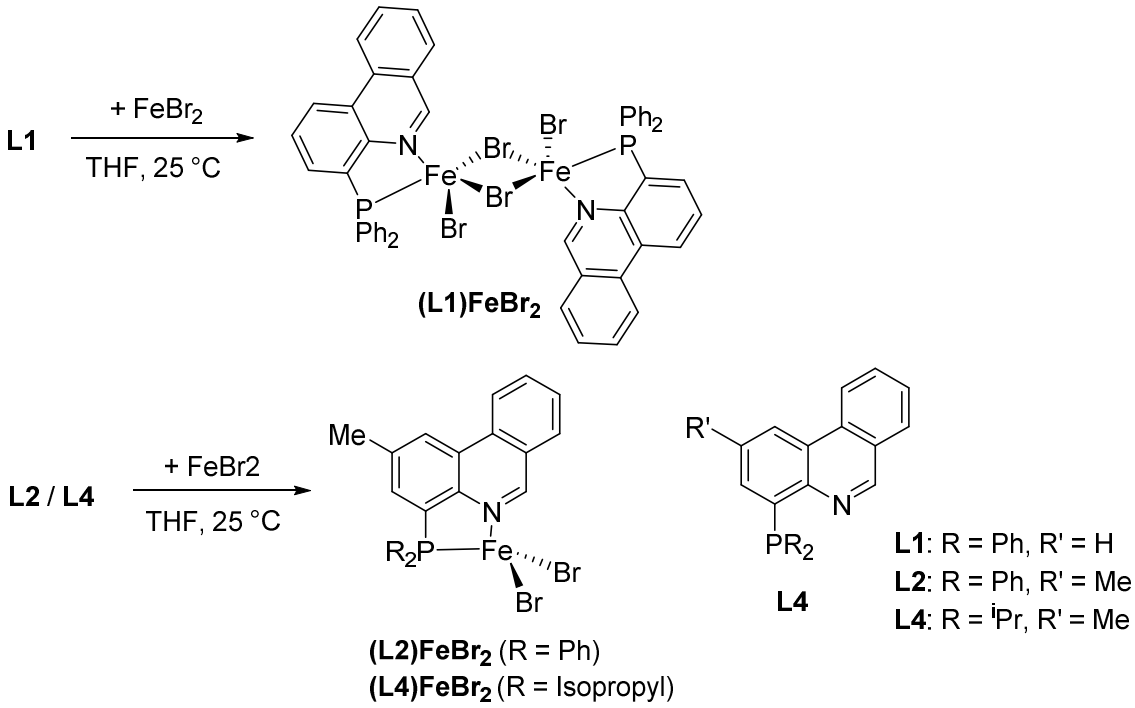

Scheme 5. 2: Bidentate *P^N* ligand based Fe complexes

The ^{1}H NMR spectra shifts of (**L1)FeBr$_2$** (**Figure 5.1**), (**L2)FeBr$_2$** (**Figure 5.2**) and **(L4)FeBr$_2$** (**Figure 5.3**) were very broad and not informative regarding proton chemical shift, enabling us to assign these complexes as paramagnetic. For (**L1)FeBr$_2$** the chemical shift range observed extended from +23.20 to -7.98 ppm, whereas for (**L2)FeBr$_2$** the range was +22.64 to -8.19 ppm, and for **(L4)FeBr$_2$:** +25.56 to -9.79 ppm. While the solid-state structures of (**L1)FeBr$_2$** and (**L2)FeBr$_2$** revealed different geometries, the NMR spectra suggest similar structures in solution. Neither ^{13}C nor ^{31}P NMR signals were detectable for these complexes.

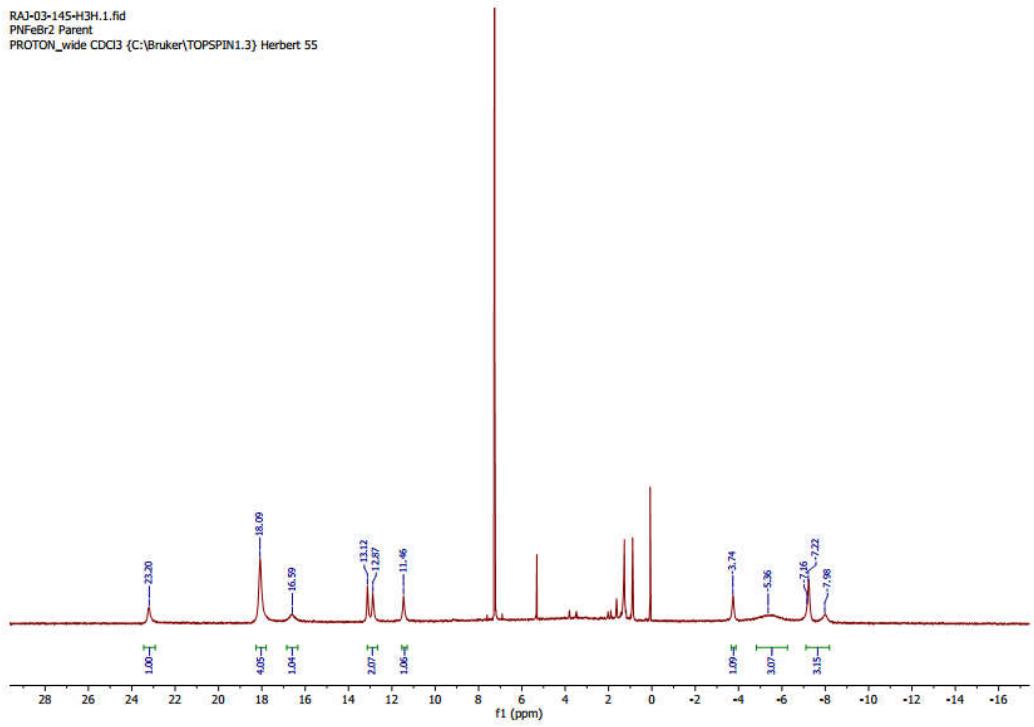

Figure 5. 1: ^{1}H NMR spectra of **(L1)FeBr$_2$** in $CDCl_3$ at room temperature.

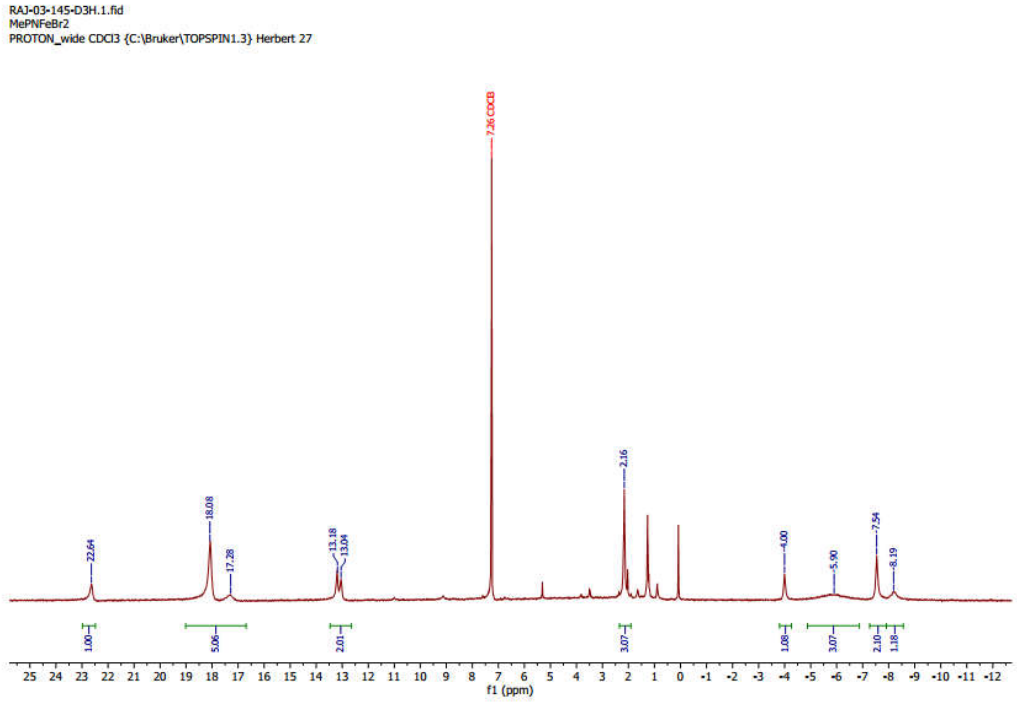

Figure 5. 2: ^{1}H NMR spectroscopy of **(L2)FeBr$_2$** in $CDCl_3$ in room temperature.

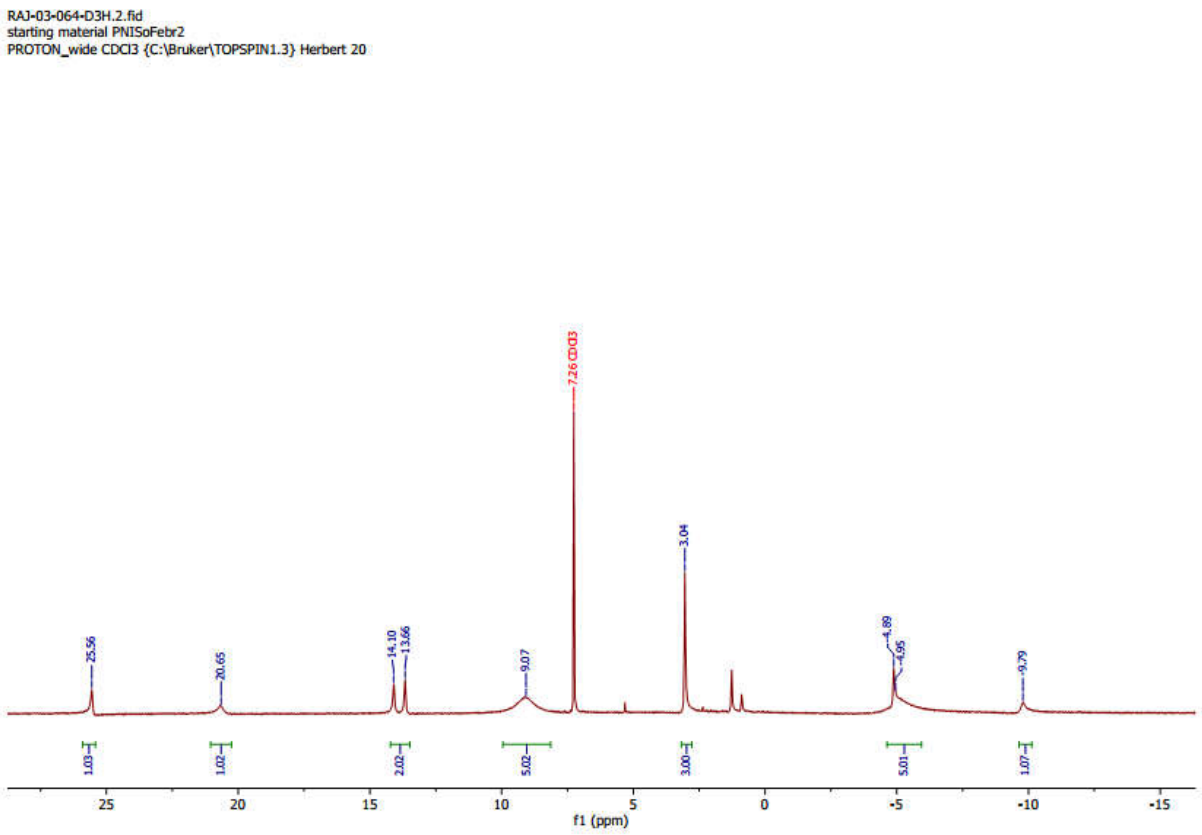

Figure 5. 3: ^{1}H NMR spectroscopy of **(L4)FeBr$_2$** in $CDCl_3$ in room temperature.

5.3.1. Solid-state structures of (L1)FeBr$_2$, (L2)FeBr$_2$ and (L4)FeBr$_2$:

Single crystals suitable for X-ray diffraction were grown by slow diffusion of Et_2O into CH_2Cl_2 solutions of complexes and used to investigate the coordination geometry in the solid-state (**Figure 5.4**). The crystals for all complexes were orange and block shaped. (**L1**)FeBr$_2$ adopted adistorted bipyramidal dimer structure in the solid state, contrary to the tetrahedral geometry for (**L2**)FeBr$_2$. Although in the solution state, ^{1}H NMR spectra was not evident for dimer structure of (**L1**)FeBr$_2$ in solution, showing very similar spectra compared to (**L2**)FeBr$_2$. The (**L4**)FeBr$_2$ complexes also showed tetrahedral geometry in solid state. In the (**L1**)FeBr$_2$ complex, Fe and bridging bromide exhibited longest distance compared to all the other Fe and Br

bond distances in all three complexes (**Table 5.1**). The Fe-Fe bond distance of (**L1**)$FeBr_2$ was close to 3. 801 Å. In (**L1**)$FeBr_2$ the Br-Fe-Br bridge bond angle was 93.76(3). The bond angle Br1-Fe-Br2 in (**L2**)$FeBr_2$: 122.002(15) whereas, in (**L4**)$FeBr_2$: 117.816(18) and N1-Fe-P1 in (**L2**)$FeBr_2$: 79.54(5) and (**L4**)$FeBr_2$: 80.40(6), representing distorted tetrahedral geometry.

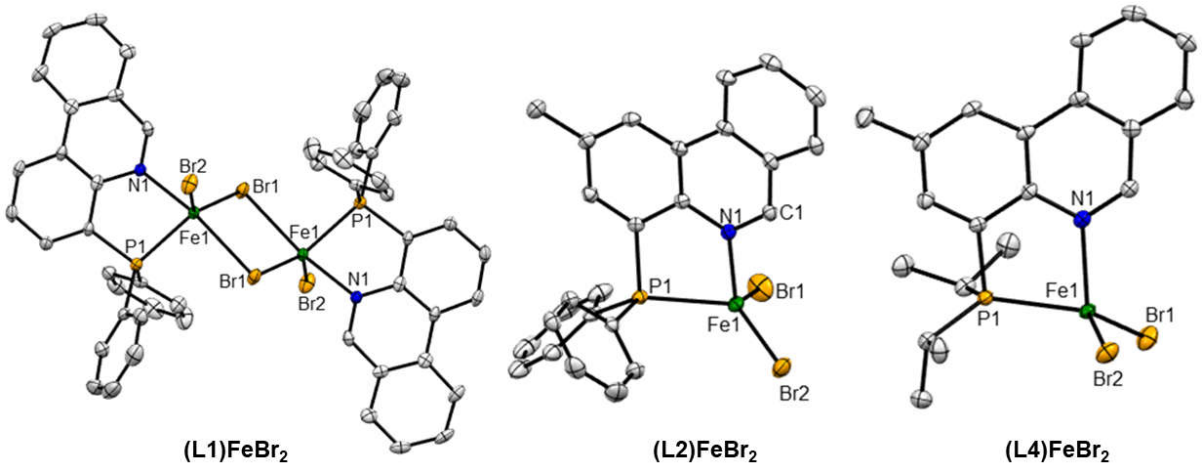

Figure 5. 4: ORTEPs[15] of the solid-state structures of (**L1**)$FeBr_2$, (**L2**)$FeBr_2$ and (**L4**)$FeBr_2$ with thermal ellipsoids shown at 50% probability levels. Hydrogen atoms omitted for clarity.

Table 5. 1: Selective bond lengths (Å) and angles (°) of (**L1**)$FeBr_2$, (**L2**)$FeBr_2$ and (**L4**)$FeBr_{2:}$

Bond lengths	**(L1)$FeBr_2$**	**(L2)$FeBr_2$**	**(L4)$FeBr_2$**
Fe(1)-Br(1)	2.4737(10)	2.3592(4)	2.3702(5)
	2.7278(10)[1]	--	--
	2.7277(10)[1]	--	--
Fe(1)-Br(2)	2.3775(10)	2.3704(4)	2.3689(5)
Fe(1)-N(1)	2.226(4)	2.1075(16)	2.123(2)
Fe(1)-P(1)	2.4209(16)	2.4183(6)	2.4210(8)
Fe(1)-Br(1)-Fe(1)	93.76(3)	--	--
N(1)-Fe(1)-P(1)	76.27(11)	79.54(5)	80.40(6)
Br(1)-Fe(1)-Br(1)	86.24(3)	--	--
Br(1)-Fe(1)-Br(2)	--	122.002(15)	117.816(18)[1]

[1] Representative Fe-Br distances

Pseudooctahedral complexes (**L2**)$_3Fe(PF_6)_2$ and (**L2**)$_3Ru(PF_6)_2$ were similarly synthesized, but using three equivalent of **L2** and one equivalent of metal salt (Scheme 5.3). (**L2**)$_3Fe(PF_6)_2$ was prepared by addition of a solution of ligand in a mixture of CH_3CN and CH_2Cl_2 (1:3) to a solution of $FeSO_4•(NH_4)_2SO_4•6H_2O$ in water and ethanol (4:1), followed by continued stirring for 2 h. Over this time, a colour change was observed to light orange, at which point an aqueous $NaPF_6$ solution was added to the reaction mixture producing a red solution of product. A dark brown solid could be separated as pure product after crystallization from CH_2Cl_2-diethylether solution. (**L2**)$_3Fe(PF_6)_2$ was fully characterized in solution via 1- and 2D ^1H, ^{13}C and $^{31}P\{^1H\}$ NMR spectroscopy and in the solid-state via single crystal X-ray and elemental analysis. Unlike paramagnetic (**L1/L2/L4)$_3$FeBr2** complexes, octahedral Fe(II) complex (**L2**)$_3Fe(PF_6)_2$ showed sharp ^1H, ^{13}C, $^{31}P\{^1H\}$ and ^{19}F NMR data representing diamagnetic electronic structures in solution resulting from an octahedral ligand field and low spin electronic structure. An overall upfield shift of the ligand resonances in (*P^N*)$_3$Fe were observed in ^1H NMR compared with the

uncoordinated proligands. In the ^{1}H NMR spectroscopy, all three methyl backbone of phenanthridine showed at 2.99 ppm and all phosphines showed at 56.86 ppm in ^{31}P NMR, which represents a 'facial' arrangement of the P^N ligands around Fe centre as the all three phosphine have same chemical environment which only possible in their 'facial' arrangement.

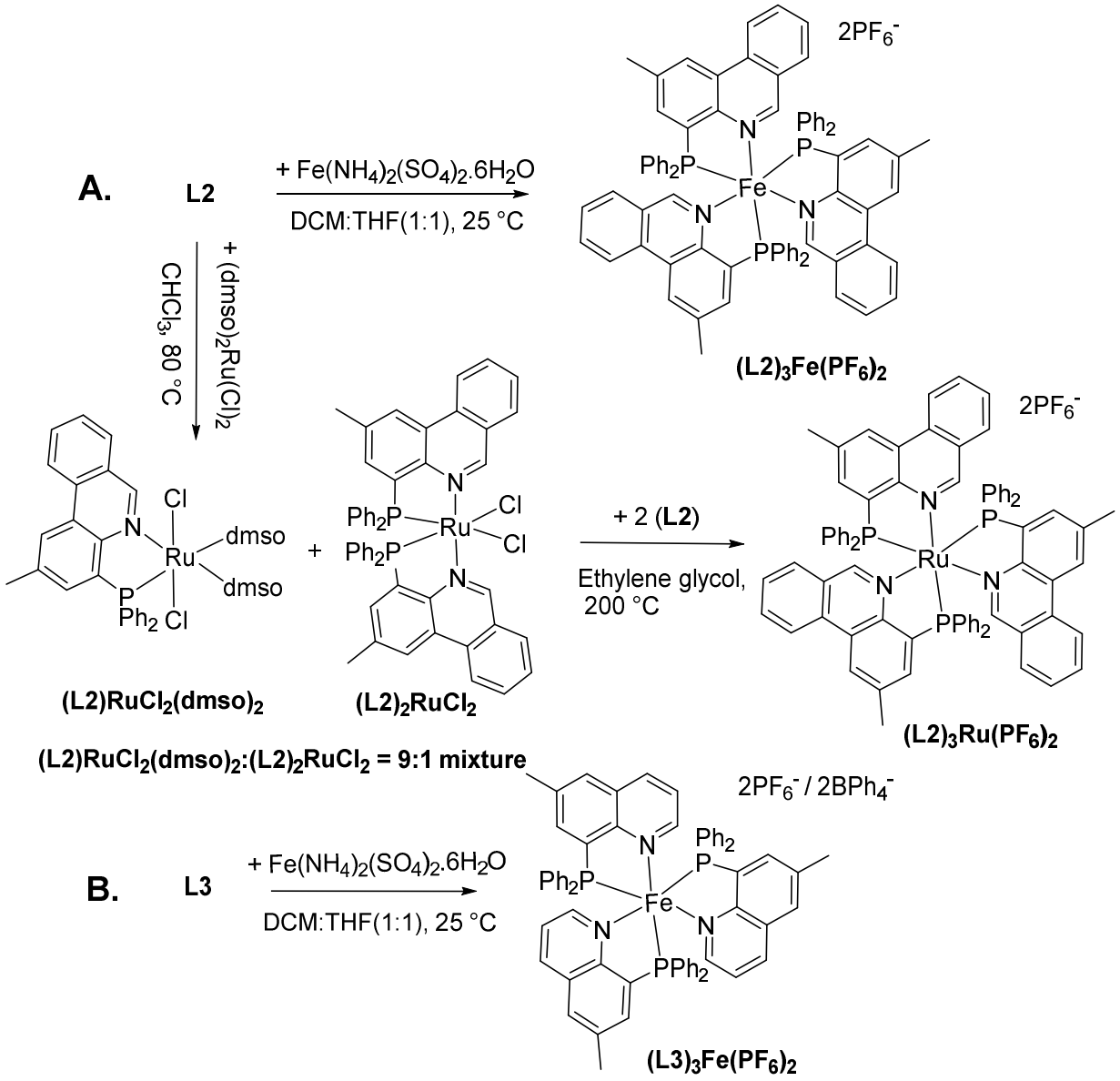

Scheme 5. 3: Octahedral Fe and Ru complexes based on bidentate *P^N* ligand.

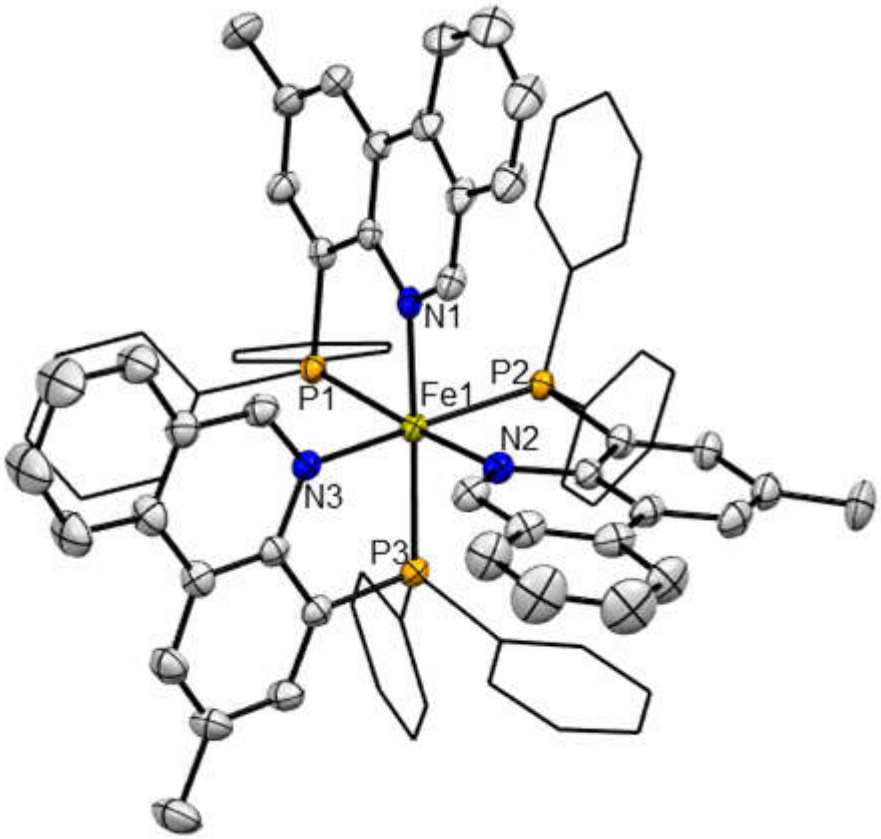

Figure 5. 5: Crystal structure of complex (**L2**)$_3$Fe(PF_6)$_2$, Hydrogen atoms and labels on phosphine, counter-ion and phenanthridine are omitted for clarity.

(**L3**)$_3$Fe(PF_6)$_2$ was synthesized from ligand **L4** following the same procedure of (**L2**)$_3$Fe(PF_6)$_2$complex synthesis. (**L3**)$_3$Fe(PF_6)$_2$ was characterized by solution state the ^{1}H, ^{31}P and ^{19}FNMR spectroscopy. X-ray quality crystal could not be grown using a number of common solvent combination. Thus I have synthesized (**L3**)$_3$Fe(PF_6)$_2$ with tetraphenylborate counter for better π-stackiing in the crystal lattice. Solid state X-ray quality crystal was grown using DCM-Et_2O solvent mixture.

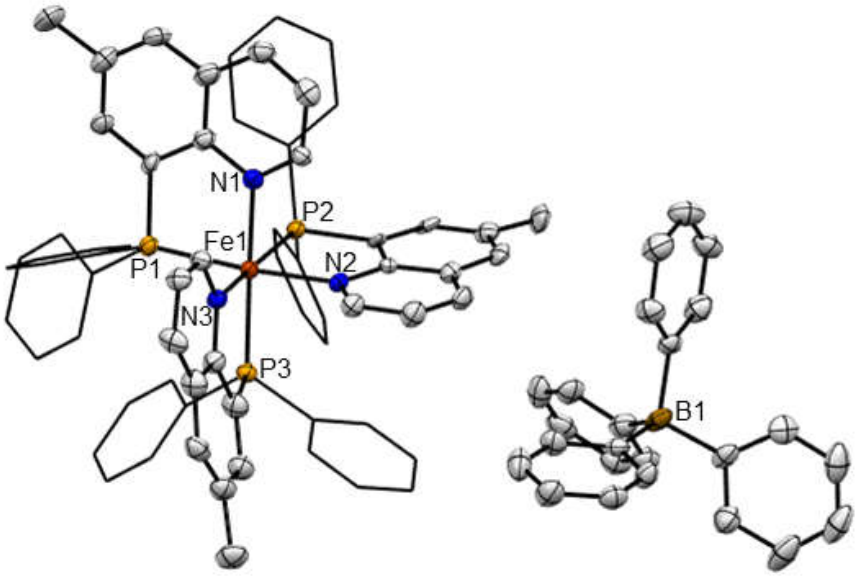

Figure 5. 6: ORTEP[15] of $(\mathbf{L3})_3Fe(PF_6)_2$ with thermal ellipsoids shown at 50% probability levels. Hydrogen atoms and labels on phosphine and phenanthridine are omitted for clarity.

Table 5. 2: Selected bond distances (Å) and angles (°) for $(\mathbf{L3})_3Fe(PF_6)_2$:

Selected Bonds	**(Å)**	**Selected Angles**	**(°)**
Fe(1)-N(1)	2.066(5)	N(3)-Fe(1)-N(1)	90.7(2)
Fe(1)-N(2)	2.063(5)	N(3)-Fe(1)-N(2)	89.0(2)
Fe(1)-N(3)	2.061(5)	N(2)-Fe(1)-N(1)	88.9(2)
Fe(1)-P(1)	2.283(2)	P(1)-Fe(1)-P(2)	99.34(7)
Fe(1)-P(2)	2.3024(19)	N(1)-Fe(1)-P(1)	84.02(16)
Fe(1)-P(3)	2.2809(19)	N(1)-Fe(1)-P(2)	84.18(15)

$(\mathbf{L2})_3Ru(PF_6)_2$ was synthesized by following a published synthetic technique of quinoline precursor[4]. At first, installation of one equivalent of *P^N* ligand on Ru was targeted by a 1:1 reaction of **L2** with *cis*-$(DMSO)_4RuCl_2$ in $CHCl_3$ at 80 °C for 2 hr. In fact, a mixture of red solids identified as $(\mathbf{L2})RuCl_2(dmso)_2$ and $(\mathbf{L2})_2RuCl_2$ (**Figure 5.4 and 5.5**) was observed. The

mixture of (**L2**)$RuCl_2(dmso)_2$ and (**L2**)$_2RuCl_2$, along with other minor unidentified species, was identified using ^1H and ^{31}P NMR spectroscopy and the solid-state X-ray structure of (**L2**)$_2RuCl_2$ was also obtained (**Figure 5.7**). An pseudo-octahedral geometry of the (**L2**)$_2RuCl_2$ was obtain, due to large phosphine group two *P^N* ligands appear to perpendicular to each other. Pyridine group of phenanthridine and phosphines are *cis* to each other.

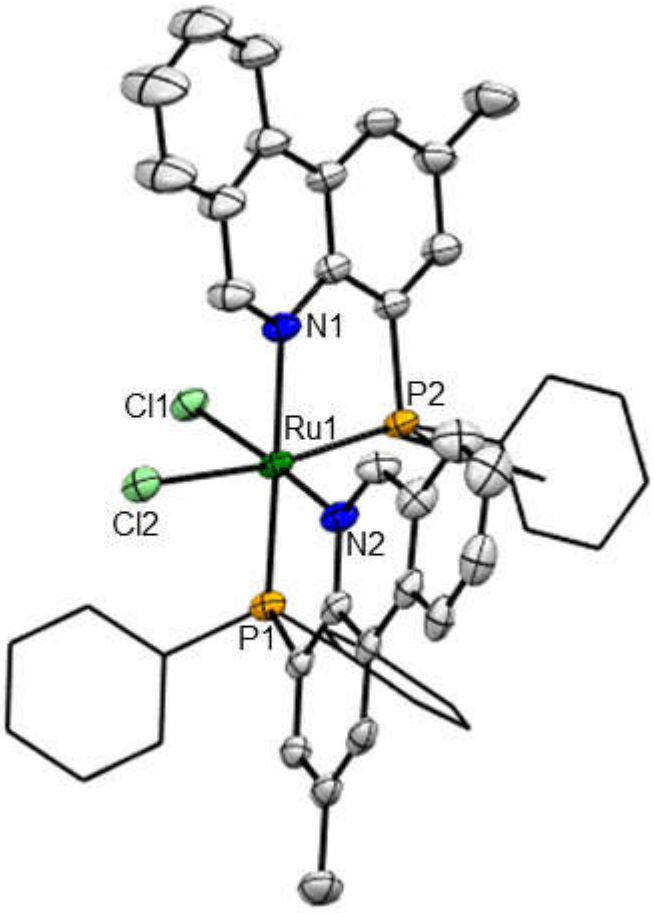

Figure 5. 7: ORTEP[15] of (**L2**)$_2RuCl_2$ with thermal ellipsoids shown at 50% probability levels.**,** Hydrogen atoms and labels on phosphine, and phenanthridine are omitted for clarity.

Table 5. 3: Selected bond distances (Å) and angles (°) for (**L2**)$_2$RuCl$_2$:

Selected Bonds	(Å)	Selected Angles	(°)
N(1)-Ru(1)	2.193(3)	N(2)-Ru(1)-P(1)	83.51(7)
N(2)-Ru(1)	2.076(3)	N(2)-Ru(1)-P(2)	94.08(8)
P(1)-Ru(1)	2.2442(8)	P(1)-Ru(1)-Cl(1)	96.71(3)
P(2)-Ru(1)	2.2401(8)	N(1)-Ru(1)-Cl(1)	83.82(7)
Cl(1)-Ru(1)	2.4238(8)	P(2)-Ru(1)-P(1)	100.69(3)
Cl(2)-Ru(1)	2.4712(8)	Cl(1)-Ru(1)-Cl(2)	90.24(3)

For (**L2**)RuCl$_2$(dmso)$_2$ and (**L2**)$_2$RuCl$_2$ the diagnostic proton signal for the *H*C=N in the 6-position of the phenanthridinyl ligand arms appeared at 10.59 ppm and 11.14 ppm, respectively, downfield shifted compared to the free ligand. This downfield shift of the diagnostic peak is evident of Ru bound single *P^N* ligand complex which was also observed for other complexes NMR shift previously in Chapter 2 and 3 while binding P^N ligand with Cu and Ni. However, tris *P^N* complexes (**L2**)$_3$Fe(PF$_6$)$_2$/(**L2**)$_3$Ru(PF$_6$)$_2$ possesses a symmetric facial octahedral environment which makes diagnostic proton more shielded resulting overall upfield shift. Similarly, the phosphorus signal of (**L2**)RuCl$_2$(dmso)$_2$ observed by ^{31}P was shifted downfield from free ligand. Two doublets at around ~ 55 and ~ 64 ppm represents the formation of complex (**L2**)$_2$RuCl$_2$. The *J* coupling value of ^{31}P NMR peaks of compound (**L2**)$_2$RuCl$_2$ are ~32 Hz, representing presence of two *cis* phosphorus environments. Peak at 64 ppm means an electron withdrawing group such as chloro is trans to that phosphine makes downfield shift by causing electron deficient phosphorus centre. Similarly, peak at 53 ppm represents weekly σ donating and strong π accepting group such as phenanthridinyl nitrogen is trans to the phosphine. The solid-state crystal structure shows compatible result with solution state phosphorus spectra.

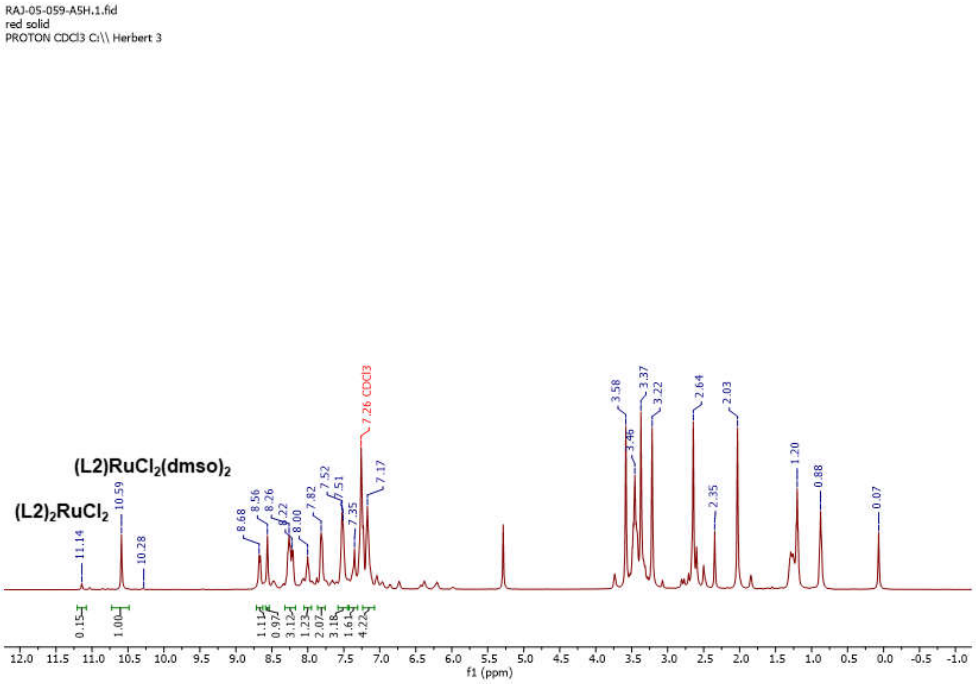

Figure 5. 8: ^{1}H NMR spectroscopy of a mixture of (**L2**)$RuCl_2(dmso)_2$ and (**L2**)$_2RuCl_2$.

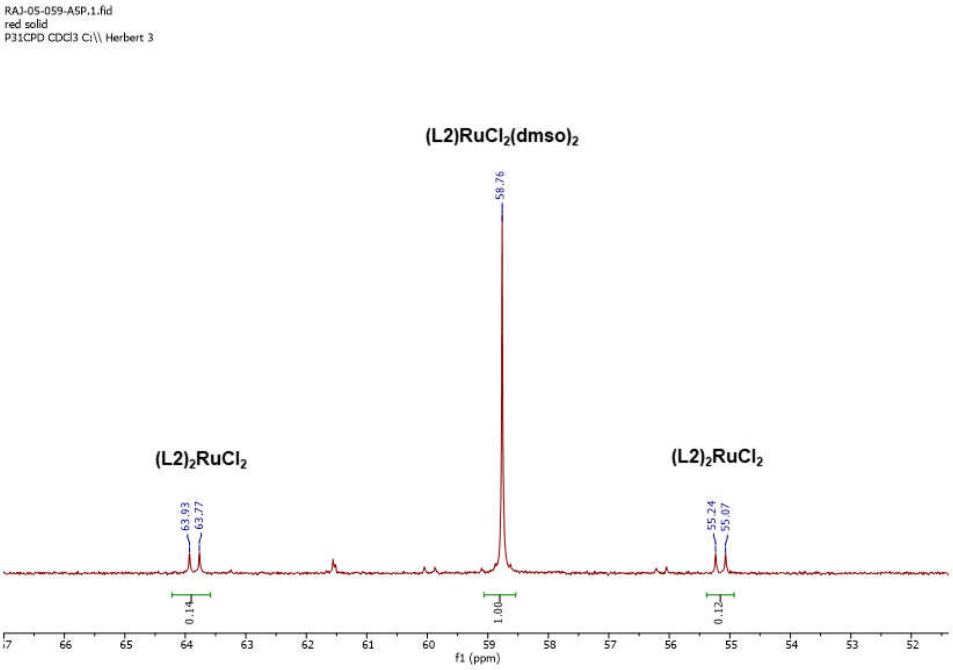

Figure 5. 9: $^{31}P\{^{1}H\}$ NMR spectroscopy of a mixture of (**L2**)$RuCl_2(dmso)_2$ and (**L2**)$_2RuCl_2$

The mixture of (**L2**)$RuCl_2(dmso)_2$ and (**L2**)$_2RuCl_2$ was refluxed with two more equivalent of *P^N* ligand in ethylene glycol for two days to give an orange solution. After addition of a $NaPF_6$ solution to the reaction mixture, an off white solid was collected as product (**L2**)$_3Ru(PF_6)_2$. The isolated product was characterized in solution using ^1H, $^{31}P\{^1H\}$ NMR spectroscopy, and in the solid-state via single crystal X-ray and elemental analysis. The octahedral complex (**L2**)$_3Ru(PF_6)_2$ formation required high energy as it needs to insert three ligand on Ru centre. First two *P^N* ligand easily displace weakly coordinating dimethylsulfoxide ligands at 80 °C, but the third *P^N* comes with displacing strongly coordination chloride ions which requires higher energy around 200 °C and longer reaction times.

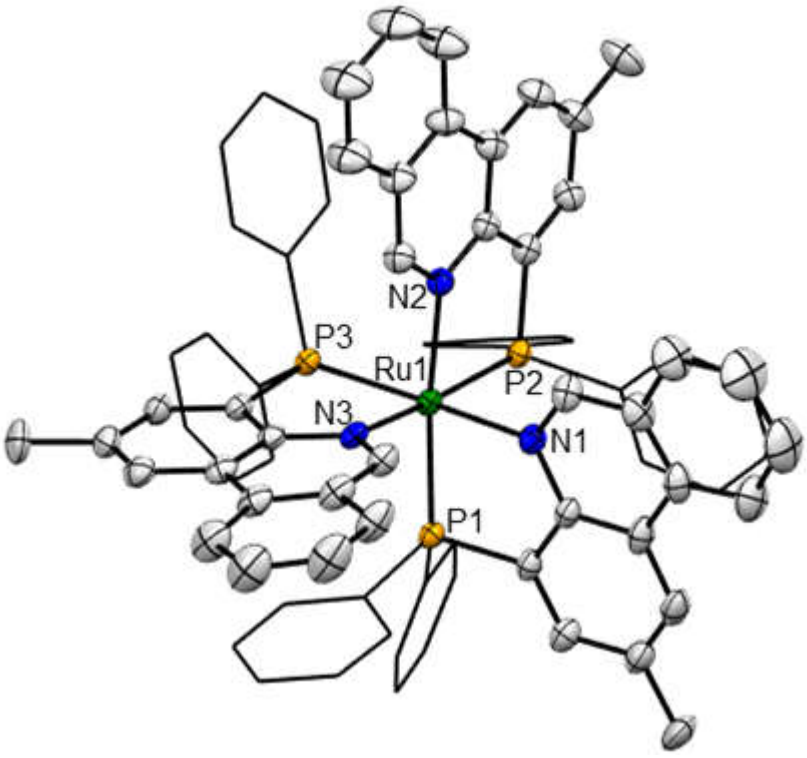

Figure 5. 10: ORTEP[15] of (**L2**)$_3Ru(PF_6)_2$ with thermal ellipsoids shown at 50% probability levels. Hydrogen atoms and labels on phosphine, and phenanthridine are omitted for clarity.

Table 5. 4: Selected bond distances (Å) and angles (°) for $(\mathbf{L2})_3Ru(PF_6)_2$:

Selected Bonds	**(Å)**	**Selected Angles**	**(°)**
N(1)-Ru(1)	2.172(4)	N(1)-Ru(1)-N(2)	90.51(15)
N(2)-Ru(1)	2.188(4)	N(1)-Ru(1)-N(3)	89.53(14)
P(1)-Ru(1)	2.3193(12)	N(1)-Ru(1)-P(1)	80.78(11)
P(2)-Ru(1)	2.3166(12)	N(1)-Ru(1)-P(2)	85.60(11)
N(3)-Ru(1)	2.183(4)	N(1)-Ru(1)-P(3)	169.81(11)
P(3)-Ru(1)	2.3258(12)	N(2)-Ru(1)-P(1)	171.04(11)

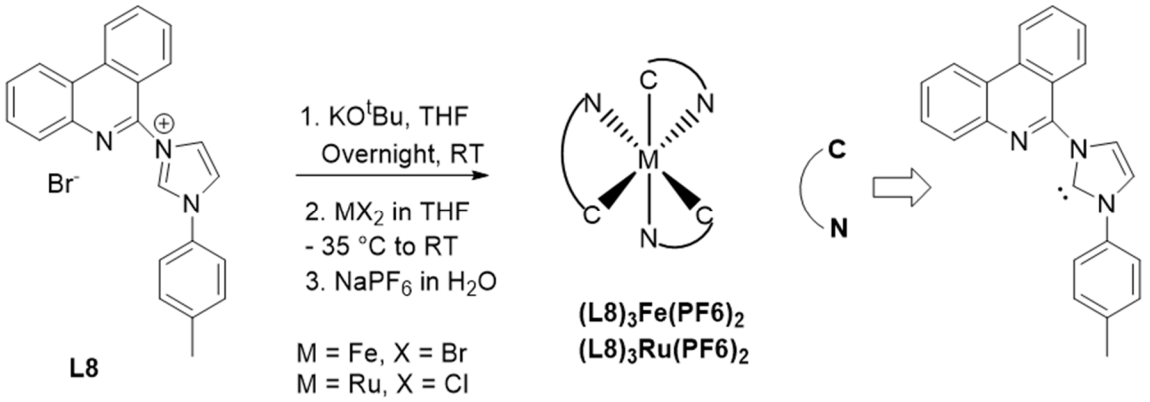

Scheme 5. 4: Bidentate *C^N* ligand based octahedral Fe and Ru complexes

Octahedral Fe(II) and Ru(II) complexes were also targeted with bifunctional *N*-heterocyclic based *C^N* ligands. The *N*-heterocyclic precursor 3-(6-phenanthridinyl)-1-(4-methylphenyl)-1H-imidazolium bromide salt was reacted with base KO^{t}Bu at room temperature to produce free neutral carbene species, followed by addition of $FeBr_2$ at -35 °C with vigorous stirring for acquiring a deep purple compound as a product. The product was filtered off the solution and washed with Et_2O. The isolated solid was crystallized with CH_2Cl_2-Et_2O. Similar synthetic technique (**Scheme 5.4**) was used to design octahedral Ru(II) complex by using *cis*-(dimethylsulfoxide)$_4RuCl_2$. The isolated solid was orange and has also been crystallized by

DCM-Et_2O. The complexes are characterized in solution by ^1H NMR spectroscopy, and in the solid-state by single crystal X-ray spectroscopy.

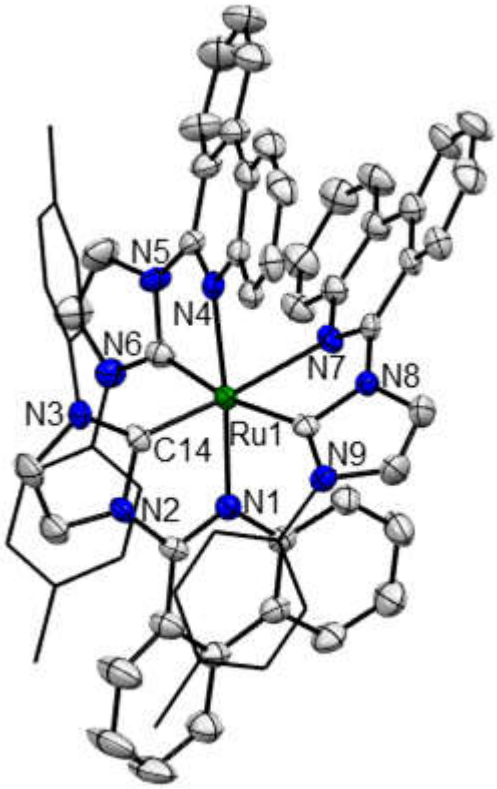

Figure 5. 11: ORTEP[15] of (**L8**)$_3$Ru(PF_6)$_2$ with thermal ellipsoids shown at 50% probability levels. Hydrogen atoms of phenanthridine, imidazole and toludiene, counter-ion are omitted for clarity.

Table 5. 5: Selected bond distances (Å) and angles (°) for $(\mathbf{L8})_3Ru(PF_6)_2$; Hydrogen atoms and labels on toluidine, counter-ion, and phenanthridine are omitted for clarity.

Selected Bonds	**(Å)**	**Selected Angles**	**(°)**
N(1)-Ru(1)	2.112(5)	C(14)-Ru(1)-N(1)	77.1(2)
C(14)-Ru(1)	1.934(6)	C(14)-Ru(1)-N(4)	99.4(2)
C(14)-N(2)	1.381(8)	N(1)-Ru(1)-N(4)	175.20(19)

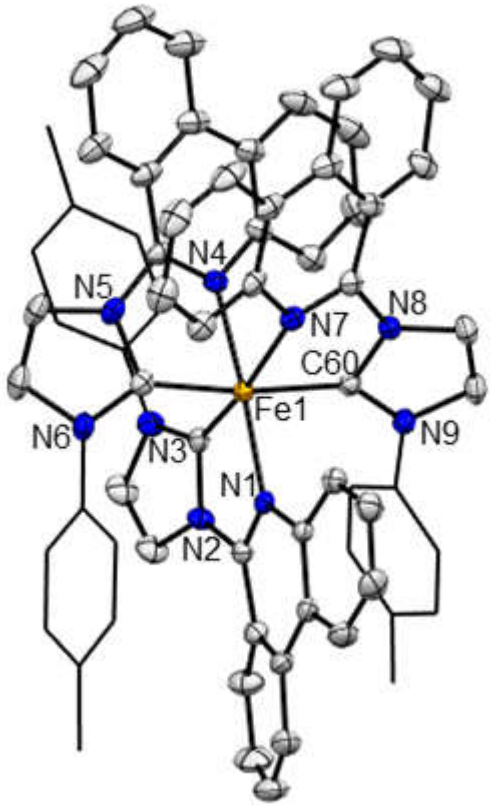

Figure 5. 12: ORTEP[15] of $(\mathbf{L8})_3Fe(PF_6)_2$ with thermal ellipsoids shown at 50% probability levels. Hydrogen atoms of phenanthridine, imidazole and toludiene, counter-ion are omitted for clarity.

Table 5. 6: Selected bond distances (Å) and angles (°) for (**L8**)$_3$Fe(PF$_6$)$_2$; Hydrogen atoms and labels on toluidine, counter-ion, and phenanthridine are omitted for clarity.

Selected Bonds	**(Å)**	**Selected Angles**	**(°)**
C(60)-Fe(1)	1.953(3)	N(9)-C(60)-N(8)	103.4(2)
N(1)-Fe(1)	2.046(2)	C(60)-Fe(1)-N(7)	76.79(10)
C(60)-N(8)	1.377(3)	N(8)-C(60)-Fe(1)	114.53(19)

5.3.2. Electronic Absorption spectroscopy:

Solution state absorption spectra were collected for dichloromethane solutions of all three complexes at room temperature. All three complexes showed strong absorption features in the UV region, with a weak tail into the visible region. The *P^N* isopropyl complex (**L4**)FeBr$_2$ showed highest molar absorptivity at UV region over phenyl precursor complexes (**L1**)FeBr$_2$ and (**L2**)FeBr$_2$. Highest molar absorptivity of (**L4**)FeBr$_2$ was also observed at the visible region tail. For all the complexes, two peak-shoulders were observed at around 310 nm and 360 nm. The high energy absorption spectra at UV region is quite significant to π-π* transition whereas the weak tail of visible region could be assigned as metal to ligand charge-transfer. The weak nature of these transitions may be due to poorer overlap between metal dπ and ligand low lying π* orbital in tetrahedral geometry of Fe(II). This weak absorption was observed and discussed previously for halide bridge Cu(I) complexes UV-Vis spectroscopy (Chapter 3).

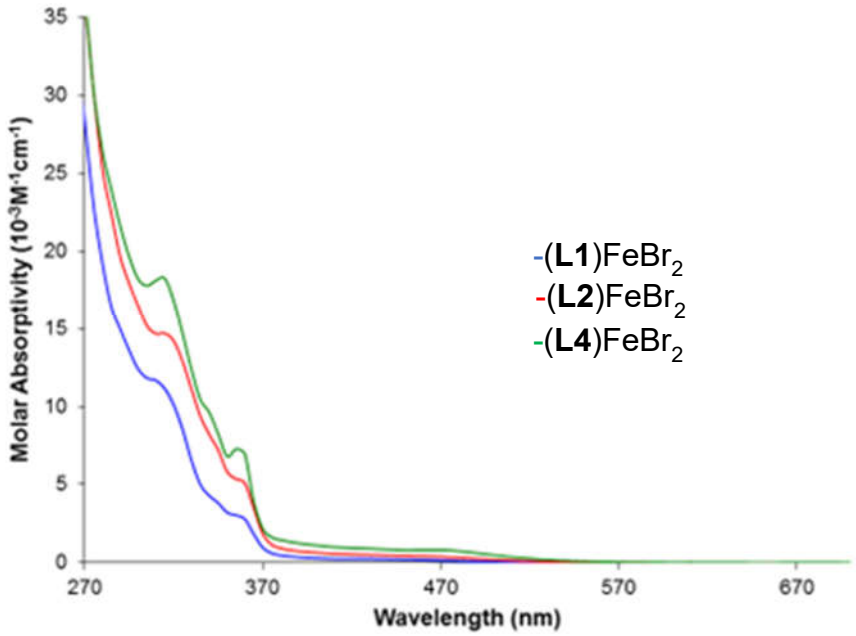

Figure 5. 13: Absorption spectroscopy of (**L1**)$FeBr_2$, (**L2**)$FeBr_2$ and (**L4**)$FeBr_2$ in CH_2Cl_2 solution at room temperature.

The absorption spectra of $(P\text{^}N)_3M(PF_6)_2$ (M = Fe, Ru) complexes were collected in acetonitrile solution of 1.4 x 10^{-4} M also at room temperature. Both of these complexes were showed strong absorption at the UV region. (**L2**)$_3Fe(PF_6)_2$ showed broad peak at visible region at 400-500 nm (highest point 435 nm), which can be assigned as MLCT band. Similar peak-shoulders were also observed at around 310 nm and 360 nm for this (**L2**)$_3Fe(PF_6)_2$ complex comparing with $(P\text{^}N)FeBr_2$ complexes. Quinoline-based complex (**L3**)$_3Fe(PF_6)_2$ also shows similar trend in the spectrum, but red shift of lowest energy absorption peak around 450 nm compared to (**L2**)$_3Fe(PF_6)_2$ complex by almost 20 nm. This counter intuitive result of π-extension therefore appears to be general, observed now for both Cu and Fe.[6,16,17,18] Lowest energy peak can be identify as MLCT band. *N*-Heterocyclic carbene-based octahedral Fe(II) complex (**L8**)$_3Fe(PF_6)_2$ showed strong intensity at the same concentrated solution. The lowest energy absorption band is shifted around 70 nm at the 500 nm region. In *P^N* ligands phosphines

are both moderate σ-donor and π-acceptor whereas pyridyl phenanthridine is good π-acceptor. On the contrary NHC ligands are strong σ-donor and poor π-acceptor, and with the same π-acceptor property of pyridyl phenanthridine. Strong σ-donor provides high electron density around metal centre which raises the energy of e_g orbital.[19] Consequently the energy between e_g of metal d orbital and LUMO (π* anti-bonding) decreases which causes red shift of (**L8**)$_3$Fe(PF$_6$)$_2$ complex over (**L2**)$_3$Fe(PF$_6$)$_2$ in the absorption spectra. Another outcome of high energy e_g orbital may be to destabilize metal centred (MC) excited states compared with MLCT ones, and extend the life time of MLCT excited state.[1] For complex (**L2**)$_3$Ru(PF$_6$)$_2$ the peaks around 293 and 320 nm could be attributed to π-π* transition based on phenanthridine ring.[4] Low energy highest absorption band was observed at 349 nm for (**L2**)$_3$Ru(PF$_6$)$_2$ with a following shoulder at 363 nm.

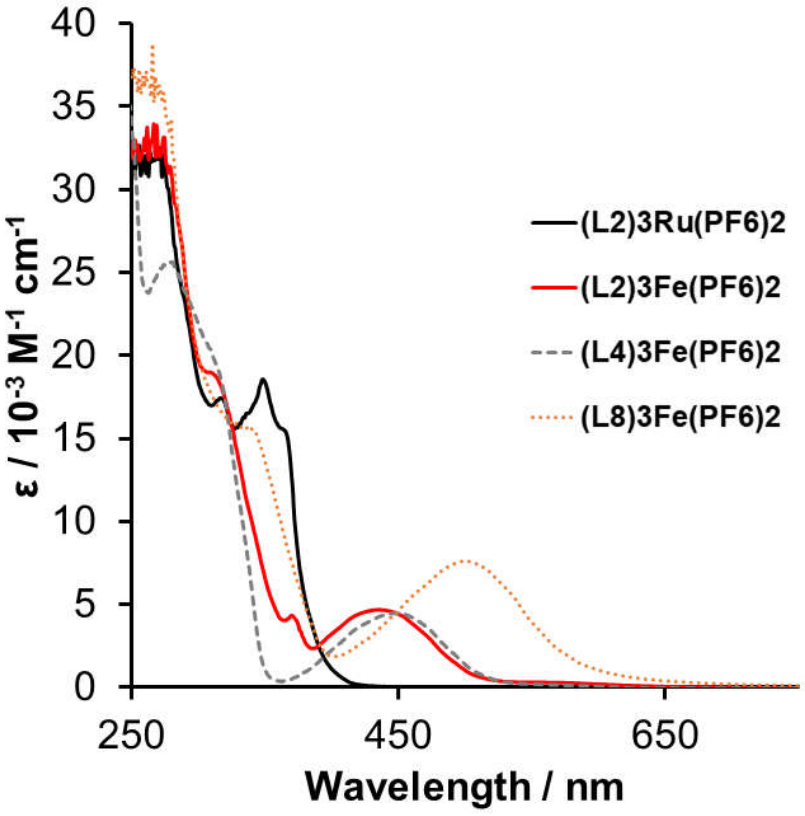

Figure 5. 14: Absorption spectroscopy of (**L2**)$_3$Fe(PF$_6$)$_2$, (**L2**)$_3$Ru(PF$_6$)$_2$, (**L3**)$_3$Fe(PF$_6$)$_2$ and (**L8**)$_3$Fe(PF$_6$)$_2$ in CH$_3$CN solution at room temperature.

5.3.3. Cyclic Voltammetry:

Cyclic voltammograms of (**L1**)FeBr$_2$, (**L2**)FeBr$_2$ and (**L4**)FeBr$_2$ were collected in dichloromethane solution at room temperature. All three complexes showed both irreversible oxidation and reduction events. Two irreversible oxidation events for (**L1**)FeBr$_2$ were at 0.65 V and 1.1 V vs Fc/Fc$^+$ and irreversible reduction at -1.99 V, comparing to (**L2**)FeBr$_2$ oxidation events at 0.60 V and 1.08 V and reduction at -2.0 V. These close potentials for (**L1**)FeBr$_2$ and (**L2**)FeBr$_2$ could explain the formation of monomer at solution state from pyramidal dimer of

(**L1**)$FeBr_2$. Two irreversible oxidation also observed at 0.4 and 0.7 V for (**L4**)$FeBr_2$ and a -2.3 V irreversible reduction peak.

(L1)$FeBr_2$:

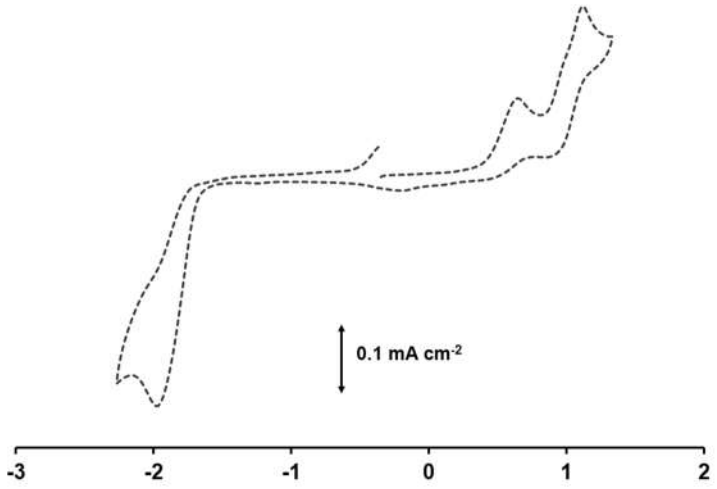

(L2)$FeBr_2$:

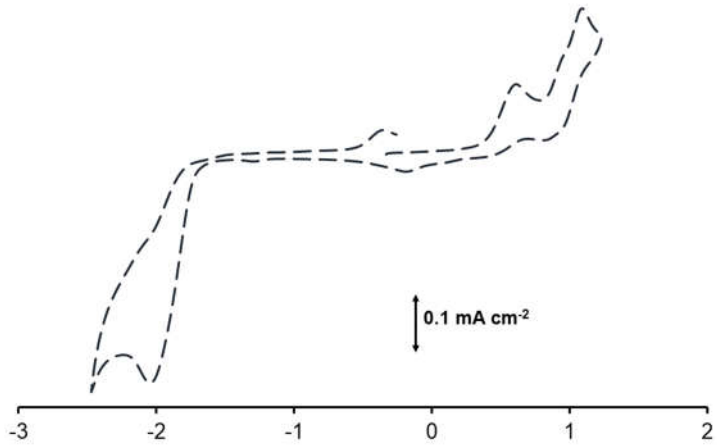

(L4)$FeBr_2$:

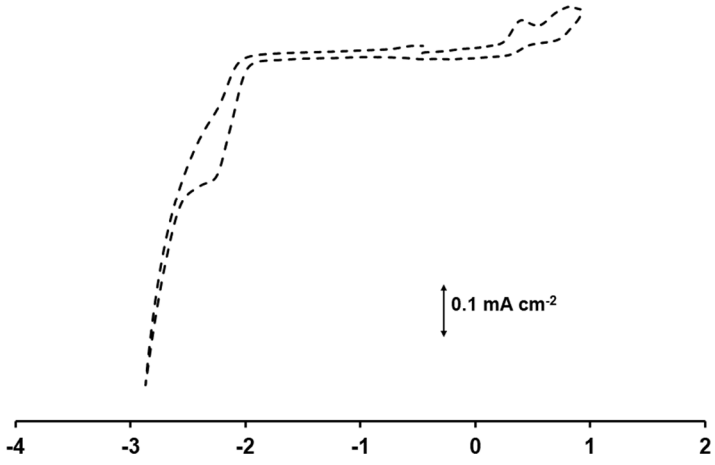

Figure 5. 15: Cyclic Voltammetry of (**L1**)$FeBr_2$, (**L2**)$FeBr_2$ and (**L4**)$FeBr_2$ oxidation and reduction wave in DCM solution ([analyte] = 1.1 mM; 1 M [nBu_4N][PF_6], 100 mV/s scan rate).

Cyclic voltammetry of (**L2**)$_3$Fe(PF_6)$_2$ and (**L2**)$_3$Ru(PF_6)$_2$ was conducted in acetonitrile solution at room temperature. The cyclic voltammogram of (**L2**)$_3$Fe(PF_6)$_2$ showed a reversible oxidation event at 0.9 V with an irreversible reduction -1.6 V followed by decomposition product formation. Similarly, for (**L3**)$_3$Fe(PF_6)$_2$ complex shows identical oxidation and reduction at 0.9 V and -1.6 V respectively, which represents identical redox activity in solution of (**L2**)$_3$Fe(PF_6)$_2$ and (**L3**)$_3$Fe(PF_6)$_2$.

$(L2)_3Fe(PF_6)_2$:

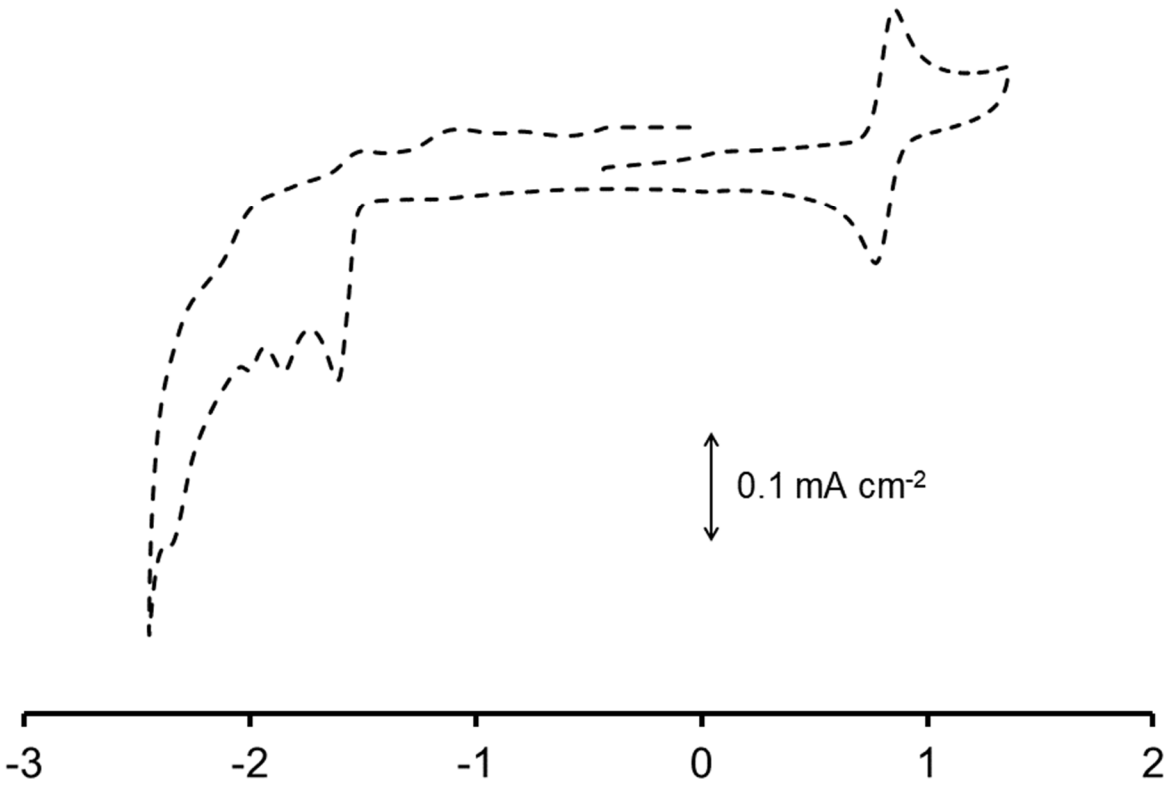

(L3)$_3$Fe(PF$_6$)$_2$:

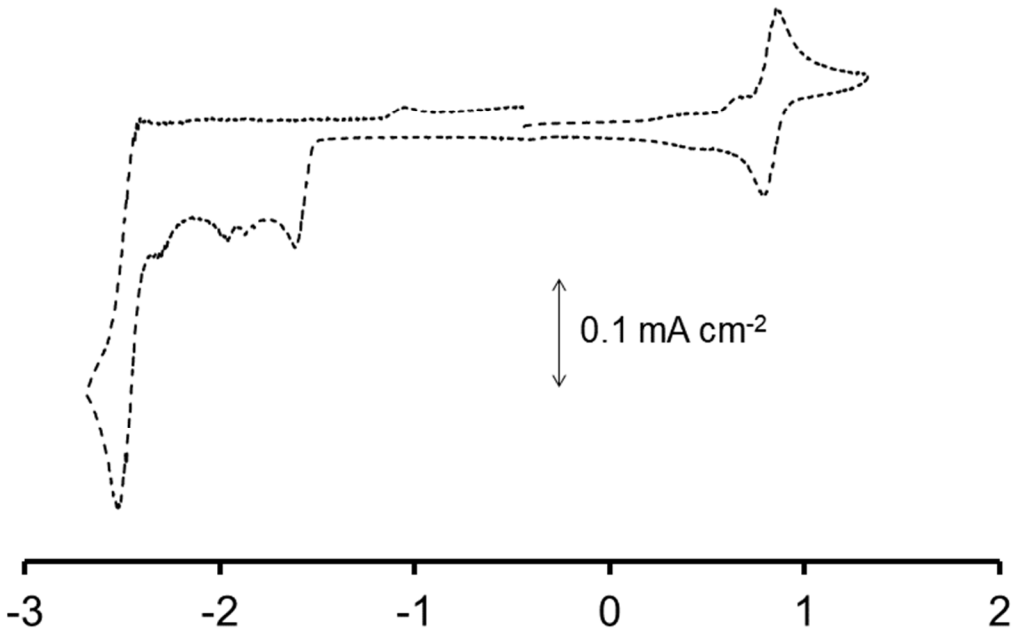

Figure 5. 16: Cyclic Voltammetry of (**L2**)$_3$Fe(PF$_6$)$_2$ and (**L3**)$_3$Fe(PF$_6$)$_2$ oxidation and reduction wave in CH_3CN solution ([analyte] = 1.1 mM; 1 M [nBu4N][PF$_6$], 100 mV/s scan rate).

However, (**L2**)$_3$Ru(PF$_6$)$_2$ showed two oxidation and two reduction peaks. Among oxidation peaks at 1.9 V is quasi-reversible redox event and the peak at 1.8 V is irreversible. For reductions -2.1 V is completely reversible reduction–oxidation couple and a quasi-reversible reduction event at around -1.8 V.

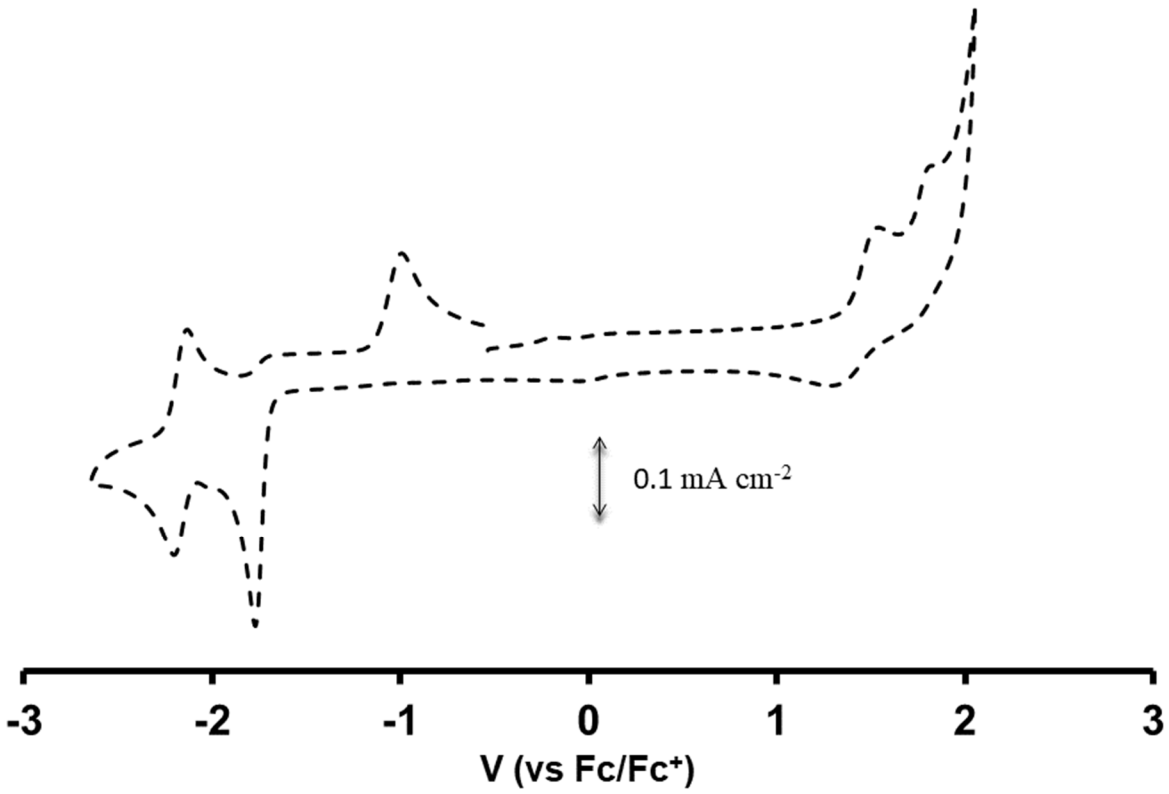

Figure 5. 17: Cyclic Voltammetry of $(\mathbf{L2})_3Ru(PF_6)_2$ oxidation and reduction wave in CH_3CN solution ([analyte] = 1.1 mM; 1 M [nBu4N][PF_6], 100 mV/s scan rate).

5.3.4. Spectroelectrochemistry:

Spectroelectrochemical oxidation of $(\mathbf{L2})_3Fe(PF_6)_2$ ($E_{applied}$ = 0.4 to 1.3) shows conversion to a single new complex with visible isosbestic points corresponding to reversible $1e^-$ redox couple observed by CV of the $(\mathbf{L2})_3Fe(PF_6)_2$ at 0.9 V.

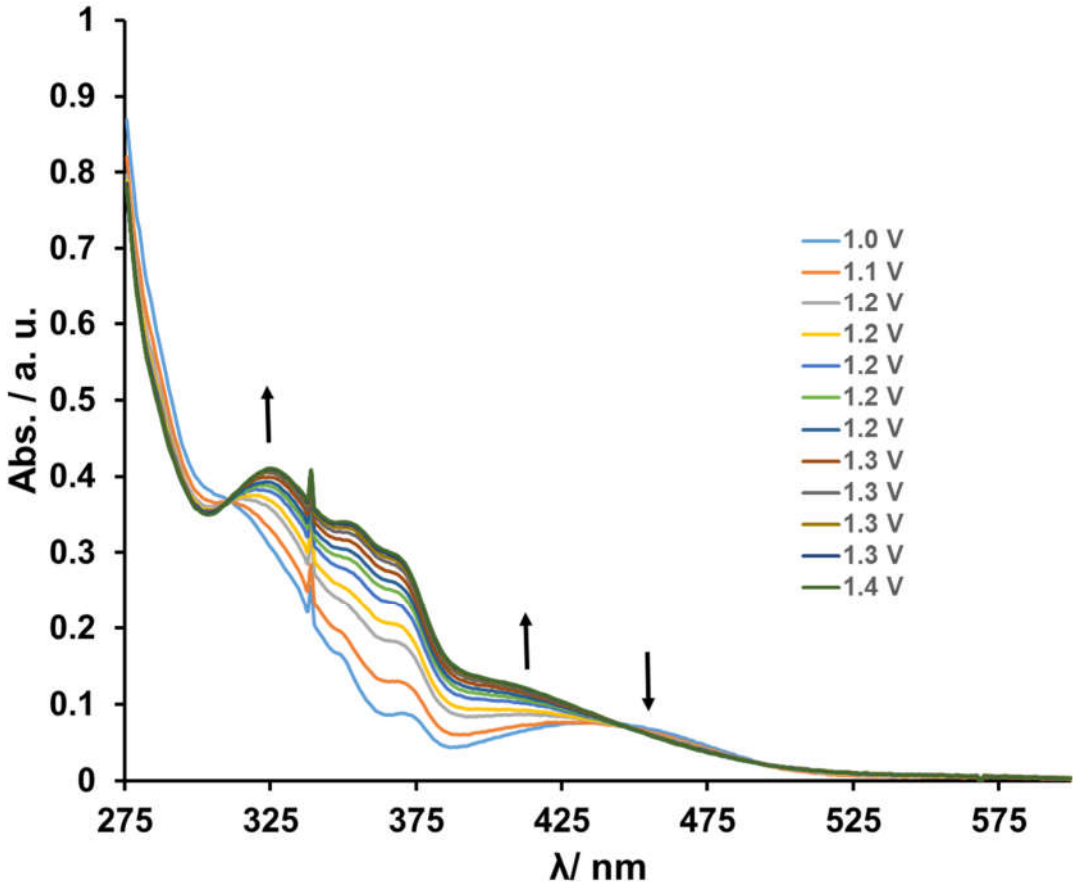

Figure 5. 18: Spectroelectrochemistry of (**L2**)$_3$Fe(PF$_6$)$_2$ CH$_3$CN solution at 22 °C in 0.1 M nBu$_4$NPF$_6$. Oxidative potential applied from +1.0 to +1.4 V.

Similarly by applying potential ($E_{applied}$ = 1.0-1.4) for complex for (**L3**)$_3$Fe(PF$_6$)$_2$ also shows conversion to one species oxidized Fe(III) from Fe(II) that also observed in CV of complex (**L3**)$_3$Fe(PF$_6$)$_2$.

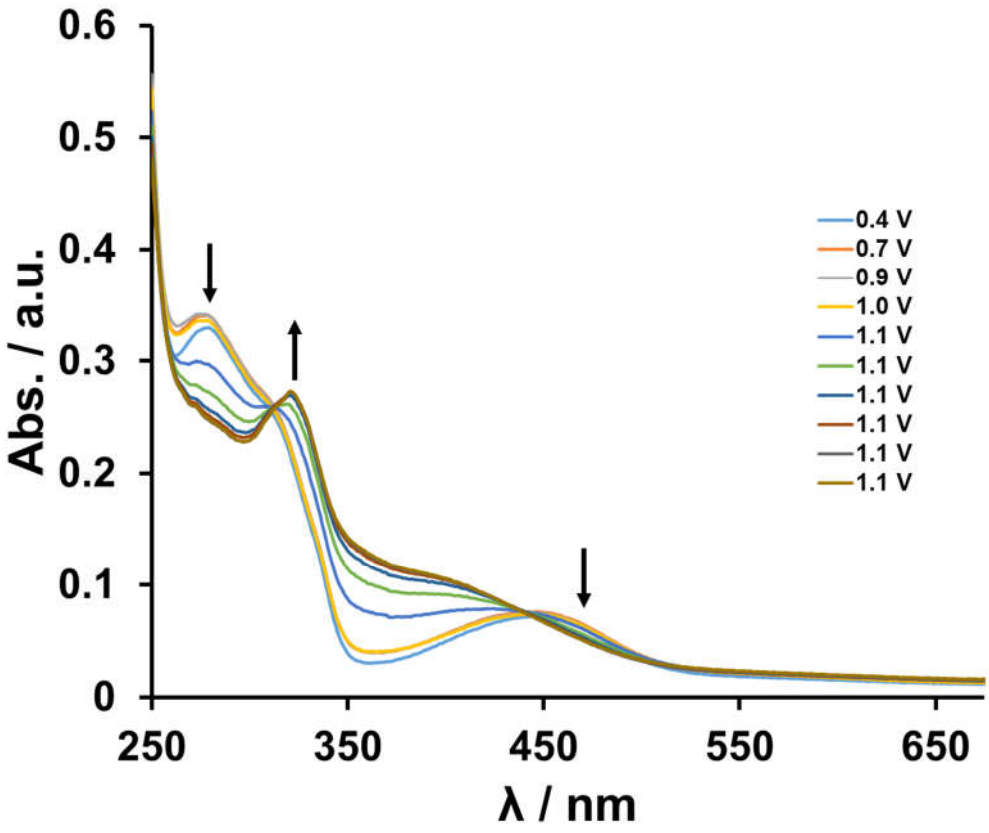

Figure 5. 19: Spectroelectrochemistry of (**L3**)$_3$Fe(PF_6)$_2$ CH_3CN solution at 22 °C in 0.1 M nBu_4NPF_6. Oxidative potential applied +0.4 to +1.1 V compareable with the oxidation peak of CV of (**L3**)$_3$Fe(PF_6)$_2$.

5.3.5. Mössbauer Spectra:

Table 5. 7: Mössbauer data of (**L1**)$FeBr_2$, (**L2**)$FeBr_2$, (**L4**)$FeBr_2$ and (**L2**)$_3Fe(PF_6)_2$ and comparison with previously published references, spectra taken at 10 K for all four complexes:

Compound	**δ (mm s^{-1})**	**ΔE_Q (mm s^{-1})**
(**L1**)$FeBr_2$	0.9569(20)	3.129(40)
(**L2**)$FeBr_2$	0.8046(13)	2.9591(25)
(**L4**)$FeBr_2$	0.8095(12)	3.1539(23)
(**L2**)$_3Fe(PF_6)_2$	0.4535(12)	0.2792(19)
Fe(*P*^*N*-$^{i}P_r$)Cl_2 [5]	0.680(2)	2.871(4)
$Fe_2(SN^H\text{-}Ph_2)_2(\mu\text{-}Cl)_2(Cl)_2$ [20]	0.881(1)	3.080(2)
$Fe(SN^H\text{-}Ph)(Cl)_2$ [20]	0.804 (Cal.)	2.787 (Cal.)

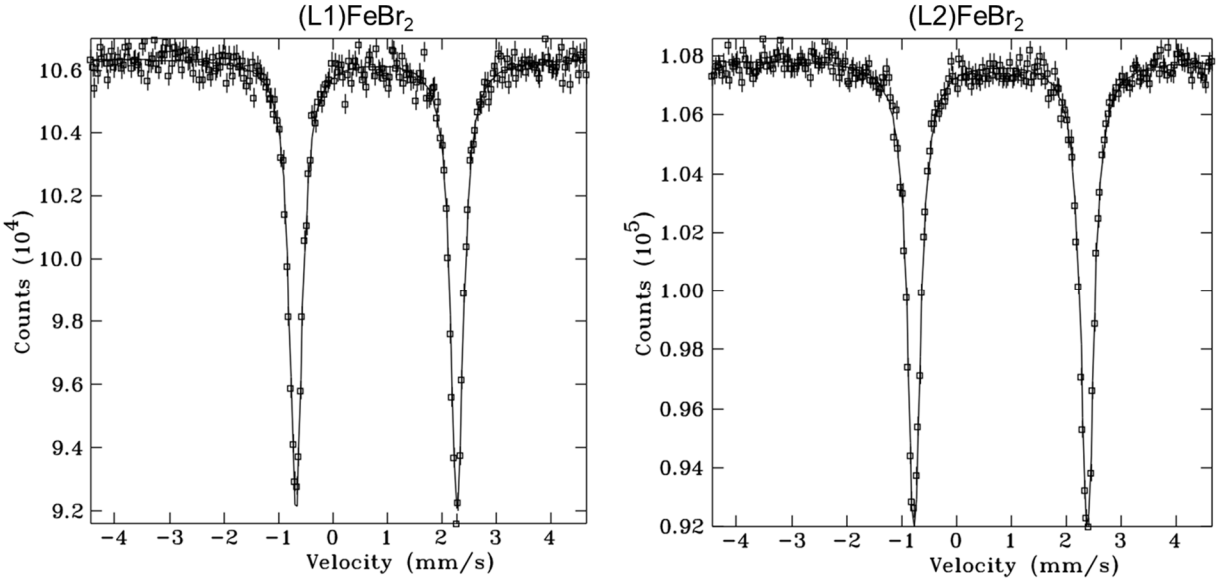

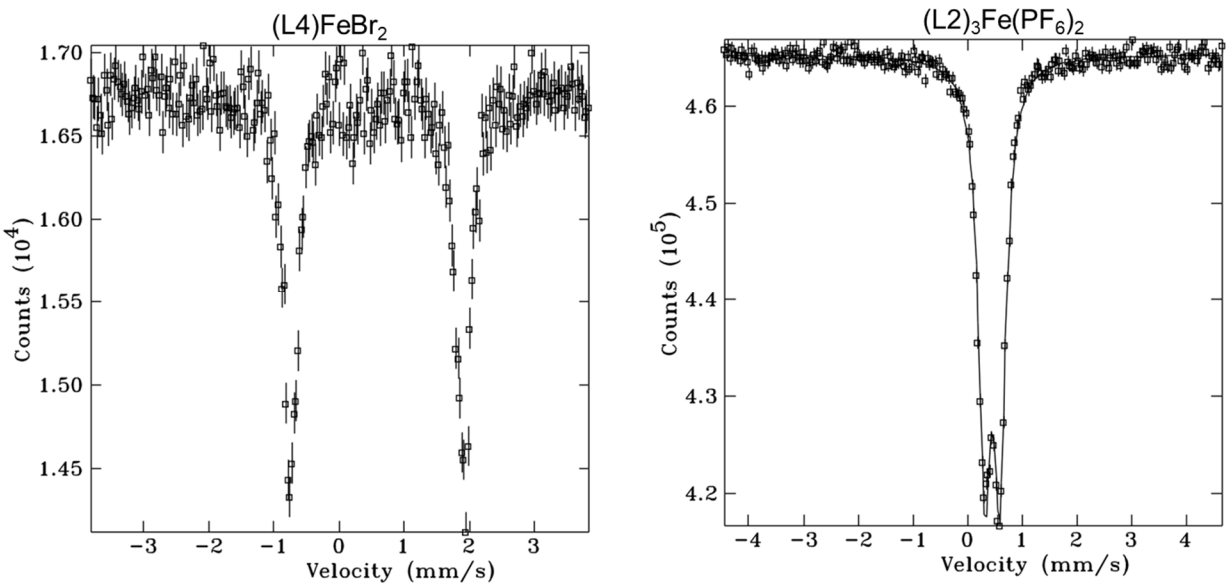

Mössbauer spectra for all four Fe(II) complexes have been collected at 10 K (Table 2). High spin Fe(II) was confirmed for the complexes (**L1**)$FeBr_2$, (**L2**)$FeBr_2$ and (**L4**)$FeBr_2$ from the isomer shift and quadrupole splitting data, which are comparable to previously published paramagnetic, tetrahedral Fe(II) complexes. Although the Mössbauer spectra for (**L2**)3$Fe(PF_6)_2$ was supported the Fe(II) low spin, could be explained as strong ligand field strength by three bifunctional *P^N* donation.

5.3.6. "Evans' Method"[21]:

"Evan's method" explains the proton resonance line's shift with respect to an inert reference molecule in caused by the presence of a paramagnetic compound in the solution phase. The Evan's method theoretical expression would be "$\Delta H/H = (2\pi/3)\Delta_k$ where Δ_k is the change in volume susceptibility".[21] The magnetic moment value[21] for all three complexes (**L1**)$FeBr_2$, (**L2**)$FeBr_2$ and (**L4**)$FeBr_2$ in solution state have been calculated using Evans' method, resulting 4-4.8 μ_B for four unpaired electrons of Fe(II), high spin, d^8 system. The experiment has been undertaken DCM as the reference solvent peak. The frequency shift observed for (**L1**)$FeBr_2$ in

present of paramagnetic environment 115.27 Hz, corresponding effective magnetic moment for 4.40 μ_B. Similar chemical shift of 118.93 Hz obtained for (**L2**)$FeBr_2$ and effective magnetic moment 4.47 μ_B. The diisopropyl precursor of the iron complex showed larger chemical shift of 228.55 Hz and corresponding higher magnetic moment of 4.86 μ_B. Solid-state magnetic susceptibility was measured using dry fine powder of all three Fe(II) complexes. The measured magnetic susceptibility of the (**L1**)$FeBr_2$: 4.25 μ_B, close to solution state Evan's method data representing four unpaird electrons. The complex (**L2**)$FeBr_2$ solid-state magnetic susceptibility 4.35 μ_B, also supporting the four unpaired electron comparing with the solution state magnetic moment. Although (**L4**)$FeBr_2$ solid state magnetic susceptibility 4.30 μ_B where in solution a higher value of 4.86 μ_B was observed.

5.4. Conclusion:

Both the Phosphine and N-hetrocyclic carbene ligand based d^8 metal ion Fe/Ru based complexes have been synthesized. The phosphine ligand bromide functionalized Fe complexes have been synthesized. X-ray structure reveled both the tetrahedral and square pyramidal geometry. The square pyramidal geometry was obtained by bridging dative interaction with bromide ligand. These complexes showed paramagnetic in nature, which was detected by NMR spectroscopy, Mössbauer Spectra and Evans' method. The octahedral complexes of both phospnine and carbene ligands of Fe showed diamagnetic nature, X-rays crystallography showed geometry of octahedral environment. The UV-Vis spectroscopy showed MLCT band for octahedral complexes and reversible Fe(II) to Fe(III) oxidation event was observed in cyclic voltammetry.

5.5. Experimental Information:

Unless otherwise stated, all air sensitive manipulations were carried out in N_2-filled glove box or on a Schlenk line (Ar). 2,6-dibromoaniline (AK Scientific), *N*-iodosuccinimide (AK Scientific), p-Toluidine (Alfa Aesar), *N*-bromosuccinimide (Alpha Aesar), 2-formylphenyl boronic acid (Combi Blocks), $Pd(PPh_3)_4$ (Alfa Aesar), Na_2CO_3 (Alfa Aesar), chlorodiphenylphosphine (VWR), $FeBr_2$ (Aldrich) were purchased and were used as received. 2-bromo-4-methylaniline,[9] 6-bromo-2-iodo-4-methylaniline,[9] 8-bromo-6-methylquinoline,[22] 4-diphenylphosphinophenanthridine[10] (**L1**) and were synthesized following published procedures or synthesized which discussed in previous chapters. All the organic solvents were dried over appropriate reagents and deoxygenated prior to use. 1,2-dimethoxyethane and water were degassed before using in Suzuki coupling reaction. All NMR spectrums were recorded on a Bruker Avance 300 MHz or Bruker Avance-III 500 MHz spectrometer. Electronic absorption spectra (750–190 nm) were recorded on a Thermo Scientific Genesys 10S UV-Vis spectrophotometer at room temperature, at concentrations on the order of 1.0×10^{-4} mol L^{-1}. Elemental analyses were performed at the University of Manitoba on a Perkin Elmer EA2400 CHN Analyzer. The solid-state magnetic moment was determined by using the Johnson Metthey M.S.B. instrument. Synthesis of all the ligands have been discussed in the Chapter 2 extensively.

Synthesis of (L1)$FeBr_2$:

A solution of **L1** (0.091 g, 0.250 mmol) in DCM (10 mL) was added dropwise to a THF (15 mL) solution of $FeBr_2$ (0.054 g, 0.250 mmol) in a 20 mL scintillation vial, with constant stirring under nitrogen atmosphere. The reaction mixture was stirred overnight, leading to a color change from yellow to deep orange. The mixture was then filtered through a plug of Celite and the filtrate

dried under reduced pressure to leave an orange solid, which was further washed with Et_2O (5 mL). Yield = 0.093 g (64.5 %). Single crystals suitable for X-ray diffraction were grown via diffusion of hexane vapours into a DCM solution. ^{1}H NMR ($CDCl_3$, 300 MHz, 25 ˚C): δ = 23.2, 18.1 (br), 16.6 (br), 13.1, 12.9, 11.5, -3.8, -5.4 (v br), -7.2, -7.9 ppm (br).

Synthesis of (L2)$FeBr_2$:

Complex (**L2)FeBr$_2$** was synthesized analogously to (**L1)FeBr$_2$** using **L2** (0.093 g, 0.250 mmol) and $FeBr_2$ (0.054 g, 0.250 mmol). Orange crystals. Yield = 0.107 g (72.3 %). ^{1}H NMR ($CDCl_3$, 300 MHz, 25 ˚C): δ = 22.6, 18.1 (br), 17.3 (v br), 13.2, 13.0, 2.2, -4.0, -5.9 (v br), -7.6, -8.2 ppm.

Synthesis of (L4)$FeBr_2$:

Complex (**C5**) has been synthesized analogously to **C1** using the **L4** (0.074 g, 0.250 mmol) and $FeBr_2$ (0.054 g, 0.250 mmol). Orange crystals. Yield = 0.830 g (64.8 %).^{1}H NMR ($CDCl_3$, 300 MHz, 25 ˚C): δ = 22.6, 20.7 (br), 14.1, 13.7, 9.1 (br), 3.0, -4.9 (br), -9.8 ppm. Anal. Calc. for $C_{52}H_{40}N_2P_2Cu_2Cl_2$: C, 45.75; H, 4.61. Found: C, 45.76; H, 4.74.

Synthesis of (L2)$_3$Fe(PF_6)$_2$:

A solution of **L2** (0.071 g, 0.1875 mmol) in DCM (4mL) and CH_3CN (2 mL) was added to a solution of $FeSO_4.(NH_4)_2SO_4$ in degassed EtOH (3mL) and H_2O (1mL) in a 50 mL Schlenk flask under Ar atmosphere. The solution was stirred for 4 hrs at room temp when solution color changed to orange. Then a solution of $NaPF_6$ in degassed H_2O (5 mL) was added to the reaction mixture, and stirring continued for 30 min after which the color had changed to deep red. Then the reaction mixture was dried in vacuum and extracted with DCM (15 mL) and pass it through celite and dried again to get a brown solid. The brown solid was crystallized with DCM-Et_2O to get the deep brown colored crystallized product. Yield = 0.043 g (46.5%). ^{1}H NMR (CD_2Cl_2, 500 MHz, 25 °C): δ 8.55 (d, 3H), 8.51 (d, 3H), 8.08 (s, 3H,), 8.01 (m, 3H,), 7.59 (m, 3H), 7.51

(m, 3H), 7.39 (br, 6H), 7.33 (br, 3H), 7.18 (d, 3H), 7.03 (m, 6H), 6.68 (m, 3H), 6.21 (m, 6H), 6.01 (br, 6H), 2.59 ppm (s, 3H, $^{phen}C_{Me}$-*H*). $^{13}C\{^1H\}$ NMR (CD_2Cl_2, 126 MHz, 25 °C): δ 162.9 (s), 148.2 (br), 141.5 (s), 137.3 (s), 135.7 (s), 135.2 (br), 133.5 (dd), 132.6 (s), 132.4 (s), 131.6 (dd), 131.2 (br), 130.3 (s), 129.9 (s), 129.8 (d), 129.7 (s, br), 128.2 (s), 128.0 (br), 127.7 (s), 127.3 (br), 122.6 (s), 21.9 ppm (C_{Me}).$^{31}P\{^1H\}$ NMR (CD_2Cl_2, 121 MHz, 25 °C): δ 58.2 (s), -143.62 ppm (sep). Anal. Calc. for $C_{52}H_{40}N_2P_2Cu_2Cl_2$: C, 63.38, H, 4.09. Found: C, 63.22; H, 4.19.

Synthesis of $(L2)_3Ru(PF_6)_2$:

The reaction occurred in two steps. In first step, I synthesized {4-diphenylphosphino-2-methylphenanthridine}$Ru(dmso)_2Cl_2$.

{4-diphenylphosphino-2-methylphenanthridine}$Ru(dmso)_2Cl_2$: This has been synthesized by following the published procedure (IC ref). A solution of **L2** (0.091 g, 0.24 mmol) in $CHCl_3$ (10 mL) was added to $(dmso)_4RuCl_2$ (0.121 g, 0.25 mmol) solution in $CHCl_3$ (10 mL) and refluxed the reaction mixture at 85 °C for 2h. After cooling down to room temp the solution was filtered through a small plug of celite and concentrated nearly to dryness. Then Et_2O (20 mL) was added to the reaction to the reaction mixture to get a deep red precipitate which was collected by filtration and washed with Et_2O (10 mL) and dry that in vacuum as a mixture of A and B. I used this mixture further as considered compound A as a single component.

The obtained red solid (0.044 g, 0.063 mmol) and **L2** (48 mg, 0.125 mmol) were taken in ethylene glycol (8 mL) and reflux the mixture at 200 °C for 2 days. After cooling it down to 50 °C, excess NH_4PF_6 solution in water (0.041g in 5 mL) was added to the reaction and continue stirring at room temp for 30 mins, by the time a yellowish precipitate was formed. The precipitate was filtered and washed with little in water (5 mL). The yellow solid was crystallized

in DCM solution with slow diffusion of Et_2O. Yield: 0.078 g (82%). ^1H NMR (CD_3CN, 500 MHz, 25 ° C): δ 8.62 (d, 3H), 8.59 (d, 3H,), 8.54 (s, 3H), 8.01 (m, 3H), 7.61 (m, 3H), 7.55-7.48 (overlapped m, 9H), 7.42 (d, 3H), 7.31 (br, 3H), 7.06 (br, 6H), 6.56 (m, 3H), 6.14 (m, 6H), 6.10-6.07 (br, 6H), 2.51 ppm (s, 3H, $^{phen}C_{Me}$-*H*). $^{13}C\{^1H\}$ NMR (CD_3CN, 126 MHz, 25 °C): δ 160.8 (s), 146.6 (br), 141.4 (br), 137.8 (s), 135.5 (br), 135.4 (s), 134.5 (dd), 133.5 (s), 132.9 (s), 132.8 (d), 137.7 (br), 131.4 (s), 130.8 (d), 130.1 (s), 129.9 (br), 129.6 (s), 128.2 (s), 128.1 (br), 128.0 (br), 127.8 (s), 123.0 (s), 21.3 ppm (C_{Me}). $^{31}P\{^1H\}$ NMR ($CDCl_3$, 121 MHz, 25 °C): δ 58.2 (s), -143.6 ppm (sep).

Synthesis of $(L3)_3Fe(PF_6)_2$:

(**L3**)$_3$Fe(PF$_6$)$_2$ complex has synthesize by following the previous method of (**L2**)$_3$Fe(PF$_6$)$_2$ by using the **L3** ligand. Yield: 0.053 g (66 %). ^1H NMR (CD_2Cl_2, 500 MHz, 25 °C): δ 8.02 (m, 3H), 7.74 (s, 3H,), 7.50 (m, 3H), 7.36 (br, 12H), 7.06-7.01 (br m, 12H), 6.58 (m, 6H), 5.99 (br, 6H), 2.50 ppm (s, 3H, $^{quin}C_{Me}$-*H*). $^{31}P\{^1H\}$ NMR (CD_2Cl_2, 121 MHz, 25 °C): δ 55.45 (s), -144.59 ppm (sep). ^{19}F NMR ($CDCl_3$, 470 MHz, 25 ° C): δ -72.9 ppm (d).

Synthesis of $(L8)_3Fe(PF_6)_2$:

A solution of KO^{t}Bu (0.021 mg, 0.188 mmol) in THF (4 mL) was added into a suspension of **L2** (0.071 mg, 0.188 mmol) in THF (10 mL) in a 50 mL round bottom flask, immediate color change to deep brown solution. The solution was stirred for 12 hrs. Then reaction mixture was cooled to -35 °C for 30 mins when a solution of $FeBr_2$ (0.013 mg, 0.063 mmol) in THF (5 mL) at -35 °C was added to the reaction mixture. The reaction mixture was taken to room temp and stirring was continued for 24 hrs. Then a purple precipitate was formed with a deep brown-red solution. Then the solution was filtered through a glass filter and precipitate was washed with

Et_2O (3 mL). The precipitate was extracted with CH_3CN (15 mL) and a degassed solution of $NaPF_6$ (25 mg, 0.063 mmol) in H_2O was added to it. The solution was stirred for 12 hrs and pumped it dry and extracted with DCM (10 mL) and crystallized with Et_2O to get a deep red solid as product. Yield: 0.103 g (41%). ^{1}H NMR (CD_3CN, 500 MHz, 25 °C): 8.77 (m, 1H), 8.61 (m, 1H), 8.36 (m, 1H), 8.29 (m, 1H), 8.21-8.17 (m, 2H), 8.13-8.11 (m ,1H), 8.03-8.01 (m, 1H), 7.97-7.93 (m, 3H), 7.85-7.80 (m, 3H), 7.73-7.62 (m, 5H), 7.59-7.56 (m, 1H), 7.50-7.41 (m, 5H), 7.37-7.33 (m, 2H), 7.27-7.25 (m, 1H), 7.16 (d, 1H), 7.06-7.03 (m, 1H), 6.94 (v br m, 1H), 6.70-6.64 (v br m, 5H), 6.43 (v br, 2H), 5.94-5.82 (v br m, 3H), 2.30 (s, 3H), 1.57 (s, 3H), 1.32 ppm (s, 3H).

Synthesis of $(L8)_3Ru(PF_6)_2$:

(**L8**)$_3$Ru(PF$_6$)$_2$ complex has synthesize by following the previous method of (**L8**)$_3$Fe(PF$_6$)$_2$ by using *cis*-(dmso)$_2$RuCl$_2$. Yield: 0.271 g (31 %). ^{1}H NMR (CD_3CN, 500 MHz, 25 °C): 8.90 (d, 1H), 8.83 (d, 1H), 8.74 (d, 1H), 8.21 (m, 1H), 8.12-8.07 (m, 4H), 8.03 (m, 1H), 7.97-7.88 (m, 5H), 7.82-7.77 (m, 2H), 7.73-7.69 (m, 1H), 7.68-7.65 (m, 1H), 7.64-7.58 (m, 2H), 7.54-7.51 (m, 1H), 7.48 (m, 1H), 7.45-7.41 (m, 2H), 7.38 (m, 2H), 7.34 (d, 1H), 7.31 (m, 1H), 7.21-7.17 (br m, 2H), 6.72 (v br m, 2H), 6.61 (v br m, 4H), 6.30 (v br, 2H), 5.97 (v br, 2H), 5.71 (v br, 1H), 2.33 (s, 3H), 1.51 (s, 3H), 1.31 ppm (s, 3H).

5.6. References:

(1) Liu, Y.; Persson, P.; Sundström, V.; Wärnmark, K. Fe N-Heterocyclic Carbene Complexes as Promising Photosensitizers. *Acc. Chem. Res.* **2016**, *49*, 1477–1485.

(2) Espinet, P.; Soulantica, K. Phosphine-Pyridyl and Related Ligands in Synthesis and Catalysis. *Coord. Chem. Rev.* **1999**, *193–195*, 499–556.

(3) Carroll, M. P.; Guiry, P. J. P,N Ligands in Asymmetric Catalysis. *Chem. Soc. Rev.* **2014**, *43*, 819–833.

(4) Suzuki, T.; Kuchiyama, T.; Kishi, S.; Kaizaki, S.; Takagi, H. D.; Kato, M. Ruthenium(II) Complexes Containing 8-(Dimethylphosphino)Quinoline (Me2Pqn): Preparation, Crystal Structures, and Electrochemical and Spectroscopic Properties of [Ru(Bpy or Phen)3-n(Me_2Pqn)n]($PF6)_2$ (Bpy = 2,2‘-Bipyridine; Phen = 1,10-Phenanthroline; n = 1, 2, or 3). *Inorg. Chem.* **2003**, *42*, 785–795.

(5) Holzhacker, C.; Standfest-Hauser, C. M.; Puchberger, M.; Mereiter, K.; Veiros, L. F.; Calhorda, M. J.; Carvalho, M. D.; Ferreira, L. P.; Godinho, M.; Hartl, F.; et al. Reversible Addition of CO to Coordinatively Unsaturated High-Spin Iron(II) Complexes. *Organometallics* **2011**, *30*, 6587–6601.

(6) Li, Z.; Sun, W. Synthesis, Photophysics, and Reverse Saturable Absorption of Platinum Complexes Bearing Extended π-Conjugated C^N^N Ligands. *Dalton Trans.* **2013**, *42*, 14021–14029.

(7) Mondal, R.; Lozada, I. B.; Davis, R. L.; Williams, J. A. G.; Herbert, D. E. Site-Selective Benzannulation of N-Heterocycles in Bidentate Ligands Leads to Blue-Shifted Emission from [(P^N)Cu]$_2$(μ-X)$_2$ Dimers. *Inorg. Chem.* **2018**, *57*, 4966–4978.

(8) Österman, T.; Abrahamsson, M.; Becker, H.-C.; Hammarström, L.; Persson, P. Influence of Triplet State Multidimensionality on Excited State Lifetimes of Bis-Tridentate Ru^{II} Complexes: A Computational Study. *J. Phys. Chem. A* **2012**, *116*, 1041–1050.

(9) Mandapati, P.; Giesbrecht, P. K.; Davis, R. L.; Herbert, D. E. Phenanthridine-Containing Pincer-like Amido Complexes of Nickel, Palladium, and Platinum. *Inorg. Chem.* **2017**, *56*, 3674–3685.

(10) Mondal, R.; Giesbrecht, P. K.; Herbert, D. E. Nickel(II), Copper(I) and Zinc(II) Complexes Supported by a (4-Diphenylphosphino)Phenanthridine Ligand. *Polyhedron* **2016**, *108*, 156–162.

(11) Chi, Y.; Chou, P.-T. Contemporary Progresses on Neutral, Highly Emissive Os(Ii) and Ru(II) Complexes. *Chem. Soc. Rev.* **2007**, *36*, 1421–1431

(12) Heinemann, F.; Karges, J.; Gasser, G. Critical Overview of the Use of Ru(II) Polypyridyl Complexes as Photosensitizers in One-Photon and Two-Photon Photodynamic Therapy. *Acc. Chem. Res.* **2017**, *50*, 2727–2736.

(13) Teegardin, K.; Day, J. I.; Chan, J.; Weaver, J. Advances in Photocatalysis: A Microreview of Visible Light Mediated Ruthenium and Iridium Catalyzed Organic Transformations. *Org. Process Res. Dev.* **2016**, *20*, 1156–1163.

(14) Maksic, Z. B.; Baric, D.; Mueller, Thomas. Clar's Sextet Rule Is a Consequence of the σ-Electron Framework. *J. Phys. Chem. A* **2006**, *110*, 10135–10147.

(15) Farrugia, L. J. ORTEP-3 for Windows - a Version of ORTEP-III with a Graphical User Interface (GUI). *J. Appl. Crystallogr.* **1997**, *30*, 565.

(16) Sicilia, V.; Fuertes, S.; Martin, A.; Palacios, Adrian. N-Assisted CPh-H Activation in 3,8-Dinitro-6-Phenylphenanthridine. New C,N-Cyclometalated Compounds of Platinum(II): Synthesis, Structure, and Luminescence Studies. *Organometallics* **2013**, *32*, 4092–4102.

(17) Li, Z.; Cui, P.; Wang, C.; Kilina, S.; Sun, Wenfang. Nonlinear Absorbing Cationic Bipyridyl Iridium(III) Complexes Bearing Cyclometalating Ligands with Different Degrees of π-Conjugation: Synthesis, Photophysics, and Reverse Saturable Absorption. *J. Phys. Chem. C* **2014**, *118*, 28764–28775.

(18) Jiang, B.; Gu, Y.; Qin, J.; Ning, X.; Gong, S.; Xie, G.; Yang, Chuluo. Deep-Red Iridium(III) Complexes Cyclometalated by Phenanthridine Derivatives for Highly Efficient Solution-Processed Organic Light-Emitting Diodes. *J. Mater. Chem. C* **2016**, *4*, 3492–3498.

(19) Wilson, D. J. D.; Couchman, S. A.; Dutton, J. L. Are N-Heterocyclic Carbenes "Better" Ligands than Phosphines in Main Group Chemistry? A Theoretical Case Study of Ligand-Stabilized E2 Molecules, L-E-E-L (L = NHC, Phosphine; E = C, Si, Ge, Sn, Pb, N, P, As, Sb, Bi). *Inorg. Chem.* **2012**, *51*, 7657–7668.

(20) Holzhacker, C.; Calhorda, M. J.; Gil, A.; Carvalho, M. D.; Ferreira, L. P.; Mereiter, K.; Stöger, B.; Pittenauer, E.; Allmaier, G.; Kirchner, K. Four- and Five-Coordinate High-Spin Iron(II) Complexes Bearing Bidentate Soft/Hard SN Ligands Based on 2-Aminopyridine. *Polyhedron* **2014**, *81*, 45–55.

(21) Evans, D. F. 400. The Determination of the Paramagnetic Susceptibility of Substances in Solution by Nuclear Magnetic Resonance. *J. Chem. Soc.* **1959**, 2003–2005.

(22) Lee, C.-I.; Zhou, J.; Ozerov, O. V. Catalytic Dehydrogenative Borylation of Terminal Alkynes by a SiNNN Pincer Complex of Iridium. *J. Am. Chem. Soc.* **2013**, *135*, 3560-3566.

Chapter 6:

6.1. Abstract:

In this chapter, I report half-sandwich Fe(II) pentamethylcyclopentadienide (Cp*; η^5-C_5Me_5) complexes of the bidentate, phenanthridine-based *P^N* ligand **L2**, introduced in Chapter 2. This neutral bidentate *P^N* donor ligand is functionalized with phenanthridine, which on its own, can be thought of as a biomimetic $NAD(P)^+$/NAD(P)H model. $NAD(P)^+$/NAD(P)H biological hydride shuttle via aromatization-dearomatizatin technique. Phenanthridine is a commercially available biomimic hydride shuttle. The potential application would be designing phenanthridine installed ligand which in presence of a suitable sacrificial hydride donor (H^++$2e^-$) reagent such as formic acid, could shuttle hydride cooperatively with the metal centre to organic substrates. The hydride transports to the phenanthridine ligand by dearomatizing the middle pyridine ring which opens up a coordination side to substrate come in, followed by hydride transfer from ligand to substrate by aromatization of the phenanthridine ligand. "Piano-stool" complexes Cp*Fe(**L2**)(CH_3CN)PF_6 and Cp*Fe(**L2**)Br have been synthesized and characterized by solution state NMR spectroscopy and solid state X-ray crystallography. Complex Cp*Fe(**L2**)(CH_3CN)PF_6 used for catalysis because of its better stability over Cp*Fe(**L2**)Br.

6.2. Introduction:

The biological hydride carrier $NAD(P)^+$/NAD(P)H, which engages in dearomatization and aromatization of nicotinamide moieties to shuttle H^- units, has inspired scientists to design bio-mimic ligand systems which can similarly cooperatively work with metal ions as a hydride shuttle. "Cooperative ligands" which are in a complex can participate deliberately with the metal ion in chemical process such as bond activation or facilitates chemical reactions in a synergistic

fashion.[1] Recently, a number of transition metal catalysts have been applied in biomimetic reduction of organic substrates in presence of such types of cooperative ligand.[2] Commercially available bio-mimic NAD(P)+/NAD(P)H models are pyridine, acridine, quinoline, hantzsch ester and phenanthridine. Milstein's group, for example, published[3,4] *bis*(di-*iso*-propyl)phosphine derivatives of an acridine-based PNP pincer, where the acridine ring cooperates with the metal centre via aromatization-dearomatization of the ligand in the reversible activation of small molecules. For example, a Ru complex of the acridine based PNP pincer was shown to reversibly activate H_2 via 1,4-hydride shifts to the central pyridine ring of the acridine unit (**Scheme 6.1)**.

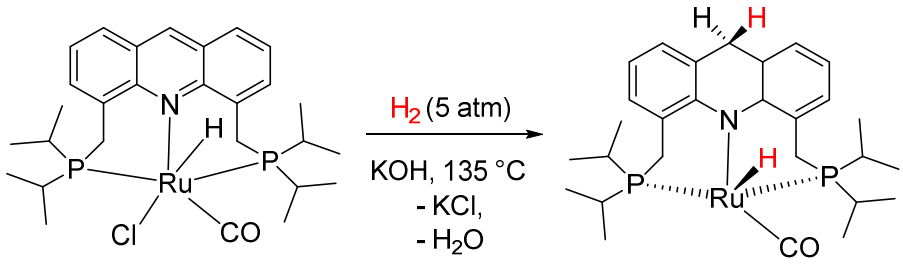

Scheme 6. 1: Hydrogen activation using Ru based *P^N^P* pincer ligand; example of metal-ligand cooperativity.

In other related work, the Colbran group installed[5] a Hantzsch ester in a bidentate neutral NN donor Rh catalyst and used these complexes in the catalytic transfer hydrogenation of imines. The Hantzsch ester substitution (2,6-dimethyl-1,4-dihydropyridine-3,5-dicarboxylate) employed as reversible organic hydride donor and acceptor via aromatization-dearomatization of the ring (**Scheme 6. 2)**.

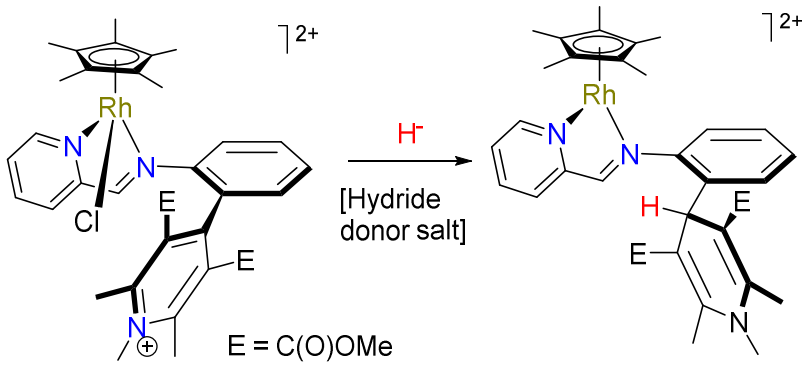

Scheme 6. 3: Metal-ligand cooperativity using Hantzsch ester as hydrogen acceptor.

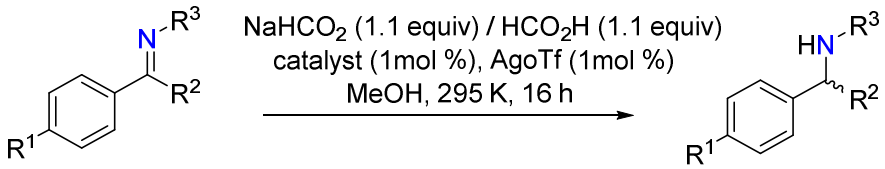

Scheme 6. 4: Hydrogenation of imine to amine using Hantzsch ester based Rh catalyst.

Zhou and co-workers showed[6] that in presence of Ru(II) catalyst, H_2 could be activated via 1,2-hydride transfer to the C=N bond of the phenanthridine ring resulting dihydrophenanthdine. The activated hydrogen equivalent of dihydrophenanthridine could be transfer to an aromatic substrate via reproducing phenanthridine enabling the development of a catalytic asymmetric hydrogenation system.

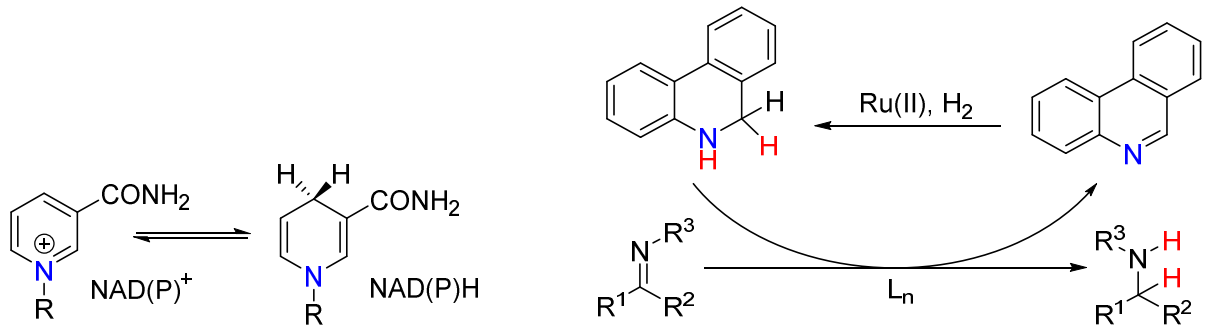

Scheme 6. 5: Hydrogenation of imine to amine using phenanthridine

Beller and coworkers[7] subsequently used the more abundant metal Fe in combination with phenanthridine for asymmetric biomimetic reduction of a series of ∝-keto-/∝-iminoesters via in situ generation of the same biomimic NAD(P)H model. Beller showed Fe(0) induced activation of molecular H_2 and in situ generation of the NADP(H) model by reduction of phenanthridine. In presence of Fe(II), H_2 is transferred to organic substrates from dihydrophenanthridine with corresponding regeneration of phenanthridine.

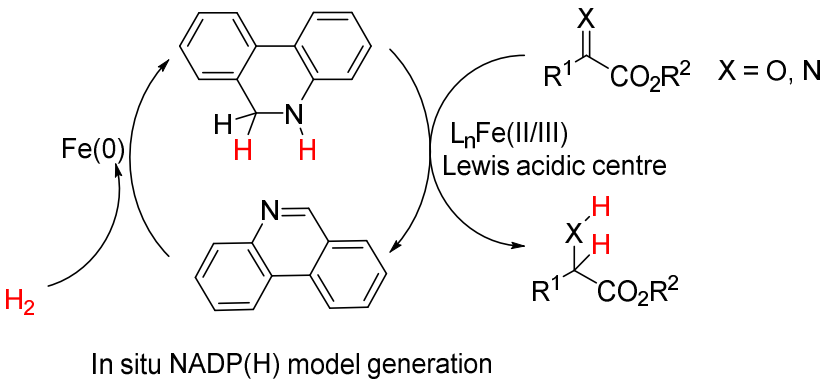

Scheme 6. 6: Fe catalyzed hydrogenation of keto-ester using phenanthridine.

As discussed in the previous chapters, our *P^N* ligand is based on phenanthridine moiety. As demonstrated in the above-mentioned work, phenanthridine is considered a potential candidate for reversible hydride donor-acceptor over pyridine and quinoline.[8,9] I considered that including phenanthridine in a bifunctional *P^N* donor could possibly enable cooperative manner reactivity with metal ions in the hydrogenation of organic substrates. Applying the notion of metal-ligand cooperation, a potential of hydride transfer from metal to phenanthridinyl carbon atom of "C=N" bond, resulting dearomatization, followed by hydride shift to the organic substrate through rearomatization of phenanthridine ring.

In this chapter, the design and synthesis of bidentate *P^N* ligand based Fe complexes and their application in Fe catalyzed hydrogenation of imines to amines is discussed. *P^N* ligand based pentamethylcyclopentadiene(Cp*) supported Fe(II) half-sandwich complexes were designed as potential catalyst precursors. Detailed complex synthesis will be discussed. Several simple imines were synthesized for catalysis while sodium formate-formic acid mixture was used as hydrogen source. Formic acid has proven to be good candidate as hydrogen donor in catalytic hydrogenation reaction as CO_2 is stable by product. However, satisfactory result from our catalysis was not obtained due to ligand disengagement from the metal centre under catalytic conditions.

6.3. Results and Discussion:

6.3.1. Synthesis:

The synthesis of (**L2**)$FeBr_2$ was discussed in Chapter 5. Here, (**L2**)$FeBr_2$ was reacted with Cp*Li (pentamethylcyclopentadienide lithium) to synthesize Cp*(**L2**)FeBr (**Scheme 6.6**). The reaction with Cp*Li and (**L2**)$FeBr_2$ in THF at room temperature which turns into a deep blue solution. Stirring was continued for 2 h and the solution was pumped dry and washed with diethylether (3×5 mL) and extracted with toluene. After drying, crude solid was obtained as the product (Cp*(**L2**)FeBr).

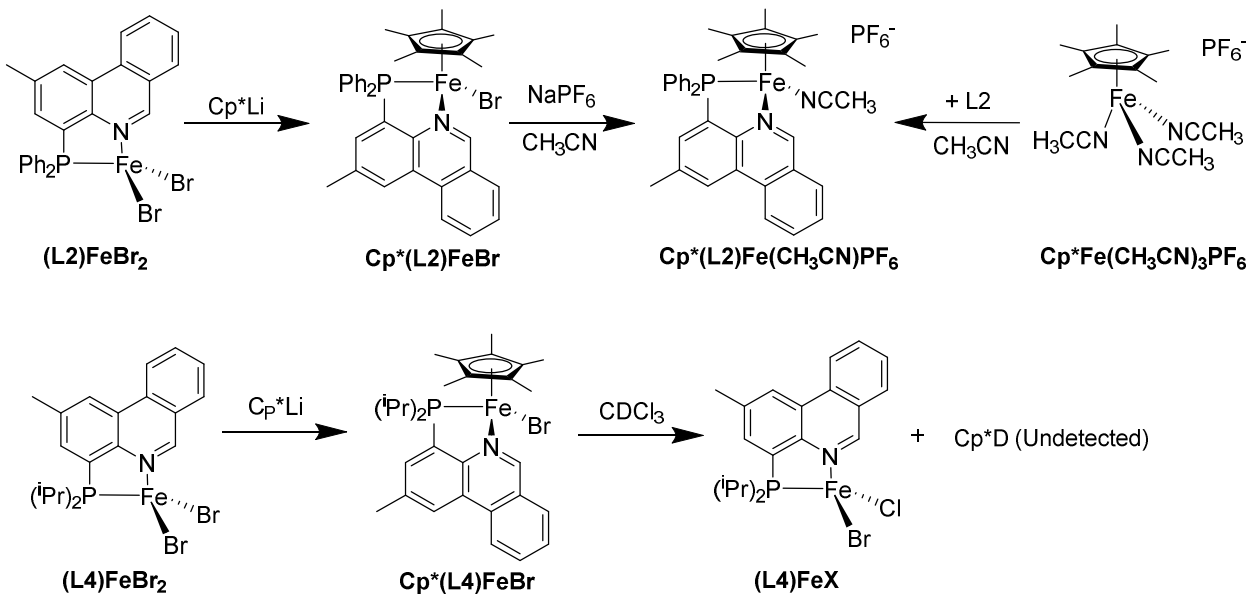

Scheme 6. 7: *P^N* ligand based "Piano-stool" complexes of Fe.

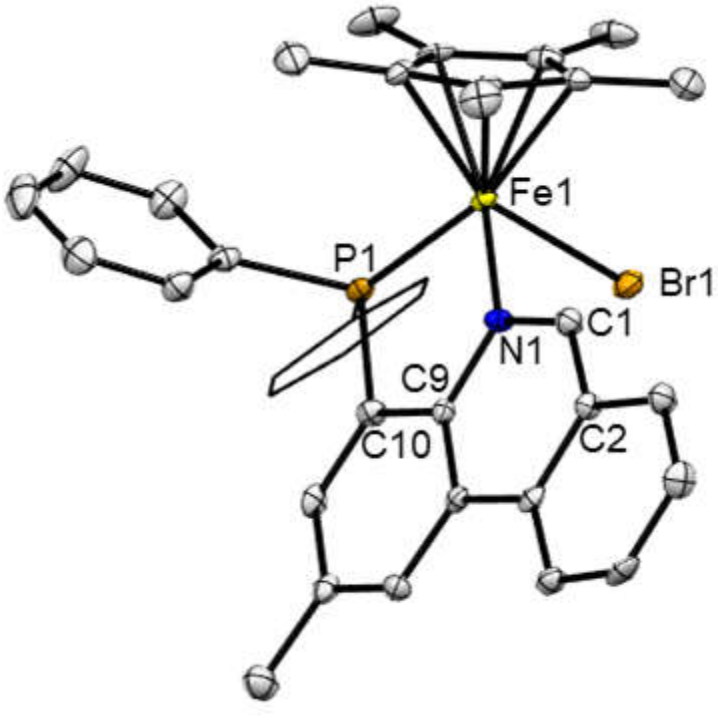

Figure 6. 1: ORTEP[10] of **Cp*(L2)FeBr** with thermal ellipsoids shown at 50% probability levels and hydrogen atoms removed for clarity.

Table 6. 1: Selected bond distances (Å) and angles (°) for **Cp*(L2)FeBr**:

Selected Bonds	**(Å)**	**Selected Angles**	**(°)**
Br(1)-Fe(1)	2.4979(7)	N(1)-Fe(1)-P(1)	84.93(11)
Fe(1)-N(1)	1.995(3)	N(1)-Fe(1)-Br(1)	83.58(10)
Fe(1)-P(1)	2.2012(13)	P(1)-Fe(1)-Br(1)	95.87(4)
C(1)-N(1)	1.323(5)	C(1)-N(1)-Fe(1)	121.5(3)

The crystal structure of Cp*(**L2**)FeBr revealed the weak interaction of Fe centre with *P^N* ligand. If I check the bond length. I can see the Fe(1)-P(1) and Fe(1)-N(1) both increased in Cp*(**L2**)FeBr compared to (**L2**)$FeBr_2$ which may caused by steric crowding at the small Fe centre by binding the pentamethylcyclopentadienide group. This may explain the unstability of this complex as well as ligand detachment during screening reaction

To further study and exchange bromide for a weakly coordinating solvent at the metal centre, Cp*(**L2**)FeBr was reacted with $NaPF_6$ in CH_3CN (3 mL). This caused an instant color change of the solution to dark black. The reaction was continued for 5 h, then dried under vacuum. The crude solid was extracted with acetonitrile and filtered twice through Celite. The product Cp*(**L2**)Fe(CH_3CN)PF_6 was dried and re crystallized with DCM-pentane. The crystals were characterized in solution state NMR spectroscopy and solid state X-ray crystallography. In the ^1H NMR spectrum, the diagnostic singlet of the phenanthridine ring was observed at 10.02 ppm, while the methyl of the Cp* group comes around 1.38 ppm in CD_3CN. In the $^{31}P\{^1H\}$ NMR spectrum, a sharp singlet was observed at 77.89 ppm. The X-ray crystal structure revealed the acetonitrile bound half sandwich Fe(II) complex with hexafluorophosphate (PF_6^-) as a counterion.

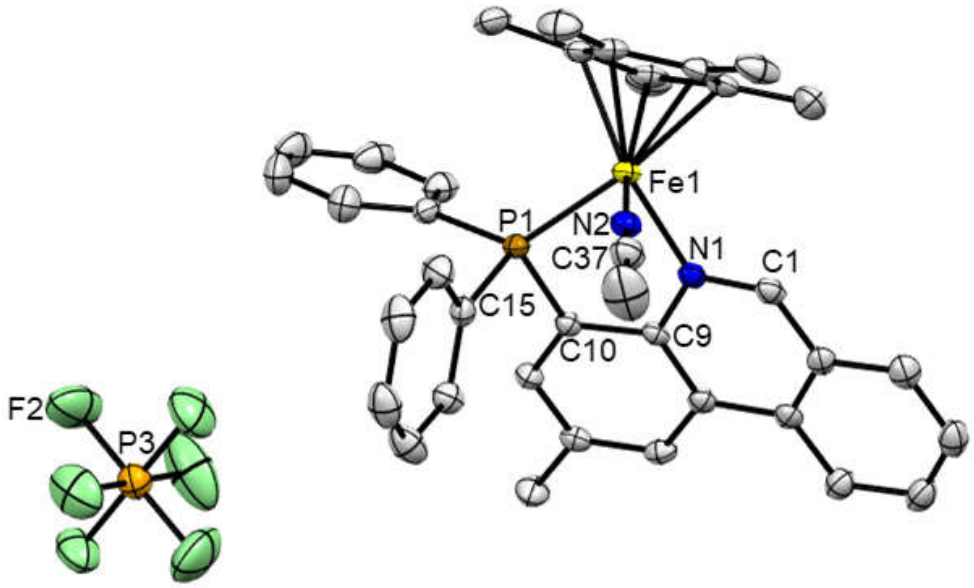

Figure 6. 2: ORTEP[10] of **Cp*(L2)Fe(CH$_3$CN)PF$_6$** with thermal ellipsoids shown at 50% probability levels and hydrogen atoms omitted for clarity.

Table 6. 2: Selected bond distances (Å) and angles (°) for Cp*(**L2**)Fe(CH$_3$CN)PF$_6$:

Selected Bonds	**(Å)**	**Selected Angles**	**(°)**
Fe(1)-N(1)	2.011(3)	N(1)-Fe(1)-P(1)	83.09(9)
Fe(1)-P(1)	2.2000(11)	N(2)-Fe(1)-P(1)	94.39(10)
Fe(1)-N(2)	1.916(3)	N(2)-Fe(1)-N(1)	87.06(13)
C(1)-N(1)	1.318(5)	C(1)-N(1)-Fe(1)	122.0(3)
Fe(1)-N(2)	1.916(3)	C(37)-N(2)-Fe(1)	178.4(4)
C(37)-N(2)	1.127(5)		

Cp*(**L2**)Fe(CH$_3$CN)PF$_6$ can also be prepared via a different route. First, Cp*Fe(CH$_3$CN)$_3$PF$_6$ was synthesized following a published procedure[11], then reacted with ligand **L2** in acetonitrile. The reaction was stirred overnight, the color changed to deep black solution, which was dried under high vacuum and washed with Et$_2$O (3 x 5 mL) and hexanes (2 x 5 mL). The solid crude was dissolved in dichloromethane and filtered through small plug of Celite. The deep black filtrate was crystallized by layering with pentane. A deep black crystal was isolated

after two days as product. The same spectroscopic evidence was observed for Cp*(**L2**)Fe(CH_3CN)PF_6 generated using either pathways of synthesis.

To improve the stability of Cp*(**L2**)FeBr, I decided to use ligand **L4** for the synthesis of complex Cp*(**L4**)FeBr. This was synthesized using (**L4**)$FeBr_2$ following the same synthetic procedure as for Cp*(**L2**)FeBr. A deep blue solution was formed after addition of Cp*Li to a THF solution of (**L4**)$FeBr_2$. The solution was dried in high vacuum and washed with pentane, followed by extraction with toluene. The toluene fraction was crystallized by layering with pentane and powder was isolated. The NMR of the powder was taken in C_6D_6. In the ^{1}H NMR spectra, the diagnostic singlet peak of imine bond of phenanthridine shows around 10.64 ppm. This compound Cp*(**L4**)FeBr was found to be not stable all solvents. For example, addition of $CDCl_3$ to Cp*(**L4**)FeBr formed a yellow mixture of (**L4**)Fe(X) X = Cl or Br. The presence of the halide mixture was determined via X-ray crystallography and NMR spectroscopy. Yellow crystals were formed while crystallized with DCM-Et_2O. ^{1}H NMR of $CDCl_3$ solution shows a paramagnetic environment. For the comparison purpose, I have synthesized (**L4**)$FeCl_2$ using proligand **L4**. A comparable paramagnetic ^{1}H NMR of (**L4**)Fe(X) was observed with respect to independently prepared samples of (**L4**)$FeBr_2$ and (**L4**)$FeCl_2$. All of those NMR spectra look very close and similar pattern of NMR chemical shifts. Reaction between **L4** and $FeCl_2$ in THF for 24 h at room temperature gives an orange suspension, which was pumped dry and wash with Et_2O. The residue was dissolved in DCM and filtered for crystallization with Et_2O. The solid state crystal structure and ^{1}H NMR supports the data of (**L4**)$FeCl_2$.

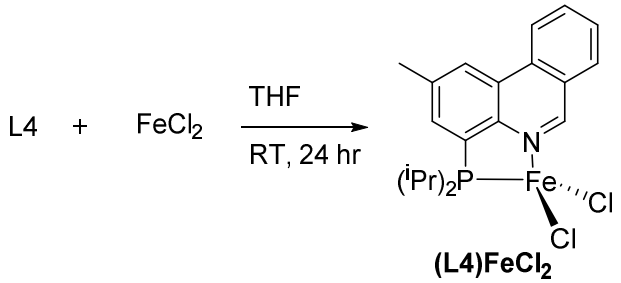

Scheme 6. 8: PN ligand based $FeCl_2$ complexes

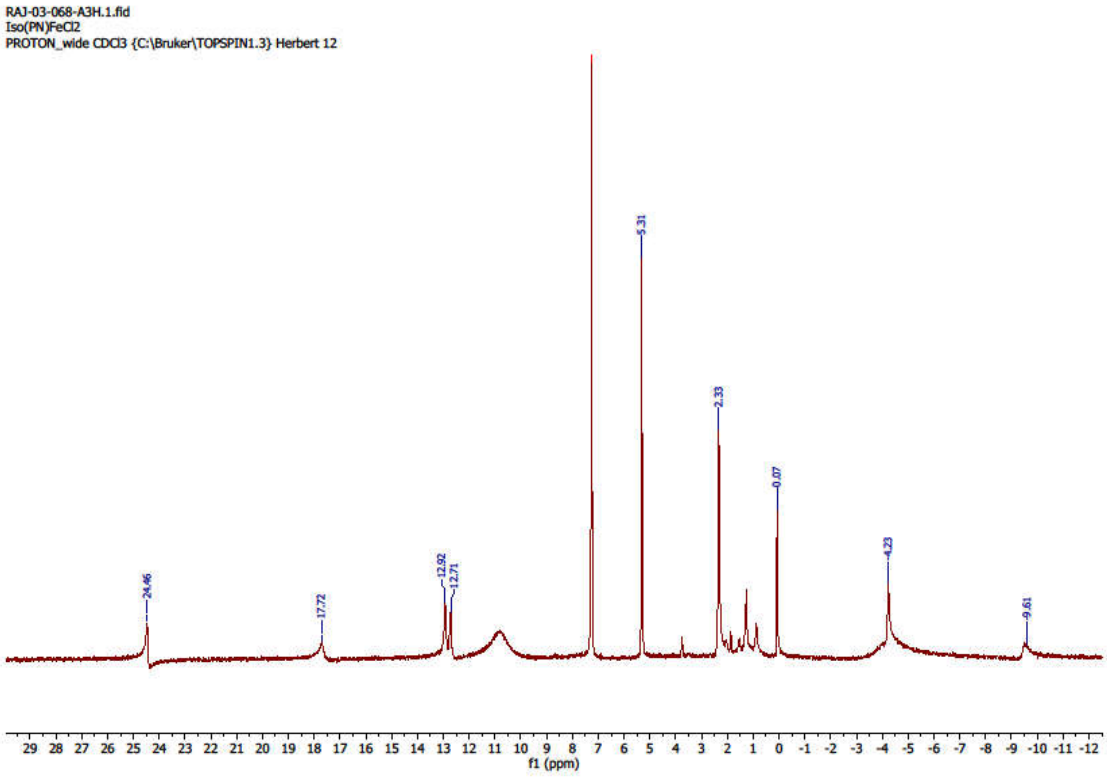

Figure 6. 3: ^1H NMR spectroscopy of (L4)$FeCl_2$ in $CDCl_3$ at room temperature.

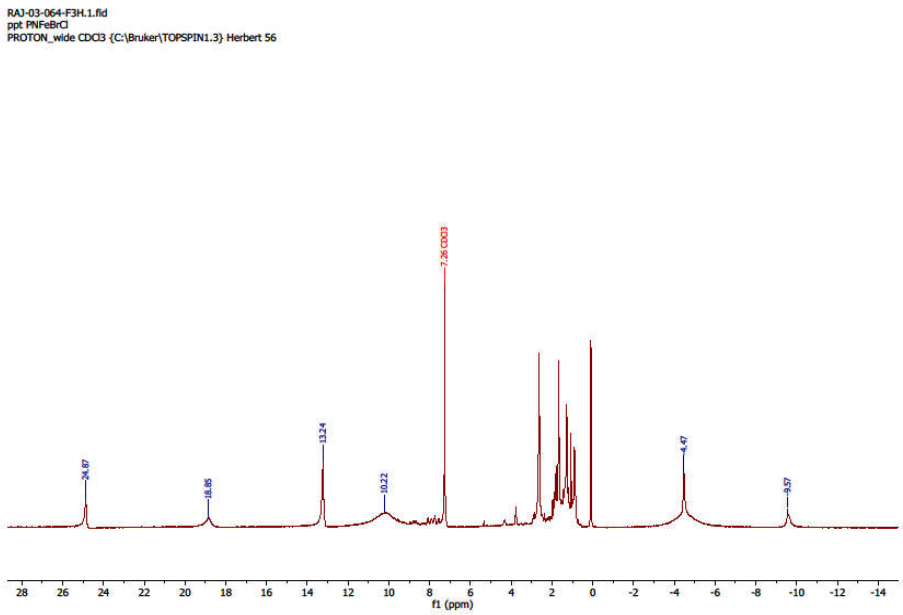

Figure 6. 4: ^{1}H NMR spectroscopy of (L4)FeX in $CDCl_3$ at room temperature.

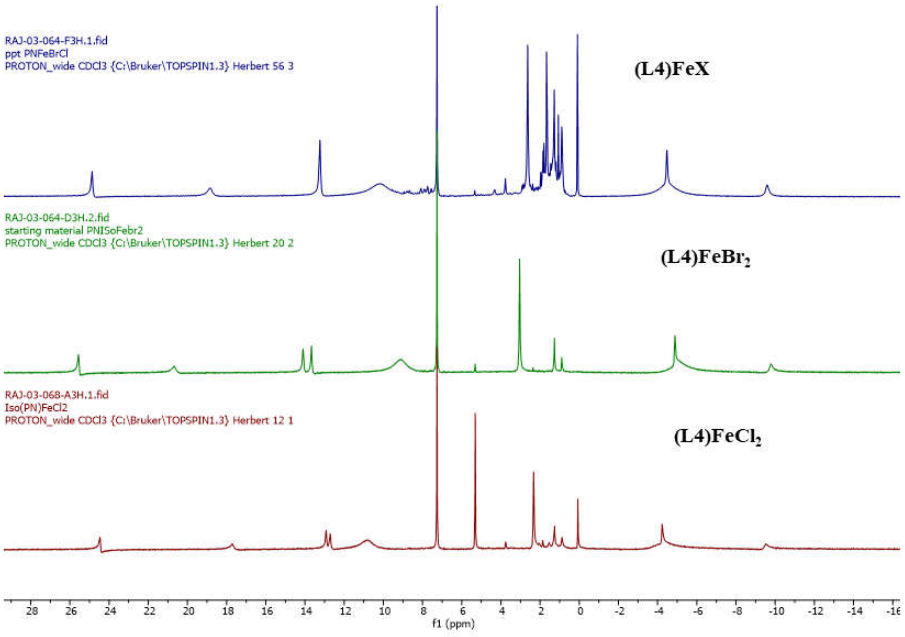

Figure 6. 5: Comparison of ^{1}H NMR spectroscopy of (**L4**)$FeCl_2$, (**L4**)Fe(X) and (**L4**)$FeBr_2$ in $CDCl_3$ at room temperature.

6.3.2. Solid-state structure of (L4)Fe(X) and (L4)$FeCl_2$:

Comparing the crystal structure of (**L4**)Fe(X) with those of isolated samples of (**L4**)$FeCl_2$ and (**L4**)$FeBr_2$ (Chapter 5), I see that the Fe-halogen bond distance changes based on the size of the halogen group attached. Fe-Cl bond lengths in (**L4**)Fe(X) around 2.226(16) and 2.283(8) Å, similarly in (**L4**)$FeCl_2$ around 2.2572(10) and 2.2675(11) Å. Whereas in (**L4**)$FeBr_2$ the bond lengths are longer around ~ 2.35 Å. Apart from that (**L4**)Fe(X), (**L4**)$FeCl_2$ and (**L4**)$FeBr_2$ are very similar tetrahedral geometry for Fe(II) high spin complex.

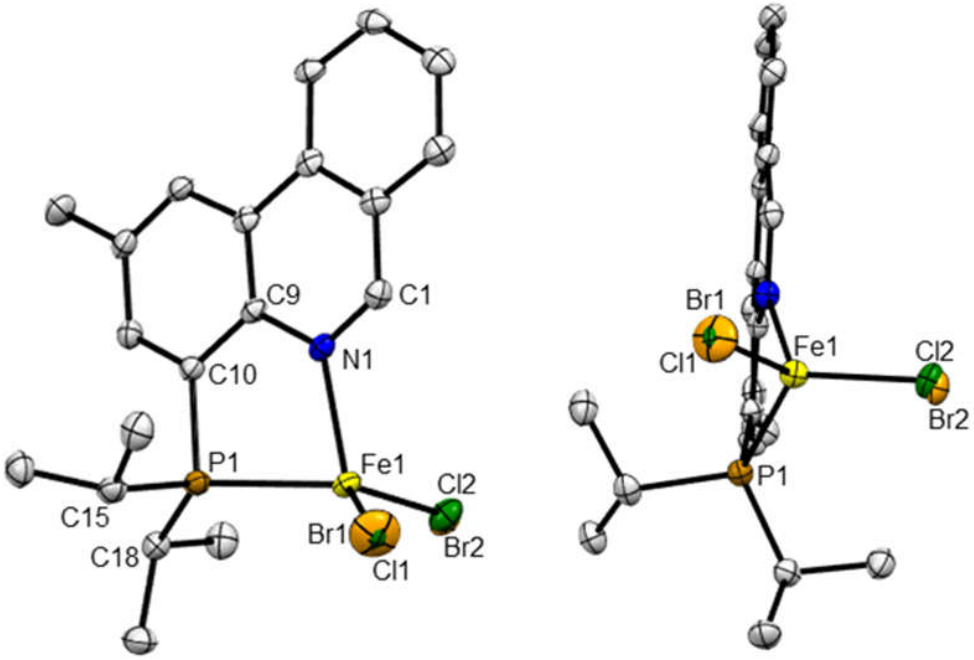

Figure 6. 6: ORTEP[10] of **(L4)Fe(X)** with thermal ellipsoids shown at 50% probability levels.

Table 6. 3: Selected bond distances (Å) and angles (°) for **(L4)Fe(X):**

Selected Bonds	**(Å)**	**Selected Angles**	**(°)**
Fe(1)-N(1)	2.130(2)	N(1)-Fe(1)-Cl(2)	109.8(4)
Fe(1)-Cl(2)	2.226(16)	N(1)-Fe(1)-Cl(1)	109.78(19)
Fe(1)-Cl(1)	2.283(8)	Cl(2)-Fe(1)-Cl(1)	117.2(4)
Fe(1)-Br(1)	2.322(3)	N(1)-Fe(1)-Br(1)	110.54(9)
Fe(1)-Br(2)	2.365(13)	N(1)-Fe(1)-Br(2)	110.5(3)
Fe(1)-P(1)	2.4329(7)	Br(1)-Fe(1)-Br(2)	119.0(3)
N(1)-C(1)	1.311(3)	N(1)-Fe(1)-P(1)	79.88(6)

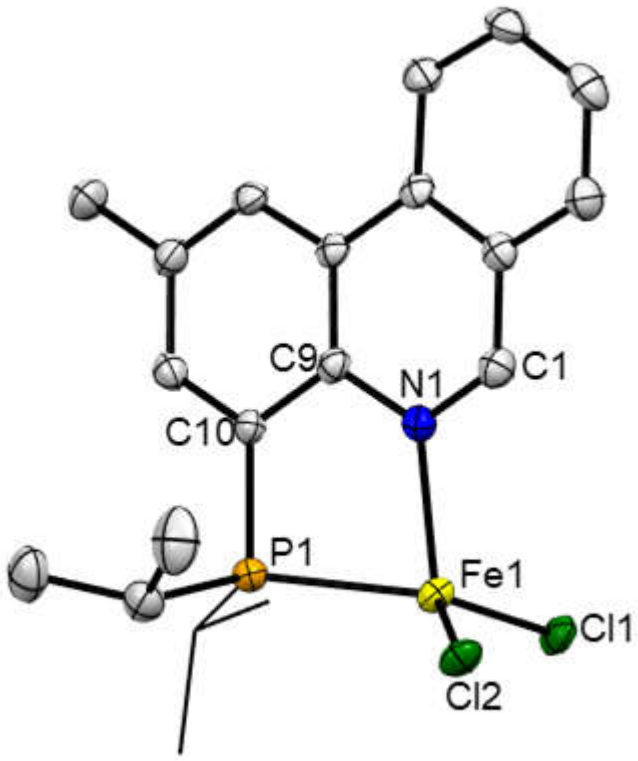

Figure 6. 7: ORTEP[10] of **(L4)FeCl₂** with thermal ellipsoids shown at 50 % probability levels.

Table 6. 4: Selected bond distances (Å) and angles (°) for **(L4)FeCl₂**:

Selected Bonds	**(Å)**	**Selected Angles**	**(°)**
Cl(1)-Fe(1)	2.2572(10)	N(1)-Fe(1)-Cl(1)	110.23(9)
Cl(2)-Fe(1)	2.2675(11)	N(1)-Fe(1)-Cl(2)	105.22(9)

Fe(1)-N(1)	2.118(3)	Cl(1)-Fe(1)-Cl(2)	120.07(4)
Fe(1)-P(1)	2.4263(11)	N(1)-Fe(1)-P(1)	80.92(8)
C(1)-N(1)	1.310(5)	Cl(1)-Fe(1)-P(1)	113.89(4)
C(10)-P(1)	1.825(4)	Cl(2)-Fe(1)-P(1)	118.26(4)

6.4. Screening Reactions for the Catalysis and Stability Check:

A series of reactions were attempted in order to check the stability of the complexes as catalyst, catalytic activity upon reaction with sacrificial hydride donor such formic acid or formate salt and the possibility of having β-hydride elimination from sodium isopropoxide to obtain acetone.[12]

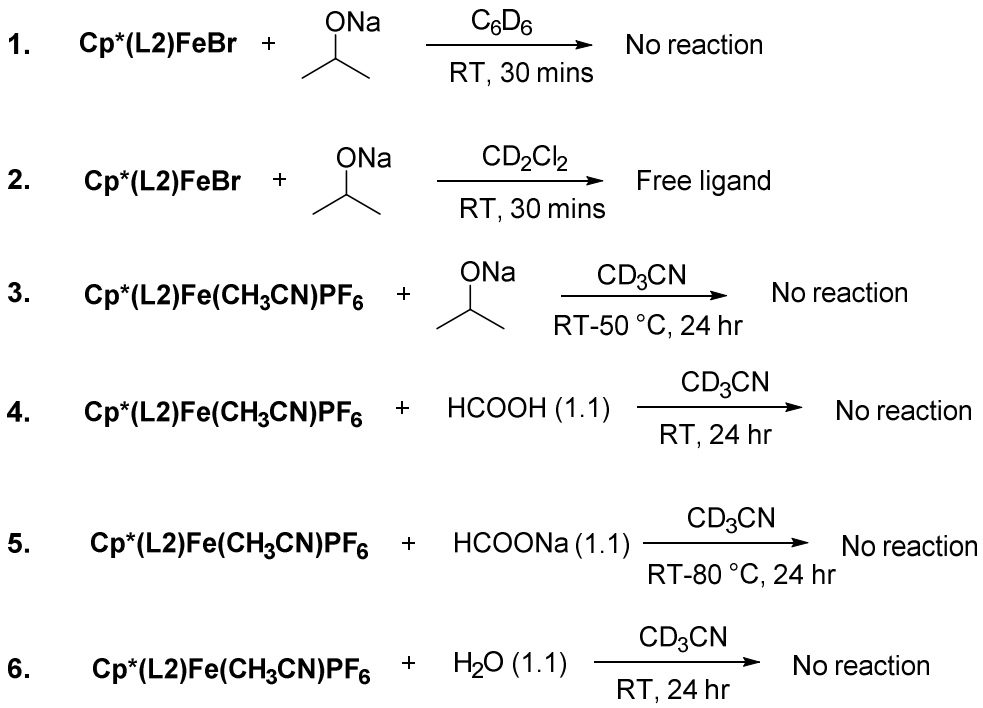

Scheme 6. 9: Screening reactions.

Complex Cp*(**L2**)FeBr found to be unstable in air. Ligand displacement was also observed during reaction with sodium isopropoxide in dichloromethane (reaction 3). No reaction was obtained when Cp*(**L2**)FeBr reaction with sodium isopropoxide in C_6D_6 (reaction 2). However, reaction of Cp*(**L2**)Fe(CH_3CN)PF_6 with sodium isopropoxide (reaction 1), formic

acid (reaction 4), sodium formate (reaction 5) and H_2O (reaction 6) was found no reaction. Although there is no change in NMR data of Cp*(**L2**)Fe(CH_3CN)PF_6 complex after the reaction. From above screening, it could be concluded that Cp*(**L2**)Fe(CH_3CN)PF_6 is more suitable and stable as catalyst over Cp*(**L2**)FeBr complex.

6.5. Synthesis of Simple Imines as Substrate and Catalysis Trial:

Simple imine substrates were been synthesized by condensation reactions between an aldehyde and amine in ethyl alcohol under reflux. NMR data for each imine was compared with previously reported data, and isolated yield are reported below.

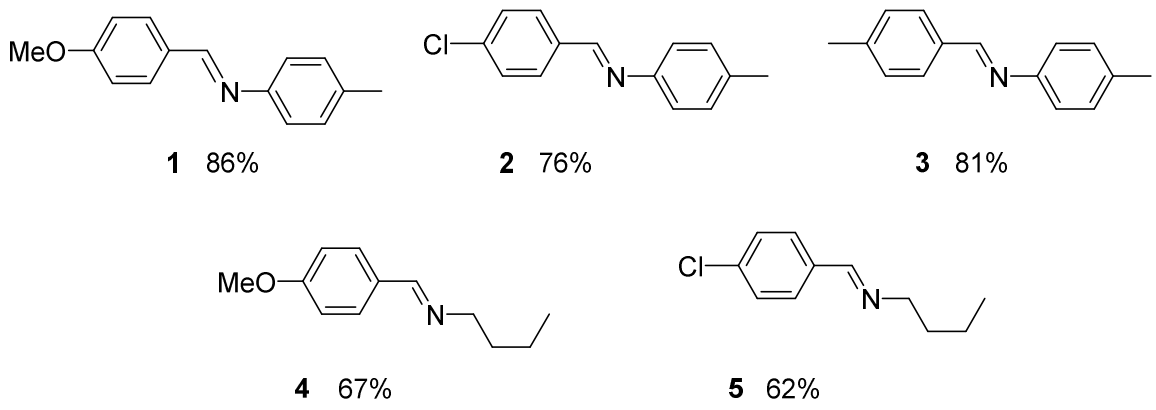

Figure 6. 8: Synthesized imine by condensation reaction

For catalysis, a mixture of sodium formate and formic acid (1:1) was studied. As found in catalysis screening the Cp*(**L2**)Fe(CH_3CN)PF_6 complex to be most stable in both CH_3CN, H_2O and acidic condition. Complex Cp*(**L2**)Fe(CH_3CN)PF_6 used for hydrogenation of **1, 2** and **3** imine at room temperature for 16 h.

6.5.1. Catalysis Examples:

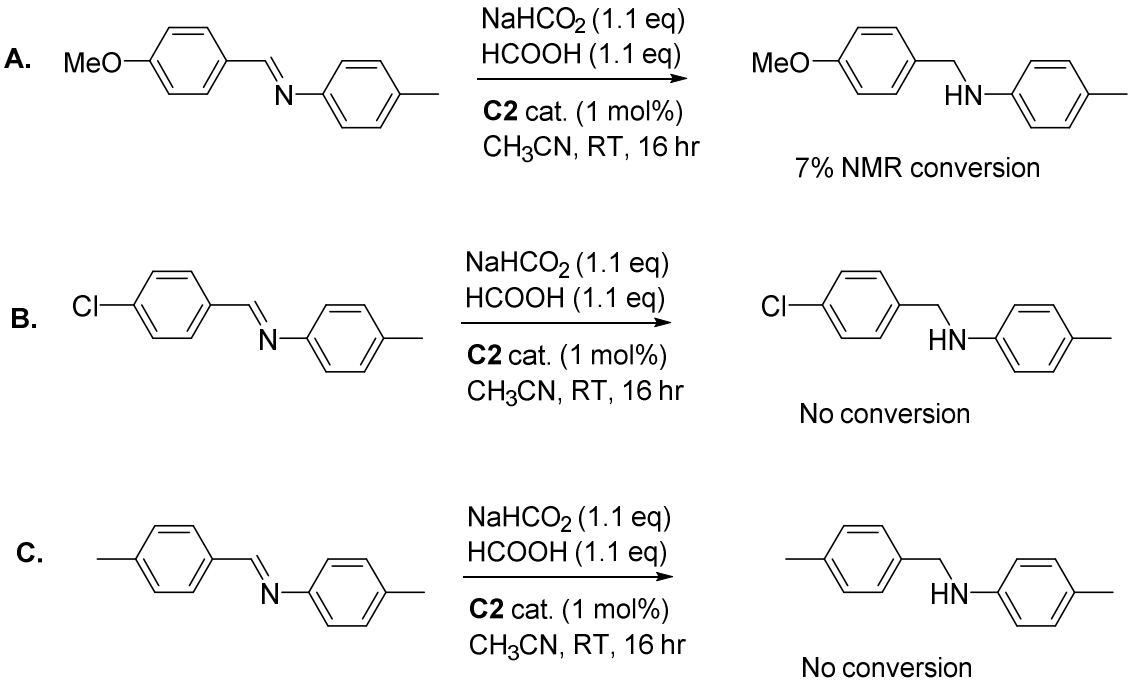

Scheme 6. 10: Catalysis trial by using catalyst Cp*(**L2**)Fe(CH_3CN)PF_6

6.5.2. ^{1}H NMR Spectroscopy of Reaction A Product:

Only 7% NMR conversion was observed for reaction **A** for imine **1**. But no conversion was obtained for reaction **B** and **C** for imine **2** and **3**.

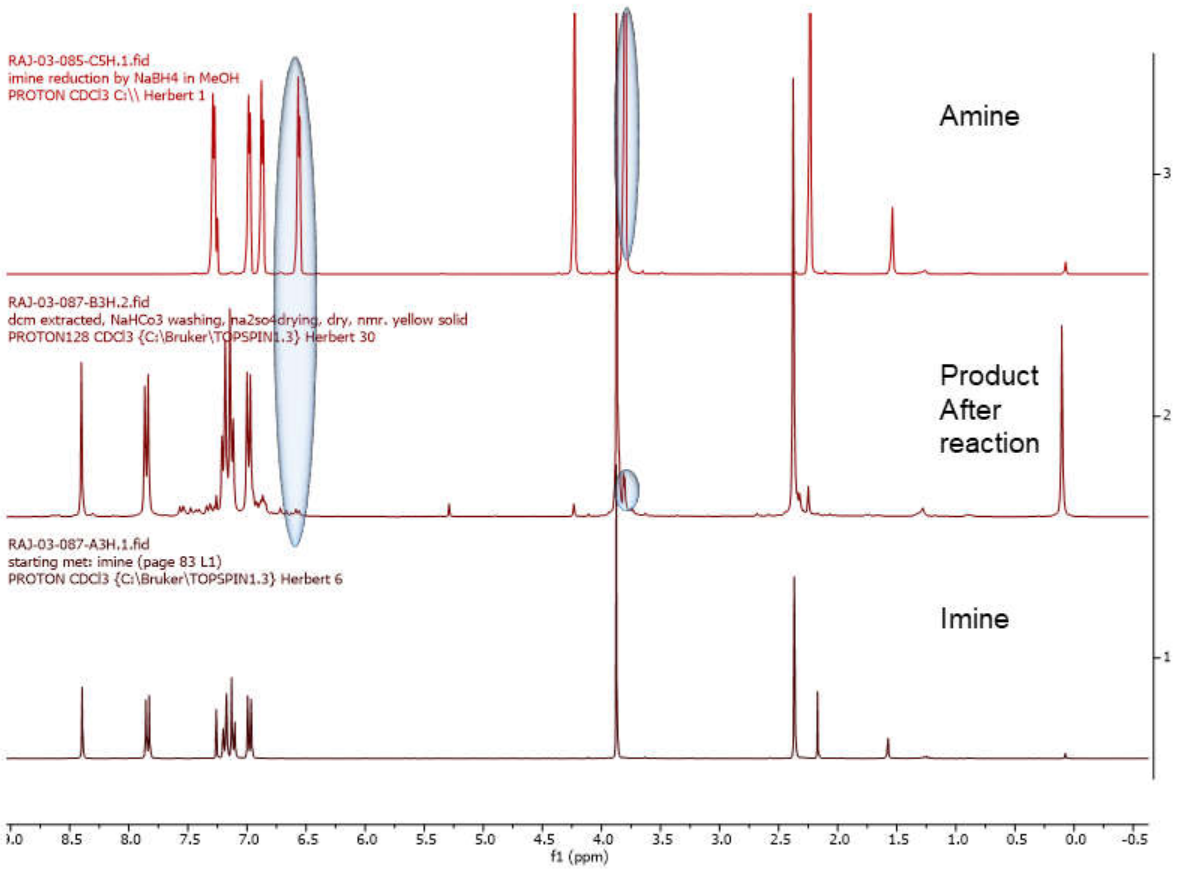

Figure 6. 9: Synthesized product of reaction **A** compared to pure product and starting material ^{1}H NMR spectroscopy.

6.6. Conclusion:

In conclusion, I have synthesized some novel pentamethylcyclopentadiene supported "piano-stool" Fe(II) complexes based on bidentate PN ligand. These are the first phenanthridine-substituted ligand-based "piano-stool" Fe(II) complexes. The complex Cp*(**L2**)Fe(CH_3CN)PF_6 was found very stable in air and water, but acetonitrile was found to be very strongly bound to the Fe centre, hampering efficient catalysis. In contrast, complex Cp*Fe(**L2**)Br was reactive but too unstable. The bromide ion is a weak field ligand, which could be replaced easily by

coordinating solvents such as acetonitrile. A suitable ligand design could provide both stability and reactivity. Overall, these Fe(II) complexes are not efficient for the hydrogenation of imines. However, subsequently ligand deign could potentially bring better result in future.

6.7. Experimental Section:

Unless otherwise stated, all air sensitive manipulations were carried out in N_2-filled glove box or on a Schlenk line (Ar). 2,6-dibromoaniline (AK Scientific), *N*-iodosuccinimide (AK Scientific), p-Toluidine (Alfa Aesar), *N*-bromosuccinimide (Alpha Aesar), 2-formylphenyl boronic acid (Combi Blocks), $Pd(PPh_3)_4$ (Alfa Aesar), Na_2CO_3 (Alfa Aesar), chlorodiphenylphosphine (VWR), $FeBr_2$ and pentamethylcyclopentadienyl (Aldrich) were purchased and were used as received. 2-bromo-4-methylaniline[13], 6-bromo-2-iodo-4-methylaniline[13], 8-bromo-6-methylquinoline[14], 4-diphenylphosphinophenanthridine[15] (**L1**) and 4-isopropylphosphinophenanthridine (**L4**) were synthesized following published procedures and previous chapters. Organic solvents were dried over appropriate reagents and deoxygenated prior to use. 1,2-dimethoxyethane and water were degassed before using in Suzuki coupling reaction. All NMR spectra were recorded on a Bruker Avance 300 MHz or Bruker Avance-III 500 MHz spectrometer.

Synthesis of Cp*(L2)FeBr: (L2)$FeBr_2$ (1 mmol) was taken in 20 mL vial in THF and a suspension of Cp*Li (1 mmol) in THF was dropwise added to the solution and stirred for 2 h at room temperature to turn color of the solution blue. The solution was dried and washed with diethyl ether and extracted with toluene. The solution was set up vapor diffusion with pentane. The crystals were collected and washed with ether and pumped dried.

Synthesis of Cp*(L2)Fe(CH_3CN)PF_6: Method 1**:** In a 5 mL solution of Cp*(L2)FeBr (1 mmol) in toluene, a solution of $NaPF_6$ in CH_3CN was added. The solution color turned dark black which was dried and extracted with acetonitrile and filtered through celite two times. The solution was pumped dried and crystallized with DCM-pentane vapour diffusion.

Method 2: Cp*(L2)Fe(CH_3CN)$_3PF_6$ has been synthesized by published procedure. In 5 mL acetonitrile Cp*(L2)Fe(CH_3CN)$_3PF_6$ and proligand L2 was mixed and stirred in room temperature for overnight. A dark black solution was formed which was pumped dried under vacuum and washed with diethyl ether (3 x 5 mL) and hexanes (2 x 5 mL). The solid crude was dissolved in dichloromethane and filtered through small plug of Celite. The deep black filtrate was crystallized by layering with pentane. A deep black crystal was isolated after two days as product.

Synthesis of (L4)$FeCl_2$: In a suspension of $FeCl_2$ in THF (2 mL), a solution of L4 in THF (2 mL) was added dropwise. Color of the solution was changed to orange after 24 hrs stirring. The orange solution was pumped dry and wash it with ether. The solid residue was dissolved in DCM and filtered through celite to crystallize with Et_2O. Orange crystals were obtained after few days.

6.8. References:

(1) Trincado, M.; Grützmacher, H. Cooperating Ligands in Catalysis. In *Cooperative Catalysis*; John Wiley & Sons, Ltd, 2015; pp 67–110.

(2) McSkimming, A.; Colbran, S. B. The Coordination Chemistry of Organo-Hydride Donors: New Prospects for Efficient Multi-Electron Reduction. *Chem. Soc. Rev.* **2013**, *42*, 5439–5488.

(3) Gunanathan, C.; Milstein, David. Metal-Ligand Cooperation by Aromatization-Dearomatization: A New Paradigm in Bond Activation and "Green" Catalysis. *Acc. Chem. Res.* **2011**, *44*, 588–602.

(4) Gunanathan, C.; Gnanaprakasam, B.; Iron, M. A.; Shimon, L. J. W.; Milstein, D. "Long-Range" Metal−Ligand Cooperation in H_2 Activation and Ammonia-Promoted Hydride Transfer with a Ruthenium−Acridine Pincer Complex. *J. Am. Chem. Soc.* **2010**, *132*, 14763–14765.

(5) McSkimming, A.; Bhadbhade, M. M.; Colbran, S. B. Bio-Inspired Catalytic Imine Reduction by Rhodium Complexes with Tethered Hantzsch Pyridinium Groups: Evidence for Direct Hydride Transfer from Dihydropyridine to Metal-Activated Substrate. *Angew. Chem. Int. Ed.* **2013**, *52* (12), 3411–3416.

(6) Chen, Q.-A.; Gao, K.; Duan, Y.; Ye, Z.-S.; Shi, L.; Yang, Y.; Zhou, Y.-G. Dihydrophenanthridine: A New and Easily Regenerable NAD(P)H Model for Biomimetic Asymmetric Hydrogenation. *J. Am. Chem. Soc.* **2012**, *134*, 2442–2448.

(7) Lu, L.-Q.; Li, Y.; Junge, K.; Beller, Matthias. Iron-Catalyzed Hydrogenation for the In Situ Regeneration of an NAD(P)H Model: Biomimetic Reduction of α-Keto-/α-Iminoesters. *Angew. Chem., Int. Ed.* **2013**, *52*, 8382–8386.

(8) Giesbrecht, P. K.; Herbert, D. E. Electrochemical Reduction of Carbon Dioxide to Methanol in the Presence of Benzannulated Dihydropyridine Additives. *ACS Energy Lett.* **2017**, *2*, 549–555.

(9) Giesbrecht, P. K.; Nemez, D. B.; Herbert, D. E. Electrochemical Hydrogenation of a Benzannulated Pyridine to a Dihydropyridine in Acidic Solution. *Chem. Commun.* **2018**, *54*, 338–341.

(10) Farrugia, L. J. ORTEP-3 for Windows - a Version of ORTEP-III with a Graphical User Interface (GUI). *J. Appl. Crystallogr.* **1997**, *30*, 565.

(11) Zhang, F.; Jia, J.; Dong, S.; Wang, W.; Tung, C.-H. Hydride Transfer from Iron(II) Hydride Compounds to NAD(P)+ Analogues. *Organometallics* **2016**, *35*, 1151–1159.

(12) Herbert, D. E.; Ozerov, O. V. Binuclear Palladium Complexes Supported by Bridged Pincer Ligands. *Organometallics* **2011**, *30*, 6641–6654.

(13) Mandapati, P.; Giesbrecht, P. K.; Davis, R. L.; Herbert, D. E. Phenanthridine-Containing Pincer-like Amido Complexes of Nickel, Palladium, and Platinum. *Inorg. Chem.* **2017**, *56*, 3674–3685.

(14) Lee, C.-I.; Zhou, J.; Ozerov, O. V. Catalytic Dehydrogenative Borylation of Terminal Alkynes by a SiNN Pincer Complex of Iridium. *J. Am. Chem. Soc.* **2013**, *135*, 3560–3566.

(15) Mondal, R.; Lozada, I. B.; Davis, R. L.; Williams, J. A. G.; Herbert, D. E. Site-Selective Benzannulation of N-Heterocycles in Bidentate Ligands Leads to Blue-Shifted Emission from $[(P^{\frown}N)Cu]_2(\mu\text{-}X)_2$ Dimers. *Inorg. Chem.* **2018**, *57*, 4966–4978.

7.1. Conclusion and Outlook:

In this thesis, I report novel bidentate neutral ligands using phenanthridine as a core and investigate their coordination chemistry and application of complexes of late transition metals.

1. I have designed a series of phenanthridine based phosphine donor *P^N* type and carbene donor *C^N* type proligands. The derivatives of all *P^N* proligands are all isolated with higher yield above ~ 60% on average. Installing methyl or *tert*-butyl groups on the ligand core increased solubility in nonpolar solvents. I observed efficient complexation of both types of ligands with late transition metal such as Ni, Zn. Metals easily bind bidentate *P^N* ligands and form stable complexes in higher oxidation (+2) states, while for lower oxidation state (such as '0') complexes, more instability was observed. For example, Ni(0) complexes of *P^N* ligands were difficult to isolate pure at ambient temperature.

   Similarly, I synthesized *C^N* type precursors in high yields as bromide/chloride/hexafluorophosphate salts. Free proligands could be generated *in situ* by deporotonation with a base before binding to metal ions. I found *C^N* stabilizes Ag metal at the oxidation state (+1) and Ru in their (+2) oxidation state and Ir(+3) oxidation state. The efficient σ-donor property of carbene ligands formed strong bonds with the metal ions in different oxidation state.
2. Halide-bridged Cu(I) complexes of *P^N* ligands showed photo-emissive property under photoexcitation in the solid state. I also synthesised a *P^N* ligand of quinoline, which is a small congener of phenanthridine. The halide bridge Cu(I) complexes of Quin *P^N* (**L3**) ligand also happens to be photoemissive at the room temperature. However, in the emission spectra, an effective blue shift was observed for phenanthridine compared to the similar quinoline version. This result was counter-intuitive compared to the general trend

of red shifts in absorption and emission spectra typically observed on π-extension. Theoretical calculation disclosed the effect of extra stability at the excited state provided by extended π-system of phenanthridine. The loss energy in the excited state leads to red shift for quinoline complexes.

3. I synthesized *bis*-(*P^N*) based Cu(I) complexes by varying counterion of tetraphenylborate and hexafluorophosphate. Installing a methyl group at the C_6 carbon centre of C=N bond of phenanthridine allowed to access ligand **L4** and corresponding Cu(I) complex $(L4)_2CuBPh_4$, which showed highest quantum yield and significantly blue shifted emission while binding with tetraphenyl borate as counter ion. Analysing the experimental and theoretical results, it can be concluded that both methyl group functionalization and counterion interaction with cationic part in the solid state prevents excited state geometric distortions, resulting in stronger, blue-shifted emission.
4. I have synthesized *P^N/C^N* ligand based Fe(II) complexes. The octahedral Fe complexes showed interesting CV, spectroelectrochemistry and electronic spectroscopy. In the UV-Vis spectroscopy, broad metal-to-ligand-charge-transfer bands were observed. An interesting blue shift of this charge transfer absorption band was observed for phenanthridine based $(L2)_3Fe(PF_6)_2$ compared with the quinoline complex, $(L3)_3Fe(PF_6)_2$. Study of these complexes could potentially lead to interesting results in the field of long-lived MLCT complexes based photosensitizer design.
5. Finally, I designed Cp* supported *P^N* ligand based Fe complexes. The potential of these complexes to act as catalysts in hydrogenation chemistry is yet to be disclosed. However, a preliminary study suggests better results in future might be achieved by efficient modification of ligand.

7.2. Outlook:

The synthesis of a novel phenanthridine-based *P^N* ligand was achieved with high yields, keeping in mind previously published *P^N* ligands. However, I was not successful in isolating a stable Ni(0) complex which could potentially be very active in various types of catalysis such as reductive couplings and related activation chemistry. By changing phosphine functionalization from phenyl to alkyl, for example *i*Pr or *t*Bu, could increase the σ-donation ability which might stabilize the Ni(0) complexes which may degrade via ligand dissociation. Such ligands could also provide better steric protection (Figure 7.1). For example, the bulky 1,2-*bis*(di-*tert*-butylphosphino)ethane ligand is well known for stabilizing Ni(0) complexes[1].

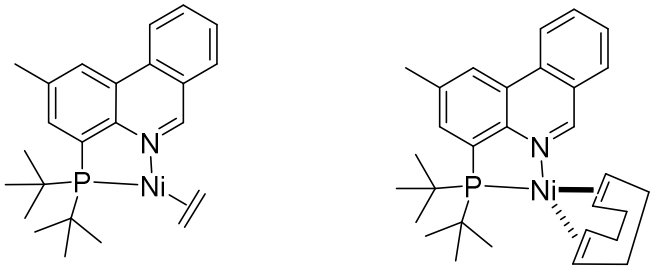

(L)Ni(ethylene) **(L)Ni(COD)**

Figure 7.1: *P^N* t*ert*-butyl phosphino phenanthridine based Ni(0) complexes

The $(P^N)_2$Cu(I)X complexes showed impressive photophysical properties and revealed an interesting synergistic effect, but still there are opportunities for development. These new variants of ligands (Figure 7.2) could potentially provide more steric bulk and further prevent excited state geometric rotations of complexes in their excited states, which may result in better outcome with regards to emission.

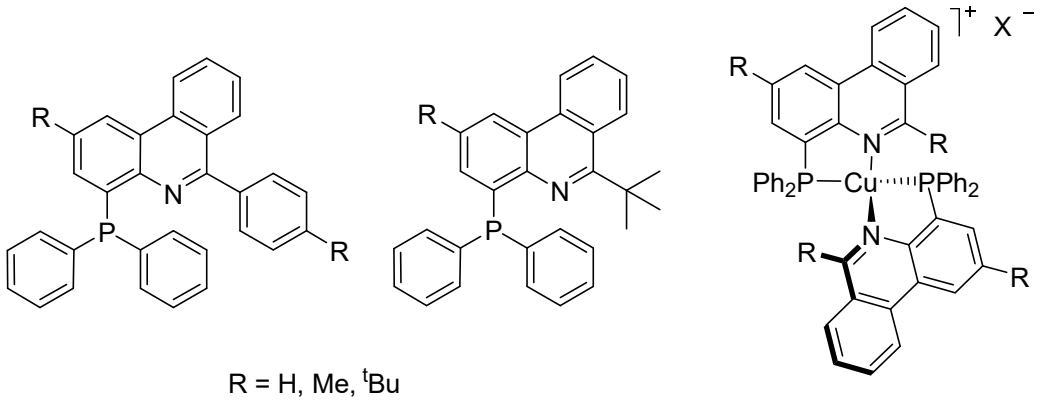

Figure 7.2: Bulky *P^N* ligand based Cu(I) complexes

Acetylide-ligand based Cu complexes $(\mathbf{L6})_2Cu_2(acetylide)_2$ and $(\mathbf{L6})_2Cu_2(acetylide)$ could potentially be very efficient solid-state emissive materials. However, ligand design is required for isolation of single compound and complete characterization. In this regard, ligands **L2** and **L5** may give better results because those ligands are less soluble than ligand **L6**. These complexes may potentially be good candidates for OLEDs design.

Similarly, more extensive study is required for $(\mathbf{L})_2M(PF_6)_2$ (L = **L2** or **L8**; M = Fe or Ru) complexes, which may exhibit the type of long lived MLCT-type excited states required for application as photosensitizers.[5] Transient absorption study of these complexes would help for better understanding about the excited state of these octahedral complexes. Full characterization of *C^N* ligand **L8** based Ag, Fe, Ru and Ir (Figure 7.3) could potentially be very intriguing for medicinal,[2] catalysis[3] and photochemistry[4] based on literature on similar complexes. In Ru complex ($[(\mathbf{L8})_2Ru_2Cl_2](PF_6)_2$), the labile chloride ligand could be replaced by different chelate ligand, such as bipyridine, 9,10-phenanthroline as well.

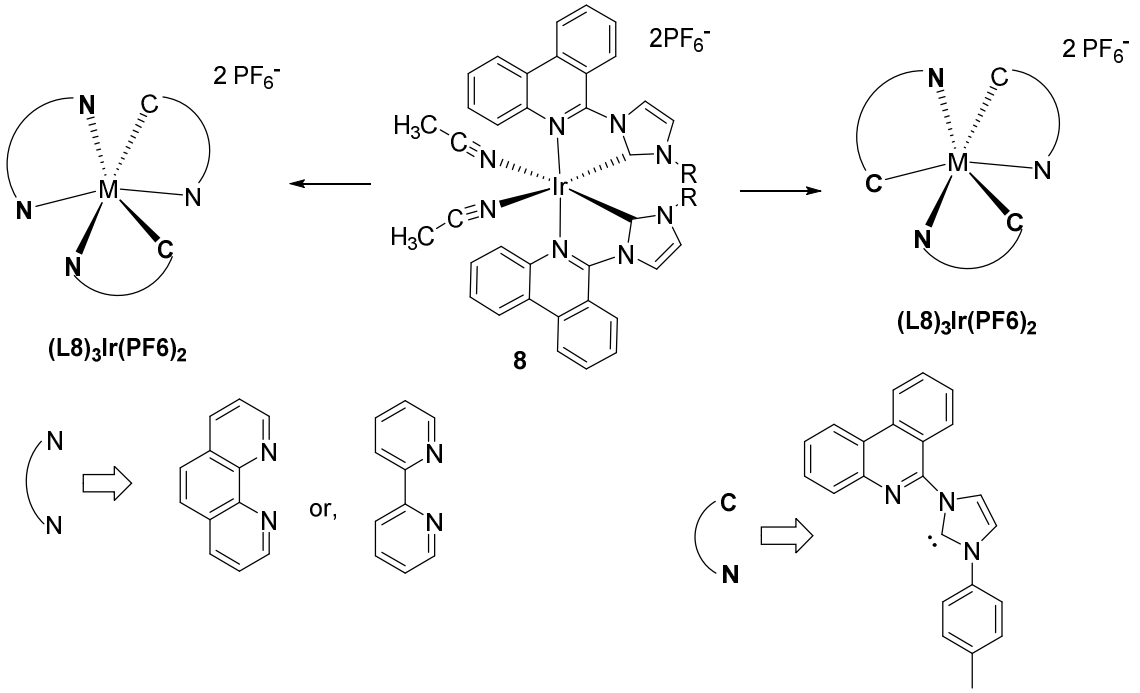

Figure 7.3: Possible photoemissive octahedral iridium complexes

Ligand modification is also required to better stabilize Cp* supported Fe complexes. The isopropyl phosphine version ligand (**L4**) with an electron withdrawing substituent at the para position of imine carbon of phenanthridine ring (Figure 7.4) may enhance the Lewis acidic character of the imine carbon (C=N), helping to promote β-hydride elimination from a metal bound formate.

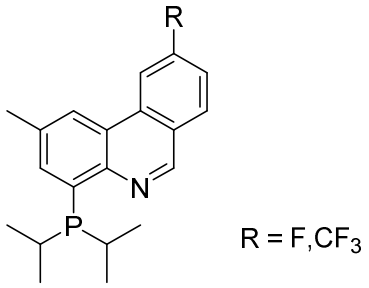

Figure 7.4: Possible ligand for hydrogenation chemistry.

In conclusion, in this thesis, I have explored a series of novel bidentate *P^N* and *C^N* ligands, their synthesis, characterization and explored their coordination properties with late transition metals. Functionalization of π-extended phenanthridine for use as a ligand with late transition metals is rare in the coordination chemistry/organometallic chemistry field. Phenanthridine has been extensively used (Section 1.3.3) in the biological field. On the contrary, the lack of reported work of phenanthridine in the chemical field is noticeable. Thus, we wanted to persue our research in this field. The reported results of this thesis help us to explore some unknown side of π-extended phenanthridine such as the effect of site-selective π-extention on emission, coordination properties with late transition metals while binding with phenanthridine installed ligand. However, a proper ligand design could bring more efficient results.

7.3. Reference:

(1) Mindiola, D. J.; Waterman, R.; Jenkins, D. M.; Hillhouse, G. L. Synthesis of 1,2-Bis(Di-Tert-Butylphosphino)Ethane (Dtbpe) Complexes of Nickel: Radical Coupling and Reduction Reactions Promoted by the Nickel(I) Dimer $[(Dtbpe)NiCl]_2$. *Inorg. Chim. Acta.* **2003**, *345*, 299–308.

(2) Hemmert, C.; Fabié, A.; Fabre, A.; Benoit-Vical, F.; Gornitzka, H. Synthesis, Structures, and Antimalarial Activities of Some Silver(I), Gold(I) and Gold(III) Complexes Involving N-Heterocyclic Carbene Ligands. *Eur. J. Med. Chem.* **2013**, *60*, 64–75.

(3) Zheng, Y.; Tan, Y.; Harms, K.; Marsch, M.; Riedel, R.; Zhang, L.; Meggers, E. Octahedral Ruthenium Complex with Exclusive Metal-Centered Chirality for Highly Effective Asymmetric Catalysis. *J. Am. Chem. Soc.* **2017**, *139*, 4322–4325.

(4) Jiang, B.; Gu, Y.; Qin, J.; Ning, X.; Gong, S.; Xie, G.; Yang, Chuluo. Deep-Red Iridium(III) Complexes Cyclometalated by Phenanthridine Derivatives for Highly

Efficient Solution-Processed Organic Light-Emitting Diodes. *J. Mater. Chem. C* **2016**, *4*, 3492–3498.

(5) Liu, Y.; Persson, P.; Sundström, V.; Wärnmark, K. Fe N-Heterocyclic Carbene Complexes as Promising Photosensitizers. *Acc. Chem. Res.* **2016**, *49*, 1477–1485.